Technische Universität München
Fakultät für Physik
Physics of Energy Conversion and Storage

# Direct Instrumental Identification of Catalytically Active Sites Using Electrochemical Scanning Tunneling Microscopy

Yunchang Liang

Vollständiger Abdruck der von der Fakultät für Physik der Technischen Universität München zur Erlangung des akademischen Grades eines

Doktors der Naturwissenschaften (Dr. rer. nat.)

genehmigten Dissertation.

Vorsitzender: Prof. Dr. Martin Zacharias

Prüfer der Dissertation:
1. Prof. Dr. Aliaksandr S. Bandarenka
2. Prof. Dr. Julia Kunze-Liebhäuser

Die Dissertation wurde am 07.01.2019 bei der Technischen Universität München eingereicht und durch die Fakultät für Physik am 24.01.2019 angenommen.

# Abstract

In modern industry, heterogeneous catalysis plays a key role, as it is essential for tackling the global environmental and energy issues. It is known that the activity of heterogeneous catalysts is determined by the electronic structure of specific surface sites with optimal binding energy to the reaction intermediates. These specific surface sites are known as the active sites (centers) of catalysts. Basic knowledge of the properties (geometry and chemical composition) of the active centers is crucial to the fundamental understanding of heterogeneous catalytic processes and the rational design of optimal catalysts for practical applications. Therefore, a direct method for identification of the active catalytic centers under reaction conditions is needed.

Herein, a novel *in-situ* methodology capable of direct identification of catalytically active centers using electrochemical scanning tunneling microscopy (EC-STM) under reaction conditions is introduced. The basic concept of this methodology is based on the fact that fluctuations in the tunneling current caused by catalytic reactions at the active centers should result in non-uniformly distributed noise features in the captured images correlated to the local activity, therefore the active centers can be distinguished. The focus of this thesis is the elaboration of this method (EC-STM noise method, denoted as 'n-EC-STM' in this work) using well-studied model catalytic systems and expanding this method to other systems, where the nature of active centers has been under debate or not clear.

To test the proposed method, catalytic systems important for future energy provision were used: the hydrogen evolution reaction (HER) and the oxygen reduction reaction (ORR) on platinum (Pt), palladium (Pd) and gold (Au) based catalysts. The obtained results were also in agreement with the existing literature reports, confirming the applicability of the method.

The n-EC-STM method was then used to address the questions concerning the electrolyte effects on the catalytic activity of Pt-based catalysts in alkaline media and identification of active centers at the surface of other bi-metallic catalysts: Pd and Pt sub-monolayers on Au(111). Finally, visualization and engineering of active centers on transition metal dichalcogenide (TMD) catalysts (*i.e.*, Molybdenum disulfide ($MoS_2$) and molybdenum diselenide ($MoSe_2$)) towards HER were performed.

This developed method is expected to contribute to the fundamental research in heterogeneous catalysis and stimulate the development of similar techniques. Additionally, the findings reported in this thesis can be used for optimization of existing electrocatalytic systems.

# Acknowledgements

My PhD journey was filled with exciting scientific findings and joy. I received great support and encouragement from many amazing people. I would like to take this opportunity to express my gratitude to the following people:

**My parents** for your unlimited care, love and support.

**Prof. Dr. Aliaksandr S. Bandarenka** for giving me the great opportunity to join the ECS group and guiding me to be a better scientist. Thank you for everything!

**Prof. Dr. Julia Kunze-Liebhäuser** for accepting to be the second reviewer and all the knowledge I acquired from your group ever since I started studying electrochemistry and EC-SPMs.

**Dr. Oliver Schneider** for being an excellent mentor in science and life.

**Jonas Pfisterer, Christoph Csoklich and David McLaughlin** for all your great works, support and patience. Those works in this thesis would not have been possible without you guys. I had a great time with you and learned a lot from you!

**Lukas Seidl, Wenbo Ju, Hongjiao Li, Sladjana Martens, Jiwei Ma and all those people who helped me during my early stages of my master and PhD** for introducing me to the electrochemistry and EC-SPM world, and being wonderful friends.

**Daniel Scieszka, Jeongsik Yun, Philipp Marzak, Viktor Colic, Marcus Pohl, Paul Scheibenbogen, Jongho Kim, Albrecht Dorsel and all the people who are still or were working in the ECS group** for making the ECS group such a warm place to work and have fun as well as supporting me during my **PhD** and thesis writing

**Elmar Mittereiter, Matthias Golibrzuch, Dr. Ursula Wurstbauer and Prof. Alexander Holleitner** for the wonderful collaboration and discussions

**Siegfried Schreier** for keeping our experiments running properly.

**My office mates Dr. Batyr Garlyyev, Song Xue, Sebastian Watzele, Johannes Fichtner, Dr. Weijin Li, the refrigerator and the old sofa** for all your help and everyday entertainment to motivate me to come to work every day.

**Our football and card games** for giving us so much fun.

**Multimode** for producing excellent images and helping us to build our patience by its hardly speculative character.

**My lovely wife Shuna** for your love and inspiration.

# Table of Contents

# 1 Introduction

## 1.1 Climate Change and Heterogeneous Catalysis

Discussions on climate changes have become commonplace nowadays [1]. Numerous consequences and even conflicts have been caused by the huge consumption of conventional energy sources, *e.g.*, coal or oil[2, 3]. Attempts in different directions have been made to decelerate and ideally stop the damage to the climate and human society. Renewable energy sources, for instance, solar energy, wind power, and bioenergy[4], and fusion power[5] instead of troublesome fission power, are promising less harmful alternatives to conventional energy sources. Also changes in the personal lifestyle can contribute to limit negative impacts on the environment. Electric vehicles including fuel cell cars are turning to be more popular[6]. Moreover, industrial processes should be improved for the sake of the environment and economy[7]. A so-called 'Hydrogen Economy',[8, 9] where hydrogen plays the role of a major energy carrier, has been suggested to replace the current carbon-dominated energy economy. In many of the aforementioned challenges and solutions, heterogeneous catalysis is involved. It accelerates the reaction rate and reduces undesired side-products without changing the catalyst phase[10]. Basically, it makes energy-related processes more efficient. Heterogeneous catalysis plays an important role in ~80% of chemical and energy industries[11]. These are key energy consumers and providers. Therefore, research and development of heterogeneous catalysis are crucial to a sustainable, efficient, and healthy future.

Observations of catalytic phenomena can be traced back to almost two centuries ago when Johann Wolfgang Döbereiner discovered that platinum powders can increase the velocity of oxidation of hydrogen into water[12]. Later, in 1835 Jöns Jakob Berzelius employed the term 'catalysis' to name this type of phenomena[13]. In the 1900s, Wilhelm Ostwald systematically investigated the fundamental principles governing chemical equilibria and reaction rates of catalytic processes and commercialization of them[14]; he was awarded the Nobel Prize in chemistry in 1909 for this research[15]. Until now, these principles (*e.g.*, chemical equilibrium, reaction rate, introduced by Ostwald) are still used in catalysis studies. The investigation on catalysis underwent revolutionary changes over the last two centuries. Döbereiner only realized that Pt can be used as a catalyst, while Ostwald tried to define the fundamental

principles of catalysis. Nowadays, scientists are trying to figure out how catalysis takes place at atomic scales and optimize the activity, selectivity and stability of catalytic materials.

One example showing the development of catalysis research is the Haber-Bosch process of ammonia synthesis. The Haber-Bosch process permitted a production of an artificial fertilizer on an industrial scale. It enables synthesis of ammonia from atmospheric nitrogen [16, 17] contributing to population growth in the 20th century[18]. The scientists, namely, Fritz Haber and Carl Bosch, who developed this process, were awarded the Nobel Prize in chemistry in 1918 and 1931, respectively. For this specific reaction, 20.000 catalysts candidates were assessed by Bosch and co-workers[17]. It was rather a trial-and-error procedure.

Indeed, there is an evolution of knowledge and technologies that changed the targets and methodologies of catalysis research. Decades after the invention of the Haber-Bosch process, Gerhard Ertl and co-workers fundamentally explained the principle of the chemical reaction on the solid surfaces including ammonia synthesis on iron catalysts[19, 20, 21, 22]. In the meantime, they developed methods for surface chemical reaction studies. Because of these, Ertl got the Nobel Prize in chemistry in 2007[23]. There are of course other important findings in the field of catalysis, particularly heterogeneous catalysis. In 1925, Hugh S. Taylor had already suggested that ‘‘only a small fraction of the surface is active’’[24]. Indeed, the active centers are often not the major portion of the whole catalyst surface, but they determine the overall catalytic activity.

## 1.2 Challenge: Identification of Catalytically Active Centers

Nowadays, a major focus of heterogeneous catalysis research is set on the catalytic process taking place at the active centers of a number of selected catalyst candidates. The fundamental understanding of the nature of the catalytically active centers is one of key aspects and the identification of these active centers has been one of the primary tasks[25, 26]. For that, experimental and theoretical works are usually combined. Model systems directly related to processes relevant to chemical and energy industries, *e.g.*, controlled hydrogen evolution, oxygen reduction reactions on single crystalline catalysts, are often utilized in laboratories[10]. A wide range of different, complementary methods is applied today, and corresponding instrumentation, *e.g.*, potentiostats, X-ray photoelectron spectroscopy (XPS)

equipment, (electrochemical) scanning probe microscopes ((EC-) SPMs), are commonly employed nowadays. Particularly, the electrochemical scanning tunneling microscopy (EC-STM) is capable of probing the electrified liquid/solid interface, where heterogeneous catalytic reactions take place at the atomic scale[27, 28]. However, EC-STM measurements were normally performed focusing on changes in morphology, often even in the absence of reactions in order to have an image resolution as high as possible. Even *in-situ* or *operando* EC-STM measurements are intended to observe topographic changes just as consequences of the reactions. Therefore, identification and evaluation processes of those active centers normally combine *ex-situ* microscopic experiments with theoretical calculations and other macroscopic studies, for instance, catalytic activity tests in electrochemical cells[29, 30]. This methodology is rather indirect and time-consuming so that a direct and readily means of *in-situ* identifying active centers is needed.

## 1.3 Identification of Catalytically Active Centers Using Electrochemical Scanning Tunneling Microscopy (EC-STM)

In the early 1980s, the scanning tunneling microscope (STM) was invented by Binnig and Rohrer[31] and a few years later the EC-STM was introduced[27, 28]. Both STM and EC-STM have made great contributions to the research field of heterogeneous catalysis[32, 33, 34]. Except topographic imaging, they have been employed on the investigations of local surface reactions[35, 36] and the local activity/reactivity[25, 37, 38] in different systems, where additional signals to the tunneling current (which only correlates with the surface topography) due to the investigated surface reactions were utilized. However, direct identification of catalytically active surface centers under reaction conditions was not accomplished in the above-mentioned studies. Indeed, these approaches still showed that EC-STM is a promising tool for local activity measurements in heterogeneous catalytic systems.

In this thesis, a novel approach for the direct identification of active centers at heterogeneous catalyst surfaces under reaction conditions is introduced and experimentally verified. It is based on the analysis of the tunneling current noise measured using conventional EC-STM experiments, and provides direct information on the local reaction rate. This method (denoted as ‘n-EC-STM’) then is utilized to shed light on recent questions concerning the electrolyte

influence on catalyst activity, as well as to identify the active centers at bi-metallic and newly developed non-metallic catalyst surfaces.

## 1.4 Aim of the Thesis

The aim of this thesis is the verification and application of the proposed methodology (n-EC-STM) of direct identification of active centers at heterogeneous catalyst surfaces under reaction conditions. A detailed explanation of the concept of the n-EC-STM is presented in Chapter 3.2.

The first task is to verify the proposed methodology with well-studied model catalytic systems where the locations of the most active centers are known. The first model system was hydrogen evolution reaction (HER) on single crystalline Pt(111) in acidic media, where the most active sites are the step-concavities as confirmed by both theoretical and experimental studies[39]. Moreover, catalytic hydrogen evolution at the surface of bimetallic catalysts, namely Pt multilayers on Au(111) and Palladium (Pd) sub-monolayer islands on Au(111), in acidic media was studied. The Pt and Pd adlayers were deposited on a Au(111) substrates via overpotential and underpotential deposition methods, respectively. In the case of Pt multilayers on Au(111), the contrast in the HER activity of the Pt and Au was utilized to confirm the actual origin of the tunneling current noise. The Pd sub-monolayer islands on Au(111) surface have a property that the most active sites towards the HER are the Pd atoms at the boundary of Pd and Au[40, 41, 42, 43]. The oxygen reduction reaction (ORR), as a ‘‘sluggish’’ reaction which highly influences the performance of fuel cells[44] and metal-air batteries[45], was also investigated. The difference in the ORR activity of Pt and Au(111) was used to test the capability of this methodology for the investigation of catalytic reactions with relatively low reaction rates. The model catalysts in the case of the ORR were Pt overlayers on Au(111) and Pt(111) single crystal electrodes. It was reported that the most active sites on Pt surfaces towards the ORR are located at the step-concavities[29, 46, 47, 48, 49, 50]. The preparation of these model samples is presented in Chapter 3.3. The results of the n-EC-STM measurements confirmed the findings mentioned above and thus verified the methodology proposed in this thesis, as presented in Chapter 4.1.

The n-EC-STM was also applied to study other catalytic systems where the activity contributions of different surface sites are not clear, namely the ORR and the HER on Pt single crystal electrodes in alkaline media, the HER on Pt sub-monolayer islands on Au(111) and on transition metal dichalcogenides (TMDs, namely molybdenum disulfide ($MoS_2$) and molybdenum diselenide ($MoSe_2$)) in acidic media. These systems are involved in future energy provision schemes. Interestingly, the catalytic activity of the various Pt surfaces in alkaline media is different compared to that in acidic media[51, 52, 53]. The activity of the Pt surfaces is seemingly influenced by the electrolyte composition. In acidic media, the Pt sub-monolayer islands on Au have distinctive HER activity-*vs*-Pt coverage trend compared with the case of Pd/Au[38, 54]. The TMDs are promising non-metallic and cost-effective HER catalyst alternatives[55, 56], however, only the active centers of nanoparticulate $MoS_2$ was reported to be the edge sites[30] and the location of the active centers on the bulk $MoSe_2$ is still under investigation. Moreover, surface defects at the $MoS_2$ basal plane can play the role of new catalytic HER active centers[57]. The n-EC-STM measurements provided direct evidence of the location of the active centers in these systems and strategies to further improve the catalytic activity of their overall activities. The applications and results of the n-EC-STM investigation on the aforementioned systems are presented in Chapter 4.2.

# 2 Fundamentals

## 2.1 Fundamentals of Electrochemistry

In general, catalysis is divided into three types: heterogeneous, homogeneous, and enzyme catalysis. Reactants and the catalysts are in the same phase in homogeneous catalysis. Enzyme catalysts are protein-based catalysts, and enzyme catalysis is often classified as a kind of heterogeneous catalysis. Heterogeneous catalysis happens at the interface of different phases, *e.g.*, the solid–liquid interface, in which the solid phase side plays the role of the catalyst. After the reaction, the catalyst can be easily separated from the reactants and products. This is advantageous for industrial applications. Electrocatalysis is a part of heterogeneous catalysis. The place where the electro-catalytic processes take place is the (electrified) solid-liquid interface. In the following, the current understanding of the latter is introduced.[10]

### 2.1.1 Electrified Solid–Liquid Interface and Electrochemical Reactions

The formation of an electrified solid–liquid interface starts with an electrode (electronic conductor) immersing into an electrolyte (ionic conductor). To establish an equilibrium, in which the electrochemical potentials ($\bar{\mu}$) of each species in the solid and the liquid phases are identical (see Equation 2.1.1-1), rearrangements of the "electronic charges" in the solid phase and the "ionic charges" in the liquid phase close to the phase boundary often take place. In some cases, the oxidation-state of certain species can be changed, and some species can transfer between two phases.[58]

$$\bar{\mu}_i^l = \bar{\mu}_i^s \qquad \textit{Equation 2.1.1-1}$$

$\bar{\mu}_i^l$ and $\bar{\mu}_i^s$ are the electrochemical potentials of species $i$ in liquid and solid phases, respectively. The electrochemical potential of $i$ in $\alpha$ phase is define as Equation 2.1.1-3.

$$\bar{\mu}_i^\alpha = \mu_i^\alpha + z_i F \phi^a \qquad \textit{Equation 2.1.1-2}$$

$$\mu_i^\alpha = \left(\frac{\partial G}{\partial N_i}\right)_{p,T,N_{j\neq i}} \qquad \textit{Equation 2.1.1-3}$$

$z_i$ is the charge of species $i$, $F$ is the Faraday constant and $\phi^\alpha$ represents the local electrostatic potential. $\mu_i^\alpha$ is the chemical potential of species $i$ in $\alpha$ phase, which is the required/released work $\partial G$ to change the particle number $\partial N_i$ of species $i$ at constant pressue $p$, constant temperature $T$ and constant particle numbers of other species $N_{j\neq i}$. $G$ is the Gibbs free energy of the $\alpha$ phase. The electrochemical potential contains the chemical potential $\mu_i^\alpha$ and the effect of local electrostatics $z_i F\phi^\alpha$ for charged species (*e.g.* ions).[59]

In 1853, Helmholtz was the first to introduce a model describing this balance, namely the Helmholtz model of the electrical double layer (EDL). He demonstrated that at the electrode/electrolyte interface two charged layers are formed. One layer is the polarized electrode surface, and the other layer is the sum of rearranged electrolyte ions representing the opposite charge in parallel with the first one.[60]

The following studies suggested that the so-called EDL consists not just simply of two parallel layers as suggested by Helmholtz, especially from the liquid side. The Gouy–Chapman–Stern–Grahame (GCSG) model modified by Bockris, Devanathan, and Müller is commonly recognized[61, 62]. The total charge of two phases should be neutralized at equilibrium. First, a water dipole layer closest to the electrode surface is oriented corresponding to the charge of the electrode surface. Second, the remaining species together with solvation shells get rearranged in a way that the concentration of ions with opposite charges to the surface decays exponentially from a specific point near the surface to the bulk electrolyte. Furthermore, some of those species, named non-specifically adsorbed ions, are accumulated in the first water layer with their solvation shell by the unbalanced surface charge. Another type of adsorption regardless of the charges of the electrolyte species and the surface is called “specific adsorption”. The specifically adsorbed species lose a certain part of their solvation shell so that they are directly in contact with the surface. The plane connecting the centers of the specifically adsorbed ions is the inner-Helmholtz plane. Another plane passing through the centers of the non-specifically adsorbed ions is the outer-Helmholtz plane. This plane is the starting point of the exponential decay of the ion concentration mentioned above. The diffuse double layer (or diffuse layer) starts from the outer-Helmholtz plane to the bulk electrolyte. The potential grows (or drops) linearly from the surface to the outer-Helmholtz plane. It increases (or decreases) non-linearly related to the concentration decay of the ions in the diffuse layer.[61, 61]

Based on the concept mentioned above, a typical EDL structure is sketched in Figure 1 for a negatively charged metallic electrode where anions are specifically adsorbed in an aqueous electrolyte. The real structure of the EDL is more complex and still under investigation. Even the specific and non-specific adsorption phenomena cannot be applied to all interfacial systems with different parameters, *e.g.*, different electrode potentials or electrolyte species.[61]

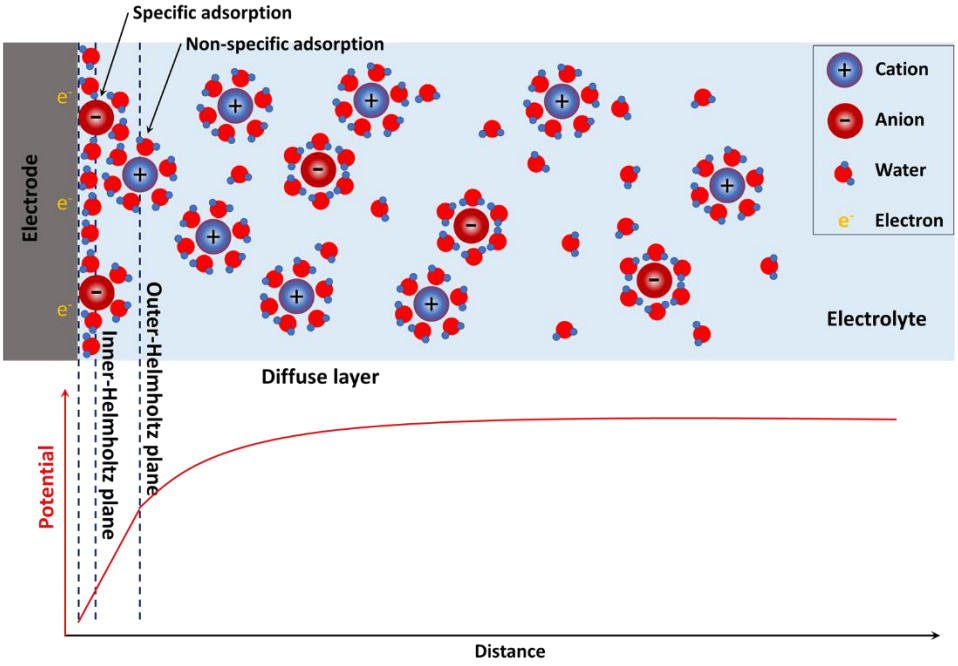


*Figure 1.* ***An EDL model of a metallic negatively charged electrode in an aqueous electrolyte.*** *The relative concentration of cation starts from the outer-Helmholtz plane. The model does not refer to any particular electrode material, electrolyte species or other parameters, and it is based on ref. 61, 61, 63.*

An important parameter, the electrode potential, is different from the chemical or electrochemical potentials. The potential of an electrode is an potential difference between the electrode and the bulk electrolyte. The absolute value of the electrode potential is not measurable, and another electrode has to be introduced into the electrolyte in order to measure the potential of the electrode of interest. Therefore, the measured value is the potential difference between two electrodes. The unit of the electrode potential is volt (V) instead of J/mol. Normally a rational electrochemical system consists of three electrodes, including a working electrode (WE), a counter electrode (CE) and a reference electrode (RE).[63] In this thesis, the electrode potential is often called 'potential' or represented by 'E'.

When charges (electrons) transfer across the interface, the involved species will change their oxidation states; this is known as oxidation or reduction of them. It results in a current flow with a completed electric circuit. For outer-sphere reactions, a strong interaction between the reactants/products and the electrode surface is not involved in the reaction processes. In between the reactants/products and the electrode surface there is at least a layer of solvent (*e.g.*, water). However, in the case of inner-sphere reactions (including the electrocatalytic reactions studied in this thesis), specific adsorption of the reactants, products and reaction intermediates on the electrode surface often takes place. It is often accompanied by phase changes of the involved species. The electron donors or acceptors are the adsorbates or surface atoms. Consumption or production of adsorbates changes the surface concentration of the involved species. This is coupled with the mass transfer between the surface and the so-called diffusion layer. [63, 64]

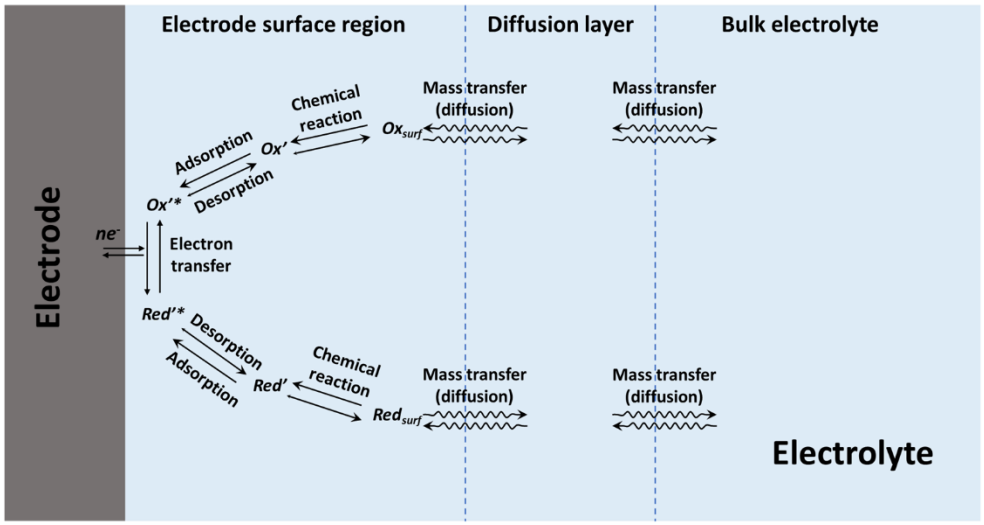


*Figure 2.* ***General pathway of electrochemical reactions at the solid–liquid interface, based on ref. 63.*** *The participating species Red and Ox will be introduced in chapter 2.1.3. The surface sites binding the adsorbates are represented as *.*

As shown in Figure 2, to complete an electrochemical reaction, a system needs to go through multiple intermediate steps including electron transfer, coupled chemical reactions (*e.g.*, catalytic decomposition, complexation and disproportionation), adsorption/desorption (or possible crystallization of the involved species), diffusion of the species (mass transfer), and reorientation of the water molecules and solvation shells (water shell in aqueous electrolytes). Among all these steps, the overall reaction rate is determined by the slowest one, which is the

rate-determining step. A reaction is governed by the charge-transfer (reaction kinetics) limit when the reaction rate is low enough that mass transfer is sufficiently fast. Otherwise, the reaction may be in the mass transfer limited region, or under mixed control.[63]

### 2.1.2 Three-electrode System

An electrochemical system, in which reactions can be conducted and studied, requires a complete circuit. The current is carried by the flow of electrons in the electrodes and the external circuit and ions in the electrolyte. Therefore, at least two electrodes immersed into the electrolyte and external electrical connections are necessary to build up a functional electrochemical system. This is the so-called electrochemical cell. Normally, only the interface at one electrode, the WE, is of interest and under investigation. The other electrode is the CE in a two-electrode system. However, even though one can directly measure the potential difference between the WE and the CE; the CE would suffer the same current and bear a certain potential difference to the electrolyte.[63]

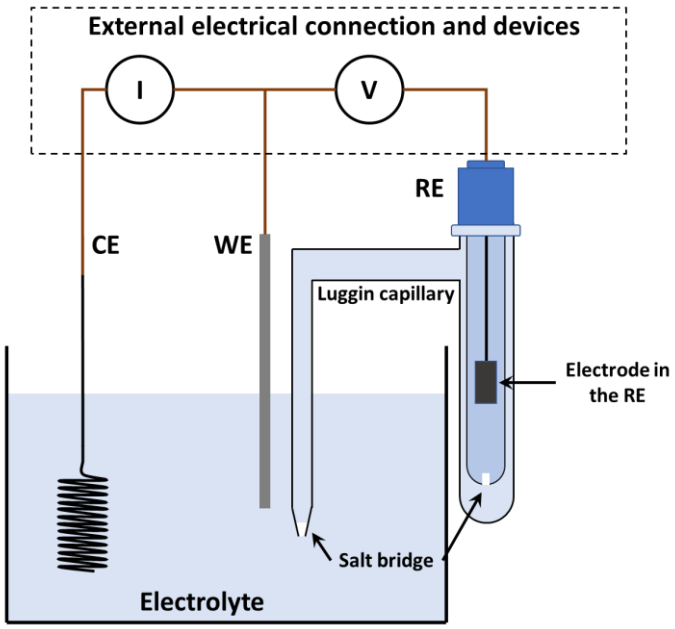


*Figure 3.* ***Basic structure of a three-electrode system.***

To address the issues mentioned above, a third electrode is introduced, which is the so-called RE. The potential of the RE needs to be stable, so it requires a well-defined electrochemical

environment (*e.g.*, electrode material, electrolyte composition, and atmosphere control) and ideally a reversible reaction. It is often placed in an independent chamber filled with electrolyte. The RE chamber is connected to the main cell by a Luggin capillary with a salt bridge. The current flow between the WE and the RE is minimized using a high input impedance for voltage measurements. The CE only provides current flow to the WE. To minimize the possible reactions at the CE, the surface area of the CE should be much larger than that of the WE[65]. The potential of the WE is measured with respect to the RE and the potential of the RE does not depend on the current between WE and CE. Based on this concept, the schematics of a completed three-electrode cell is shown in Figure 3. The interface of the WE, where the individual half-cell reaction takes place, can thus be studied.

### 2.1.3 Reaction Kinetics

A simple one-step reaction system can be used to exemplarily discuss reaction kinetics, as in Equation 2.1.3-1.

$$Red \underset{k_r}{\overset{k_o}{\rightleftharpoons}} Ox + ne^- \qquad \textit{Equation 2.1.3-1}$$

*Red* and *Ox* represent a redox (reduction-oxidation reaction) couple. *Red* is the reduced species and *Ox* represents the oxidized species. The oxidation (anodic) and reduction (cathodic) reaction rates are $k_o$ and $k_r$, respectively. The number of electrons transferred within one reaction is *n*. The reaction rate is often evaluated by measuring the current through the WE. The reaction currents and the electrode potentials determine the electric energy of an electrochemical reaction.

An equilibrium is established when there are still reactions taking place: the net reaction current and changes of the substances are zero, *i.e.*, $k_{o,eq} = k_{r,eq} = k^0$, where $k^0$ is the standard rate constant which depends on the nature of the reaction. The absolute value of the current of each direction is the so-called exchange current, or exchange current density when current is normalized by the electrode surface area.

In non-equilibrium states, the overall reaction shifts toward one side, which has the lower Gibbs free energy *G*. However, in general case, the reactants cannot just transform straight

into products, as shown in Figure 4.A. Both the reactants and products are two relatively stable states of species. The reaction needs to overcome an activation barrier (activation energy $E_A$) to move to the products side, shown in Figure 4.B. The energy released from the reaction is described as the change of the Gibbs free energy $\Delta G$. $\Delta G$ defines the maximum non-expansion work from a thermodynamically closed system. To describe an electrochemical reaction, the change of the Gibbs free energy, $\Delta G$, is more practical. The reaction rate related to the activation energy was proposed by Arrhenius[66, 67], and later developed by Eyring, Evans, and Polanyi[68, 69] as shown in Equation 2.1.3-2.

$$k = \frac{k_B T}{h} e^{-\frac{\Delta G^{\ddagger}}{RT}} \qquad \textit{Equation 2.1.3-2}$$

Where $k_B$ is the Boltzmann constant, $h$ is the Planck's constant, and $R$ is the gas constant. Temperature is represented as $T$. $\Delta G^{\ddagger}$ is the standard Gibbs free energy of activation.

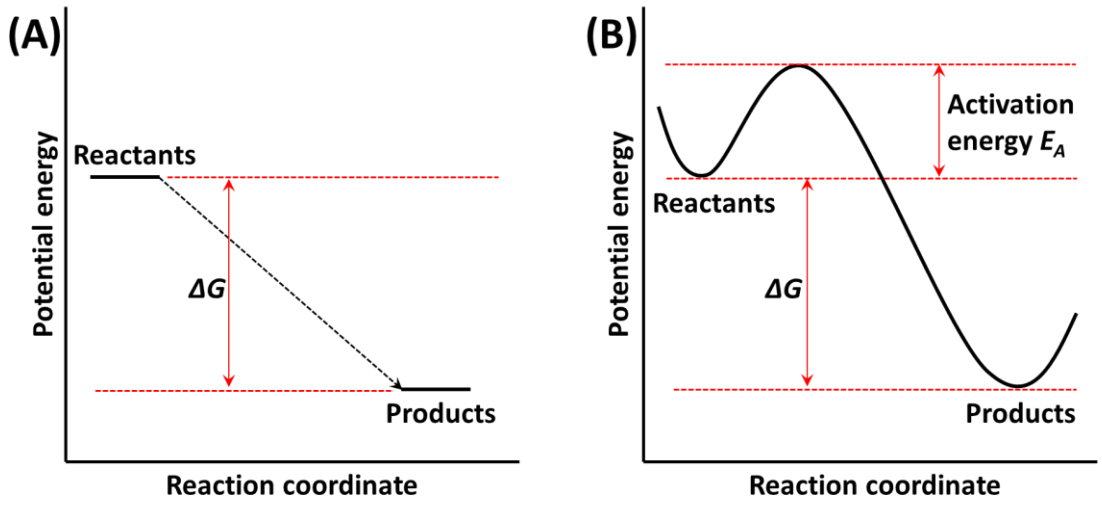


*Figure 4.* ***Simple illustrations of reaction paths (energy diagram) without (A) and with (B) an activation energy barrier and a transition state.*** *ΔG is the change of Gibbs free energy.*

For a reaction with a relatively low activation energy, the reaction direction can be changed easily. In general, two fundamental equations describing the equilibrium and non-equilibrium scenarios should be briefly discussed here. At the electrochemical equilibrium, the net current is zero. The electrode potential is determined by several parameters in the case of the reaction

mentioned above (Equation 2.1.3-1) at the electrode, as given by the Nernst equation (Equation 2.1.3-3)[63].

$$E_{eq} = E^0 + \frac{RT}{nF} ln \frac{a_{Ox}^{\nu_{Ox}}}{a_{Red}^{\nu_{Red}}} \qquad \textit{Equation 2.1.3-3}$$

$E^0$ is the standard electrode potential, $F$ is the Faradaic constant, $\nu$ is the stoichiometric coefficient. The parameter a is the chemical activity of the species, which can be in practice replaced by the ratio of the concentrations of the solutes (or the partial pressure in the case of gas) to their standard values.

At non-equilibrium, the relationship between current and potential without mass transfer limitation can in the simplest case be described by the Butler-Volmer equation[63, 70], as shown in Equation 2.1.3-4.

$$\begin{aligned} i &= nFA[k_r C_{Ox} - k_o C_{Red}] \\ &= nFAk^0 \left[ C_{Ox} e^{\frac{-\alpha n(E-E_{eq})}{RT}} - C_{Red} e^{\frac{(1-\alpha) n(E-E_{eq})}{RT}} \right] \end{aligned} \qquad \textit{Equation 2.1.3-4}$$

$A$ is the electrode surface area, $\alpha$ is the charge transfer coefficient, $C_{Ox}$ and $C_{Red}$ are the surface concentrations of the electroactive species. The term $(E-E_{eq})$ is the ''added'' potential to the equilibrium potential at the electrode, which is known as so-called overpotential $\eta$.

$$\eta = E - E_{eq} \qquad \textit{Equation 2.1.3-5}$$

When a reaction has a large enough $k^0$, a small overpotential can cause a high current density. In this case, the reaction is called a quasi-reversible reaction. Else, the reaction is named an irreversible reaction. If $k^0$ is extremely large that the reaction is always at a state described by Equation 2.1.3-3, the reaction is reversible. The electrode potential of a reversible reaction at with a well-defined electrochemical environment can be easily determined and maintained. Therefore, reference electrodes often utilize such reactions.

To have efficient reactions, for instance, higher current output at lower overpotential applied at the electrode, one option is to increase the standard reaction rate. It requires a decrease of the activation energy, or the standard Gibbs free energy in Equation 2.1.3-2, which can be achieved by introducing catalysts into the system. The focus of this thesis is the kinetics of catalytic (inner-sphere) reactions.

### 2.1.4 Heterogeneous Catalysis

For (electro)chemical reactions taking place at the liquid-solid and gas-solid interface, heterogeneous catalysts are commonly employed. A simple diagram explaining the benefit of a catalyst to a reaction kinetics is shown in Figure 5.A. The activation energy is lowered by the presence of the catalyst. More specifically, the catalyst participates in the reaction by binding the reactants and facilitating the charge transfer process. Afterwards, the products will leave the catalyst surface and diffuse into the bulk phase (*e.g.*, electrolyte). Therefore, there is often a series of reaction intermediate steps with different potential energies as shown in Figure 5.B. It should be noted that, in reality, the reaction pathway with a catalyst is more complicated and in many cases some intermediate reaction steps need to go uphill (to higher potential energy) to form the next reaction intermediates.[10]

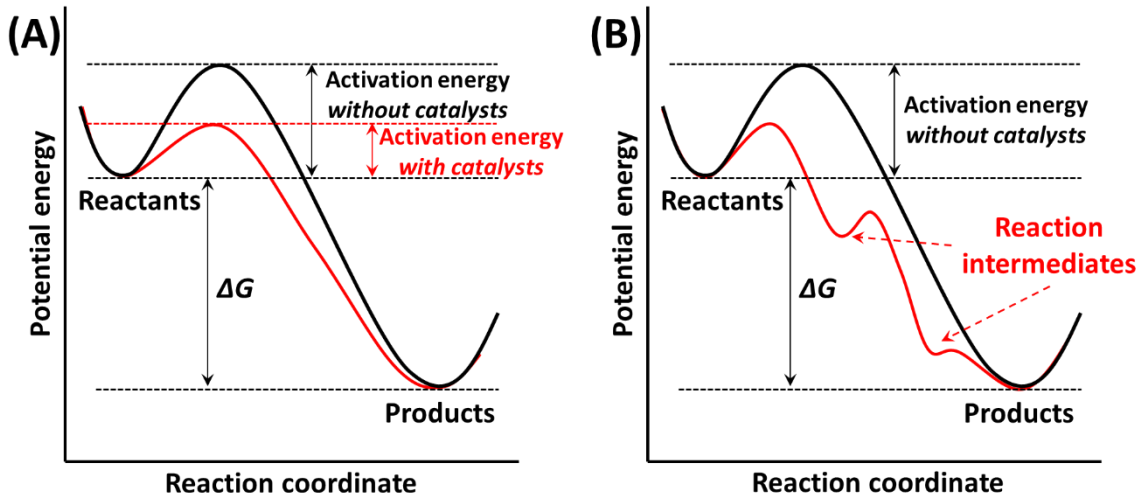


*Figure 5.* ***Simplified explanation of the benefit of the catalyst to the reaction.*** *(A) Reducing activation energy. (B) Changing the reaction mechanism and Introducing reaction intermediate steps.*

Considering that any electrode surface plays a similar role in electrochemical reactions, *i.e.*, an electrode surface is a place where the reaction species are adsorbed on and performing the charge transfer processes, one question can be raised: what makes the catalysts capable of properly catalyzing certain reactions? To answer this question, several properties of a proper catalyst should be discussed: i) a catalyst adsorbs the reactants easily, keeps them staying on the surface to finish each intermediate step with minimized activation energies until the final products are formed; ii) it allows the products to leave the surface quickly

enough to keep the surface sites free for the next reaction event to take place; iii) it governs the reaction in the desired way, so that undesired side-products can be prevented; iv) the performance of a proper catalyst should be preserved over a reasonably long period (long lifetime). These properties can be summarized as the activity, selectivity, and stability of a catalyst.[10]

The optimization procedure of the catalyst material for a certain reaction should be with respect to the properties mentioned above, balanced with the material cost and availability. There are plenty of candidates for each reaction in existence, *e.g.*, pure metallic materials, metal oxides, and alloys[10, 71]. The overall goal is to find or even design the best of them and the process is complicated and time-consuming[10].

### 2.1.5 Catalyst Activity

Among the three properties of heterogeneous catalysts, activity is often the first one to be considered and evaluated[10]. In order to describe the activities of all possible materials with a limited number of descriptors, in 1911 Sabatier (Nobel Prize in Chemistry, 1912) proposed that the bond strengths (binding energy) between the reaction species and the catalyst surface should be optimal[72]. It was named the Sabatier principle afterwards and later illustrated by so-called 'volcano plot'.

In 1972, Trasatti[73] demonstrated the applicability of the Sabatier principle in electrocatalysis using a volcano plot, shown in Figure 6. The investigated reaction was the hydrogen evolution reaction (HER) catalyzed by pure metal electrodes. The descriptor utilized in Figure 6 was the experimentally measured bond strength between intermediate hydrogen and the metal surfaces. According to the plot, there are metals on the right side of the volcano that form 'too strong' binding with hydrogen and that of the others on the left side are 'too weak'. The best candidate for this particular reaction should be located at the top of the volcano. This agrees with properties of a proper catalyst mentioned above.

Different pure metals have different binding energies with hydrogen atoms, and they are either too strong or too weak. To find or even rationally design the best catalysts, the intrinsic properties of catalysts which influence the binding energy need to be explained. One idea is the electronic structure of catalyst surface atoms. Most of the metals that can be used as

catalysts belong to the transition metal family. They have wide and similar s- and p-bands but narrow and dissimilar d-bands. The coupling between the d-states of different metals and the valence states of the same adsorbate species (adsorbed reaction intermediates) result in different binding energies[74, 75]. Based on density functional theory (DFT) calculations, the so-called d-band model, a theoretical model describing the relationship between the metal d-bands and their catalytic activities, was reported by Hammer *et al*.[76, 77, 78].

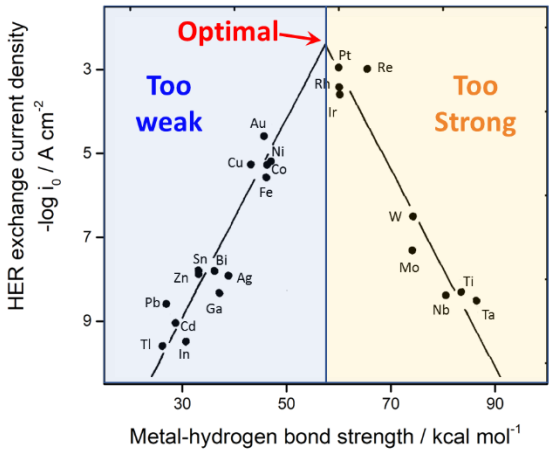


*Figure 6.* ***Volcano plot of the HER activity vs the bonds strength of metal-hydrogen.*** *Adapted with permission from ref. 73. Copyright © 1972 Published by Elsevier B.V.*

As shown in Figure 7.A, one state of the adsorbate interacts with the d-bands of the metal and results into two major states with different energies. The lower state is the bonding state, and the upper state is the antibonding state which prevents the adsorption. For the metallic catalysts, it can be simply explained that the position of the bonding and antibonding states with respect to the Fermi level is the determining factor of the interaction of the metal with the adsorbates. In other words, if only the bonding state is occupied the interaction is attractive, the more antibonding states are filled, the more repulsive the interaction is (weaker binding).[79] For more precisely studies, one has to take into account the so-called coupling matrix elements and the overlap matrix elements[10]. Four different metal model surfaces with H-adsorption were calculated and the results[76] are shown in Figure 7.B. Comparison and further calculation based on the filled states of metal d-bands and H s-band can lead to the conclusion that Pt(111) and Ni(111) are more active towards HER than the other two and Au(111) is the least reactive among them. This approach can be applied to various reaction intermediates with different metal surfaces and gives the volcano plot of the system[76].

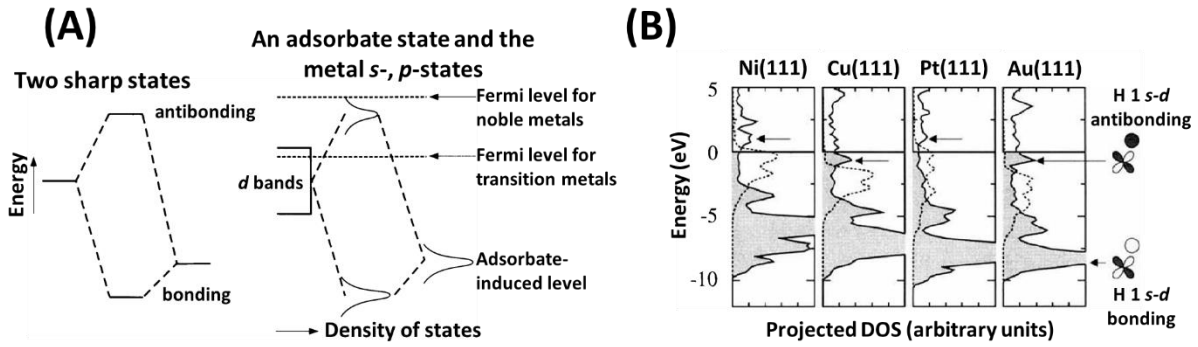


*Figure 7.* ***Schematic illustration of electronic states interaction and theoretical calculation results.*** *(A) Interaction between two electronic states. The left shows the case of two sharp states resulting in antibonding and bonding states with different energies. The right shows the interaction between a state of an adsorbate and the s-, d- bands of a transition metal. It is broadened out to a resonance because of the interaction. The position of the antibonding state with respect to the energy of the Fermi level determines the strength of the adsorption. (B) The density of one-electron states of atomic H adsorbed on Ni, Cu, Pt, and Au (111)-surfaces (solid lines) and the original d-band density of states (DOS) of the metal surfaces (dashed lines). The energy scale is normalized with respect to the Fermi level. With all the four metal surfaces, the H 1s-d bonding states are filled. However, the antibonding states indicated by arrows are only filled within the cases of Cu and Au. Therefore, Ni(111) and Pt(111) surfaces form stronger binding with H atoms than Cu(111) and Au(111). Adapted with permission from ref. 76. Copyright © 1995, Springer Nature.*

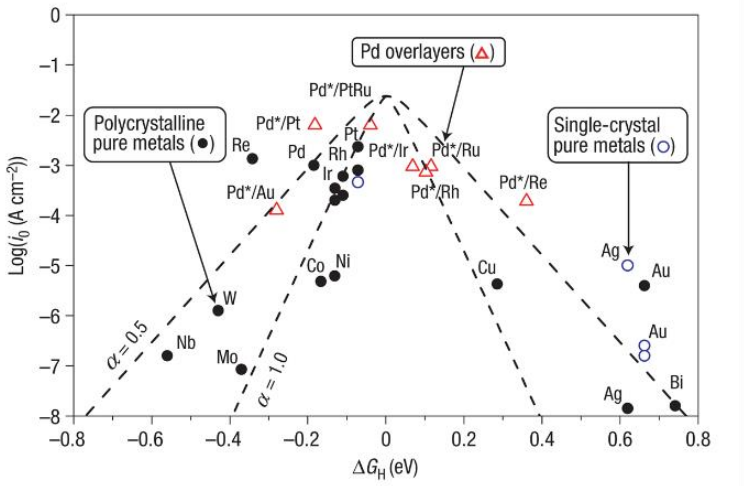


*Figure 8.* ***Updated volcano plot for the HER on single-, poly-crystalline pure metals and metal overlayers.*** *Pd overlayers on metals are represented as Pd*/Metal. The two dashed volcano curves are the activity trends assuming transfer coefficients α of 0.5 and 1.0, respectively. $\Delta G_H$ values are calculated at 1 bar of $H_2$ (298 K) and at a surface hydrogen coverage of either 1/4 or 1/3 monolayer (ML). Figure taken with permission from ref. 81. Copyright © 2006, Springer Nature.*

However, the volcano plot discussed so far does not include all parameters as only (111)-surfaces and pure transition metals are considered. Catalyst surfaces have a high diversity of

geometric structure and chemical composition. All those parameters can influence the electronic structure of the surface atoms and vary the activity[10, 29, 80]. More data points can be added into the volcano plot of HER activity by introducing geometric factors and metal overlayers. Greeley *et al.* summarized related experimental and computational data and reported an updated HER volcano plot (Figure 8)[81]. The plot indicates that even the same material but with different surface geometries (*e.g.*, single-crystalline *vs* poly-crystalline) will have different activities. The surface geometry influences the coordination number of the metal surface atoms (*i.e.*, neighboring atoms of the atom under investigation), and then the bandwidth of the d-DOS of the surface. It is suggested that a higher coordination number results in a wider band. In contrast, a lower coordination number leads to less electronic overlap of a metal surface atom in the vicinity, and subsequently, the d-DOS distribution becomes narrower. To maintain the number of d-band electrons the d-band center shifts up, as shown in Figure 9. Therefore, the metal surface becomes more reactive.[10] Furthermore, Pd overlayers on different substrates demonstrate different activities (substrate effect).

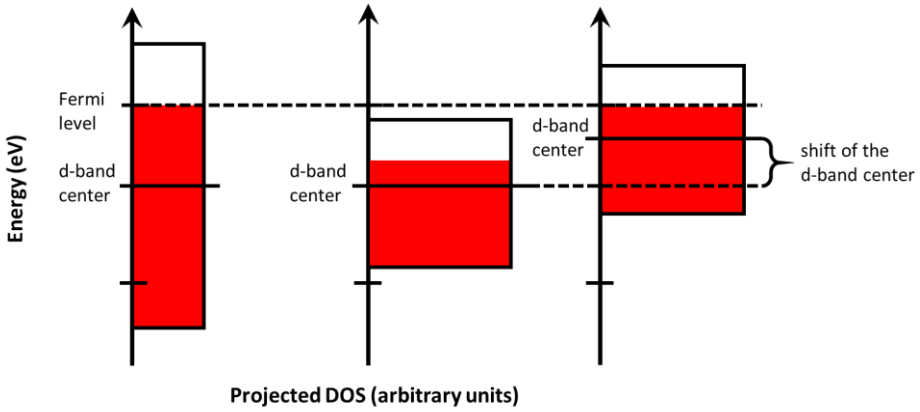


*Figure 9.* ***Schematic illustration of the shift of the metal d-band center (with more than half-filled d-shell) and an electron band with fixed d electron number in response to the change (narrower) of the bandwidth.*** *The d-band center shifts up when the bandwidth becomes narrower to keep the number of d electrons constant. Based on ref. 10.*

Additionally, for instance, a complete oxygen reduction reaction (ORR) cycle involves not only O atoms but also OH, OOH and molecular $O_2$ adsorbed on the catalyst surface. In many cases this complication can be simplified because of a linear dependence of the binding energies of similar adsorbates on each other[82, 83, 84], which are the so-called scaling relations (Figure 10). They can be divided into two types: chemisorption energy scaling relations and transition state

scaling relations. The first describes a linear scaling relation between the adsorption energies of related reaction intermediates. The second scaling relation is between the adsorption energies of an initial state and the transition state. The breaking of the scaling relation happens when the connecting atoms (of the adsorbates or the catalyst surface site atoms) change to others.

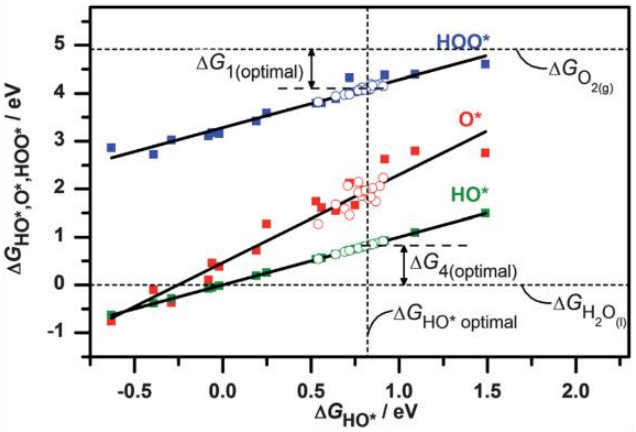


*Figure 10.* ***Plots of binding energies (represented in terms of Gibbs free energy) of adsorption of HOO*, HO*, and O* versus the binding energy of adsorption of HO*, respectively.*** *All data were adapted from theoretical calculations, filled squares represent relations for (111), (100), and (211) pure metal surfaces, open circles represent the relations for Pt overlayers on Pt-alloys surfaces. Taken with permission from ref. 85. Copyright © 2012, Royal Society of Chemistry.*

The major contribution to the catalytic activity consists in the interaction between the catalyst surface and the reaction species. However, the effect of the electrolyte composition on surface processes is not entirely negligible. It has already been taken into consideration for a long time[86, 87, 88]. Until now, experimental studies but no theoretical analysis[89] have proven the importance of electrolyte composition, for instance spectator species, in the activity of the heterogeneous catalysts.

### 2.1.6 Active Centers

Heterogeneous catalysts have complex surface structures and they are often manufactured as nanoparticles to have high surface-to-volume ratios. Therefore, different facets and edges of the nanoparticles are exposed to the electrolyte[10]. Figure 11.A illustrates a catalyst nanoparticle supported by a substrate[90]. Several possible parameters influencing the activity

of the nanoparticle are pointed out, including the surface structure mentioned above. The facets structure and fractions of different facets also depend on the size of the particle. Two palladium (Pd) nanoparticle models with the diameters of 3 nm and 5 nm are shown in Figure 11.B, green, orange, pink, and blue colors correspond to (100), (110), (111) facets, and the boundary atoms, respectively[91]. It should be noted that the ratio of (111) to (100) is reduced for the smaller nanoparticle (3 nm).

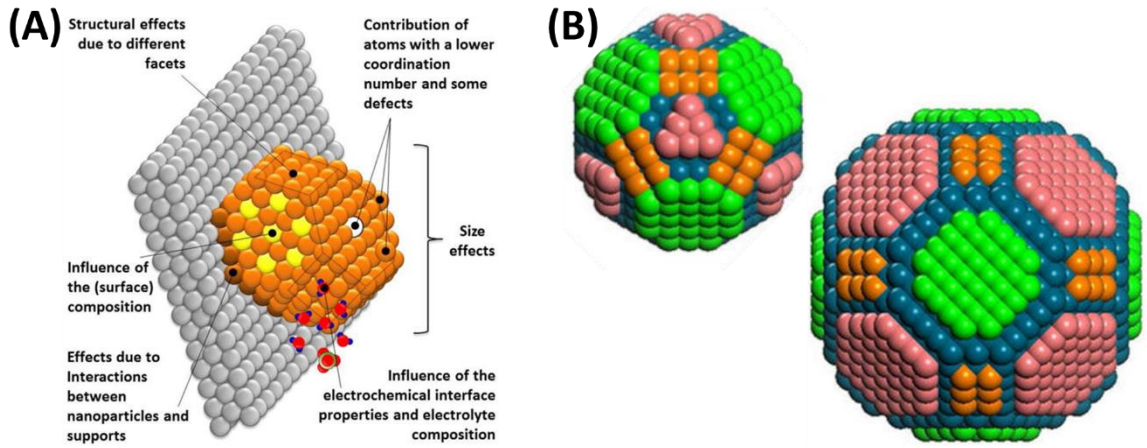


*Figure 11.* ***Illustrations of catalytic nanoparticles.*** *(A) The performance of the supported catalyst nanoparticle influenced by several factors, (B) Facets composition depends on the size of the particle, green, orange, pink, and blue colors correspond to (100), (110), (111) facets, and the boundary atoms, respectively. Images adapted with permission from ref. 90, Copyright © 2013 Elsevier Inc., and 91, Copyright © 2014, Springer Nature.*

As mentioned earlier, Figure 8 indicates that the activities of (111) crystalline and polycrystalline surfaces are not the same. Calle-Vallejo *et al.* reported assessing the optimal active surface sites can be achieved by a simple calculation of the "generalized coordination numbers" and the detailed relation between the coordination number and the activity[29]. Therefore, the activity of the entire catalyst surface should be the overall contributions of all containing structures. However, under a certain reaction condition, each structure contributes differently. In 1925, Taylor suggested that ''only a small fraction of the surface is active''[24], *i.e.*, the overall catalyst activity is determined by the active centers. The active centers should have the optimal binding energies with respect to reaction intermediates. Identification of those active centers is essential to the fundamental understanding of heterogeneous catalysis and manufacturing of better catalyst materials.

## 2.2 Model Reactions and Catalysts

To accomplish the verification and applications of the n-EC-STM methodology, well-studied and economically important catalytic reactions and related catalysts are utilized.

### 2.2.1 Water Electrolysis and Fuel Cell Reactions

There are several reactions that are crucial for sustainable energy systems including water electrolyzers and fuel cells, which play the key roles for the so-called ''hydrogen economy''[92, 93]. These are the oxygen evolution reaction (OER), the oxygen reduction reaction (ORR), the hydrogen oxidation reaction (HOR), and the hydrogen evolution reaction (HER). The current *vs* potential dependencies for all four reactions can be plotted together with simplified reaction equations as shown in Figure 12. The electrolyzers utilize water electrolysis to produce oxygen and hydrogen through OER and HER, respectively, and the products can be consumed electrochemically by performing spatially separated ORR and HOR in fuel cells. In an electrochemical cell filled with an aqueous electrolyte, all four reactions can occur and form two redox reactions as illustrated in Equation 2.2.1-1 and Equation 2.2.1-2.

$$2H_2 \rightleftharpoons 4H^+ + 4e^- \qquad \textit{Equation 2.2.1-1}$$

$$2H_2O \rightleftharpoons O_2 + 4H^+ + 4e^- \qquad \textit{Equation 2.2.1-2}$$

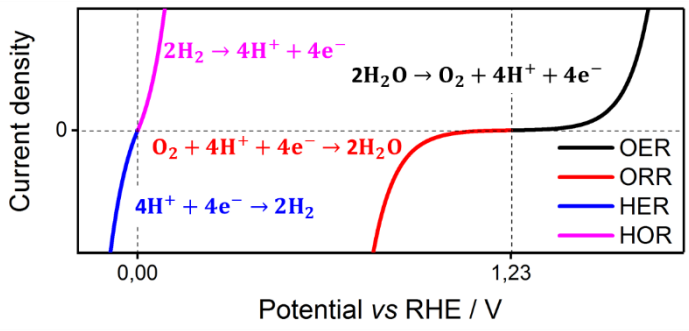


*Figure 12.* ***Fuel cell reactions, HOR and ORR, and water electrolysis reactions, OER and HER.*** *The equilibrium potentials of the redox couples are 0 and ~1.23 V (vs RHE) under standard conditions. The shapes of the curves indicate the difference in the reaction kinetics, following general trends in electrolyzers and fuel cells but not referring to any particular experimental or theoretical calculation result.*

Ideally, the energy required to produce oxygen and hydrogen in electrolyzers should be converted back mostly from the reactions in fuel cells. However, this would only be possible if there was no overpotential for each reaction, regardless of other energy losses through the whole energy conversion and material delivery processes. Indeed, there are always overpotentials. ORR and OER normally have much higher overpotentials compared to HER and HOR as can be seen in Figure 12. To increase the kinetic current densities at a given potential, *i.e.*, reducing the overpotentials needed to maintain efficient current densities, catalysts should be employed. In the following, the basic reaction mechanisms, will be firstly discussed, particularly that of ORR and HER, which were investigated in this work primarily.

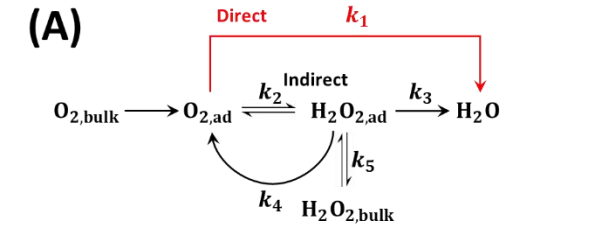


| | | |
|---|---|---|
| 4-electron pathway | $O_2 + 4H^+ + 4e^- \rightleftharpoons 2H_2O$ | Acid |
| | $O_2 + 2H_2O + 4e^- \rightleftharpoons 4OH^-$ | Alkaline |
| 2-electron pathway | $O_2 + 2H^+ + 2e^- \rightleftharpoons H_2O_2$<br>$H_2O_2 + 2H^+ + 2e^- \rightleftharpoons 2H_2O$ | Acid |
| | $O_2 + H_2O + 2e^- \rightleftharpoons HO_2^- + OH^-$<br>$HO_2^- + H_2O + 2e^- \rightleftharpoons 3OH^-$ | Alkaline |

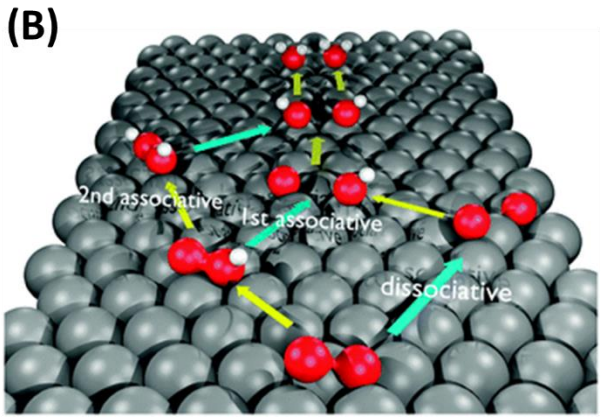


*Figure 13.* ***ORR pathways.*** *(A) General, simplified model of reaction pathways and table of reaction equations in acidic and alkaline media. 2-electron and 4-electron reaction pathways are listed separately. Adapted with permission from ref. 94. Copyright © 1976 Published by Elsevier B.V. (B) 3D schematic representation of ORR on catalyst surface through dissociative mechanism and associative mechanism. Red and white balls represent oxygen and hydrogen atoms, respectively. The yellow arrows indicate electron transfer steps and the azure arrows indicate O–O bond-breaking steps. Taken from ref. 98.*

As a reaction with slow kinetics, the ORR is one of the determining factors for the fuel cell energy losses[85] and even the efficiencies of other devices, for instance, metal-air batteries[45] and a special type of chlor-alkali electrolyzers[95] where the ORR is carried out at the cathode to reduce the operating voltage. Possible reaction pathways and a 3D schematic of proposed reaction mechanisms of the ORR are shown in Figure 13. Apparently, the direct 4-electron pathway is more efficient compared to the indirect 2-electron pathway. Furthermore, peroxide ($H_2O_2$) has been reported to have an undesirable impact on the stability of fuel cells[96]. Therefore, catalyst materials and reaction conditions (*e.g.*, working potentials, pH values)

should be carefully selected or designed to have the selectivity toward the 4-electron pathway[96, 97, 98]. More importantly, the catalysts should have high activities, so that the kinetic current of the reaction can be enhanced[97].

The reaction mechanism of the HER is simpler compared to that of the ORR. Two basic reaction mechanisms were proposed, both start with the Volmer reaction resulting in the reduction of protons (H-species adsorbed at the electrode surface). The Volmer-Tafel mechanism involves a combination of two adsorbed hydrogen atoms to form $H_2$ as schematically shown in Figure 14 with light blue arrows. The Volmer-Heyrovsky mechanism represents the situation when the second proton reduces and bonds to the adsorbed hydrogen and then the $H_2$ is desorbed from the surface[99].

The state-of-the-art catalysts, for both ORR[100, 101, 102, 103] and HER[99] taking place in acidic media, are expensive and scarce Pt-group-based catalysts, including pure Pt-group metals and their alloys. Recently, Molybdenum disulfide ($MoS_2$) was reported to be a promising alternative catalyst for HER [104]. Later, more evidence was found that other transition metal dichalcogenides are potential HER catalysts[105, 106]. Several model catalyst electrodes were investigated in this work to understand the fundamentals of their catalytic activities, especially the locations and microscopic structures of the active centers under reaction conditions.

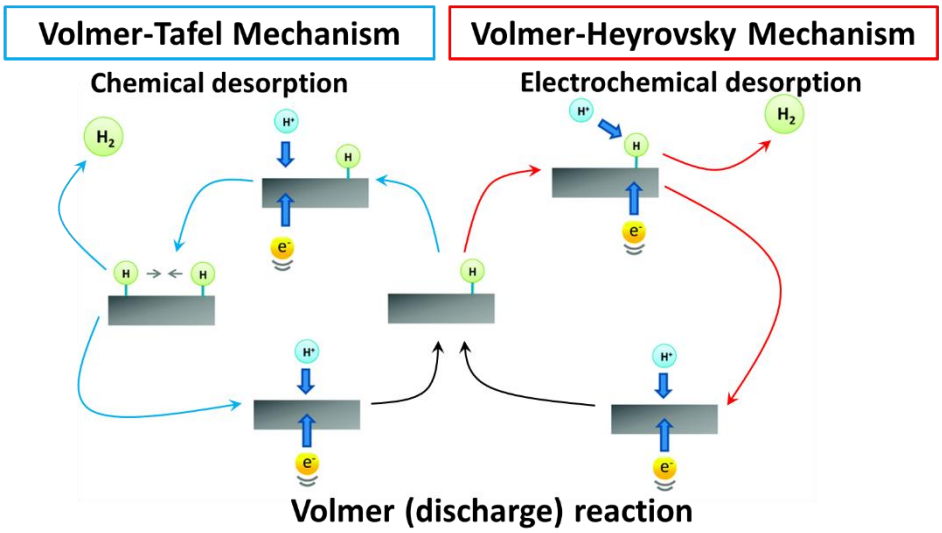


*Figure 14.* ***HER mechanisms, particularly in acidic media.*** *Adapted with permission from ref. 99. Copyright © 2014, Royal Society of Chemistry.*

### 2.2.2 Model Catalyst Electrodes

Nanoparticle catalysts often utilized in industries are not always suitable for experimental investigations, particularly when SPMs are involved. Extended surfaces, particularly surfaces of single crystals are more practical for the elucidation of some of the factors (*e.g.*, structure and chemical composition[85]) that also determine the catalytic activity of corresponding nanoparticles. Specially manufactured single crystal surfaces were used as samples in this work, namely single-crystalline Pt(111), palladium (Pd) sub-monolayer islands on Au(111), Pt sub-monolayer/multilayers islands on Au(111), and TMD multilayers on Au(111) or glassy carbon (GC) substrates. Another system worth mentioning is Pt nanoparticles on HOPG, which was not the main focus of this work. However, the SPM measurements on this particular system provided the first evidence of the proposed methodology in this thesis (see Chapter 3.2.2). The properties of the model catalyst electrodes will be discussed here.

To assess the proposed n-EC-STM methodology, the samples were carefully selected. Well-studied catalytic systems involving single crystalline and bi-metallic surfaces, of which the geometric properties of the active centers are known or reported, were among the candidates. Therefore, Pt(111) single crystals, Pd and Pt deposits on Au(111) were used. Additionally, different morphologies of those samples can be easily distinguished by STM.

The metallic systems studied in this work crystallize in the face-centered-cubic (fcc) structure. The surface of a single crystal has facets that can be characterized by the so-called Miller indices (hkl). Low-index facets including (111), (110), and (100) are the ‘‘basic” facets of the fcc-metals. The (111) facet has the most closely-packed surface and is the energetically most stable one. High-index facets with different periodic defects can also be manufactured.[107]

#### 2.2.2.1 Single Crystalline Pt(111) Electrodes

Figure 15.B is an STM image of a clean single-crystalline Pt(111) surface[108]. It shows in fact that even a well-prepared (111) surface has more structures than just a single (111) facet like the one in Figure 15.A. Structures like the step edges in Figure 15.B separate the (111) surface into flat but irregularly shaped terraces. Consequently, any characterization of a single-crystalline (111) surface contains contributions from step edges and other structures, for instance, other

high-index facets and defects[107]. Therefore, studies on a Pt(111) electrode can investigate the properties of various surface structures simultaneously under the same conditions.

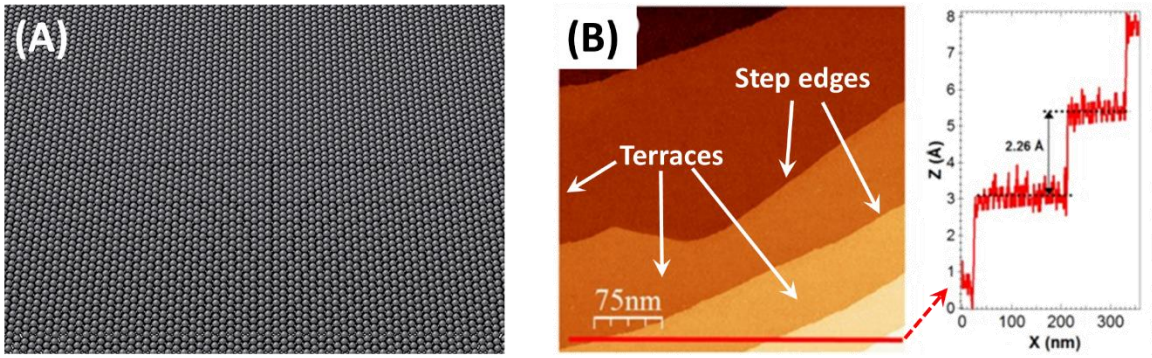


*Figure 15.* ***Pt(111) surfaces.*** *(A) A ball model of an ideal (111) surface. (B) STM image of a real-world Pt(111) surface and the height profile along the red line in the image, adapted with permission from ref. 108.*

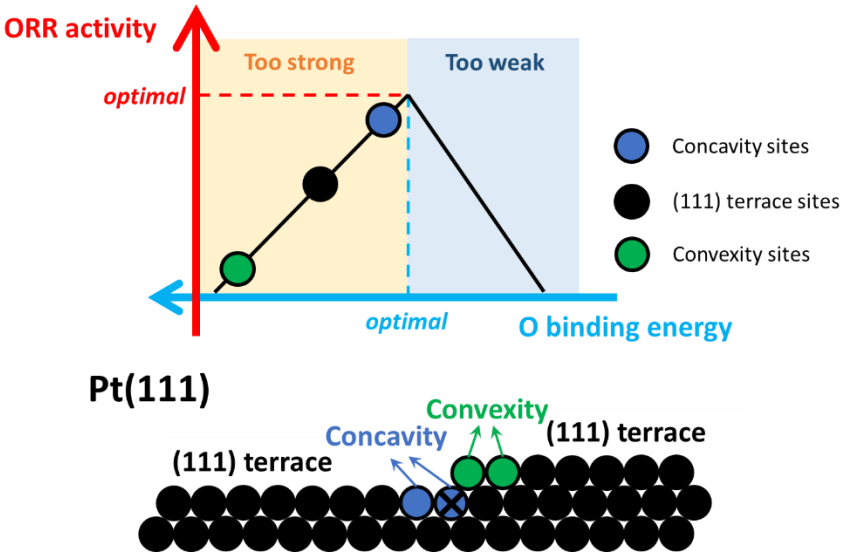


*Figure 16.* ***An illustration of the O binding energy on the Pt(111) concavity, convexity and (111) terrace sites and the ORR activity.*** *The ball model shows the typical structures of a Pt(111) surface, e.g., the (111) terrace, the step-concavity (blue) and the step-convexity (green).Based on ref. 109.*

The importance of Pt(111) for investigations on ORR should be discussed here. The results from DFT calculations suggested that the binding energy between the Pt(111) facet and the hydroxyl species (*OH) is about 0.1 eV (2.3 kcal/mol) stronger than the predicted optimal value[85, 110]. Therefore, surface sites with slightly higher coordination numbers should have better activities (weaker binding) according to the d-band model[10, 76, 77, 78]. An illustration of

the O binding energy on the Pt(111) concavity, convexity and (111) terrace sites and the ORR activity is depicted in Figure 16. As shown in Figure 17.A, a summary of experimental data from different Pt single-crystal surfaces and near-surface alloys (specific activity *vs* estimated *OH binding energy) in 0.1 M $HClO_4$ confirmed the higher activities of wide-terrace (n>2) step-edge sites compared to that of the (111) terraces[50]. Interestingly, following this argument, the most active sites of a Pt(111) with step-like defects are located at the bottom of the steps (step concavities), where the binding energy to the O-species is slightly weaker than that of (111) terrace and more close to the top of the volcano plot. This is very well explained by a newly introduced parameter, the generalized coordination number.[29]

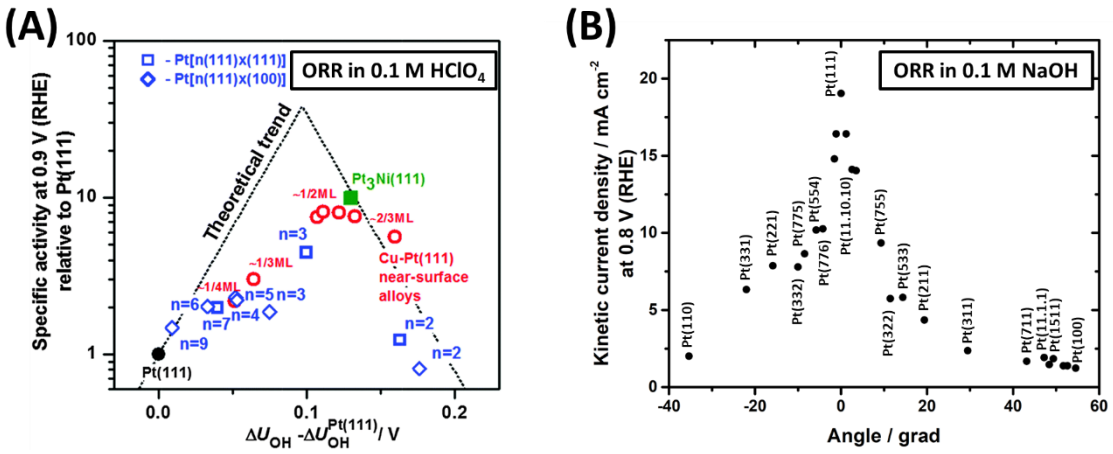


*Figure 17.* ***Volcano plots involving different facets of Pt-based single crystal model catalysts.*** *(A) Experimental results (ORR activity vs estimated *OH binding energy at 0.9 V vs RHE) of Pt(111), Cu–Pt(111) near-surface alloys with different sub-surface Cu coverage, Pt[n(111) × (111)] and Pt[n(111) × (100)] stepped surfaces in 0.1 M $HClO_4$, taken with permission from ref. 50. Copyright © 2014, Royal Society of Chemistry. (B) ORR kinetic currents measured at 0.80 V vs RHE for the different electrodes vs the angle of the surface with respect to the (111) plane, adapted with permission from ref. 53. Copyright © 2013, Royal Society of Chemistry.*

However, all the investigations mentioned above were done in acidic media without considering the electrolyte species effects. The influence of the electrolyte species should also be taken into account as mentioned in Chapter 2.1.5. Particularly, considerable effects of the alkali metal cations exist when reactions are performed in alkaline media. ORR activities of a series of Pt single crystalline surfaces of different orientations have been tested in 0.1 M NaOH, and the resulting kinetic current densities are plotted according to the angles of the surfaces normal with respect to the (111) plane in Figure 17.B.[53] The Pt(111) surface has the best activity toward the ORR in NaOH compared to the other tested surfaces, which is opposite to

the observations in acidic media. The descriptor of the plot, the angle of the surface to (111) plane, is only a preliminary attempt to explain the phenomenon, which is limited to explain the actual reason for the different activity trend in alkaline media.

It is unclear, whether the statement made for ORR in acidic media, for instance, steps are normally more active, can be applied in the case of alkaline media. Considering the activity comparison of Pt(111) and stepped single-crystalline Pt(221) in acidic and alkaline electrolytes in Figure 18.A, the presence of the alkali metal makes a positive impact on the ORR activity of Pt(111) but inhibits that of Pt(221) with more step structures[111].

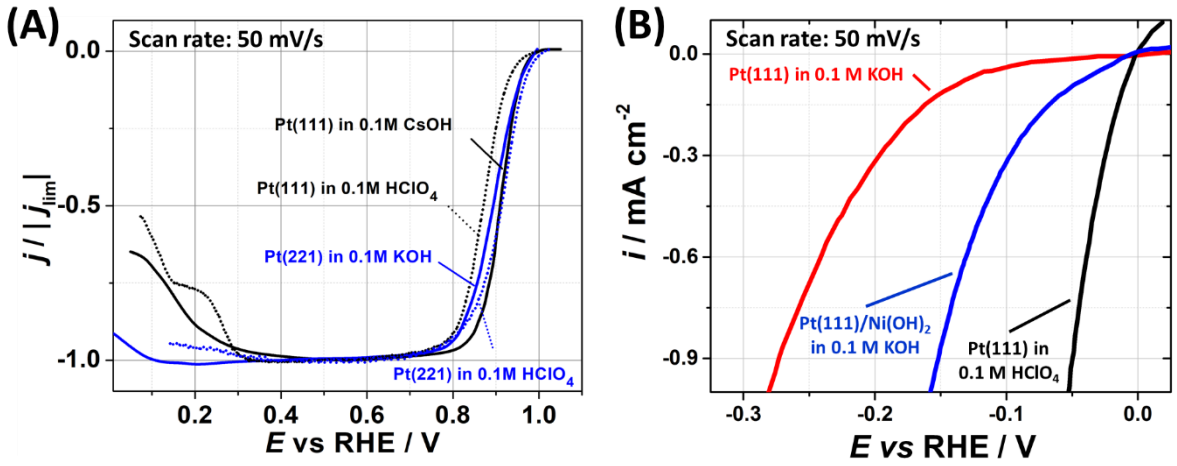


*Figure 18.* ***ORR and HER activities of Pt single crystals in different media.*** *(A) The iR-corrected RDE-voltammograms (currents normalized to the diffusion-limit currents, respectively) for the Pt(111) electrodes ORR activities in $O_2$-saturated 0.1 M $HClO_4$ and 0.1 M CsOH and that of Pt(221) electrodes in $O_2$-saturated 0.1 M $HClO_4$ and 0.1 M KOH electrolytes. Adapted with permission from ref. 111. Copyright © 2018 American Chemical Society. (B) RDE-voltammograms with iR-correction of Pt(111) and Ni-based cluster on Pt(111) for HER in $H_2$-saturated 0.1 M KOH and 0.1 M $HClO_4$ electrolytes. Data taken with permission from ref. 113. Copyright © 2011, American Association for the Advancement of Science.*

Like in the case of ORR, Pt is on the stronger side of the HER volcano plot shown in Figure 6. More studies reported that in acidic media the polycrystalline (pc) Pt has higher HER activity than single-crystalline Pt(111) electrodes, indicating the structure sensitivity of HER on Pt surfaces and different contributions of steps, defects, and (111) terraces[39, 112]. However, Pt(111) has lower HER activity in alkaline media compared to the case of $HClO_4$ (Figure 18.B, red and black curves)[113], suggesting a considerable influence from the pH value or the alkali

metal cations. The non-covalent interactions between the alkali metal cations and the reaction intermediates have drawn attentions recently[51, 114].

Therefore, the identification of active sites of Pt single-crystalline surfaces, or simply Pt(111) with steps and defects, is crucial for the fundamental understanding of ORR and HER electrocatalytic processes in both acidic and alkaline media.

#### 2.2.2.2 Palladium (Pd) Sub-monolayer Islands on Au(111)

A small amount of nano-structured active catalyst material deposited on inert substrates can significantly increase the activity of the electrodes. For instance, Pd monolayers on Au enhance the HER activity by about two orders of magnitude compared to the bare Au, and Pd sub-monolayer islands decorated Au surfaces demonstrate even higher activity.[41] The Pd-sub-monolayers/Au-substrate system has attracted great attention because of its good capability of catalyzing not only HER but also other reactions, *e.g.*, formic acid oxidation[40, 115]. Additionally, the property of hydrogen absorption in Pd bulk materials is no longer pronounced in nano-structured Pd islands[41].

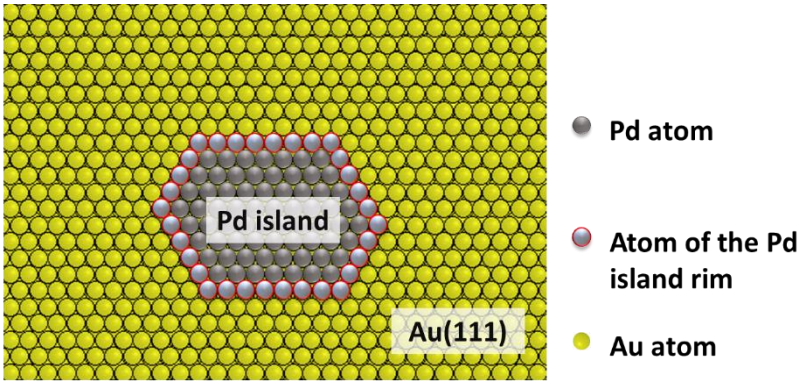


*Figure 19.* ***Model of a Pd sub-monolayer island on Au(111).*** *The Pd atoms of the island rim (highlighted by red circles) are supposed to be more active than the other Pd atoms.*

To optimize the activity of this system, experimental[40, 42] and theoretical[43] approaches that evaluate the size-effect (particularly Pd coverage and sub-monolayer islands size) and the effect of the Au substrate were reported. The results showed that the activity of the entire surface is not directly proportional to the size of Pd islands and the rim of an island is probably the most active part of it[42, 43], as illustrated in Figure 19. The confirmation of this hypothesis

will strongly contribute to the rational design of certain catalytic systems. Therefore, Au(111) decorated with Pd sub-monolayer islands was selected as a good model system for the proposed active sites identification method validation (see Chapter 3.2). Cyclic voltammograms (CVs) of single crystalline (111) surfaces of both Pd[116] and Au[117] are plotted in Figure 20 as references for the Pd islands on Au(111) system.

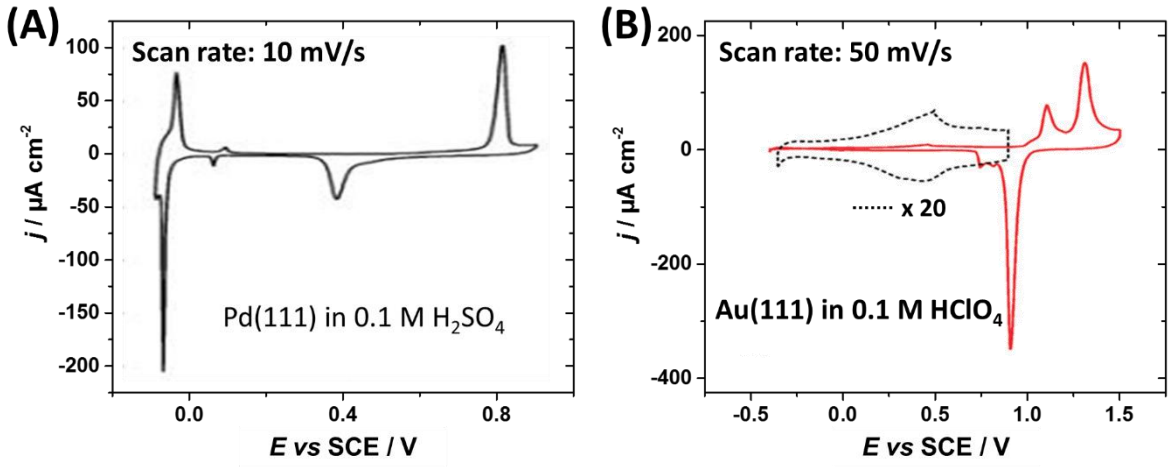


*Figure 20.* ***CVs of single crystalline Pd and Au samples.*** *(A) Pd(111) in 0.1 M $H_2SO_4$ at a scan rate of 10 mV/s and (B) Au(111) in Ar saturated 0.1 M $HClO_4$ at a scan rate of 50 mV/s. The dotted trace is enlarged 20 times. Data adapted with permission from ref. 116 (Copyright © 2006 Elsevier Ltd.) and ref. 117 (Copyright © 2011, Royal Society of Chemistry), respectively.*

### 2.2.2.3 Pt Sub-monolayer/Multilayers on Au(111)

The importance of the system consisting of the Pd sub-monolayer islands on Au(111) was discussed above. However, as an even better catalyst material in many aspects, Pt is also immobilized on inert substrates to tune the catalytic performance of the substrate surface[118, 119, 120]. Investigation on a similar model, *i.e.*, Pt sub-monolayer islands on Au(111), would also be beneficial.

Multilayer Pt deposited on Au(111) can be utilized in a particular case which will be discussed later in Chapter 3.3. The electrochemically deposited Pt covered Au(111) surface should have approximately the same surface roughness compared to the bare Au surface but have catalytic properties of Pt for many reactions including HER.

### 2.2.2.4 Transition Metal Dichalcogenide Multilayers on Au(111)/Glassy Carbon (GC)

Nanosheets of transition metal dichalcogenides (TMDs), *e.g.*, molybdenum disulfide ($MoS_2$) and molybdenum diselenide ($MoSe_2$), have been reported to be promising cheap and stable non-metallic alternative HER catalysts in acidic electrolytes[105].

Most Mo dichalcogenides ($MoX_2$) are semiconductors, which are potential solar cell and photocatalytic materials[55]. The approximate lattice constants of $MoS_2$ and $MoSe_2$ with different structures are shown in Figure 21 together with a 3D illustration and 2D top view (only for the 2-H phase, which is more stable than the 1-T phase) of the TMD atomic structure[55, 121, 122, 123]. Note that slightly different values of the lattice constants and layer thickness were obtained from different measurements. Sub-monolayer and multilayer films have different properties[124]. For multilayer or bulk TMDs, different phases, namely 2-H and 3-R were found, especially in $MoS_2$. The digits 2 and 3 indicate the number of layers in a crystallographic unit cell, and letters H and R represent the type of symmetry exhibited: H for hexagonal ($D_{3h}$ group), and R for rhombohedral ($C_{53v}$ group).[125]

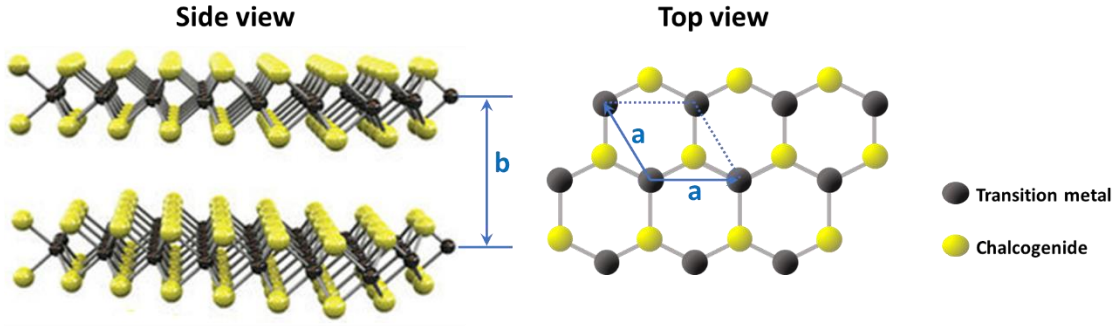


| Dichalcogenides | | -$S_2$ | -$Se_2$ |
|---|---|---|---|
| Mo | Electronic characteristics | **Bandgap:**<br>Monolayer: 1.8 eV<br>Bulk: 1.2 eV | **Bandgap:**<br>Monolayer: 1.5 eV<br>Bulk: 1.1 eV |
| | Lattice constants and thickness | **a ≈ 0.315 nm**<br>**b = 0.6 – 0.7nm** | **a ≈ 0.33 nm**<br>**b = 0.6 – 0.7nm** |

*Figure 21.* ***Schematics of the TMD structure (2-H phase) and the electronic characteristics, lattice constants, and thickness of $MoS_2$ and $MoSe_2$.*** *Image adapted with permission from ref. 55 (Copyright © 2012, Springer Nature), and data taken from ref. 121, 122, 123.*

As they are promising catalyst materials, the identification of active sites of the TMDs is important. It was reported that the active centers for hydrogen evolution are located on the edge of $MoS_2$ nanoparticles. The $MoS_2$ edge site could be adapted into the HER volcano plot

and sits on the weak-binding side of the volcano[30]. Bulk materials of $MoS_2$ as HER catalysts should be manufactured with more exposed edge sites[126]. More parameters can influence the activity, for instance, the layer thickness. Activity test for exfoliated $MoS_2$ flakes (shown in Figure 22.A, bare substrate graphenic carbon (GrC) and Pt electrodes are references) towards solar driven HER resulted in the activity trend of the monolayer > bilayer > bulk material[124]. A recent study suggested that sulfur-vacancies on the terrace of $MoS_2$ increase the HER activity significantly by creating more active sites and changing the binding energy to H-species[57], as shown in Figure 22.B.

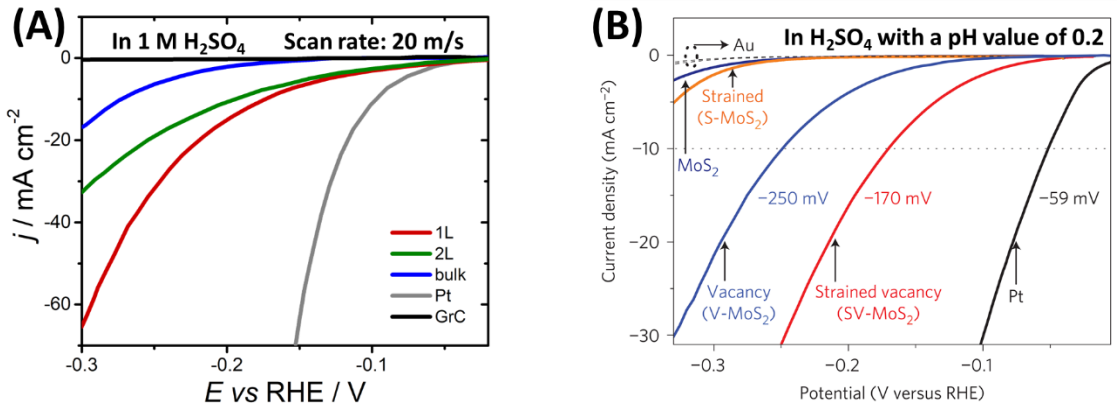


*Figure 22.* ***HER activity of monolayer (1L)-, bilayer (2L)-, and bulk-$MoS_2$ flakes deposited on graphenic carbon (GrC) compared with the activity of bare GrC and Pt, and the optimization of the activity of $MoS_2$.*** *(A) Polarization curves in 1 M $H_2SO_4$ at a scan rate of 20 mV/s. Data adapted with permission from ref. 124. Copyright © 2017 Elsevier Ltd. (B) Activation of $MoS_2$ basal plane. Activities of bare Au substrate, Pt electrode, as-transferred $MoS_2$ (strain: 0% and S-vacancy: 0%), strained $MoS_2$ without S-vacancies (S-$MoS_2$, strain: 1.35 ± 0.15% and S-vacancy: 0%), unstrained $MoS_2$ with S-vacancies (V-$MoS_2$, strain: 0% and S-vacancy: 12.5 ± 2.5%), and strained $MoS_2$ with S-vacancies (SV-$MoS_2$, strain: 1.35 ± 0.15% and S-vacancy: 12.5 ± 2.5%). Taken with permission from ref. 57. Copyright © 2015, Springer Nature.*

## 2.2.3 Aspects Related to Model Catalyst Electrodes Preparation

### 2.2.3.1 Single Crystal Electrode Preparation

A single crystal electrode should have a well-oriented surface and ideally its overall surface properties should be identical for each electrochemical and microscopic measurement. Therefore, a rather simple and reproducible preparation method of noble metal single crystal electrodes was introduced[41]. If necessary, prior to the preparation procedure the surface of the electrode is cleaned in aqueous electrolyte by electrochemical polishing[127]. Once a cleaned electrode surface is obtained, the single crystalline surface structure needs to be restored. The

electrode is heated up by the flame-annealing method and subsequently cooled down to room temperature in well-controlled gas atmosphere. The gas atmosphere is suggested to be $O_2$ free and contains CO. Due to the CO poisoning (a monolayer of CO adsorbed at the metal surface), the electrode surface is turned out to be well-oriented single crystalline surface. This method is successfully utilized for the preparation of noble metal samples, for instance, Pt and Pd single crystals. In the case of Au single crystals, cooling down in CO atmosphere after flame-annealing is not required.[41]

#### 2.2.3.2 Electrochemical Deposition of Sub-monolayer Amounts of Metals on Single Crystal Electrodes

For the preparation of model catalysts, suitable techniques to make samples with defined amounts of catalytically active materials on inactive substrate materials are required. Electrodeposition of metals follows the basic electrochemical reaction process at the solid–liquid interface. Metal ions diffuse to the electrode and adsorb onto the surface. Then, adsorbed ions are reduced to the neutral oxidation state and possibly undergo a crystallization process. Typically, the required electrode potential is more negative than the equilibrium potential of the metal/metal$^{n+}$ redox couple. This type of deposition is the so-called overpotential deposition (OPD). It is a continuous process if a new equilibrium is not established. However, in many cases, deposition can occur on a foreign metal substrate when the electrode potential is more positive than the equilibrium potential of the redox couple, namely the underpotential deposition (UPD). It is suggested that UPD is only possible when energetically adsorbate-substrate interaction is stronger than that of substrate-substrate in the bulk material. Therefore, UPD stops when the substrate is totally covered by a monolayer of deposited metal.[63, 128]

OPD is capable of 3-dimensional structure deposition. The deposition process can be divided into two steps, nucleation and growth. Metal particles nucleate preferably at step sites or other types of defects, depending on the strength of metal/substrate interaction. Nucleation typically is correlated with an additional overpotential, the nucleation overpotential. Afterwards, the nuclei grow even at reduced overpotential, depending on the applied potential and time.

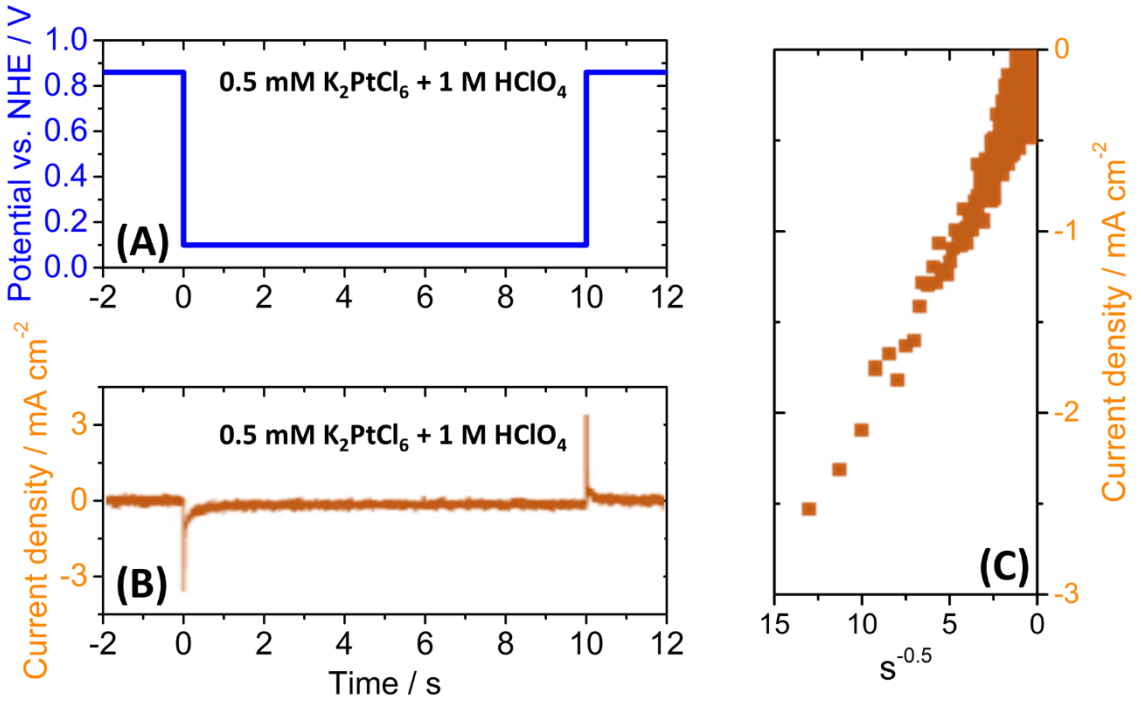


*Figure 23.* ***Single pulse deposition of Pt nanoparticles on HOPG in 0.5 mM $K_2PtCl_6$ + 1 M $HClO_4$.*** *(A) Potential vs time, initial and final potential: 860 mV vs NHE, deposition potential: 100 mV vs NHE (10s). (B) Resulting current vs time dependence, and (C) current vs a different time scale ($s^{-0.5}$). Data taken with permission from ref. 129. Copyright © 2009 Elsevier B.V.*

One application of OPD is the controlled deposition of metallic nanoparticles via a potential step method. In the electrolyte containing deposition precursors ($M^{n+}$ or other compounds), the potential of the substrate is switched from a potential where no reduction of $M^{n+}$ is possible to a potential which is (much) more negative than the equilibrium potential. This is the so-called single pulse deposition. An example can be seen in Figure 23. Pt nanoparticles were successfully deposited in 0.5 mM $K_2PtCl_6$ + 1 M $HClO_4$ electrolyte on highly oriented pyrolytic graphite (HOPG) by the potential control (Figure 23.A). Figure 23.B shows the resulting current. Under the deposition potential, the current starts with a peak followed by a more stable value over time (slightly decreases as shown in Figure 23.C). Figure 23.C shows the current in the peak region (current vs $t^{-0.5}$). The rapid drop is caused by the mass transfer limitation.[129]

To better control the size and distribution of the metal particles, double pulse deposition is preferred, in which nucleation and growth are controlled separately with different potentials. A lower overpotential leads to a more gradual growth of the particles and to prevent new

nucleation from taking place.[128] Figure 24 shows a typical Pt double pulse deposition from a 5 mM $K_2PtCl_6$ + 0.1 M $H_2SO_4$ electrolyte on a diamond-based substrate. Potential and current vs time are shown in Figure 24.A and B. Details of the nucleation pulse can be seen next to the curves. The nucleation pulse is much shorter, so that only nuclei with relatively small sizes can be created. Figure 24.C is the AFM image of the deposited particles. Tip broadening effects can be seen around the particles.[130]

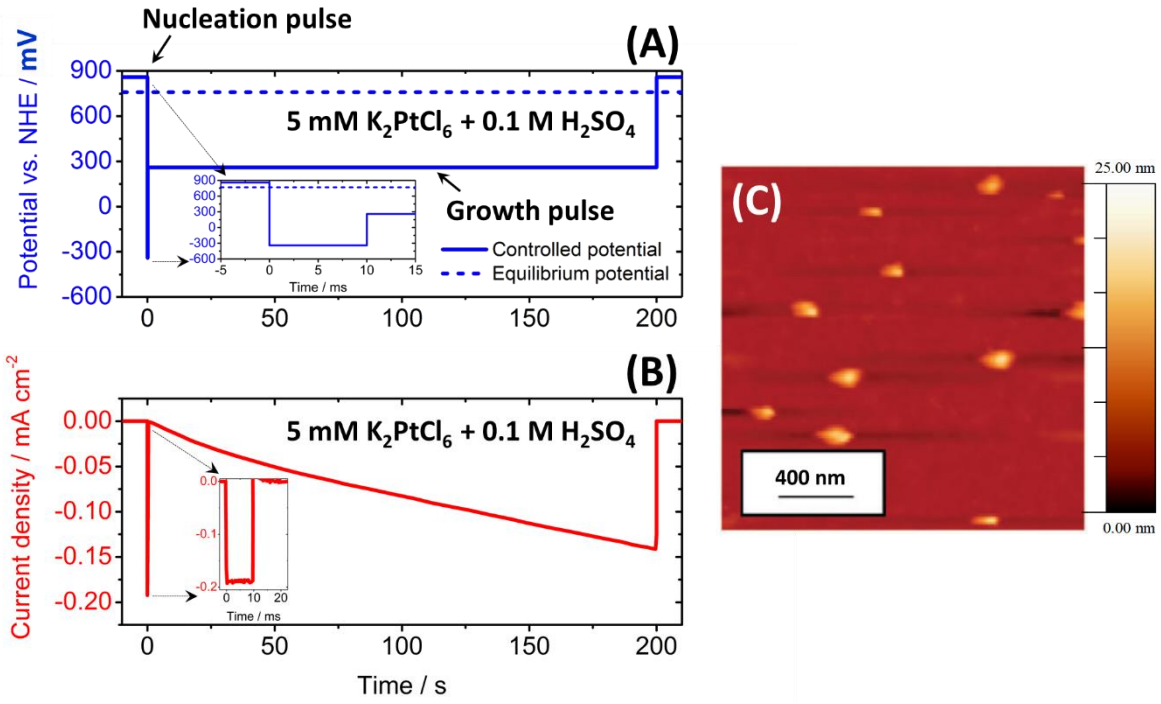


*Figure 24.* ***Double pulse deposition of Pt nanoparticles on diamond-based substrate in 5 mM $K_2PtCl_6$ in 0.1 M $H_2SO_4$.*** *(A) Potential vs time (solid line) with respect to the equilibrium potential (dash-line). Initial and final potential: 860 mV vs NHE, nucleation potential: -340 mV vs NHE (10 ms), and growth potential: 260 mV vs NHE. (B) Resulting current vs time dependence. (C) AFM image of the deposited particles. Adapted with permission from ref. 130. Copyright © 2011, Royal Society of Chemistry.*

UPD is suitable for monolayer deposition, for example to form a Cu monolayer on Au(111) substrates that is commonly carried out in electrolytes containing $Cu^{2+}$. EC-STM measurements were reported on Au(111) substrates in 0.05 M $H_2SO_4$ +1 mM $CuSO_4$.[131] CV was done with a very low scan rate, 1 mV/s, before EC-STM imaging. All results are shown in Figure 25.A and B. Three regions can be seen in the CV including two adsorption/desorption coupled peaks (2 and 3) and the bulk deposition (*i.e.*, OPD, 1). Images of the surface were taken at the potentials of 0.55 V *vs* SCE at which no Cu UPD happens (Figure 25.B1) and 0.15 V *vs* SCE where adsorbates are present (Figure 25.B2).[131] The larger lattice structure of the latter was

explained by the model in Figure 25.C. Figure 25.C1 and C2 are top- and side-view of the surface with Cu and adsorbed sulfate.[132] However, the surface coverage is not 1 but about 2/3[131, 132]. To obtain a Pt monolayer on Au, UPD deposited Cu can be replaced by a layer of Pt via galvanic displacement. The morphology of the Pt layer strongly depends on the oxidation state of the Pt-complex in the electrolyte.[63]

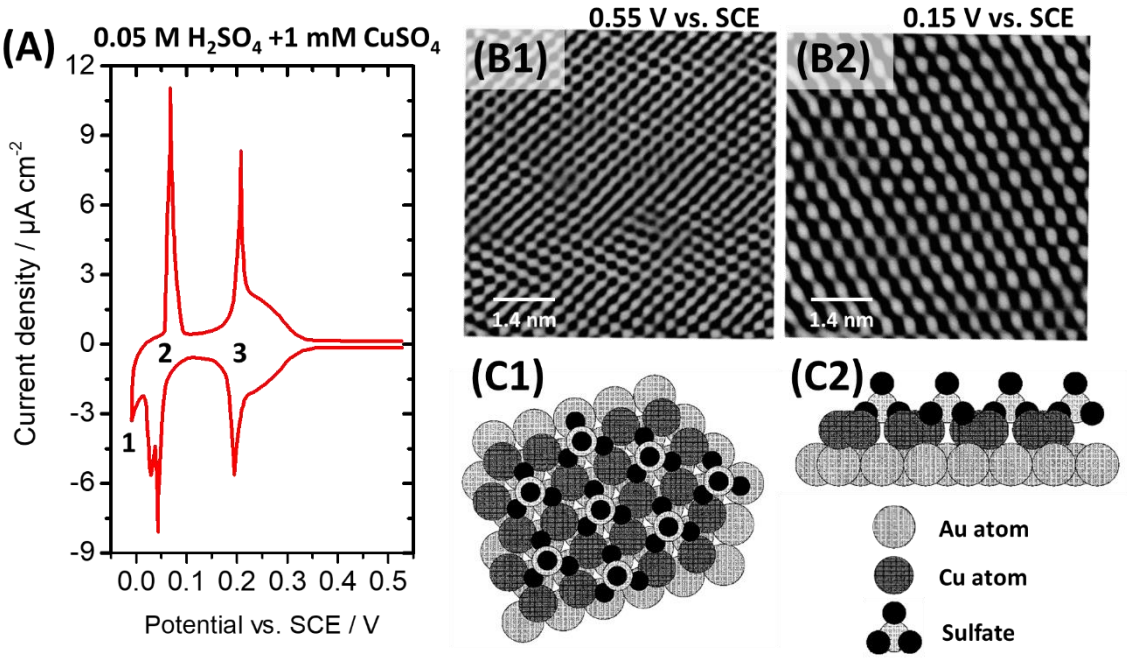


*Figure 25.* ***Cu UPD in 0.05 M $H_2SO_4$ +1 mM $CuSO_4$ on Au(111) electrodes.*** *(A) CV of Au(111) in 0.05 M $H_2SO_4$ + 1mM $CuSO_4$ at a scan rate of 1 mV/s. Bulk deposition and two UPD regions are labeled by 1, 2, and 3, respectively. (B) EC-STM images of Au(111) at the potentials of (B1) 0.55 V and (B2) 0.15 V vs SCE. Tip potential is 0.6 V vs SCE. The tunneling current was 10 nA. Scan speed was (B1) 20 ms/line and (B2) 50 ms/line. CV and EC-STM images are adapted with permission from ref. 131. Copyright © 1991 Published by Elsevier B.V. (C1) and (C2) Top- and side-view of the structure in B2, showing the adsorption of the sulfate. Reprinted with permission from ref. 132. Copyright © 2014, American Chemical Society.*

Recently, a self-terminating deposition of Pt monolayer films on Au substrates was reported. As shown in Figure 26.A, RDE-cathodic scans were done in two electrolytes, Ar-saturated 0.5 M NaCl and 0.5 M NaCl + 3 mM $K_2PtCl_4$. Pt deposition was observed in the presence of $PtCl_4^{2-}$. However, the deposition is terminated by hydrogen UPD, which has been proven by the electrochemical quartz crystal microbalance (EQCM) measurement independently. This suggests that hydrogen adsorption on Pt atoms limits the normal growth of the Pt layer on Au, schematically represented in Figure 26.B. Therefore, Pt monolayer deposition on Au is possible by the single pulse method, initial and final potential: 0.4 V *vs* SSCE, pulse potential: -0.8 V *vs*

SSCE (hydrogen UPD takes place on Pt). At the pulse potential, clean Au surface is available for Pt deposition. However, all Pt atoms adsorb hydrogen atoms and the deposition stops, when almost the whole Au surface is covered by a monolayer of Pt. The amount of deposited Pt is independent of the length of the deposition pulse time once a nearly complete monolayer has been formed.[133]

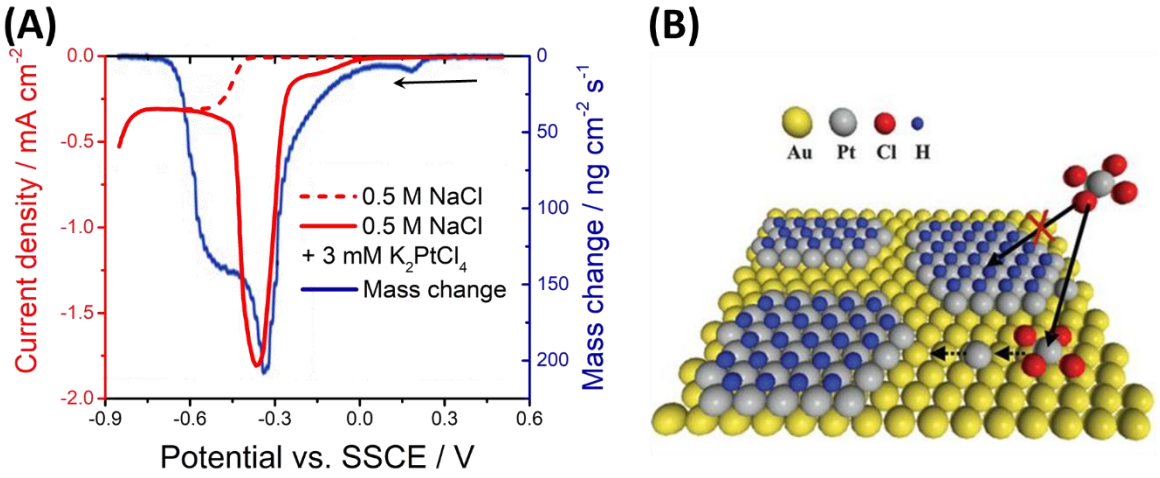


*Figure 26.* ***Self-terminating growth of platinum films on an Au substrate.*** *(A) RDE-cathodic scan of Pt with respect to sodium-saturated calomel reference electrode (SSCE) in Ar-saturated 0.5 M NaCl and 0.5 M NaCl + 3 mM $K_2PtCl_4$ and the corresponding change of the mass (derivative of the mass as a function of time) in Ar-saturated 0.5 M NaCl + 3 mM $K_2PtCl_4$ independently obtained by EQCM. All measurements have a scan rate of 2 mV/s. Pt growth stops in the region where hydrogen UPD on Pt starts. (B) An illustration of the deposition mechanism. Data and image are adapted with permission from ref. 133. Copyright © 2012, the American Association for the Advancement of Science.*

## 2.3 Fundamentals of Quantum Tunneling

The STM and EC-STM have been contributing to the surface-science related research for decades since Binnig and Rohrer demonstrated that the quantum tunneling phenomenon can be applied as a distance-sensitive signal between a sharp tip and a conductive surface[31, 134, 135]. Firstly, the underlying concept of quantum tunneling will be discussed here.

### 2.3.1 Background and Concept of Quantum Tunneling

In the late 19th century, F. Paschen reported in his study about the breakdown voltage in gases as a function of parameters including pressure and gap length[136]. His observations inspired a series of investigations later summed up as the so-called Paschen's law[137]. One of them was

the experiment made by R. F. Earhart. The experimental setup consisted of a spherical and a planar surfaces with very small distance from a few to hundreds of micrometers. The resulting breakdown voltage *vs* separation distance curves had two regions. At small distances, the breakdown voltage decreased dramatically.[138] However, the reason was not discussed correctly back then (when ether was believed to exist[139]).

By the late 1920s, the concept of field emission was introduced by R. H. Fowler and L. Nordheim based on experimental and theoretical studies[140]. It explains the electron emission phenomena (*e.g.*, breakdown behavior at small distances in Earhart's and other similar experiments[138, 141, 142]) in a quantum mechanical way[140]. In parallel, the so-called tunneling effect, which was originally found in the field of radioactivity research, was recognized as a common explanation for other phenomena, including also the electron field emission.[143]

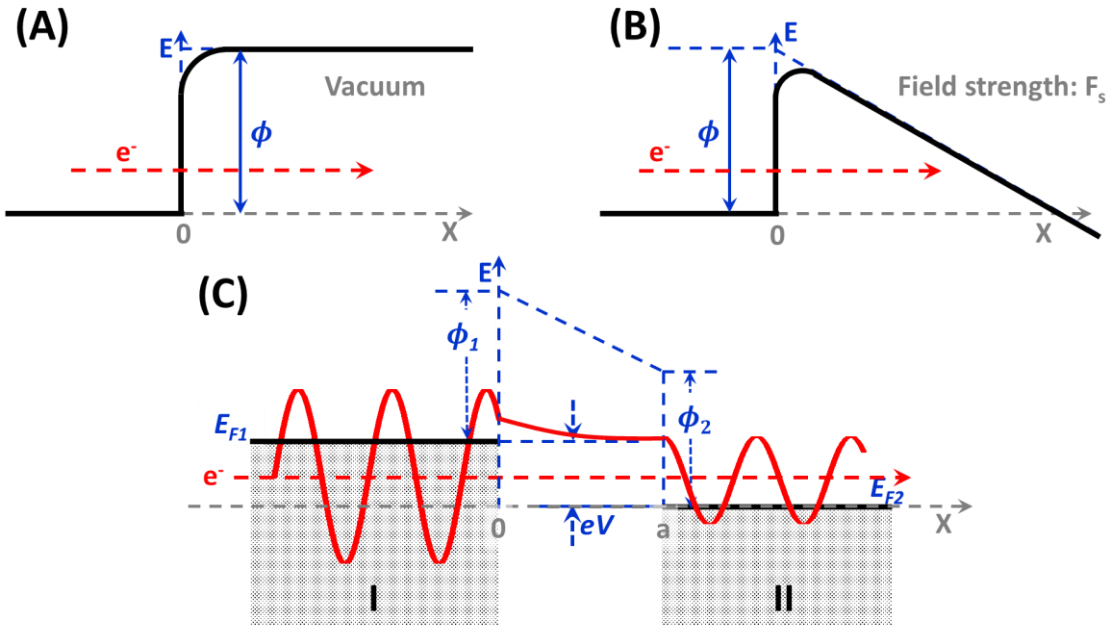


*Figure 27.* ***Field electron emission through a rounded barrier $\phi$ (work function)****, from solid metal to (A) vacuum and (B) a field with a strength of $F_s$. based on ref. 140. (C) Schematic of the so-call metal-vacuum-metal (MVM) tunneling. The work functions of both side are considered. The electron is represented as its possible wave function. The voltage bias is V.*

The basic concept of electron field emission (or field electron emission) is schematically shown in Figure 27. Figure 27.A describes the situation when under an electrostatic field an electron with energy $W$ passing through a finite energy barrier of $\phi$ (work function of the material, that needed to emit an electron from it), from a solid surface to vacuum or other dielectrics.

Classically, the latter is impossible for an object if $\phi$ is higher than $W$. However, from the point of view of quantum mechanics, it is possible. The answer is a calculable value of 'probability' represented as a current flow. Here, the current or current density normalized by the surface area is commonly used to represent the probability of electron emission.[140] The tunneling effect through a gap which is in the range of angstroms (Å) allows the electrons to arrive directly at the second electrode, as illustrated in Figure 27.C. The highest initial and final energies are the Fermi-levels of the two electrodes.[144]

Young *et al.* reported a voltage bias (between two electrodes) *vs* distance curve at a fixed current density of 50 A/cm$^2$ as shown in Figure 28.A. A linear part can be seen, where the distance is larger than ~30 Å. When the distance is smaller than ~10 Å (MVM), the voltage drops exponentially with the distance. If one extends the Fowler-Nordheim part to shorter distances and compares the calculated current density to that of the MVM tunneling, the difference is clearly visible in Figure 28.B. It suggested that, the MVM tunneling effect is potentially a high-resolution microscopic tool.[145]

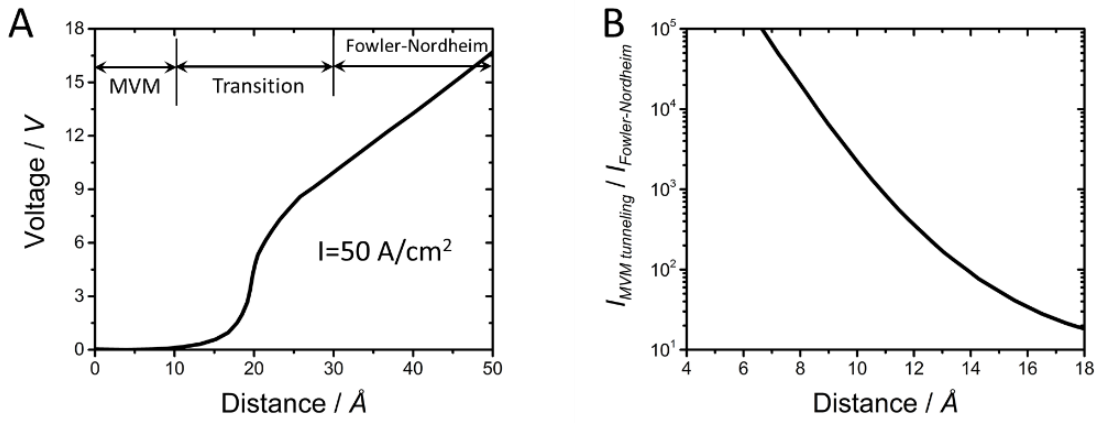


*Figure 28. (A) Required voltage to have a current density of 50 A/cm$^2$ as a function of metal-metal distance. Three regions are the MVM region, the transition (intermedia) region, and the Fowler-Nordheim region. (B) Calculated ratio of tunneling current density to the value from Fowler-Nordheim calculation for a fixed voltage at the first electrode of 0.3 V/Å. Adapted with permission from ref. 145. Copyright AIP Publishing.*

The wave equations (time-independent Schrödinger equation) Equation 2.3.1-1 and Equation 2.3.1-2 are employed to solve the emission through the energy barriers shown in Figure 27.A and B. The emission current is calculated as shown in Equation 2.3.1-3. $\psi(x)$ is the wave function of the electron as a function of the distance $x$ from the emitter, and it is equivalent

to the thermodynamic partial potential of the electron[140]. The mass of the electron is $m$, the energy of the electron is $W$, the energy barrier is $\phi$ and the field strength is $F_s$. Another constant $\kappa$ is defined in Equation 2.3.1-2, where $h$ is the Planck constant. There are still open questions and uncertainties in these calculations[140], but the applications of it were already reported, however, mainly as spectroscopic tools[144].

$$\frac{d^2\psi(x)}{dx^2} + \kappa^2(W - \phi + F_s x)\psi(x) = 0 \qquad x > 0 \qquad \textit{Equation 2.3.1-1}$$

$$\frac{d^2\psi(x)}{dx^2} + \kappa^2 W\psi(x) = 0, \text{ and } \kappa^2 = 8\pi^2 m/h^2 \qquad x < 0 \qquad \textit{Equation 2.3.1-2}$$

$$I = \frac{16\pi m\varepsilon}{\phi h^3}\int_0^{\mu} W^{\frac{1}{2}}(\phi - W)^{\frac{1}{2}}(\mu - W)e^{-4\kappa(\phi - W)^{\frac{3}{2}}/3F_s}dW \qquad \textit{Equation 2.3.1-3}$$

In the case of MVM tunneling (Figure 27.C), electron tunneling happens from the occupied states of the electrode I to the unoccupied states of electrode II. The barrier can be roughly approximated by taking the average of the work functions of the two electrodes or simply the work function of electrode I. The wave function decays exponentially in the vacuum (see Equation 2.3.1-5). Note that, the tunneling process through a vacuum gap is considered as an elastic process, so that the energy of the tunneling electron will not be changed.[146]

$$\phi = \frac{\phi_1 + \phi_2}{2} \textit{ or } \phi = \phi_1 \qquad \textit{Equation 2.3.1-4}$$

$$\psi(a) = \psi(0)e^{-\frac{2\pi a\sqrt{2m(\phi - W)}}{h}} \qquad \textit{Equation 2.3.1-5}$$

The tunneling current depends on the DOS of the electrode II at the Fermi edge $\rho_{II}(E_F)$. The tunneling current can be written as in Equation 2.3.1-6.

$$I \propto V\rho_{II}(E_F)e^{-\frac{4\pi a\sqrt{2m(\phi - W)}}{h}} \qquad \textit{Equation 2.3.1-6}$$

More theoretical investigations have been performed to quantify the tunneling current with all possible factors. Even though there is no exact precise equation reported, existing models are already clear enough to point out the dominating factors. One of them is the Tersoff-Hamann Model[147, 148] based on the Bardeen approach[149]. The current is a function (Equation 2.3.1-7) of the DOS of both sides and the probability of passing through the vacuum gap. In that equation *f* is the Fermi function which is defined in Equation 2.3.1-8. $M$ is the so-called tunneling matrix element given by Equation 2.3.1-9. It is calculated as the surface integral of

the wave functions of region I and II ($\psi_I$ and $\psi_{II}$) across the tunneling gap. The variable of the energy is $\varepsilon$, and the local density of states is $\rho$ [146, 150]

$$I \propto \int_{-\infty}^{\infty} [f(E_{f2}+\varepsilon) - f(E_{f1}+\varepsilon)]\rho_{II}(E_{f2}+\varepsilon)\rho_I(E_{f1}+\varepsilon)M^2 d\varepsilon \qquad \textit{Equation 2.3.1-7}$$

$$f(W) = \frac{1}{1+e^{(W-E_F)/k_BT}} \qquad \textit{Equation 2.3.1-8}$$

$$M = \frac{h}{4\pi m}\int d\vec{s}\cdot(\psi_I^*\,\vec{\nabla}\psi_{II} - \psi_{II}\,\vec{\nabla}\,\psi_I^*) \qquad \textit{Equation 2.3.1-9}$$

For low voltage bias, Equation 2.3.1-7 can be simplified as

$$I \propto \int_{0}^{eV} \rho_{II}(E_{f2}+\varepsilon)\rho_I(E_{f1}+\varepsilon)M^2 d\varepsilon \qquad \textit{Equation 2.3.1-10}$$

For both Equation 2.3.1-6 and Equation 2.3.1-7, factors that determine the tunneling current are the local energy density of both electrodes (or applied bias potential), the DOS of them, the property of the gap (dielectric media), the surface area where tunneling is possible, and also the distance of the electrodes.[146, 150]

### 2.3.2 Quantum Tunneling in Electrolytes

Electrochemical STM is capable of *in-situ* and *operando* measurements[151] in the presence of electrolytes. Here, tunneling current in liquid phase will be further discussed. Equation 2.3.1-6 and Equation 2.3.1-9 will result differently or have different forms in case of electron tunneling through the electrolyte-filled gap, which is suggested to be an indirect process. First, the energy barrier is reduced due to multiple intermediate states in the gap. Those states are related to the dipole resonances of the well-oriented water dipoles modeled in Figure 29.A.

A simplified calculation of the effective barrier is shown as Equation 2.3.2-1. The number of intermediate states is *n*.[152]

$$\phi_{eff} = \phi/(n+1)^2 \qquad \textit{Equation 2.3.2-1}$$

Therefore, the tunneling current decays in an oscillatory way instead of exponentially.

The model is confirmed by both experimental and theoretical studies. The effective barrier can be calculated by the measured tunneling current ($I$) and tunneling distance ($x$).[153, 154, 155, 156]

$$\phi_{eff} = \frac{h^2}{32\pi^2 m}\left(\frac{\partial \ln I}{\partial x}\right)^2 \qquad \textit{Equation 2.3.2-2}$$

Characterizations of the effective barrier have been achieved by performing distance tunneling spectroscopy (DTS) with EC-STM setups. The DTS measurement is conducted by scanning a sharp electrode (EC-STM tip) normal to another electrode (EC-STM sample) surface in the electrolyte with constant voltage bias. The current is measured as a function of distance. Neglecting the water dipoles, the current *vs* distance curve will result as the gray line in Figure 29.B based on Equation 2.3.1-6. The red curve is the measured data. It starts with a rather constant value when tunneling is barely possible, and only Faradaic contributions can be measured, as the leakage current. 0 nm distance means the two electrodes reach a jump-to-contact point, which is defined as the zero-point of the DTS measurements. An oscillation contribution around the calculated value can be seen. It is due to the changes of the tunneling barrier with distance. The effective barrier (blue) can be determined from the current difference (orange) by Equation 2.3.2-2. This is in agreement with the reported explanation[152].

Further studies proposed that not only water dipoles but also other dipolar species in the tunneling gap, *e.g.*, sulfate ($SO_4^-$) and hydronium ($H_3O^+$), contribute to the oscillation of the effective energy barrier. Figure 29.C combines the side view of co-adsorption of sulfate and hydronium ions (left), determined effective barrier (middle) as a function of distance from the DTS measurements according to Equation 2.3.2-2, and DFT results of the distribution of negative and positive charge density on the electrode surface (right). Sulfate and hydronium ions play considerable roles in the effective barrier, similar to the water dipoles. The effective barrier oscillates directly related to the physical location and distribution of charge (dipoles) of the ions/water dipolar.[156]

In summary, at the solid–liquid interface, electron tunneling is strongly influenced by the local dipolar substances in the electrolyte-filled gap. The tunneling is no longer straightforward, but an process through the effective tunneling barrier. The resulting current will exhibit ‘‘oscillating’’ features. When fixing the position of the tip or scanning it parallel to the sample surface (for instance, topographic imaging), these ‘‘oscillating’’ features should not appear

(considering a laterally homogeneous double layer structure). However, when there is a reaction (for instance, an electrocatalytic reaction) taking place at the surface, the local structure and the lateral homogeneity of the double layer are disturbed. This will also lead to the oscillations of the tunneling barrier and subsequently cause noise signals in the resulting tunneling current or topographic image. The noise should be higher over the active sites, and therefore these active sites can be distinguished. This is the main idea of the proposed n-EC-STM methodology in this thesis. More details will be discussed in Chapter 3.2.

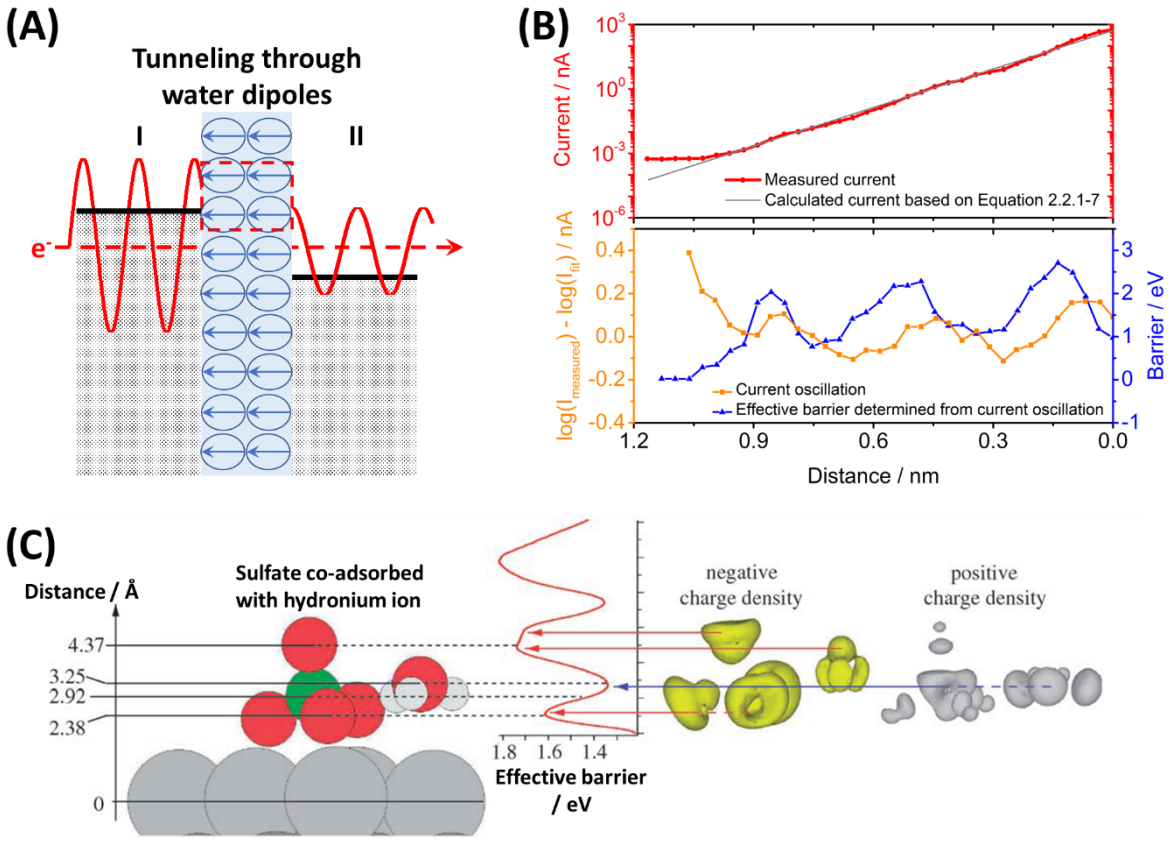


*Figure 29.* ***Tunneling current through the electrolyte-filled gap, tunneling barrier is reduced.*** *(A) Water dipoles in the gap as the proposed reason for decrease of tunneling barrier. Based on ref. 152. (B) Red, in situ measurements on an Au(111) electrode surface with Au STM tip in $N_2$-saturated 0.02 M $HClO_4$. Voltage bias is +100 mV. Current starts becoming constant at large distances, since electron tunneling is inhibited and only background current can be seen (details will be discussed in Chapter3.1.2). Gray: calculated tunneling current according to Equation 2.3.1-6. The measured current oscillated around the calculated value, the difference between logarithms of them is represented as an orange curve. Blue: effective barrier determined from the orange curve according to Equation 2.3.2-2. Adapted with permission from ref. 153. Copyright © 2003 Elsevier B.V. (C) Investigation on the influence of other electrolyte species on the effective barrier on Au(111) in Ar-saturated 0.1 M $H_2SO_4$. Left: side view of co-adsorption of sulfate ($SO_4^-$) and hydronium ion ($H_3O^+$). Middle: effective barrier vs distance based on the DTS according to Equation 2.3.2-2. Right: distribution of negative and positive charge density on the electrode surface from the DFT calculations. Adapted with permission from ref. 156. Copyright © 2007, John Wiley and Sons.*

# 3 Instruments and Experimental Procedures

In this chapter, details of all experimental procedures performed in this thesis are described. It is structured as follows: In Chapter 3.1, the main instruments used in this thesis are described. Chapter 3.2 discusses the concept of the n-EC-STM methodology and shows the experimental details of the n-EC-STM measurements. Chapter 3.3 deals with catalyst sample preparation processes and characterization of prepared samples.

## 3.1 Experimental Instruments

### 3.1.1 Electrochemical cell and Potentiostat

#### 3.1.1.1 Basics of Electrochemical Cell and Potentiostat

Electrochemical cells based on the three-electrode configuration (Chapter 2.1.2) can be designed differently to fulfill special experimental requirements. One example of the cell design is shown in Figure 3, which can also be adapted to use with other instruments, for instance, SPMs.

According to Equation 2.1.3-3 and Equation 2.1.3-4, temperature and concentrations (pressures) of participating substances influence the reaction behavior. In a rigorous electrochemical measurement, comparison of different catalysts toward the same reaction is normally conducted under exactly the same conditions. Therefore, the design of a proper electrochemical cell should take all possible factors into account. Figure 30.A is an example of an electrochemical cell for measurements at single crystals consisting of four parts, a main cell, a preconditioning cell, a RE chamber, and the WE holder[157]. The preconditioning cell has gas inlets and outlets for degassing the electrolyte prior to measurements. The preconditioned electrolyte flows to the main cell which also enables the atmosphere control. In the main cell, the single crystal WE contacts the electrolyte in a so-called hanging meniscus configuration, so that only the crystal face of interest is investigated. The WE holder can be connected to a rotating disc electrode (RDE) motor to control the mode of the mass transfer. This is crucial for the precise evaluation of catalytic properties of single-crystalline electrodes. The RE stands in an independent chamber connected to the main cell by a salt bridge. The whole setup also

provides good cleanliness for the measurements inside.[157] One example where the atmosphere control is critically important is activity studies for HER as the presence of $O_2$ would lead to undesired current contribution from the ORR.

In an EC-SPM system, the electrochemical cell must compromise with the design of the SPM, particularly the space constraints. As can be seen in Figure 30.B, the electrolyte is kept inside the cell by a sealing ring pressed on the planar WE, RE is a quasi-reference electrode made of metal wire. Additionally, the SPM tip needs to pass through the electrolyte and interact with the sample surface within a microscopic scale. No built-in atmosphere/temperature control is available in most commercial off-the-shelf systems.[28]

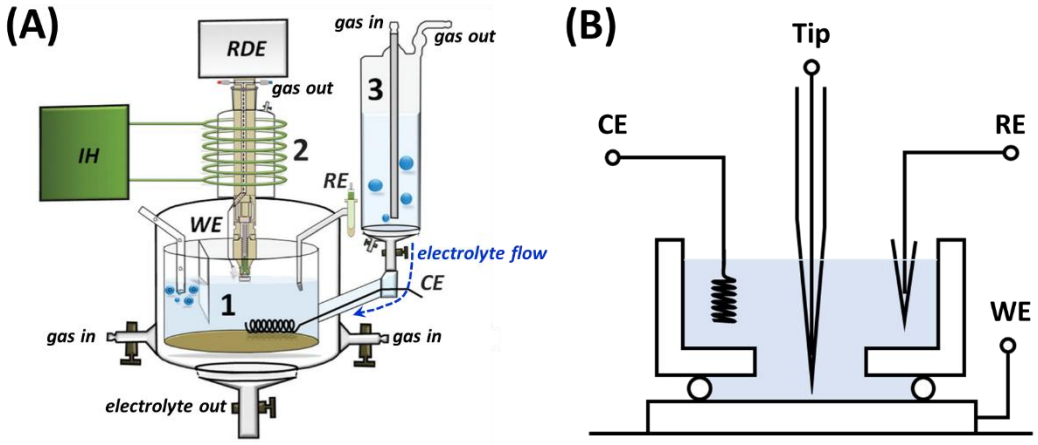


*Figure 30.* ***Schematic drawings of electrochemical cells.*** *(A) A versatile cell consisting of 1) the electrochemical compartment (main cell) with atmosphere control, 2) a high frequency inductive heater (IH) for temperature control and a rotating disc electrode (RDE) motor for reducing the mass transfer influence on the WE, 3) electrolyte preconditioning compartment and a RE chamber. Taken with permission from ref. 157. Copyright © 2013, Royal Society of Chemistry. (B) Configuration of an EC-SPM cell. Several compromises can be seen, e.g., the RE is a quasi-reference electrode made of metal wire and atmosphere/temperature control is absent. Adapted with permission from ref.28. Copyright © 1988 Published by Elsevier B.V.*

A reliable RE is the basic requirement of any electrochemical measurement. For a cell like the one shown in Figure 30.A, for instance, the normal hydrogen electrode (NHE), an Ag/AgCl electrode in KCl saturated aqueous solution (SSC), or a $Hg/HgSO_4$ electrode in $K_2SO_4$ saturated aqueous solution (MMS) are often employed. The NHE consists of a platinum electrode dipped in pH = 0 acidic media with 1 bar $H_2$ and pure hydrogen gas purging. Theoretically, for a Pt electrode under the condition of 1 atm $H_2$ and $H^+$ activity $a$ = 1 (1 M $H^+$) at 25°C, the electrode potential is defined as 0 V in electrochemical systems, and the electrode is the so-called

standard hydrogen electrode (SHE). Both SSC and MMS have stable potential differences with respect to the NHE, respectively[63]. Equilibrium potentials of electrocatalytic reactions are often pH-dependent, *e.g.*, HER and ORR. A pH-independent reference scale is therefore often preferred in practice, for instance, the reversible hydrogen electrode (RHE) which uses a configuration as the SHE, but operates in the same electrolyte in which the catalytic reaction is studied, *i.e.*, at pH ≠ 0. Resulting from calculations based on the Nernst equation, the potential applied on WE with respect to RHE is taken as WE (*vs* RHE) = WE (*vs* RE) + RE (*vs* SHE) + 0.0591 V × pH.[63]

Both the current and potential of the WE can be controlled to study electrochemical phenomena or recorded as consequences of electrochemical processes. For the studies covered in this thesis, the WE potential is often controlled and varied to shift the electrochemical equilibrium and tune the targeted reactions. Consequently, the current is recorded as a function of time or potential (or both). This is done using a device called "potentiostat", with the measurement scheme shown in Figure 31.A. The potentiostat controls the potential and current of the WE according to the principle of the three-electrode configuration explained in Chapter 2.1.2. Two basic operation modes of a potentiostat, *i.e.*, the potential step method and the potential sweep method, are often represented by their typical potential input and current response as a function of time and potential, respectively (Figure 31.B and Figure 31.C). Commonly used techniques based on these modes are pulse voltammetry, linear sweep voltammetry (LSV) and cyclic voltammetry (CV), depending on whether the potential is manipulated stepwise or linearly from one value to another one.[63]

Normally in a pulse voltammetry experiment, the WE is forced to jump from its steady-state to a non-steady state value and often arrives in the mass transfer limitation region of the targeted reactions. The system will need a certain time to reach a new equilibrium if it is possible. The resulting current transient is commonly a decay curve. The magnitude of the current depends on the extent of the potential change (and thus the applied overpotential), the bulk concentrations of the participating electrolyte species, and the kinetic and thermodynamic parameters of the electrode reaction(s). When the potential is switched back to the initial value, an opposite current can usually be observed indicating the reverse reaction, at least for reversible or quasi-reversible reactions.[63]

LSV and CV sweep the WE potential linearly at a constant speed (scan rate: $v = dE/dt$). During one scan, the WE can experience several reactions in different potential ranges, but there may be also potential regions where no Faradaic reaction takes place (so-called double layer region). When the scan goes across the equilibrium potential of a specific (outer-sphere) reaction, not only the approximate starting point but also effects of different overpotentials can be determined, as shown in Figure 31.C. Current peaks can be seen in the current *vs* potential plot (the cyclic voltammogram, also abbreviated as 'CV') due to the mass transfer limitation, which is strongly influenced by the scan rate. If there are adsorption/desorption or deposition processes of electrolyte species, corresponding features will appear at the right potential range on the recorded plot.[63, 128]

With an electrochemical cell and a potentiostat, many electrochemical investigations and processes on catalyst materials can be performed successfully, including surface cleaning, activity tests, and sample preparations and characterizations[63]. Details of all applications utilized in this thesis will be discussed in the following chapters.

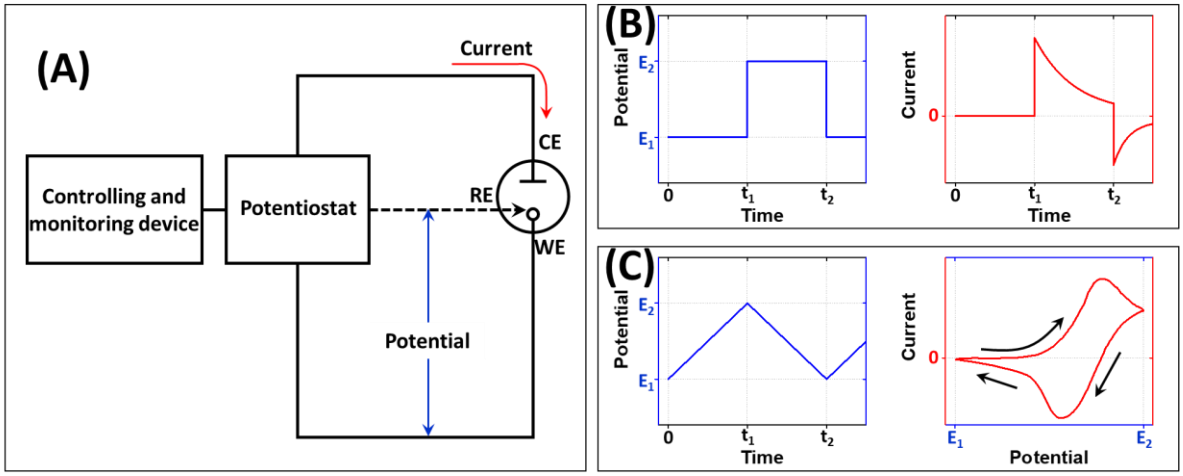


*Figure 31.* ***Potentiostat and its basic operations.*** *(A) Experimental arrangement for potential-controlled measurements using a potentiostat; (B) A plot of a step potential control and characteristic measured current flow with time; (C) Waveform for a sweep potential control and typically resulting current vs potential curve with direction indicators (black arrows). Adapted with permission from ref.63. Copyright © 2000, John Wiley and Sons.*

As mentioned above, CV is often used as a characterization tool for electrode materials in defined electrolytes[63]. Some examples of cyclic voltammograms for Pt single-crystals studies are shown in Figure 32. In Figure 32.A, CVs of Pt(111) in Ar-saturated acidic and alkaline

solutions (0.1 M $HClO_4$ and NaOH) are shown. The voltammograms reveal adsorption and desorption of H, OH, and O species (corresponding peaks are designated in the figure).

As shown in Figure 32.B, in the same electrolyte (0.1 M $HClO_4$), H adsorption and desorption have peaks with similar shape (peak 1) around 0.15 V *vs* RHE on Pt(110), and another pair of peaks (peak 2) disclose the adsorption of OH-species.

CV can also trigger changes in the electrode surface structure. One example is shown in Figure 32.C for sulfuric acid, where the Pt(111) electrode response is "stable" and characteristic in the range where the CV is taken (black curve). However, when the potential is scanned between 0.06 and 1.4 V *vs* RHE, thus too much more positive potentials, (111)-associated features disappear gradually while new peaks appear and grow (red curves, blue curve: last cycle).

Figure 32.C also shows how cyclic voltammogram reflects damages introduced to the single-crystal surface made by anodic polarization of the electrode. However, damaged electrode surfaces can be restored by flame-annealing treatment in reducing atmosphere (carbon monoxide (CO) /Ar or $H_2$/Ar mixture).[158]

Figure 32.D compares CVs of Pt(111) electrodes in $O_2$-saturated and Ar-saturated electrolytes. The CV in oxygen-saturated 0.1 M $HClO_4$ is shifted down to more negative currents as a result of the oxygen reduction reaction (ORR). In principle, for many reactions, for instance, in the case of HER and ORR, CV can approximately point out the 'onset' potentials, where the reactions start. Additionally, the current increase with increasing overpotentials and the mass transfer limitation of the current also can be seen in the CVs (Figure 32.D). In other words, CV experiments can be used to acquire "fingerprints" of the Faradaic processes taking place at the electrode surface.[159, 160]

The specific surface area estimation can also be done using CV experiments performed in certain electrolytes. For example, integration of hydrogen adsorption peaks in Figure 32 in Ar-saturated electrolytes can help in the estimation of the true surface area of Pt electrodes. The charge density associated with adsorption/desorption of a monolayer of hydrogen atoms corresponds to ~210 μC $cm^{-2}$ for polycrystalline Pt, and ~241 μC $cm^{-2}$ for single crystalline Pt(111) and ~ 200 μC $cm^{-2}$ for single crystalline Pt(110) (measured values, differ from calculated values).[63, 161, 162, 163, 164]

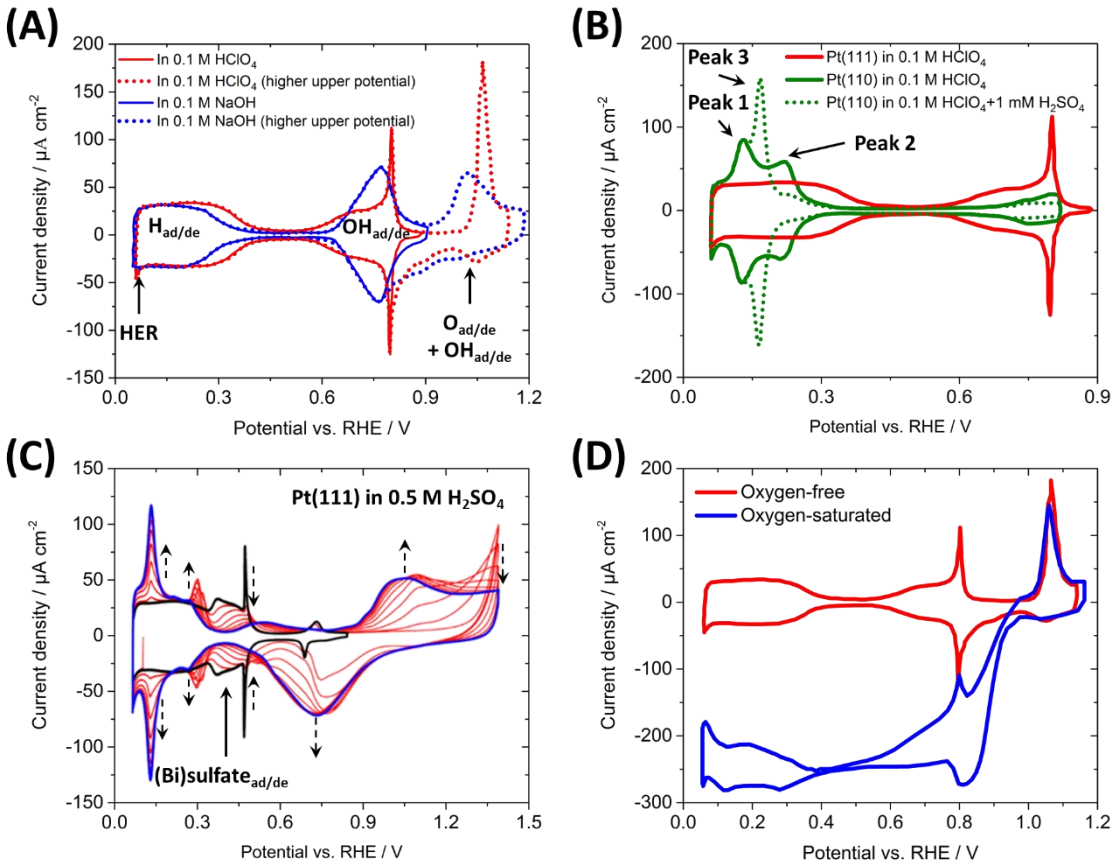


*Figure 32.* ***CV characterizations of Pt single-crystalline surfaces.*** *(A) CVs of Pt(111) in 0.1 M $HClO_4$ and NaOH electrolytes with different vertex potentials. Adsorption/desorption of species results in different features at corresponding potentials. The beginning of HER can be seen in case of $HClO_4$ (red) at more negative potentials. (B) Comparison of Pt(111) and Pt(110) in 0.1 M $HClO_4$. Peak 1 corresponds to the adsorption of H-and peak 2 of OH-type species. When $H_2SO_4$ is added, Peak 3 appears, indicating the adsorption of (bi)sulfate (Sulfate with hydronium). (C) Continuous CV of Pt(111) in 0.5 M $H_2SO_4$. (D) CVs of Pt(111) electrodes in $O_2$-saturated and Ar-saturated 0.1 M $HClO_4$. Scan rate: 50 mV/s. Data are adapted from ref. 159, and with permission from ref. 160. Copyright © 2004, American Chemical Society.*

### 3.1.1.2 Experimental Setup and Preparation

In this thesis, macroscopic electrochemical measurements were conducted using a potentiostat (VSP-300, Bio-logic) and electrochemical cells. The electrochemical cells were manufactured according to the design shown in Figure 30.A. However, the RDE and IH compartments were not equipped since they were not necessary. The specific atmosphere was controllable in the cells by purging required gases, for instance, Ar (Westfalen, Ar 5.0) for $O_2$-free atmosphere and Ar/CO mixture (Westfalen, Ar 5.0 + 1000 ppm CO) for reducing atmosphere required for cooling down the single crystals after flame-annealing treatment.

Both the MMS and the SSC electrodes (+0.664 V and +0.196 V *vs* SHE, respectively, both SI Analytics) were used as reference electrodes. Caro's acid, roughly 70% $H_2SO_4$ (96%, Suprapur®, Merck KGaA) and 30% $H_2O_2$ (30%, Suprapur®, Merck KGaA), was used for cleaning the cells and other glassware. Afterwards, all glassware was cleaned by ultrapure de-ionized water (18.2 MΩ cm, Evoqua, Germany) by boiling it several times. The working electrode contacted the electrolyte using a hanging meniscus configuration so that a well-defined geometric surface area of the working electrode was maintained.

The electrochemical characterization methods were used in all sample preparation and activity evaluation processes, to complement the EC-STM measurements and the interpretations of the recorded images. CV measurements were utilized when the surface chemical composition and structural information was required, especially after metal deposition processes and for single crystal surface quality assessments.

## 3.1.2 (Electrochemical-) Scanning Tunneling Microscopy

### 3.1.2.1 Working Principle of (Electrochemical-) Scanning Tunneling Microscopy

The working principle of the STM, depicted in Figure 33.A, did not change much since Binnig and Rohrer invented it[31]. A zoom-in schematic to the tunneling gap is illustrated in Figure 33.B. It consists of a sharp metallic electrode as the tip and another electrode as the sample. The tip is positioned by rectangular piezo systems to scan it over the sample surface. One piezo actuator approaches the tip close to the sample surface at angstroms (electron tunneling is possible) and adjusts the height (z-direction) of the tip, if it is necessary during scanning. The other two axes of movement (x, y-direction) are also controlled individually to scan the tip over the area of interest of the sample surface.[31]

Piezo elements position the objects (*i.e.*, tip, or the sample is moved in some STM devices) by physical deformation of the piezoceramic material with the applied electrical field, the converse piezoelectric effect[165]. The piezoelectric effect and its reverse phenomenon were discovered by Jacques and Pierre Curie in the early 1880s[166, 167, 168]. It is caused by the electric dipole moments in certain materials. Electric charges can be generated in response to external mechanical stress, and a reversibly applied voltage can change the lattice structure of the material.

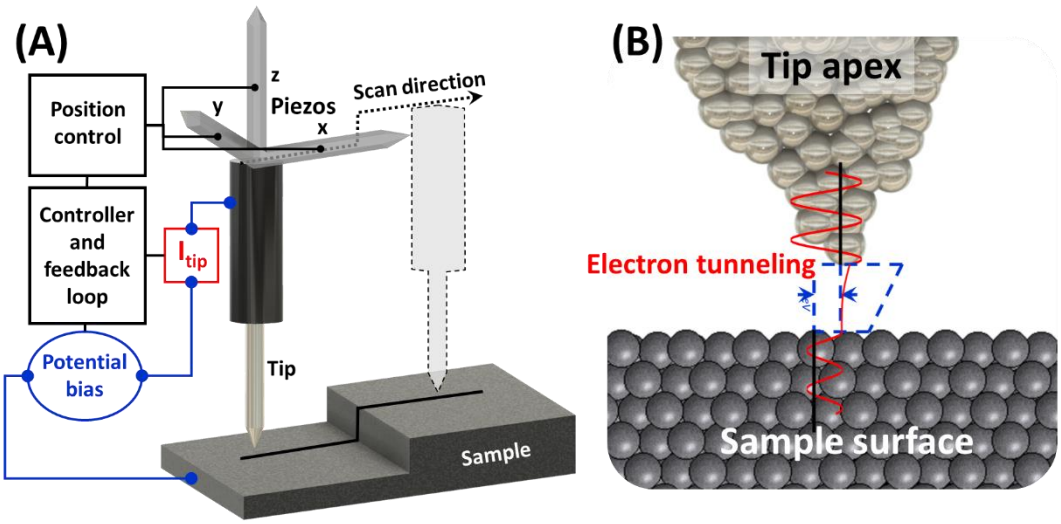


*Figure 33.* ***Working principle of STM****. (A) Schematic of STM setup and (B) a zoom-in at the interaction between tip apex and sample surface. Based on the principle presented in ref. 135.*

There are two operation modes of STM that are commonly used. Those are the constant height mode (Figure 34.A) and the constant current mode (Figure 34.B). In constant height mode, the height of tip is fixed. The tip current varies during scanning due to the change of the surface topography or surface density of states, which determine the tunneling probability. It is suitable for measuring on atomically flat surfaces. Due to the small size of the tunneling gap, any large surface height change will crash the tip. However, high-resolution imaging can be achieved within this mode, since the tip can be forced to stay close to the sample surface.

The constant current mode maintains the tunneling current constant (current setpoint) by adjusting the tip height, *i.e.*, the tip-sample surface distance. A feedback loop combines the current read-out and the piezo control. The surface topography is imaged by recording the height of the tip over the scanned area. Basically, constant height mode generates a current map with mixed topographic and conductivity (surface density of states) information, the constant current mode produces a height map but is also influenced by other surface properties (*e.g.*, electronic structure).

Note that in both Figure 34.A and B, the curve of the current (or height) does not exactly match the surface profile. The reason is that the tip is not only one atom but a sharp apex with numerous atoms, as shown in Figure 34.B. Each atom in the range of the tunneling distance contributes to the total tip current. When the tip is approaching closer to higher parts of the

surface (like the step in Figure 34), likely the side atoms of the apex instead of the actual last atom of the tip will firstly generate tunneling current. Therefore, a broadening effect caused by the geometry of the tip (*e.g.*, tip curvature radius) is common in many STM images. An oscillation of the tunneling current in the constant current mode can be observed because of the feedback-loop adjustment.[150]

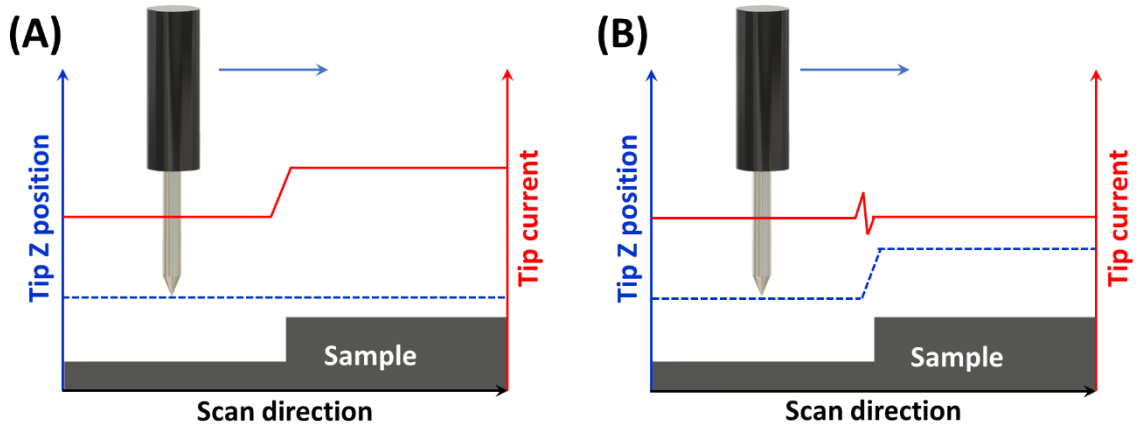


*Figure 34.* ***Operation modes of STM.*** *(A) Constant height mode. (B) Constant current mode.*

Before approaching the tip towards the sample, a background current caused by the internal electronics and leakage currents (normally in EC-STM), the so-called offset current, already exists at the tip. To have a reasonable resolution, a current setpoint at least a few times larger than the offset is recommended.

As shown in Figure 35.A, EC-STM performs the STM measurement in an electrolyte under potential control. Like in normal EC cells, RE and CE are employed. STM tips are often made of metal wires including Au and Platinum/Iridium (Pt/Ir) alloy. An insulating coating is necessary to make sure that the majority of the tip current is from electron tunneling but not from Faradaic processes at the tip. Faradaic currents at the whole surface of a bare tip in contact with an electrolyte can be orders of magnitude larger than tunneling current, since those tip materials are likely active or reactive in electrochemical environment. Even double layer charging/discharging is noticeable. Tip and sample potentials are controlled individually by a bipotentiostat with respect to the RE. The potential bias is the potential difference between the tip and the WE ($E_{tip} - E_{WE}$). While imaging topography, the potentiostat can perform electrochemical measurements at the sample. First, topographic changes related to

electrochemical processes can be simultaneously (*in-situ*) observed, and the obtainable resolution of it is comparable to that of STM in air. Moreover, EC-STM can detect surface adsorbates as an additional signal in the topography or current imaging, depending on the operation mode.[146]

Figure 35.B represents a cross-section of an insulated tip. It is not completely covered by the coating. A tiny apex is exposed to the electrolyte to allow electron tunneling but avoid large undesired Faradaic currents. Therefore, the tip potential is normally kept in the double-layer region of the system.

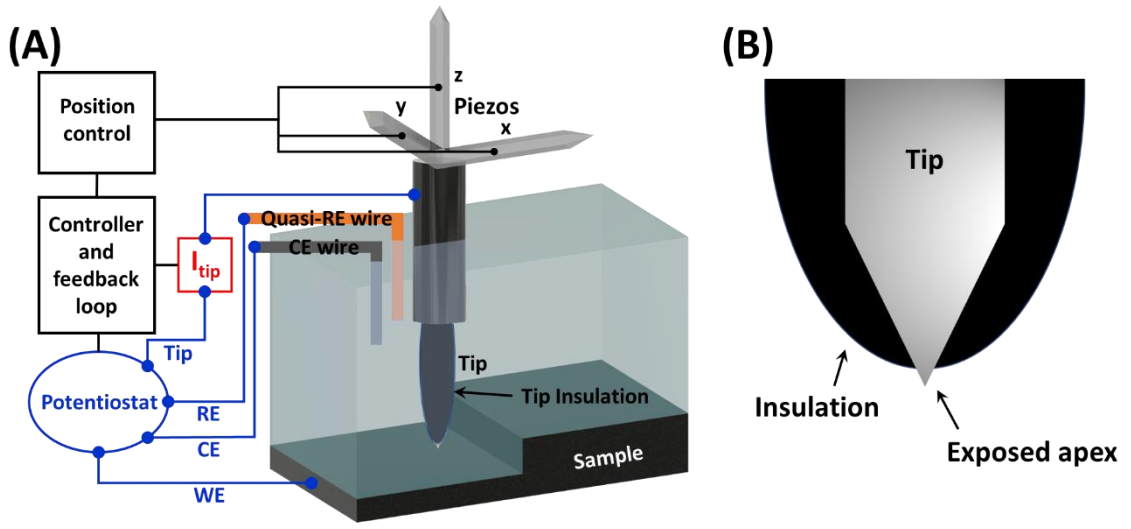


*Figure 35.* ***Schematic of an EC-STM setup.*** *(A) A potentiostat controls the potential of the tip and the WE with respect to the quasi-RE and measures the currents. The potential bias is the potential difference between tip and WE. The tip is insulated by a chemical- and electrochemical-resistant material, and only a tiny apex is exposed to the electrolyte. (B) Cross-section of an insulated tip.*

The quasi-RE can be a pure or coated metal wire, for instance, Pt or Ag/AgX, where X stands for Cl or Br. The potential of the metal wire is the equilibrium potential of the metal/electrolyte interface (reactions determine the potential at this interface), for instance, the equilibrium potential of the redox reactions of the metal when $O_2$ presents in the electrolyte. The Ag/AgX quasi-reference electrode is a silver wire fully coated with silver chloride. In $X^-$ free electrolytes (for instance, 0.1 M $HClO_4$, which is used in this thesis), the potential is defined by the dissolution of AgX (Equation 3.1.2-1)[169]. Both AgCl and AgBr are hardly soluble in water[170], and the potentials of the AgX quasi-reference electrodes are stable

when there is no metallic Ag exposed to the electrolyte[169]. In halide solutions, the potential of Ag/AgX is directly determined by the concentration (activity) of $X^-$ in the electrolyte.

$$AgX(s) \rightleftharpoons Ag^+ + X^- \qquad \textit{Equation 3.1.2-1}$$

### 3.1.2.2 (Electrochemical-) Scanning Tunneling Microscopy Setup and Preparation

The (EC-) STM setup (Figure 36.A and B) is a Multimode EC-STM/EC-AFM instrument (Veeco Instruments Inc.) equipped with a Nanoscope IIID controller. It is capable of (EC-) STM, (EC-) AFM, and scanning electrochemical potential microscopy (SECPM) measurements. The software used for operating the microscopes was Nanoscope 5.31r1. All recorded microscopy data were analyzed by WSxM software[171]. Details of the sample cell are shown in Figure 36.C and D, depending on the shape of the samples. The Teflon® ring presses the sample on an iron plate and is tightened by four screws. The Teflon ring provides a liquid-tight hole for the electrolyte and other electrodes including the tip. A conductive and ferromagnetic iron plate is attached to the piezo system. For samples without z-direction conductivity, for instance, Au on glass chips, a clean gold wire connects the Au side and the iron plate to ensure the conductivity.

For the STM tip preparation, a platinum/iridium alloy wire (Pt80/Ir20, ⌀ = 0.25 mm, GoodFellow) was mechanically sheared and pulled apart using a wire cutter (Knippex) and a holder (Figure 37.A). All prepared tips were tested by performing normal STM measurements in air. EC-STM tips require insulation to prevent any leakage current. The insulation procedure is described in Figure 37.B. The very end of the tip apex is still exposed to have the tunneling current signal. Typically, the leakage current should be less than 10% of the current setpoint in order to have an acceptable resolution. Freshly prepared EC-STM tips were characterized by CV and SEM.

Pt or Au wires (both MaTecK, ⌀ = 0.5 mm) were used as CE. Only quasi-reference electrodes were available for EC-STM. In the case of $HClO_4$ electrolytes, Pt or Ag/AgCl wires served as RE (further designated as Pt and Quasi-SSC, respectively). Ag/AgCl wires were freshly prepared by applying 5 V for 30 s to a Ag wire (MaTecK, ⌀ = 0.5 mm) in concentrated HCl (37%, technical grade) prior to each experiment. In $H_2SO_4$ electrolytes, Pt and oxidized Au wires were the

alternative options. The Au wires ($AuO_x$) used as REs were electrochemically oxidized in ~1 M $H_2SO_4$ by applying 5 V for 30 s. All REs and CEs were cleaned with ultrapure water and treated with flame-annealing, except the Ag wires. All the REs were assessed by performing CV of the samples before EC-STM measurements, so that potentials at which targeted reactions are taking place can be determined.

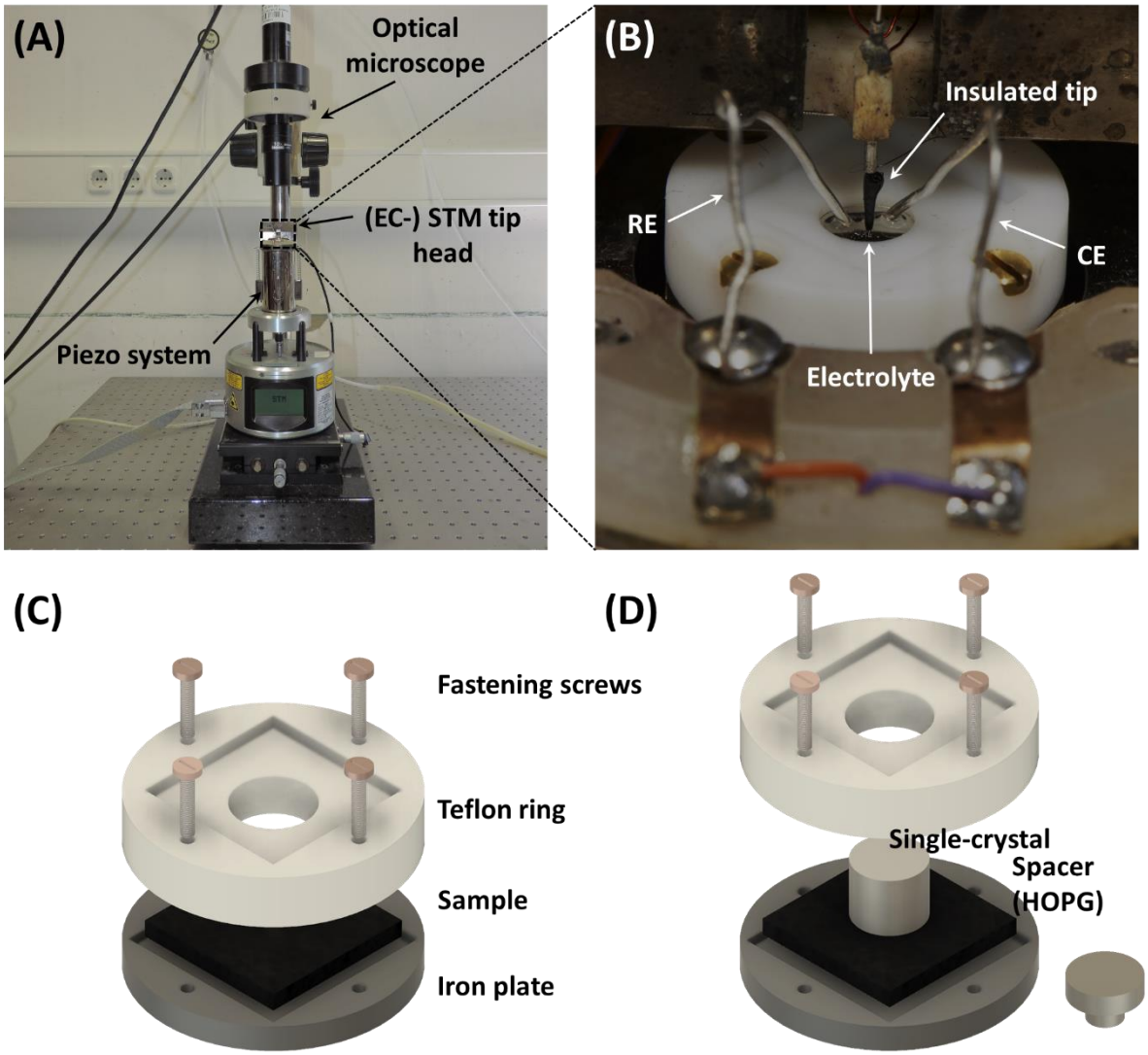


*Figure 36.* ***Multimode microscope instrument equipped with (EC-) STM head settled on a damping stage and an air table (Newport).*** *(A) A photograph of the setup with (EC-) STM mounted on top of the piezo system. (B) Insulated tip, sample cell and the electrodes. The tip position is fixed, and the sample is scanned by the piezo system. All electrodes are immersed in the electrolyte which is exposed to air. (C) The investigated plate-shaped samples are tightly pressed onto a conductive iron plate with a Teflon® ring. (D) In case of cylinder-shaped or similarly shaped single-crystal samples, a similar configuration was used.*

The home-made quasi-reference electrodes were less stable relative to the commercial ones. Hence, the actual potentials were slightly different compared to other literature values, particularly if it needs to be in well-controlled atmosphere. Since the cell was exposed to the air, roughly 5 mM $O_2$ was dissolved in the electrolyte[172]. Additionally, electrolyte evaporation and rapid reactions at the sample surface can change the electrochemical environment (*e.g.*, electrolyte composition) in the cell. Therefore, the actual potentials applied to the samples were not converted with respect to RHE or other standard reference values in this thesis.

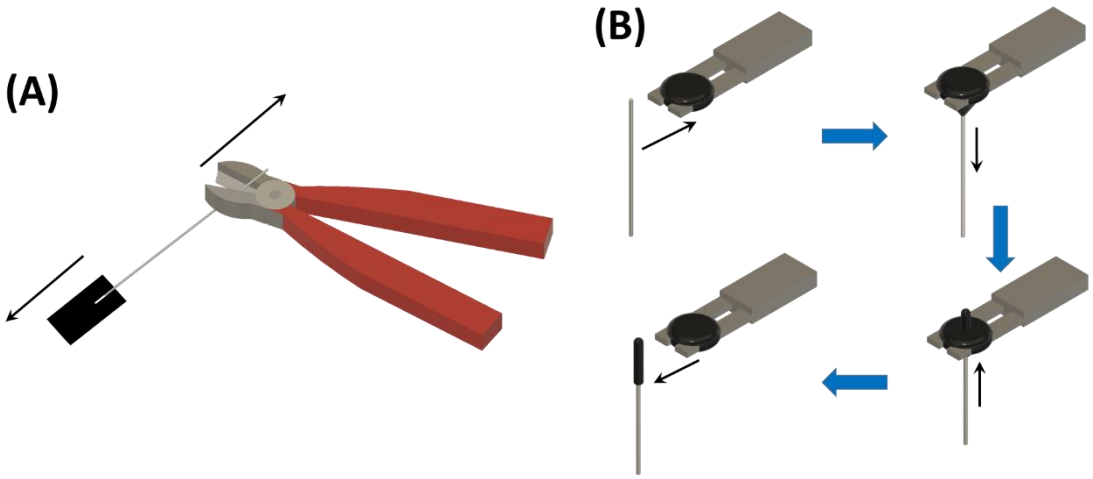


*Figure 37.* ***Tip preparation.*** *(A) STM tip sheared mechanically by a wire cutter and a holder. (B) Tip insulation procedure with wax and a fork-like tip fixed on soldering iron.*

Routinely, (EC-) STM instruments were used to measure conductive sample surface topography with high resolution. Prepared samples including single-crystalline electrodes and a various sub-monolayer catalyst material on different substrates were investigated in order to obtain their topographic properties.

The EC-STM cell used in this thesis was exposed to air and the electrolyte was slowly evaporating during the experiments. The electrolyte concentration can thus be changed influencing the reactions at the sample surface. Occasionally, due to the evaporation of the electrolyte, more electrolyte was added to the cell using a pipette during all measurements. Reaction products formed at the sample and the CE can also change the electrochemical environment in the cell. For instance, the reference potential of a Pt wire quasi-RE can be strongly influenced by the $H_2$ dissolved in the electrolyte. To tackle this issue, CV of the sample

was performed frequently to ensure that the right potential was applied to the sample and to check if maintenance of the electrolyte was needed.

#### 3.1.2.3 Characterizations of the Tips

Before the EC-STM measurements, the prepared EC-STM tips were characterized electrochemically. CVs were measured for freshly prepared insulated tips in Ar-saturated 0.1 M $HClO_4$ in the electrochemical cell using a Bio-logic potentiostat, and in the EC-STM cell. The typical CV (Figure 38.A) of the EC-STM tips obtained by the EC-STM potentiostat can be used to determine the exposed metallic area of the tip by calculating the total charge of the hydrogen desorption peak. Therefore, the peak current was integrated over time, and converted using the common value of 210 µC $cm^{-2}$ into the surface area[173]. The surface area value varies for different homemade tips. However, they are of the order of $10^{-6}$ $cm^2$, which is enough to have considerable faradaic current at the tip. The value is in agreement with that determined from CVs of multiple tips shown in Figure 38.B in the electrochemical cell with atmosphere-control.

The geometry of the insulated EC-STM tip was measured using scanning electron microscopy (SEM). SEM was performed on freshly cut tips (Figure 38.C) and insulated ones (Figure 38.D) afterwards. The apex of the non-insulated tip has irregular edges. This is common in mechanically cut tips. Additionally, SEM provided a closer look at the exposed part of the insulated tip. A clear boundary (marked by the red dashed line) between wax and rough metal surface can be seen on the insulated tip. The width and height of the exposed part are of tens of µm. Both CV and SEM characterizations were designated to evaluate the exposed surface area of the metallic tip and the extent of a Faradaic current at the tip.

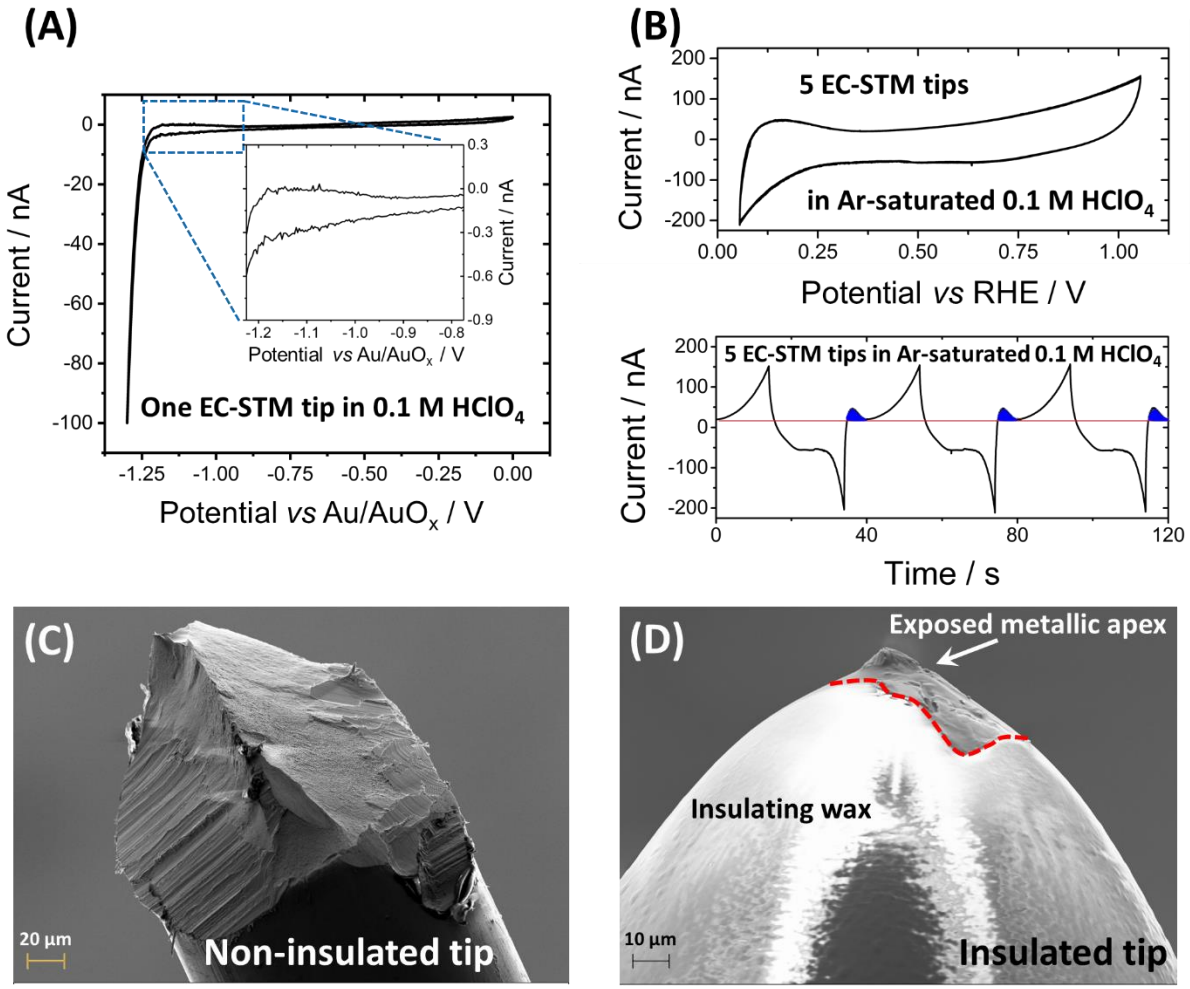


*Figure 38.* ***Characterizations of (EC-) STM tips.*** *(A) CV of an EC-STM tip obtained in the EC-STM cell at a scan rate of 50 mV/s. (B) CV of five EC-STM tips (five tips connected to the sample holder in parallel as one WE) measured in Ar-saturated electrochemical cell at a scan rate of 50 mV/s and a current-vs-time plot (the hydrogen desorption peak marked in blue). (C) and (D) SEM images of freshly cut and insulated tips. Different materials are distinguished by color contrast. A red dashed line acts as a guide to the eyes for the metal/wax boundary.*

For the proposed n-EC-STM, the tip will be scanned over the sample surface under reaction conditions. The tunneling current noise should play the major role in the observed overall noise features. In order to estimate the contributions of tunneling and Faradaic currents, characterizations of the EC-STM tips were performed while changing the reaction conditions of the sample.

Single crystalline Pt(111) was chosen as the sample. Prior to measurements, the tip was approached to the sample and then retracted, and a distance of about 21.8 µm between sample and tip was kept for further measurements. CVs and potentiostatic potential holds

were carried out at the tip; Figure 39.A and B are the resulting CV and current transient, respectively. In both cases, the tip current was shifted to more positive values when HER is 'on' at the sample due to the HOR at the tip. Therefore, a sample-generation-tip-consumption-loop is built up between the sample (HER) and the tip (HOR). The tip current is therefore likely to be influenced by reactions at the sample. However, the current from the oxidation of hydrogen at the tip is about 20 pA which is at least one order of magnitude less than the typical current setpoint (≥200 pA) of EC-STM measurements in this thesis. This suggests that approximately the overall Faradaic current at the tip is minor compared to the overall tip current during topographic imaging under HER 'on' conditions. Taking into account the surface area of the tip determined from the CV methods, the current density at the tip is approximately 20 µA $cm^{-2}$. Therefore, only some of the evolved hydrogen will be re-oxidized at the tip.

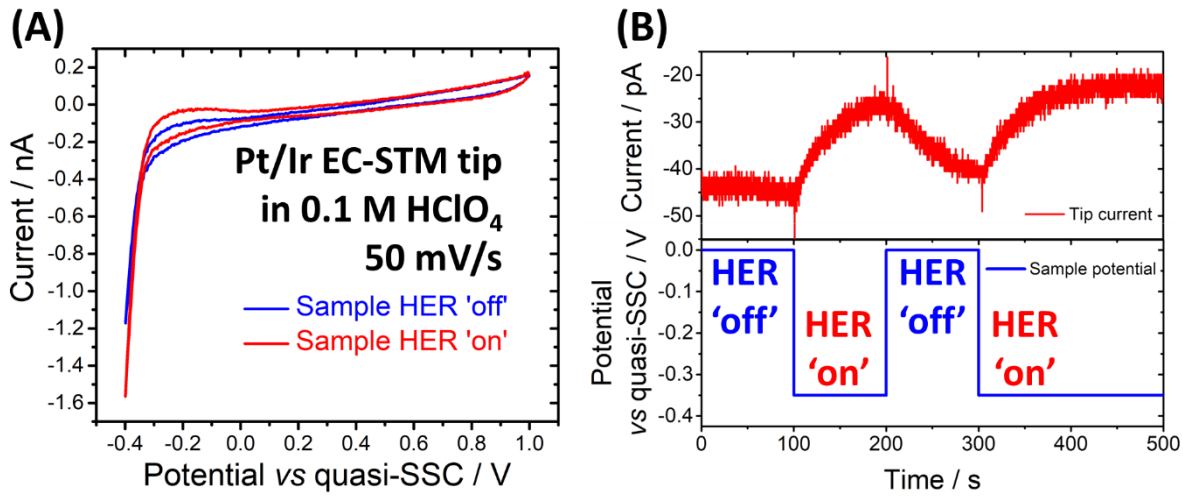


*Figure 39.* ***Characterizations of EC-STM tips combined with Pt(111) sample behavior.*** *(A) CV of a tip measured when the Pt(111) sample was evolving $H_2$ and in contrast, when HER on the sample was stopped. Scan rate: 50 mV/s. (B) chronoamperometric current transient of a tip recorded with different sample potential steps. The Pt(111) sample potential was 0 mV vs quasi-SSC in the case of HER 'off' and changed to -350 mV to start the HER.*

## 3.2 Direct Identification of Catalytically Active Centers Using Electrochemical Scanning Tunneling Microscopy

### 3.2.1 Electrochemical Scanning Tunneling Microscopy on Heterogeneous Catalysis

#### 3.2.1.1 Topographic Imaging of (Electrochemical-) Scanning Tunneling Microscopy

Topographic mapping can provide indications for other processes. Besides structural changes directly caused by surface reactions[174], surface atom mobility[107] and adsorbates (Figure 40)[175] can be visible in EC-STM images. It was reported that atoms of a Ag(100) step are unstable in 0.05 M $H_2SO_4$ + 1 mM $CuSO_4$ at 0.04 V *vs* SCE, while the terrace atoms are relatively steady[107].

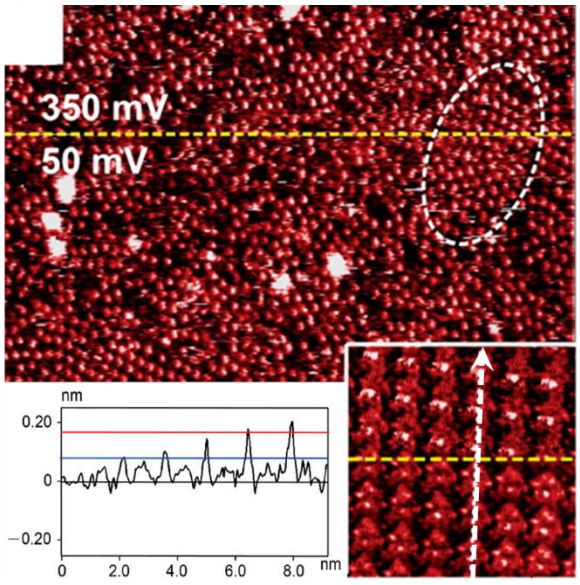


*Figure 40.* ***EC-STM image containing information of surface adsorbates.*** *An EC-STM image of iron-phthalocyanine (FePc) monolayer on Au(111) in $O_2$-saturated 0.1 M $HClO_4$ at different WE potentials, 0.35 V and 0.05 V vs SCE. The white square (9 nm × 9 nm) shows a high-resolution image together with a cross-section profile along the white dotted arrow across the potential change line (yellow). Blue and red line in the profile indicate the average height of the peaks of different potentials. Potential bias = −0.3 V, current setpoint = 1.0 nA. Adapted with permission from ref. 175. Copyright © 2016, American Chemical Society.*

Figure 40 is an EC-STM image of an iron-phthalocyanine (FePc) monolayer on Au(111) in $O_2$-saturated 0.1 M $HClO_4$ at two different reaction states of oxygen reduction. The sample potential was started at 0.35 V *vs* SCE at which O-species (ORR intermediates) adsorb on the sample, but no ORR is possible. Then, it was switched to 0.05 V vs SCE where ORR takes place. A high-resolution image and the cross-section profile along the white arrow compare the

height change of the surface, indicating the O-species adsorption before ORR and consumption of them during ORR. The active surface sites (where adsorption occurs) are located at the center of the FePc.[175]

### 3.2.1.2 Additional Information in Images

EC-STM is capable of imaging phenomena related to electrochemical reactions[174, 175]. As shown in Figure 40, EC-STM can observe the topographic changes due to the adsorption or desorption of the reactions intermediates. Other attempts were made by STM under atmosphere-control for gas phase reactions. Imaging of intermediate species at the surfaces directly locates the corresponding active sites where catalytic reactions take place[25]. The tunneling electrons can be used to activate a catalytic reaction at the sample surface[35, 36]. Well-developed STM systems with gas and temperature-control have been elaborated[176]. However, as shown in Figure 41.A, typical measurements described in literature require relatively steady surface adsorption or oxidation states, so that (EC-) STM can capture the ''frozen'' reaction-related species or consequences[35]. The dynamic processes under real reaction conditions (for instance, under industrially relevant conditions) are not fully revealed.

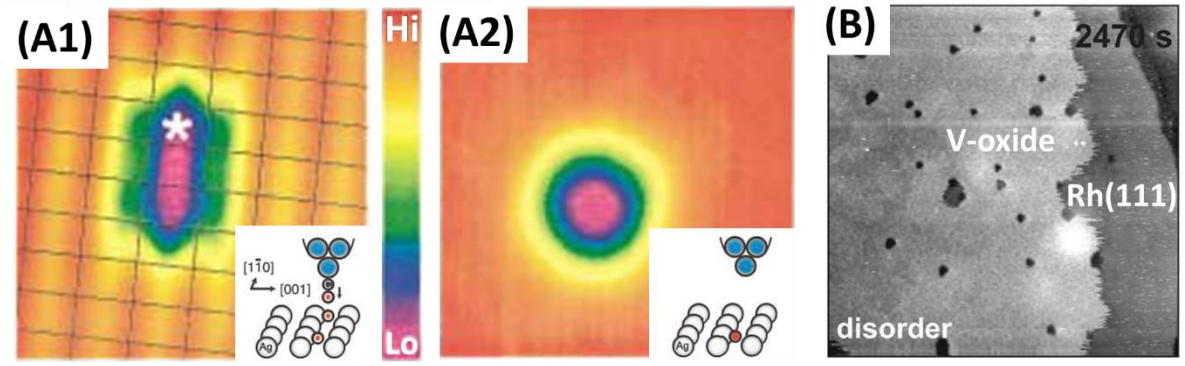


*Figure 41.* ***Reactions captured by STM.*** *(A) Oxidation of a CO molecule from a CO-poisoned STM tip by an O-atom adsorbed at the sample surface. (A1) CO-poisoned tip scans over two O atoms adsorbed on Ag surface. (A2) After a sample bias pulse of 470 mV to oxidize the CO with one O atom from the sample surface, resulting $CO_2$ has been released from the tip and one O atom is left at the sample surface. Image size: 0.25 nm × 0.25 nm. STM performed at 13 K. Adapted with permission from ref. 35, Copyright ©2001, American Physical Society. (B) Reduction of 0.25 monolayer V-oxide on Rh(111) surface in 1 × $10^{-9}$ mbar $H_2$ at 400 °C. Noisy boundary of V-oxide can be seen. Reaction times: 2470 s, image size: 80 nm × 80 nm, voltage bias = 0.75 V, I = 0.1 nA, image recording time 70 s. Adapted with permission from ref. 179. Copyright © 2005, Springer Science Business Media, Inc.*

The presence of a noise signal is characteristic for any measurement technique, and noise has been observed before in the measured tunneling current. It has been indeed suggested that noise features in the tunneling current are potentially distance-sensitive and can be used to observe local reactions in electrolytic environments, even though the presence of noise limits the performance of STM.[177, 178] In gas phase environment, local noise in STM has been revealed during imaging of a 0.25 monolayer of vanadium (V) oxide on a Rhodium (Rh) (111) surface in $H_2$ atmosphere. Reduction of the V-oxide phase leads to a topographic change and noise features on the oxide boundary (Figure 41.B), which are caused by rapidly moving ad-particles and diffusion of material at the surface.[179]

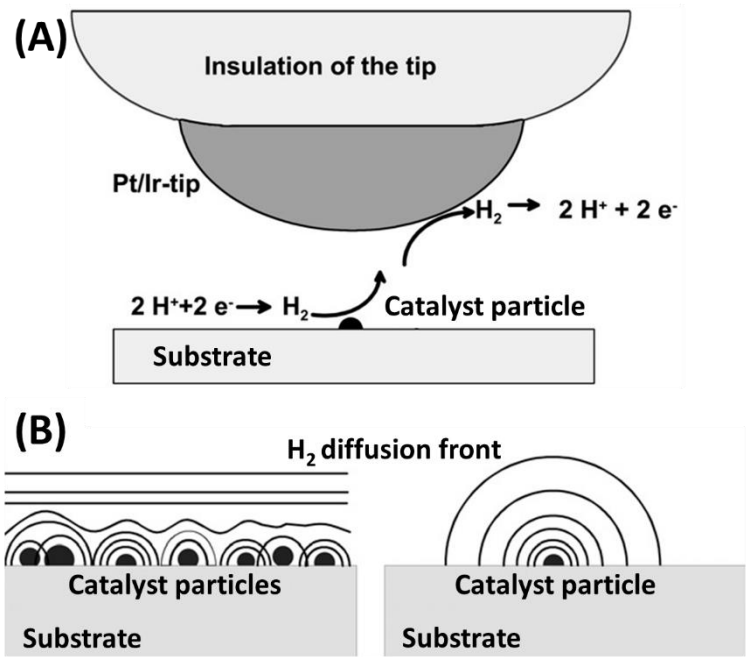


*Figure 42.* ***Illustration of catalyst particle activity measurement by EC-STM.*** *(A) EC-STM tip and particle form coupled redox reactions (HER and HOR) under reaction conditions, while the tip stays over the particle. (B) Merged diffusion front of produced $H_2$ from multiple particles close to each other, and spherical shape of that from single particles. Adapted with permission from ref. 37, Copyright © 2002, Royal Society of Chemistry.*

Since typical EC-STM tips are made of metals, in certain tip potential regions Faradaic current noises at the tip cannot be avoided. The Faradaic contribution can be useful if the reactants are generated by catalytic reactions at the sample surface, corresponding to one of the main principles of scanning electrochemical microscopy (SECM)[180]. An example from literature concerns the HER catalytic properties of active nanoparticles that were investigated under

reaction conditions while an EC-STM tip was positioned above the particles at constant distance. Faradaic contributions (HOR) to the tip current directly reflect the activity of the particle underneath.[37, 38] However, in this experiment the tip was not scanning but staying at fixed x,y position a few nanometers above the sample (Figure 42.A), so that lateral resolution was impossible. Even z-direction resolution is questionable, since the tip is collecting $H_2$ in the diffusion layer of the sample surface (Figure 42.B), which is far away from the actual place of reactions[37].

Even though tunneling noise and Faradaic noise features are undesired when perfect topographic imaging is needed, these features can nevertheless be informative for catalysis investigating purposes particularly under reaction conditions. This will be discussed in the next section.

### 3.2.2 Concept of Direct Identification of Catalytically Active Centers Using Electrochemical Scanning Tunneling Microscopy (EC-STM)

As mentioned above STM tunneling noise can indicate the "location of reactions" under specific conditions. Integrating this phenomenon with the concept of the effective tunneling barrier in electrolyte discussed in Chapter 2.3.2, EC-STM can be capable at revealing local electrocatalytic processes at the surface *in-situ*. First, adsorption/desorption of reaction intermediates changes the tunneling distance continuously. Second, the local work function (density of states) is being altered by changing of the surface adsorbates or the ''recovery'' of the bare surface. Additionally, the effective tunneling barrier is altered by reactants and products passing through (mass tranfer) the tunneling gap.[181]

Figure 43 sketches the basic idea of how reactions at the catalyst surface determine noise in the tunneling current. In case of constant current mode, any tip current variation will be converted to a corresponding change of the tip z-position. As shown in Figure 43.A and B, when no reaction (reaction 'off') takes place at the surface, the tip current stays relatively constant over time independent of the activity of the surface sites underneath. Under reaction conditions (reaction 'on'), the tunneling current is still undisturbed over a non-active site (Figure 43.C). However, a large fluctuating noise should be observed over an active site (Figure 43.D) due to the reactions.

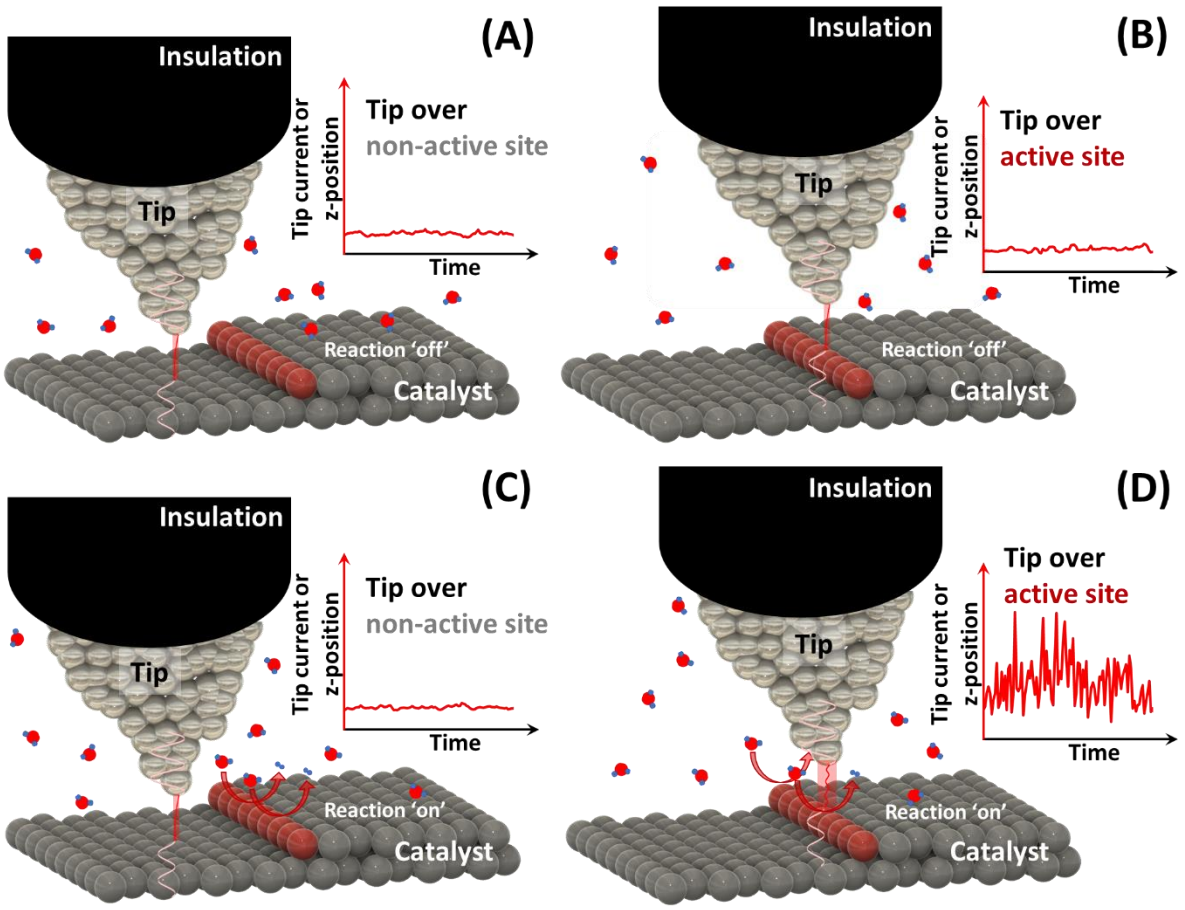


*Figure 43.* ***An illustration explaining the proposed concept to use EC-STM in order to "visualize" electrocatalytically active sites.*** *Active sites are marked as red atoms. (A) and (B) In case of no reaction taking place, the tip current is steady without noticeable noise, independent of the catalytic properties of the surface sites. (C) When the reaction is turned on, the current remains steady over non-active sites. (D) Large fluctuating signals recorded over time over an active site under reaction conditions. In constant current mode, the tip z-position is directly adjusted to counter-act current changes, thus resulting in a noise in the z-height.*

In reality, (EC-) STM systems suffer from thermal drift at room temperature[182, 183, 184]. Recording the current on top of a selected site over a long time is thus challenging. Therefore, letting the tip scan across the surface containing both non-active and active sites, *i.e.*, simply performing EC-STM imaging under reaction conditions, is an alternative option. In constant current mode, noise features should be seen as additional signals to the topographic profile while the reaction is proceeding, as shown in Figure 44. An EC-STM image under reaction condition will have non-uniformly distributed noise features. The locations of these features indicate where the active sites (centers) are.

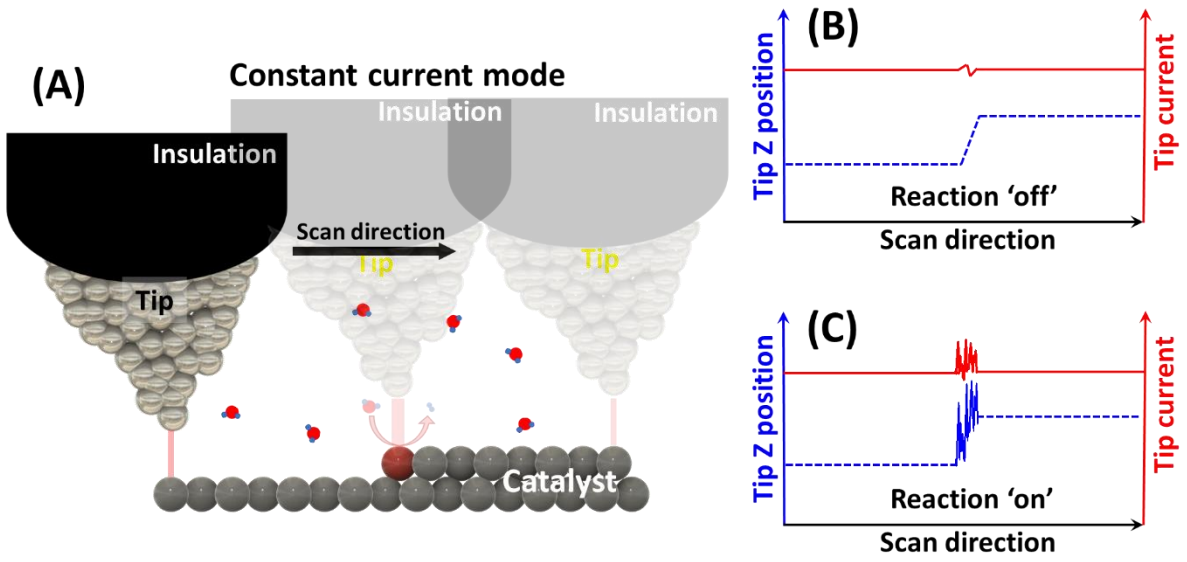


*Figure 44.* ***Combining the EC-STM noise measurements with constant current mode EC-STM imaging.*** *(A) Tip scans across the surface with both non-active and active sites in constant current mode. (B) and (C) Resulting current and the tip z-position under (B) no-reaction and (C) reaction conditions.*

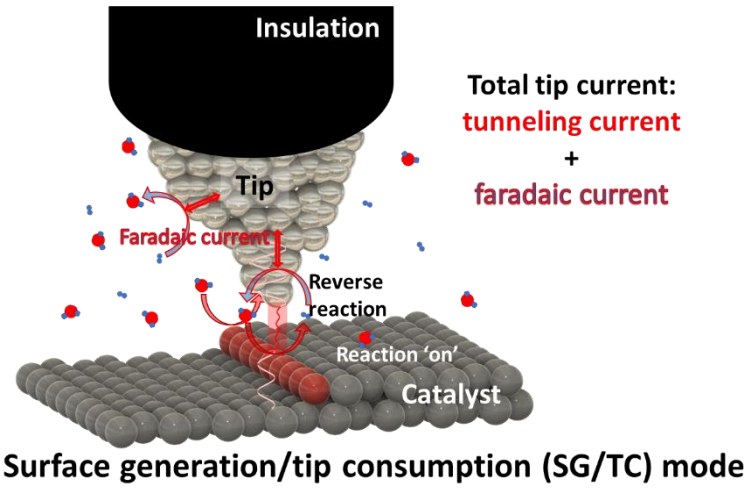


*Figure 45.* ***Additional Faradaic current at the exposed metallic part of the tip when the reverse reaction (to the process catalyzed at the surface) is possible at the tip potential.***

The products of some reactions taking place on the sample surface, for instance, $H_2$ in case of HER, can in principle be oxidized at the tip, if the tip potential is positive enough (Figure 45). This Faradaic contribution can therefore contribute to the tip current, which is not pronounced when the reaction does not take place. This is an extra noise coming from active sites that can in many cases simplifies their identification. However, the resolution under

these circumstances is supposed to be worse than that of tunneling noise, as the Faradaic reactions can take place at any spot of the exposed metallic part of the tip in the diffusion region of $H_2$.

The methodology of direct instrumental identification of active centers using EC-STM under reaction conditions (n-EC-STM) is the main theme of this thesis. Noise features in normal topographic images under reaction conditions are the key for identification of electrocatalytically active centers. The focus of this thesis is on the verification and applications of the proposed concept.

### 3.2.3 Experimental Details of n-EC-STM

The n-EC- STM measurements were carried out as the conventional EC-STM imaging, however, the potentials applied to the samples were shifted into the potential regions where reactions take place (reaction 'on'). To make sure that the noise features appearing over the active centers are not caused by undesirable instrumental artifacts, which are not related to the reactions at the sample surface, another image of the same location without reactions taking place (reaction 'off') was normally captured as a reference.

Prior to each EC-STM experiment, the quality of the tip insulation was assessed by reading out the current offset, which indicates the leakage current and exposed metallic surface at the tip. Only those tips with minimized current offset (typically 30 to 60 pA) can be employed.

Faradaic currents at the tip can be beneficial to the measurements of for instance, HER on Pt(111). Consequently, the oxidation of the hydrogen at the tip contributes a Faradaic current to the overall tip current and additionally increases the noise level over the active centers. The overpotentials should be carefully chosen, so that the HOR current at the tip is not comparable to the tunneling current: The tunneling current must still remain dominating and the tip must not retract from the sample surface completely. To additionally ensure this, particularly under HER 'on' conditions, the current setpoint was set to be higher than in regular EC-STM measurements to make sure the tunneling current is much higher than the HOR current at the tip. During the EC-STM measurements under the ORR 'on' conditions, an additional Faradaic current due to the ORR at the tip lowers the overall resolution of the resulting images. This

can be solved by applying more positive potentials at the tip. In the meantime, oxidation of the tip (Pt/Ir alloy) must be prevented at the applied tip potentials.

Some reactions, for instance the HER, have gaseous products. The possible bubble formation at the sample surface and the CE can affect the measurements at sufficient overpotentials. Therefore, the sample surface and the CE were frequently checked to avoid the formation of hydrogen bubbles during the measurements. Relatively low overpotentials were applied in the case of the HER to prevent excessive hydrogen production. Moreover, the typical size of hydrogen nanobubbles produced by electrochemical reactions is in the range of 45–1000 nm[185], which is much larger than the noise features in the EC-STM images.

To obtain a statistical evaluation of the level of the expected noise features in the resulting EC-STM images, a derivative frequency analysis was introduced. Along the fast scan direction (x-axis of the images), the derivative of the recorded tip height in constant current mode (or tip current in constant height mode) was calculated over the width (x-scan direction). A lager derivative value indicates a stronger disturbance in the tunneling current. The frequency of the resulting derivative values was counted separately for selected surface regions (for instance, defined terraces, step edges regions) with identical width and number of lines (*i.e.*, identical number of data points). Then the count from each region was plotted as a function of the derivative value. The regions, where the active centers were, resulted in wider histograms compared to the other regions (no active centers) of the surface under reaction conditions.

## 3.3 Sample Preparation

### 3.3.1 Single Crystal Preparation

Au(111) samples utilized in this thesis were Au chips (Au coated glass chips, arrandee™, square: 1.1 cm × 1.1 cm or 1.2 cm × 1.2 cm) and two Au(111) single-crystal samples (⌀ = 5 mm, MaTecK and ⌀ = 2.5 mm, Icryst). Two single crystalline Pt(111) and Pt(110) samples (both ⌀ = 5 mm, MaTecK) were also employed. The single-crystal samples were additionally cleaned by the CV method up to $O_2$ evolution potentials to remove possible residuals from previous experiments before the flame-annealing treatment. Subsequently, all samples were prepared

with the flame-annealing method using a gas burner filled with butane gas (Leifheit Proline) to restore the (111) surface and then thoroughly rinsed with ultrapure de-ionized water. Afterwards, the samples were characterized by STM and CV to confirm the predominance of (111) facets. This process was repeated several times until the desired clean single-crystalline surfaces were obtained.

A typical CV of freshly prepared Au(111) samples in 0.1 M $HClO_4$ is shown in Figure 46.A. Directly after the flame-annealing treatment, the (111) facet's oxidation peak is most pronounced (red curve). An STM image (Figure 46.B) recorded after flame-annealing shows the (111) terraces and the steps of the Au(111) surface. The height of a step edge is around 2.3 Å. These results are in agreement with the literature[107, 186]

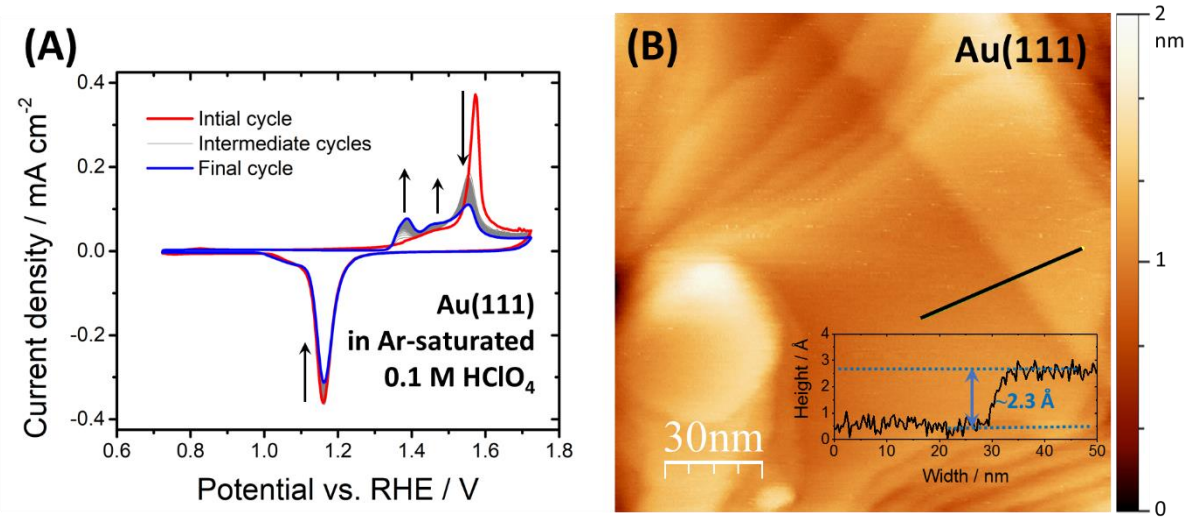


*Figure 46.* ***Typical CV and STM characterization of freshly prepared Au(111) samples.*** *(A) CV in Ar-saturated 0.1 M $HClO_4$ at a scan rate of 50 mV/s. Red: Initial cycle, blue: last cycle, gray: intermediate cycles. Arrows show changing direction of most pronounced peaks. (B) STM image of Au(111) after flame-annealing, 500 nm × 500 nm. Scan rate: 0.5 Hz, potential bias: 100 mV, current setpoint: 0.2 nA. The inset is the height profile across a one-atom step edge as indicated by the black line in the image.*

As can be seen in Figure 46.A, during continuous potential cycling, surface defects were created, causing the appearance of two more anodic peaks (see upward arrows) at more negative potentials, which indicates the generation of defects or steps on the (111) surface. This potential cycling procedure was used to clean the surfaces. However, the surface was restored by a flame-annealing treatment.

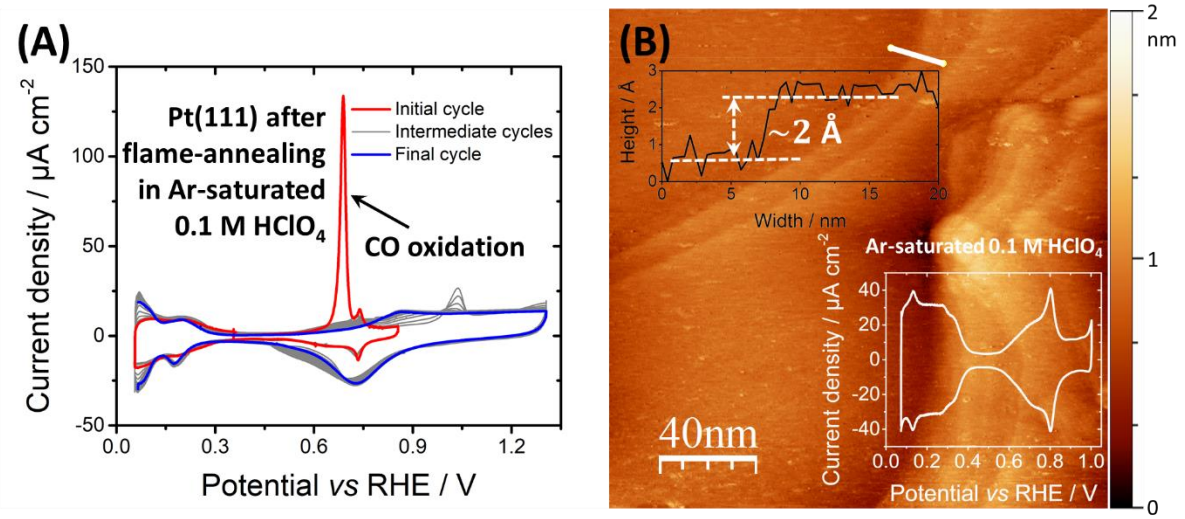


*Figure 47.* ***Preparation of single crystalline Pt(111).*** *(A) CV treatment of Pt(111) in Ar-saturated 0.1 M $HClO_4$ after initial flame-annealing in Ar/CO atmosphere. The large peak around the potential of 0.7 V vs RHE belongs to oxidation of CO adsorbed on the Pt surface. During the cleaning potential cycling, the surface gradually degraded to polycrystalline by reaching the final cycle. (B) STM image of a fully prepared single crystalline Pt(111) after cleaning and repeated flame annealing treatments. A sample was ready to use after flame-annealing when STM revealed approximately a 2 nm step-height layer structure and the obtained CV (inserted in the image) shows the typical butterfly shape.*

The preparation of single crystalline Pt(111) is described in Figure 47, which was repeated several times before each further investigation. Figure 47.B shows an STM image of a cleaned Pt(111) surface restored by flame-annealing. The (111) surface had (111) terraces and step edges or step-like defects. All these structures are desired in the following studies because their activities are expected to be different under the same conditions.

### 3.3.2 Pd Sub-monolayer Deposition on Au(111)

Pd island deposition was started with the UPD of Cu sub-monolayer islands on single crystal Au(111) electrodes from 0.5 M $H_2SO_4$ and 0.05 mM $CuSO_4$ (EMSURER, Merck) electrolytes. The Cu UPD procedure, including the CV of Au(111) in the deposition electrolyte and the deposition transient, is shown in Figure 48.A.

Afterwards, Pd islands were deposited by galvanic replacement of the Cu islands in a $Pd(NO_3)_2$ solution (palladium(II) nitrate hydrate, 99.95% metals basis, MaTecK). Note that the galvanic replacement precursor was chosen to be a $Pd^{2+}$ solution in order to replace each Cu atom with

one Pd atom, so that the deposited Pd islands were fully packed with a minimum amount of vacancies. Before performing further measurements, the samples were cycled in 0.5 M $H_2SO_4$ between 0.42 V and 1.02 V *vs* RHE at a scan rate of 20 mV/s to remove possible Cu residues. After the galvanic replacement, the surface contained Pd, which was confirmed by the CV (Figure 48.B) obtained in the EC-STM cell, in which the ORR and HER features of Pd sub-monolayer can be seen. There are noise features (oscillating features) in the CV and the reason is still unknown. Possible sources of the noise are the external electrical field and current oscillation caused by system electronics, therefore, a better Faraday shielding and a good grounding of the EC-STM instrument are needed. Additionally, the use of the quasi-reference electrode can influence the measurements. However, it is still clear enough to distinguish between the potential ranges of reaction 'on' and 'off' on the CVs recorded in the EC-STM cell.

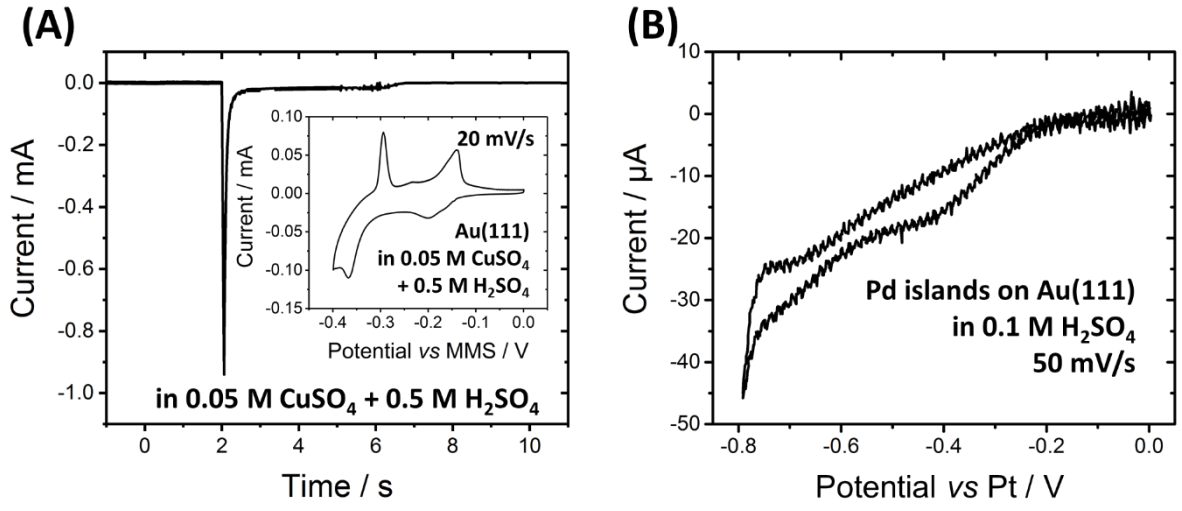


*Figure 48.* ***Pd sub-monolayer islands deposition on Au(111).*** *(A) Sample preparation in 0.05 M $CuSO_4$ + 0.5 M $H_2SO_4$. The deposition pulsed potential, −0.32 V vs MMS, was determined from the CV inset. The pulse time was 4s. (B) CV of the as-prepared sample in air-saturated 0.1 M $H_2SO_4$ measured in the EC-STM cell at a scan rate of 50 mV/s.*

### 3.3.3 Pt Deposition on Au Substrate

Pt nanoparticles were electrochemically deposited on Au(111) substrates in Ar-saturated 0.1 M $H_2SO_4$ + 4 mM $H_2PtCl_6$ (Chloroplatinic acid hydrate, ≥99.9% trace-metals basis, Sigma-Aldrich). For the Pt nanoparticle deposition, the single pulse deposition method was employed. Before the deposition, pulse potentials were determined with CV measurements on bare Au substrates in designated deposition electrolytes. The deposition transient is shown in Figure

49.A, and the inset displays a closer look at the deposition-pulse current. The CV of the sample (Figure 49.B) shows the HER and HOR peaks suggesting the presence of Pt nanoparticles.

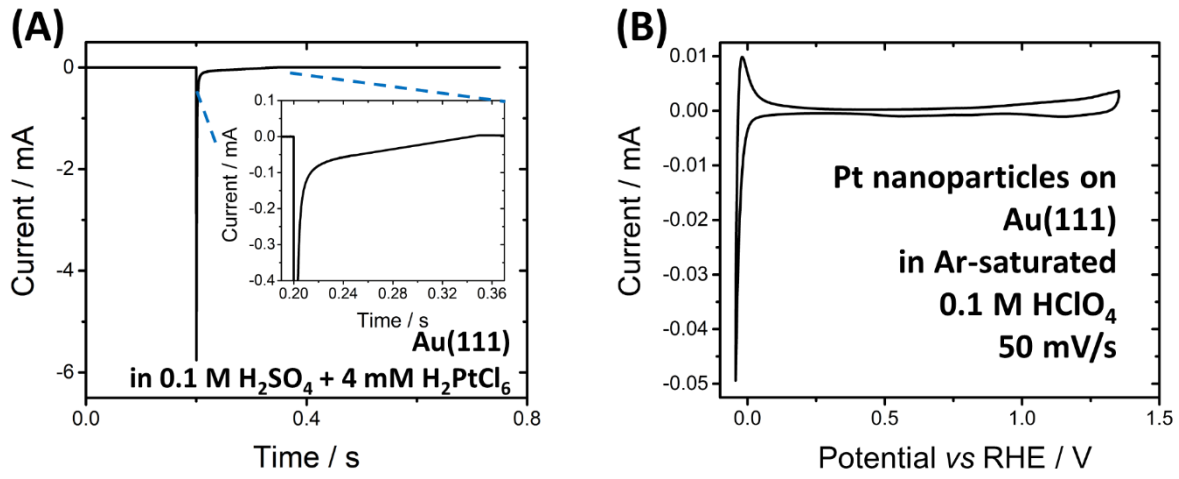


*Figure 49. **Deposition of Pt nanoparticles on Au(111).** (A) Current transient of Pt nanoparticle single-pulse deposition on Au(111) at 0.473 V vs RHE for 0.05 s in Ar-saturated 0.1 M $H_2SO_4$ + 4 mM $H_2PtCl_6$. (B) CV obtained in 0.1 M $HClO_4$ after the deposition.*

Pt multilayers on Au(111) were prepared in Ar-saturated 0.5 M NaCl + 3 mM $K_2PtCl_6$ (Potassium hexachloroplatinate(IV), ≥99.99% trace metals basis, Sigma-Aldrich) using the self-terminating growth method[133]. Note that only one half of the Au electrode was immersed into the deposition electrolyte, in order to have a bare Au surface on the other half of the electrode. Five deposition pulses were applied to fully cover the immersed Au surface with approximately 5 Pt layers and reduce the influence from the Au substrate on the activity properties of the Pt surface atoms, as shown in Figure 50.A and B. The CV of the prepared sample shown in Figure 50.C is similar to typical Pt CVs, thus enough Pt atoms must have fully covered one half of the Au(111). XPS results confirmed that as shown in Figure 50.D and E, where orange and blue indicate the data recorded over the Au and Pt sides, respectively. Most importantly, no Pt was found on the bare Au side from the XPS analysis according to the analysis of the peaks belonging to different elements. Comparing the peaks in Figure 50.D and E, the peaks belonging to Pt are not pronounced on the Au side. It should be noted that the shoulder around 72.0 eV (Au side) in Figure 50.E most likely originates from scattered Pt at the Pt/Au boundary. The EC-STM measurements for the bare Au surface should be perfomed far away from the boundary region.

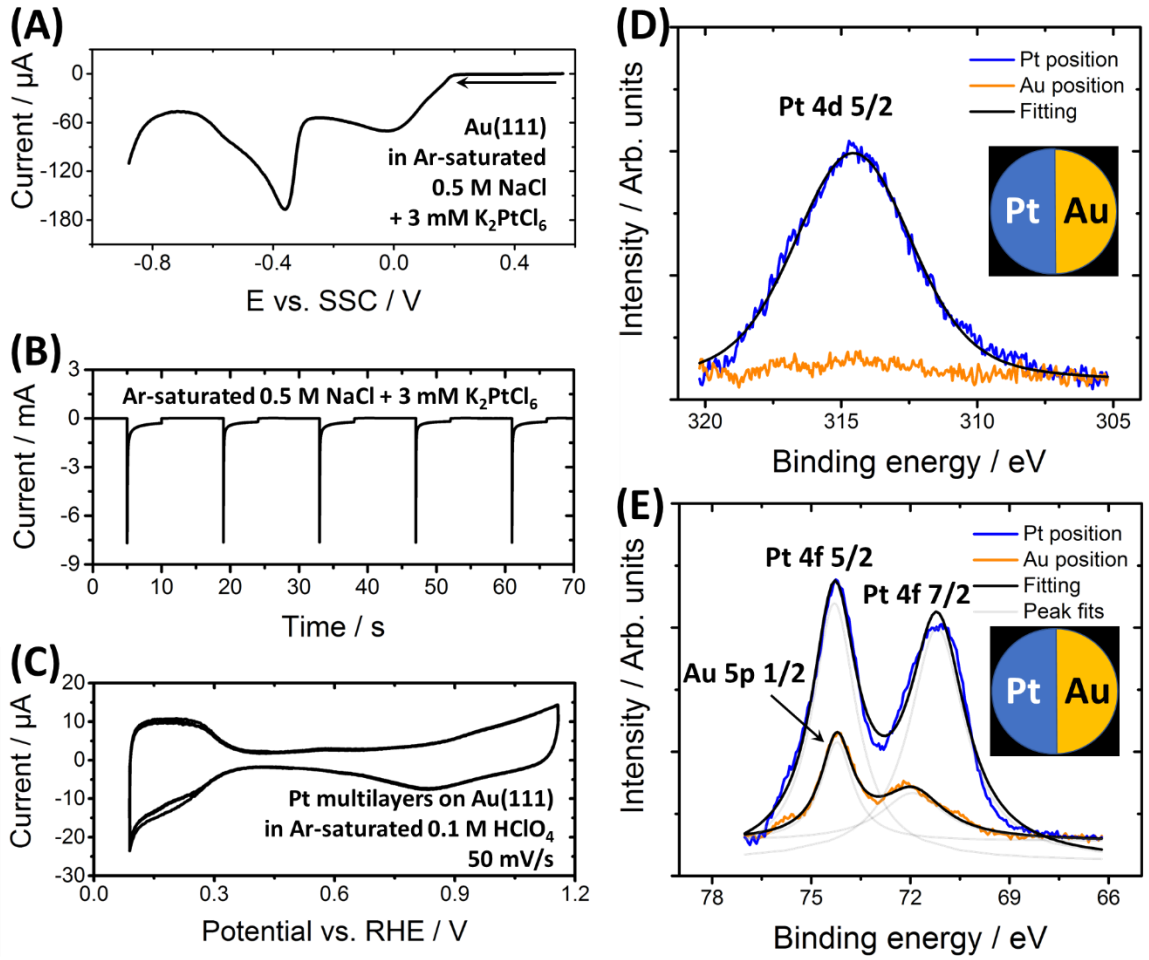


*Figure 50.* ***Pt multilayers on Au(111), sample preparation and characterizations.*** *(A) CV of the Au(111) in the deposition electrolyte to determine the deposition potential. (B) Deposition current transient. The same procedure was repeated 5 times only on one half of the whole Au(111) surface. (C) CV of the prepared sample in Ar-saturated 0.1 M $HClO_4$ measured in the electrochemical cell at a scan rate of 50 mV/s. (D) and (E) X-ray photoelectron spectroscopy (XPS) of the sample on the Pt-coated and bare Au part separately, where (D) shows the Pt 4d 5/2 (~314.5 eV) peak on Pt and Au and (E) presents Pt 4f 5/2 (~74.4 eV) and Pt 4f 7/2 (~71.0 eV) and Au 5p 1/2 (~74.0 eV) peak on both Pt and Au. Note that the Pt 4f 5/2 peak and the Au 5p 1/2 peak have similar binding energy.*

Another method used to deposit a thick Pt overlayer on one half of the Au substrate was CV performed on one half of the substrate in 0.1 M $H_2SO_4$ and 4 mM $H_2PtCl_6$ (Chloroplatinic acid hydrate, ≥99.9% trace metals basis, Sigma-Aldrich). The potential was cycled from -0.05 V to 0.93 V *vs* RHE at a scan rate of 20 mV/s for 10 cycles, as shown in Figure 51. After 10 cycles, half of the surface became silvery, showing that a thick layer of Pt (polycrystalline) had been deposited.

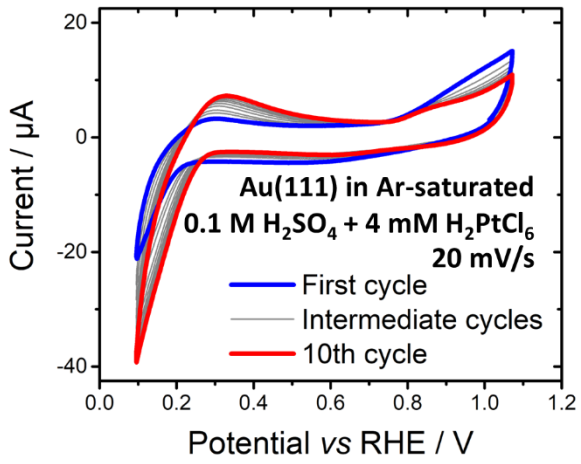


*Figure 51.* ***Deposition of Pt overlayers on Au by the CV method in Ar-saturated 0.1 M $H_2SO_4$ + 4 mM $H_2PtCl_6$ at a scan rate of 20 mV/s.*** *Half of the Au sample surface was immersed into the electrolyte. Pt was deposited and grew to a thick layer that totally covered the immersed Au surface.*

Pt sub-monolayer islands deposition on the Au(111) substrates was accomplished by the galvanic replacement of the UPD Cu sub-monolayer islands (UPD method, see chapter 3.3.2) in $H_2PtCl_6$ solutions. After the galvanic replacement, the CV was performed for each sample in order to remove possible Cu residuals and other contaminations from the deposition solutions. Figure 52 shows one cycle from the resulting CV after several cleaning cycles in 0.1 M $HClO_4$.

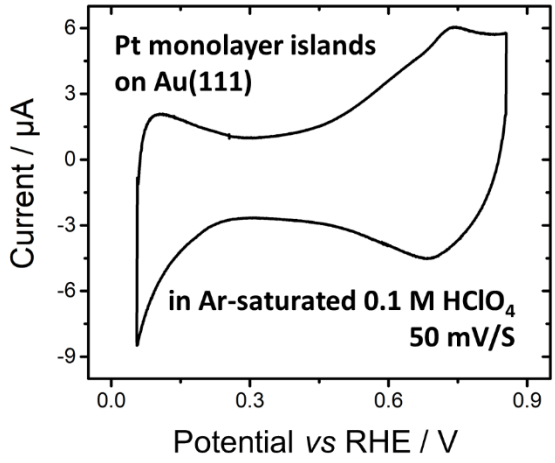


*Figure 52.* ***CV characterization of the deposited Pt sub-monolayer islands on Au(111) in 0.1 M $HClO_4$ at a scan rate of 50 mV/s.*** *The CV was recorded after several cleaning cycles and shows the typical features of polycrystalline Pt.*

### 3.3.4 Preparation of Transition Metal Dichalcogenide Multilayers on Au(111)/Glassy Carbon

TMD samples were provided by the scientific partners E. Mittereiter and M. Golibrzuch of Prof. Holleitner's group in the Walter Schottky Institute (WSI), Center for Nanotechnology and Nanomaterials (ZNN). TMD flakes were prepared with the micro-mechanical cleavage method[187] using an adhesive tape. Afterwards, the flakes were transferred to a poly (dimethyl-) siloxane (PDMS) stamp to measure the morphology and quality. Finally, the selected flakes were deposited on the substrates, namely Au(111) and GC electrodes, using viscoelastic stamping. All samples were cleaned with acetone and isopropanol prior to the (EC-) STM and the activity measurements. The helium ion microscope (HIM) was originally designated to measure the geometric properties of the TMD flakes, but in this work the HIM was used to introduce point-like defects in the samples, particularly at the surface. The defects can be generated as a result of scattering at electrons and nuclei by ion beam penetration into the sample. The Raman spectra shown in Figure 53 correspond to an inter-defect distance of about 2 nm. In order to create the same amount of point-like defects, the intensity of the helium ion beam used for the $MoS_2$ flakes supported on GC was ~4 times of that on Au(111). After rational ion beam treatments, the sample was expected to be more active towards the HER. The focus of n-EC-STM was on identifying active centers of non-HIM-treated and HIM-treated TMD flakes and assessing the benefit of HIM treatments.

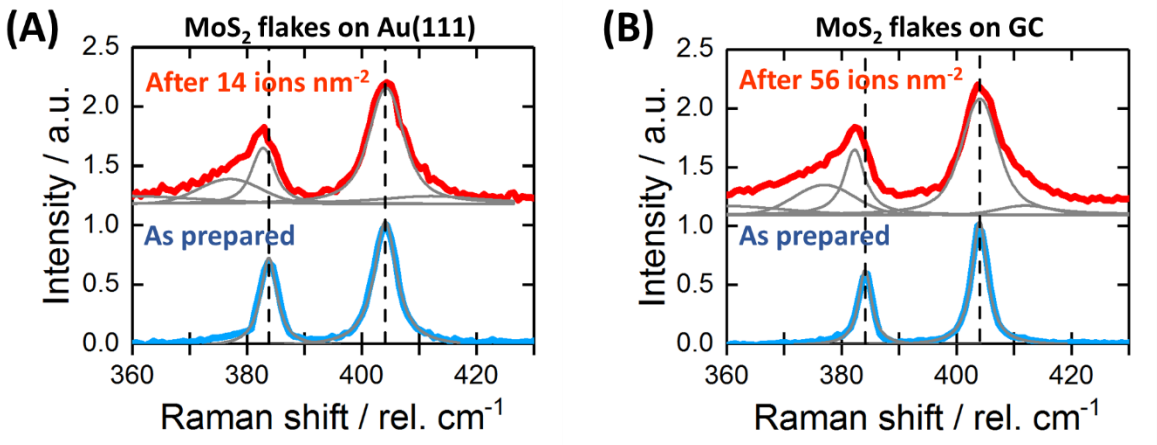


*Figure 53.* ***Raman spectra of a $MoS_2$ sample before and after the HIM treatment.*** *(A) Raman spectra of $MoS_2$ flakes supported on Au(111) before (light blue) and after (red) 14 ions $nm^{-2}$ helium ion treatment. (B) Raman spectra of $MoS_2$ flakes supported on GC before (light blue) and after (red) 56 ions $nm^{-2}$ helium ion treatment.*

# 4 Results and Discussion

## 4.1 N-EC-STM – Verification of the Proposed Concept

The capability of the proposed n-EC-STM methodology in identifying electrocatalytically active sites has been verified by using well-studied catalytic systems. The HER and the ORR were chosen as model reactions. The HER was studied on single crystalline Pt(111), Pd monoatomic islands and Pt multilayers on single crystalline Au(111) and the ORR was investigated on Pt multilayers on single crystalline Au(111) and single crystalline Pt(111). The locations of the active sites identified by the n-EC-STM directly validate hypotheses from literature that had before only been based on indirect evidence and theoretical considerations.

### 4.1.1 HER on Pt(111) in Perchloric Acid ($HClO_4$)

Figure 54 shows a typical CV of the single crystalline Pt(111) in 0.1 M $HClO_4$ recorded in the EC-STM cell. It should be noted that the CV of the prepared Pt(111) is slightly tilted due to the dissolved $O_2$ in the electrolyte from air, which can be reduced on Pt at sufficiently negative potentials. The potential range where the HER or the ORR are able to take place can be seen in the CV.

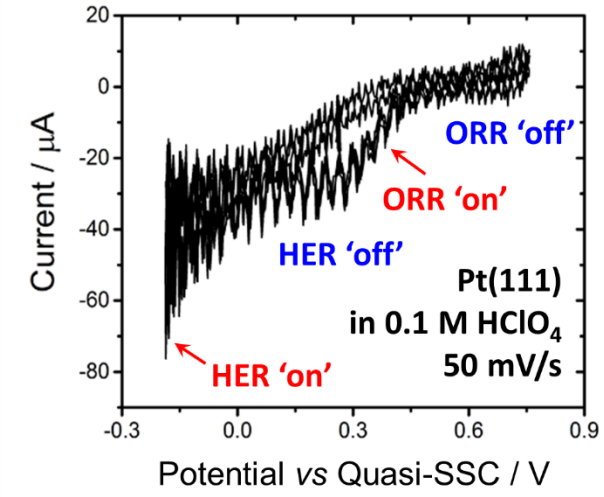


*Figure 54.* ***Typical CV of Pt(111) in 0.1 M $HClO_4$ recorded in the EC-STM cell at a scan rate of 50 mV/s.*** *The red arrows indicate the potential range where the HER or the ORR can take place.*

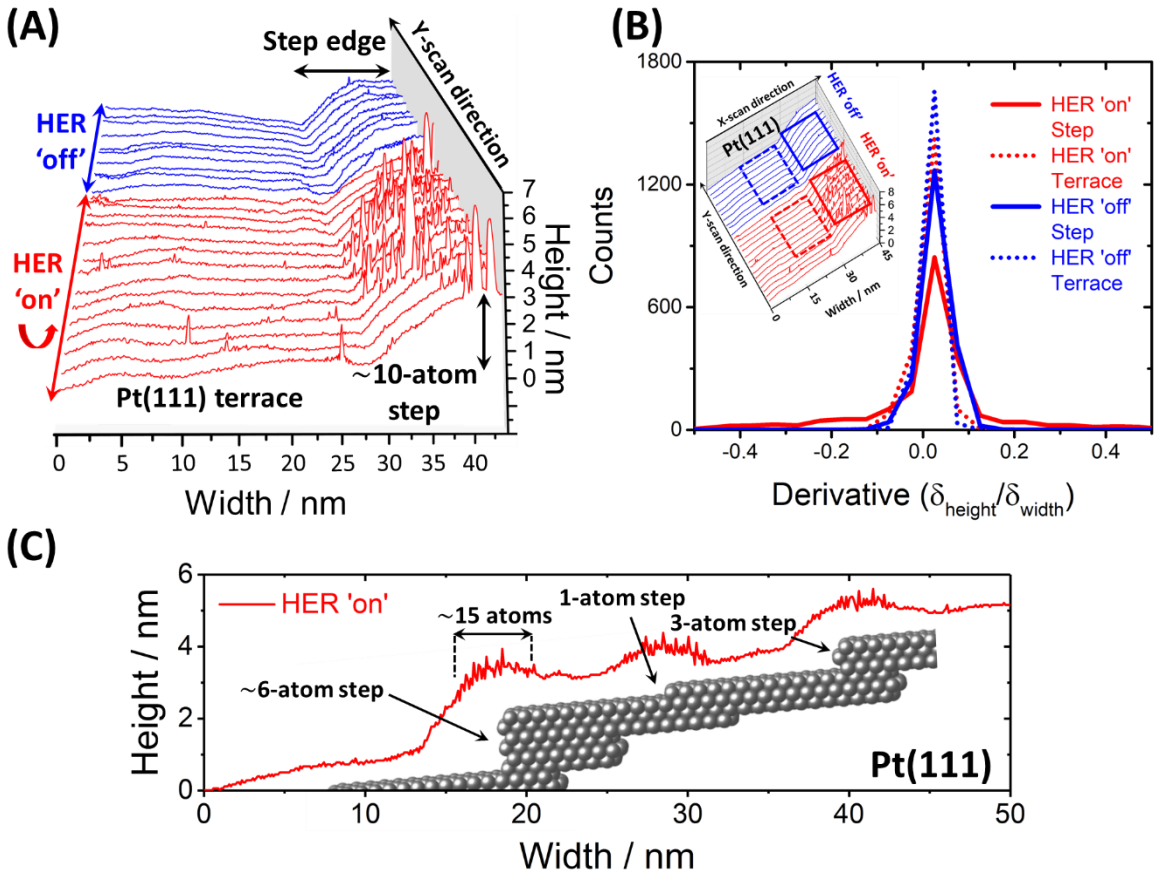


*Figure 55.* ***The n-EC-STM measurements of the Pt(111) surface in 0.1 M $HClO_4$.*** *(A) 3D view of line scans over a step-like structure while the potential was shifted from HER 'on' to HER 'off' (-350 mV to -200 mV vs quasi-SSC). The tip potential was changed from 150 mV to 0 mV vs quasi-SSC to maintain the potential bias. (B) Statistics (derivatives of height over width) of the noise level from four regions of (A). (C) A line scan resulted from the EC-STM measurement performed on a Pt(111) surface with several steps of different heights. Sample and tip potentials were -300 mV and 0 mV vs quasi-SSC. The 3D ball model is a guide to the eyes. It visualizes a stepped Pt crystal as a possible structure corresponding roughly to the line scan.*

Figure 55.A shows the EC-STM line scans measured over the Pt(111) surface in constant current mode. Under the HER 'on' condition, the noise features systematically appeared on the step-like structure and significantly less noise was observed on the terrace (red line scans in Figure 55.A). Afterwards, the HER was turned 'off' and the noise features disappeared; in the meantime the surface topography was recorded (blue line scans in Figure 55.A). The structure of the step-like defect was not well-resolved likely due to the tip broadening effect. However, this defect was about 10-atoms high and it probably was composed of a number of smaller steps. The HER 'on' scans exhibited significantly pronounced noise features (peaks) on the step-like defect compared to the HER 'off' ones.

Figure 55.B introduces a statistic analysis of the line scans noise level in Figure 55.A. Derivatives of height over width were calculated along all selected square regions in the 3D inset (representation of Figure 55.A) in Figure 55.B. These four regions were selected from four areas, namely step-like defect (step) under HER 'on', step-like defect (step) under HER 'off', (111) terrace under HER 'on' and (111) terrace under HER 'off' areas. All selected regions have the same number of lines and data points. The frequency of the derivative values was independently counted for each region and the number of counts is plotted as a function of the derivative value. Only in the case of HER 'on', there is a broadened frequency curve (lower peak maximum and more counts at extreme derivative values) at the step, which indicates that at the step the line scan is ''noisy'' under the HER 'on' condition, *i.e.*, the step is electrocatalytically more active towards the HER than the (111) terrace.

To confirm the reproducibility of this finding, the same measurement was repeated many times over different Pt(111) surfaces. Figure 55.C exhibits an exemplary line scan over different step-like defects under the HER 'on' condition. The same phenomenon was observed that the noise features appeared only on the step-like defects. Interestingly, the noise features on every step are approximately 15-atoms wide, which is presumably related to the width of the active center around the step edge, or in other words, the amount of the atoms at which the activity is promoted by the different electronic structure around the step edge. Additionally, a tip broadening effect related to the geometry of the tip should be taken into account when analyzing the width of the noise features.

These noise features suggest that there were processes between the tip and the sample surface changing the effective tunneling barrier continuously. Under HER 'on' conditions, all surface reaction steps, *e.g.*, diffusion of reactants and products, adsorption/desorption of reaction intermediates and changes of the local density of states, are likely among these processes. As mentioned in Chapter 2.3.2, even steady dipolar substances (*e.g.*, water dipoles) introduce oscillations to the tunneling current[153, 156]. Under reaction conditions, those substances are much more dynamic, particularly near the active centers. Therefore, noticeable noise features are expected to appear at the active centers of the catalyst surface. The heights of some peaks are in the order of nanometers, which is beyond the tunneling distance, indicating the contribution of inevitable faradaic currents at the tip. However, the tip stayed close to the sample surface (not retracted completely) during the EC-STM

measurements even under reaction conditions. Note that the contribution of Faradaic current plays a minor role in the noise features and the dominant contribution comes from the tunneling current noise.

The results of HER on Pt(111) in aqueous 0.1 M $HClO_4$ electrolyte are the first evidence of successfully using the n-EC-STM method. Even though a sub-nanometer resolution was not reached, the results are in agreement with literature suggesting that the active centers of Pt(111) towards the HER are located at the bottoms of steps (so-called step-concavities). This is a well-known fact confirmed by indirect experiments and theoretical studies.[39, 112]

### 4.1.2 HER on Pt Multilayers/Au(111) in Perchloric Acid ($HClO_4$)

The fluctuation in the level of tunneling current noise originated from the difference in the catalytic activity (not the structure) of the surface sites, as noticeable noise features only appeared on the active centers when there were catalytic reactions taking place. To exclude surface structure factors and other instrumental or experimental artifacts, specially prepared Pt multilayers/Au(111) samples, where the Pt multilayers (approximately five layers deposited by the self-terminating growth method[133], see Chapter 3.3.3) covered one half of the Au(111) substrate, were used. The Pt side was much more active towards the HER compared to the Au side under the same conditions.

A series of measurements following the n-EC-STM methodology were performed on both the Pt and Au sides with the same experimental parameters. For all the EC-STM measurements, the tip potential was kept at 200 mV *vs* quasi-SSC. At first, the sample potential was 0 V *vs* quasi-SSC (HER 'off') to avoid HER at the surface. Then the sample potential was changed to -350 mV *vs* quasi-SSC (HER 'on') which can trigger HER on Pt but not on Au. The potential was shifted between HER 'on' and HER 'off' during all scans. Two series of EC-STM images were recorded on approximately equally large surface areas on the Pt and the Au sides, respectively.

On the Pt side (Figure 56.A-F), the noise features covered the whole scanned area under HER 'on' condition and disappeared immediately when the HER was switched 'off' on each image, no matter when or where the potential was changed. However, only the 'clear' Au surface can be seen in each image shown in Figure 56.G-J. No noise feature can be seen even though the

applied potentials were the same as on the Pt side. The results were obtained as expected, since the Au is much less active towards the HER than the Pt.

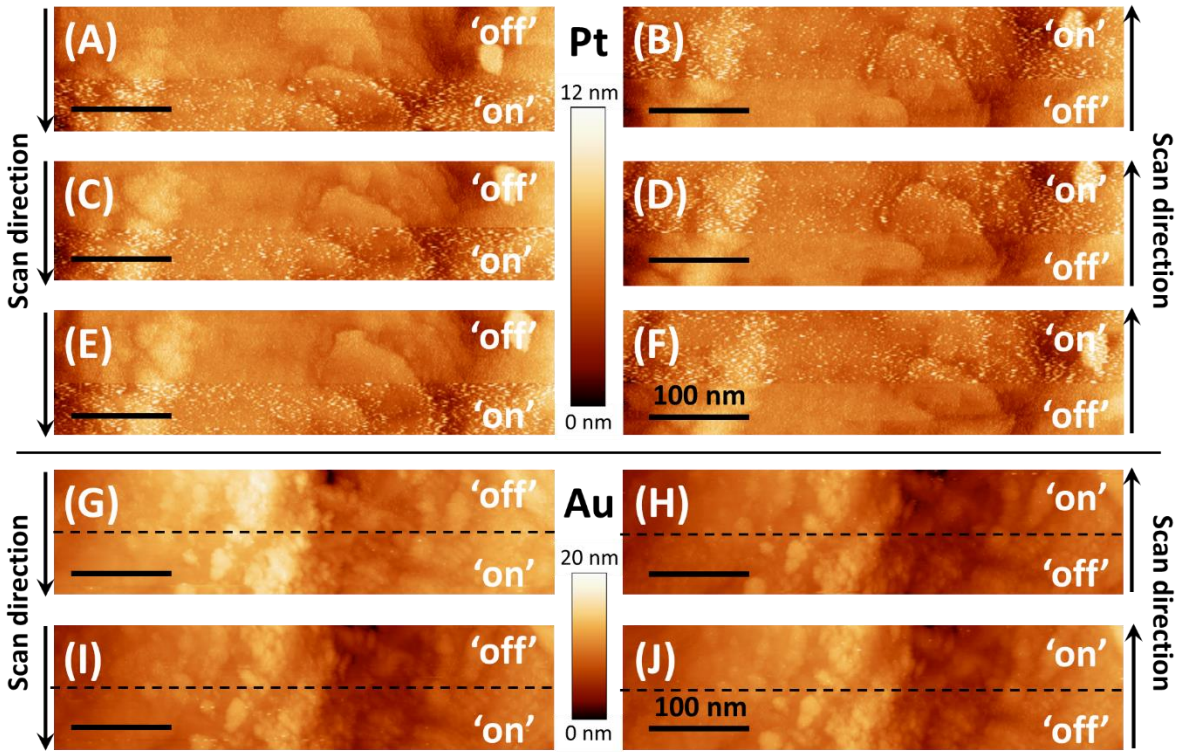


*Figure 56.* ***Constant current mode EC-STM images on Pt multilayers coated Au(111) in 0.1 M $HClO_4$.*** *Two series of EC-STM images (scale bars inserted) of approximately the same surface areas belong to the Pt-coated and bare Au(111) sides, respectively. The sample potential was shifted between that of the HER 'on' (-350 mV vs quasi-SSC) and the HER 'off' (0 mV vs quasi-SSC) as labeled in the images. (A-F) Images obtained on the Pt side. (G-J) Images taken on the Au side. Black dashed lines mark the location where the potential was changed.*

Figure 57 presents 3D views of the EC-STM images in Figure 56, where the difference in the noise level can be recognized easily. On the Pt side, noise ''spikes'' can be seen all over the surface under HER 'on'. The boundary between HER 'off' and 'on' regions can be recognized in each image. However, on the Au side, such a boundary is not visible because both sample potentials (-350 mV and 0 mV *vs* quasi-SSC) resulted in almost no noise features, even on large defects.

This study can be considered as an assessment of the n-EC-STM methodology. There was no noticeable difference in the surface morphologies of the Pt and Au sides. Moreover, the measurement procedure was the same on both surface sides. All results confirmed the methodological approach that the appearance of the noise features is directly correlated to

the local activity (or reactivity) of the sample surface, not structural, instrumental or experimental factors or artifacts.

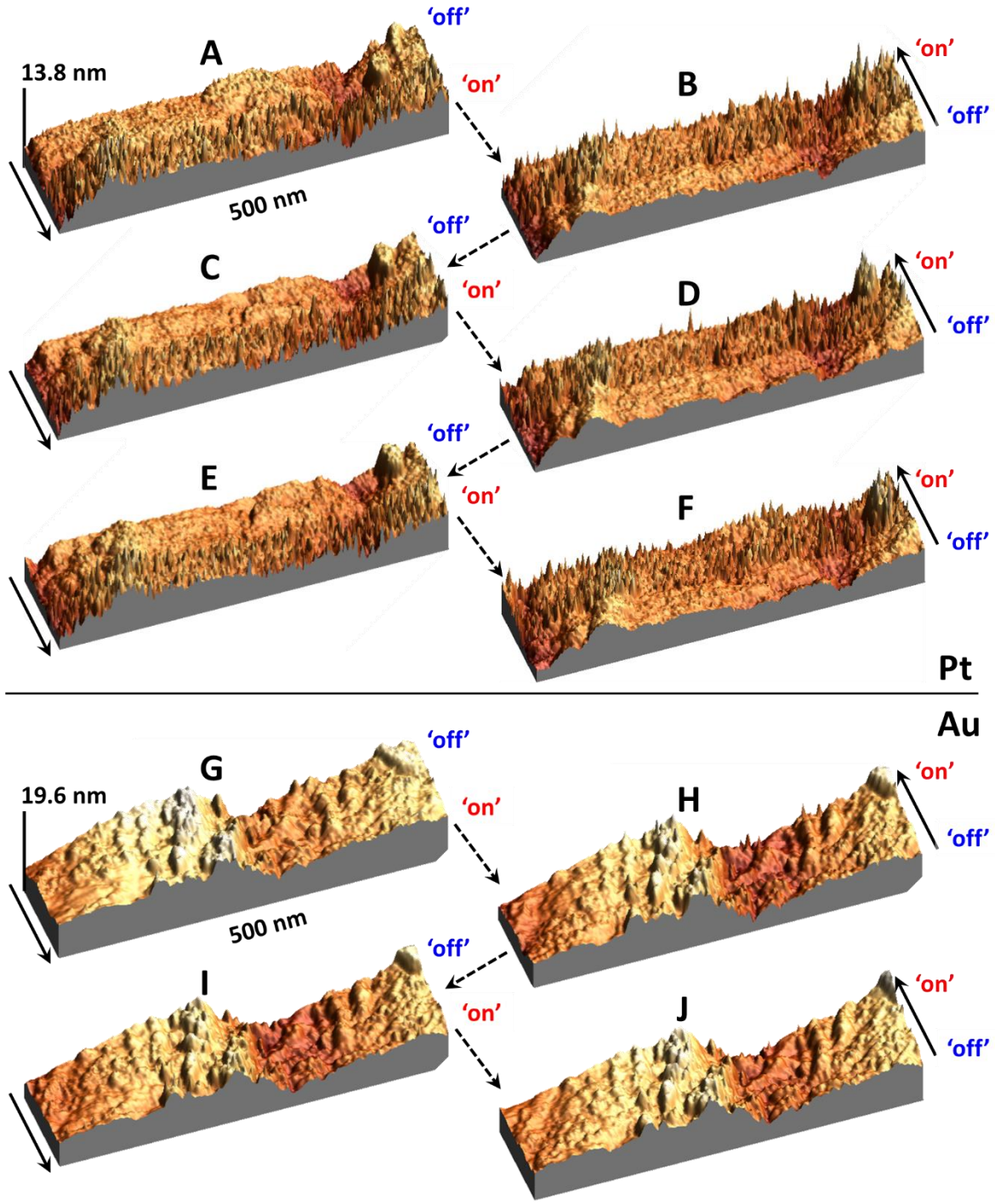


*Figure 57.* ***3D views of the images shown in Figure 56****. Dashed black arrows indicate the sequence of the recorded EC-STM images. Scan directions are indicated by solid black arrows. The sample potential was switched halfway through all the images between that of the HER 'on' (for Pt) and the HER 'off'.*

### 4.1.3 HER on Palladium (Pd) Islands Covered Au(111) in Sulfuric Acid ($H_2SO_4$)

As shown above, the n-EC-STM is able to identify active centers towards the HER. However, atomic resolution, which would be of great benefit in fundamental research of electrocatalysis, was not achieved so far. In the previous examples, a sub-nanometer resolution was not necessary to distinguish the active centers from the rest of the surface, for instance, in distinguishing the step-like defects from the terraces at Pt(111) surface, particularly as in this case the findings were already predicted by literature[39, 112]. However, in the next examples, n-EC-STM was studied for catalytic systems where the active centers have dimensions in the sub-nanometer scale. For this, as model system HER on Pd sub-monolayer islands covered Au(111) in 0.1 M $H_2SO_4$ was selected. It is known that Au is much less active than Pd towards the HER. Figure 58.A is an STM image recorded in air of the deposited Pd islands on a typical triangle-pattern Au(111) surface. The height profiles of the selected line scans show the monoatomic height of the Pd islands.

Under the conditions where HER is possible on Pd (-750 mV *vs* Pt), an EC-STM image (Figure 58.B) of a boundary between a Pd island and the Au substrate was obtained in constant current mode in 0.1 M $H_2SO_4$. In the image, the (111) orientation on the Au (with FFT filtering) and bright edges around the Pd island can be seen. As can be seen in the inserted height profile of the selected line scan in Figure 58.B, the highest noise features appeared at the Pd/Au boundaries.

To have a closer view on the noise features at the Pd island edge, one section of the sample at the boundary indicated by the dashed blue box was selected, and the line scans inside this area are shown as a 3D plot in Figure 58.C (also a 2D plot in Figure 58.D). The 3D plot can be divided into three parts with identical width, the Au substrate, the Pd/Au boundary and the Pd island surface. The Pd/Au boundary continuously shows the largest noise features in every line scan. There is less noise on the Pd island surface, but it is still more ‘‘noisy’’ than the Au substrate. The derivative frequency analysis in Figure 58.E provides the same conclusion.

In this case, the Pd/Au boundary sites are the most active ones towards the HER compared to those in the center of the island. Interestingly, the width (along the x-axis) of these large noise features is about 1 nm as can be seen in Figure 58.C. Considering the tip broadening effect of (EC-) STM measurements, the highest active center located on the Pd/Au boundary contains

approximately 3 or even less Pd atoms. An explanation is that the electronic properties of the Pd atoms are influenced by their coordination (for instance, island edge atoms *vs* atoms in the center of the island) coupled with the influence from the Au substrate (strain and ligand effects), and only the Pd atoms on the edge of the island turn out to be the most active centers towards the HER.

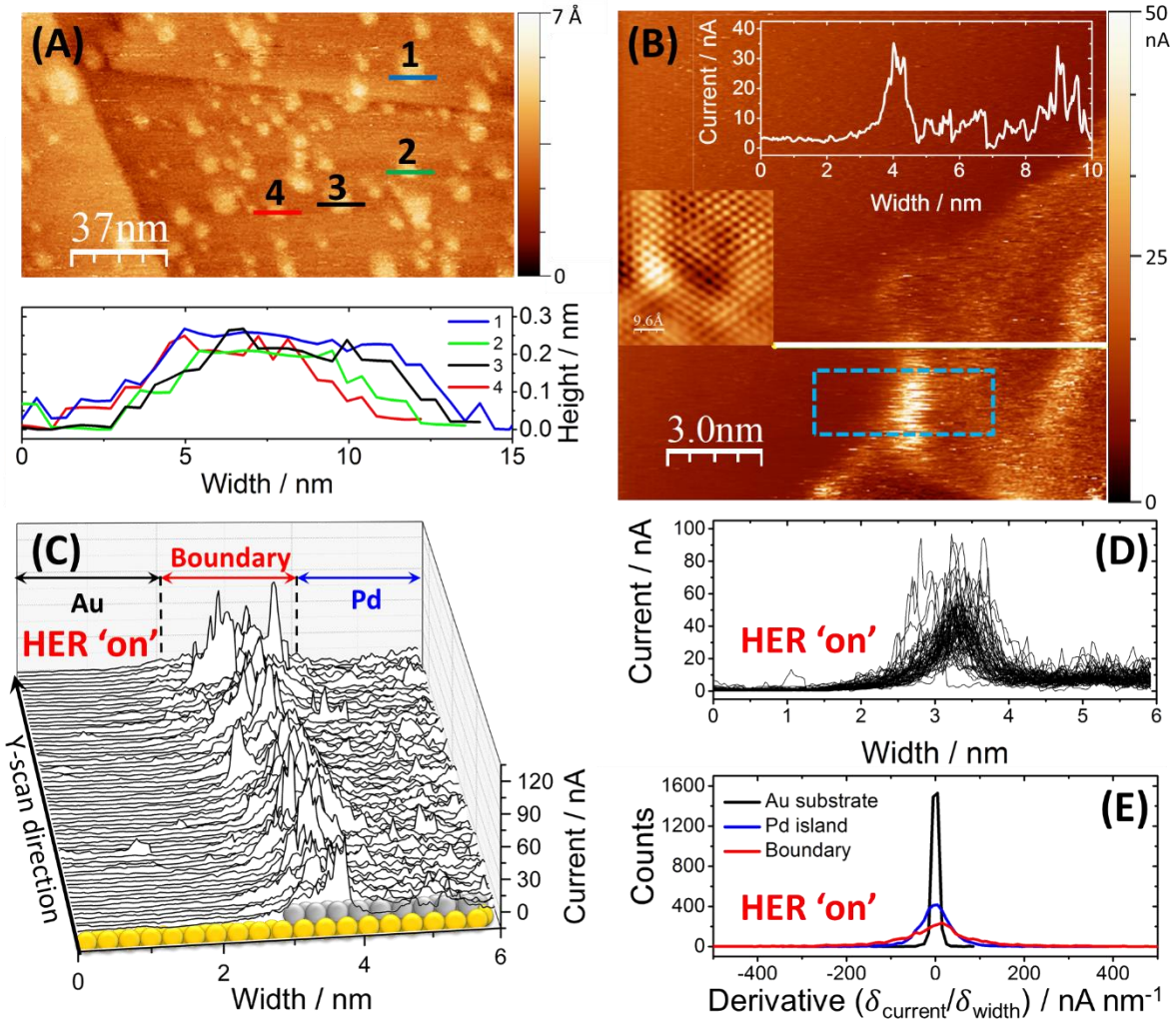


*Figure 58.* ***Active center identification of a Pd sub-monolayer island on Au(111).*** *(A) Constant current mode STM image of the sample obtained with a current setpoint of 0.5 nA. The heights of randomly selected islands are all around 0.2 nm, which is the typical height of a Pd monolayer. (B) EC-STM of a Pd island measured in constant height mode in 0.1 M $H_2SO_4$ at a scan rate of 10 Hz and a current setpoint of 4 nA under HER 'on' condition, and the feedback is minimized. The potentials of the sample and tip were -750 mV and -100 mV vs Pt, respectively. The profile measured along the white line is shown in the inset. (C) Line scans in the blue dashed box in (B). The ball model underneath the plots is a guide to the eyes. (D) 2D projection of all line scans of (C). (E) Frequency analysis of the derivatives of line scans on Au, Pd and the boundary with equal size and data point numbers. The distribution from the boundary region is most broadened.*

The (EC-) STM instrument captures the conductivity map of the sample surface, so that the atomic resolution is not always available. It is difficult to clarify exactly how many Pd atoms contribute most to the HER activity. However, a sub-nanometer resolution was achieved, and the active centers of nanostructured catalytic systems can be successfully distinguished.

Additionally, the results suggest a strategy to optimize the HER activity of this catalytic system. For Pd monoatomic islands supported on a Au(111) electrode, rather than simply covering the Au substrate with more and more Pd deposits, increasing the total length of the Pd islands edge can sufficiently increase the overall HER activity of the electrode. Indirect experimental evidence[40, 41, 42] and theoretical calculations[43] support this conclusion.

### 4.1.4 ORR on Pt Overlayers/Au in Perchloric Acid ($HClO_4$)

Hydrogen evolution on a Pt (or Pd) surface in acidic media is one of the fastest catalytic reactions with a relatively simple reaction mechanism. However, there are many significantly slower reactions important for energy provision, for example ORR, which have more complicated reaction mechanisms. Additionally, the solubility of $O_2$ (as the reactant of the ORR) in aqueous electrolytes was reported to be only few mM at room temperature[172]. To test the applicability of the n-EC-STM for the identification of the catalytically active centers for ORR, a Pt overlayers/Au sample prepared by CV method (see Chapter 3.3.3), namely thick Pt overlayers coated on one half of a less active Au substrate, was used in air-saturated 0.1 M $HClO_4$.

To compare the tunneling noise level of the Pt (active) and the Au (less active) sides under ORR 'on' condition, the tunneling current was recorded in constant current mode while the tip was approached and kept at a constant x and y position on both sides, separately. During recording, the tip was possibly slightly shifting in the lateral direction due to unavoidable drift. Therefore, the recording time was relatively long to have an average noise level of the current over time and to minimize the influence of the surface structure.

Figure 59 shows the distribution of the current data on the Pt and the Au sides recorded within 1200 s which are divided into three equal parts (each part is 400 s). The current distribution was approximately the same in all three periods for each side, and is directly correlated with the noise level of the tunneling current. In fact, the noise level on Pt was drastically larger than

that on Au. This result is not surprising, considering that Pt has much higher activity towards the ORR compared to Au.

Even though the ORR is much more ‘‘sluggish’’ compared to HER and the $O_2$ concentration very low, the tunneling noise obtained under ORR ‘on’ conditions does still reveal the local activity of the sample surface, particularly in the absence of noticeable Faradaic reactions (*e.g.*, HOR) at the tip. It should be noted that the oxygen close to the sample surface was not depleted during measurements and the ORR at the sample surface was stable. At the same time, the noise level of the tunneling current (directly correlated with the oxygen reduction reaction rate) stayed roughly the same over a rather long time.

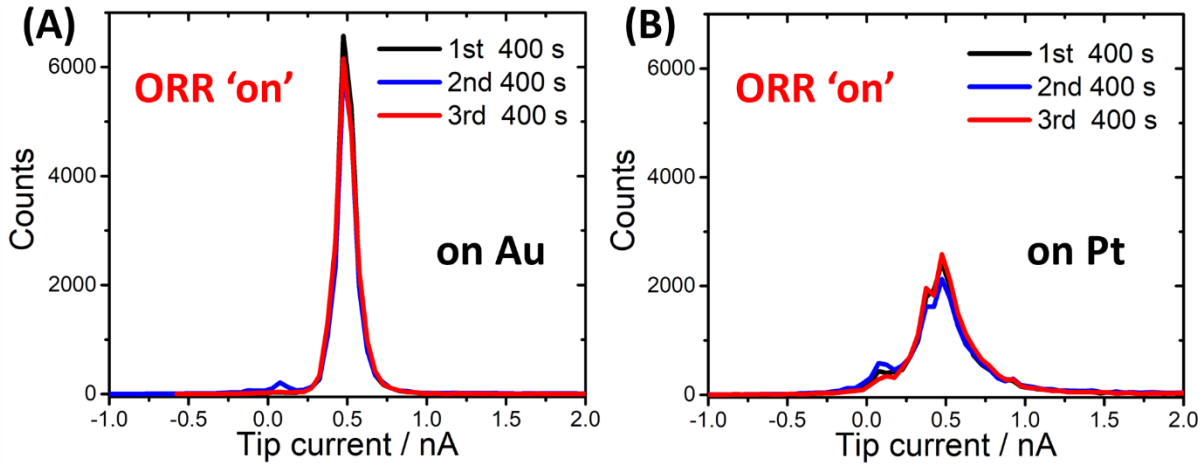


*Figure 59.* ***Frequency analysis of tip current recorded over time without scanning the tip over (A) the bare Au(111) and the (B) Pt multilayer parts of the sample in 0.1 M $HClO_4$.*** *Current setpoint: 0.5 nA, sample potential: 100 mV vs quasi-SSC (ORR ‘on’), tip potential: 200 mV vs quasi-SSC.*

### 4.1.5 ORR on Pt(111) in Perchloric Acid ($HClO_4$)

The n-EC-STM methodology was utilized for investigating the ORR in 0.1 M $HClO_4$ on a Pt(111) single crystal sample where both (111) terrace and step-like structures were present. The applied potentials for ORR ‘on’ and ‘off’ conditions on Pt(111) were chosen according to the CV obtained in the EC-STM cell, as shown in Figure 60. To prevent the Pt surface degradation, particularly surface oxidation, EC-STM images in the case of ORR ‘off’ were captured at the potentials around 0 mV *vs* the quasi Pt reference electrode. Apparently, the Faradaic contributions at the tip should play a minor role in the tip current signal, because there were no reaction products from the sample surface like $H_2$ that can react at the tip in the case HER.

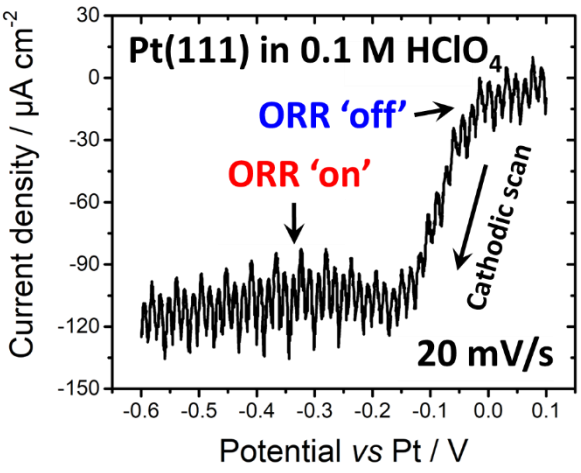


*Figure 60.* ***Cathodic scan of a CV for a single crystalline Pt(111) in 0.1 $HClO_4$ in the EC-STM cell.*** *Scan rate: 20 mV/s.*

To make sure that the presence of the noise features is caused by the ORR rather than artefacts, the n-EC-STM was firstly performed on a (111) terrace. Figure 61. A-C show the 3D plots of line scans taken from three successively recorded EC-STM images at approximately the same position, while the sample potential was switched halfway through each image between one where ORR can occur ('on') and one where ORR cannot take place ('off'). 2D plot of these line scans are shown in Figure 61.D-F, respectively.

When the sample potential was set to stop the ORR, the Pt(111) terrace displayed no noticeable noise features. In contrast, in each image, when the sample potential was shifted to have ORR taking place, the noise level increased significantly. The heights of the noise features (constant current mode) are around 1 to 2 nm which is smaller than those in HER 'on' images. This can be explained by the absence of Faradaic currents (*e.g.*, HOR) at the tip under ORR 'on' conditions, and the slow kinetics of the ORR. Moreover, the most active sites are suggested to be the step concavities[29, 50] not the surface sites on the (111) terrace.

Afterwards, the ORR activities of the (111) terraces and the step-like defects on Pt(111) were compared. An EC-STM image (Figure 62.A) containing both structures was obtained under ORR 'on' condition. The line scans in the selected area in Figure 62.A are plotted as a 3D view (Figure 62.B) and in a 2D plot (Figure 62.C) showing clear contrasts of the noise level. Figure 62.D presents the derivative analysis of the current signal in the marked areas in Figure 62.B and C.

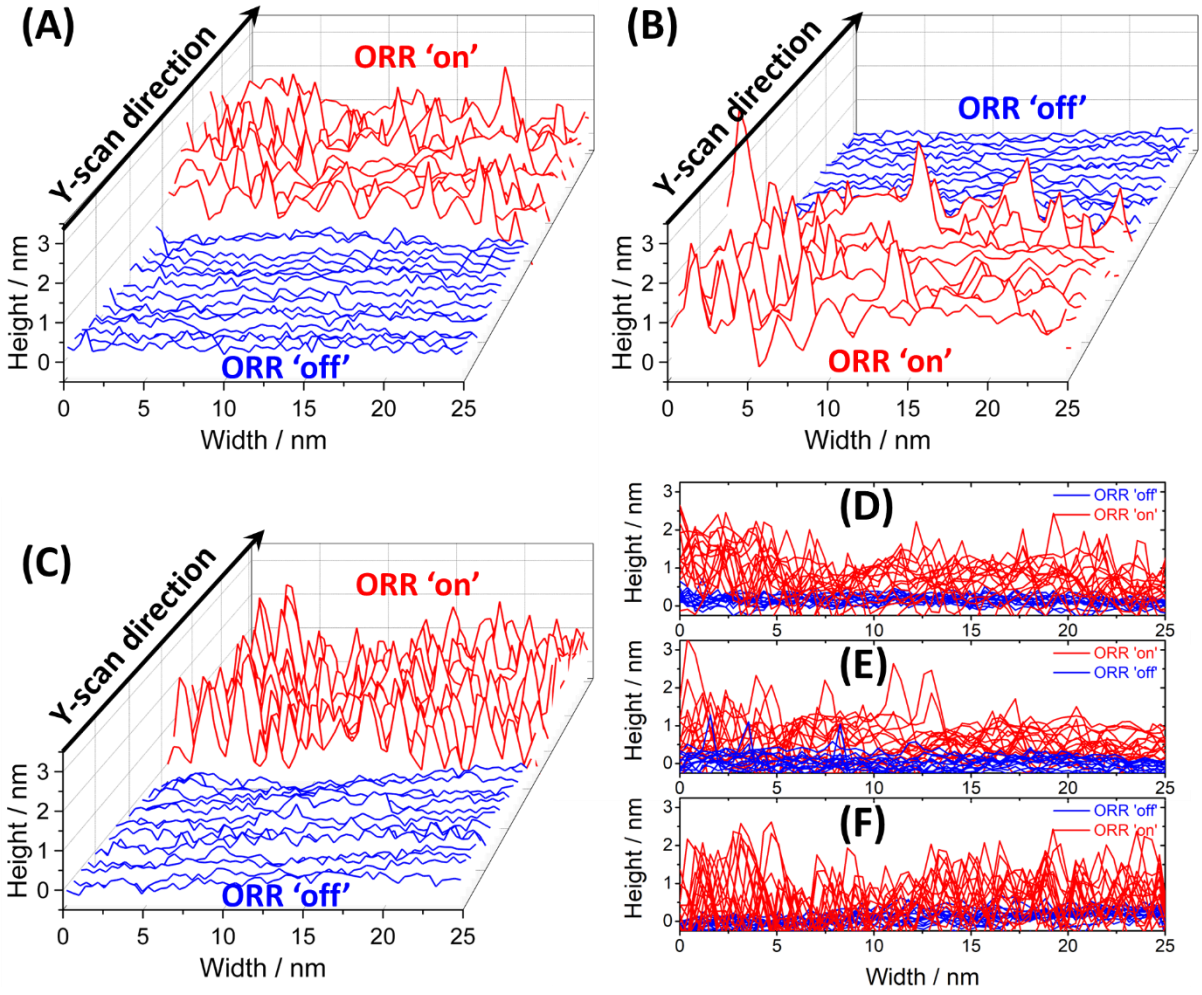


*Figure 61.* ***EC-STM (constant current mode) measurements of the ORR on a Pt(111) terrace in air-saturated 0.1 M $HClO_4$.*** *(A-C) Line scans on a Pt(111) terrace taken from 3 successively captured EC-STM images, with potentials of -300 mV vs Pt (ORR 'on') and 0 mV vs Pt (ORR 'off'). Tip potential: −150 mV (the sign of the value of the potential bias changed between ORR 'on' and 'off'), current setpoint: 0.2 nA. (D-F) 2D plots of (A-C).*

In this case, noise features can be seen all over the Pt surface, because oxygen can be reduced on both the terrace and the step at the applied potential. However, the step had relatively larger noise features indicating that the active centers should be located in its vicinity. This result confirms the findings[29, 46, 47, 48, 49] that the step concavities are the active centers at a Pt(111) surface towards the ORR in acidic media.

Even though the ORR is a relatively slow reaction compared to the HER, n-EC-STM is still able to distinguish ORR active centers at electrode surfaces, *e.g.*, single crystalline Pt(111) with noticeable defects.

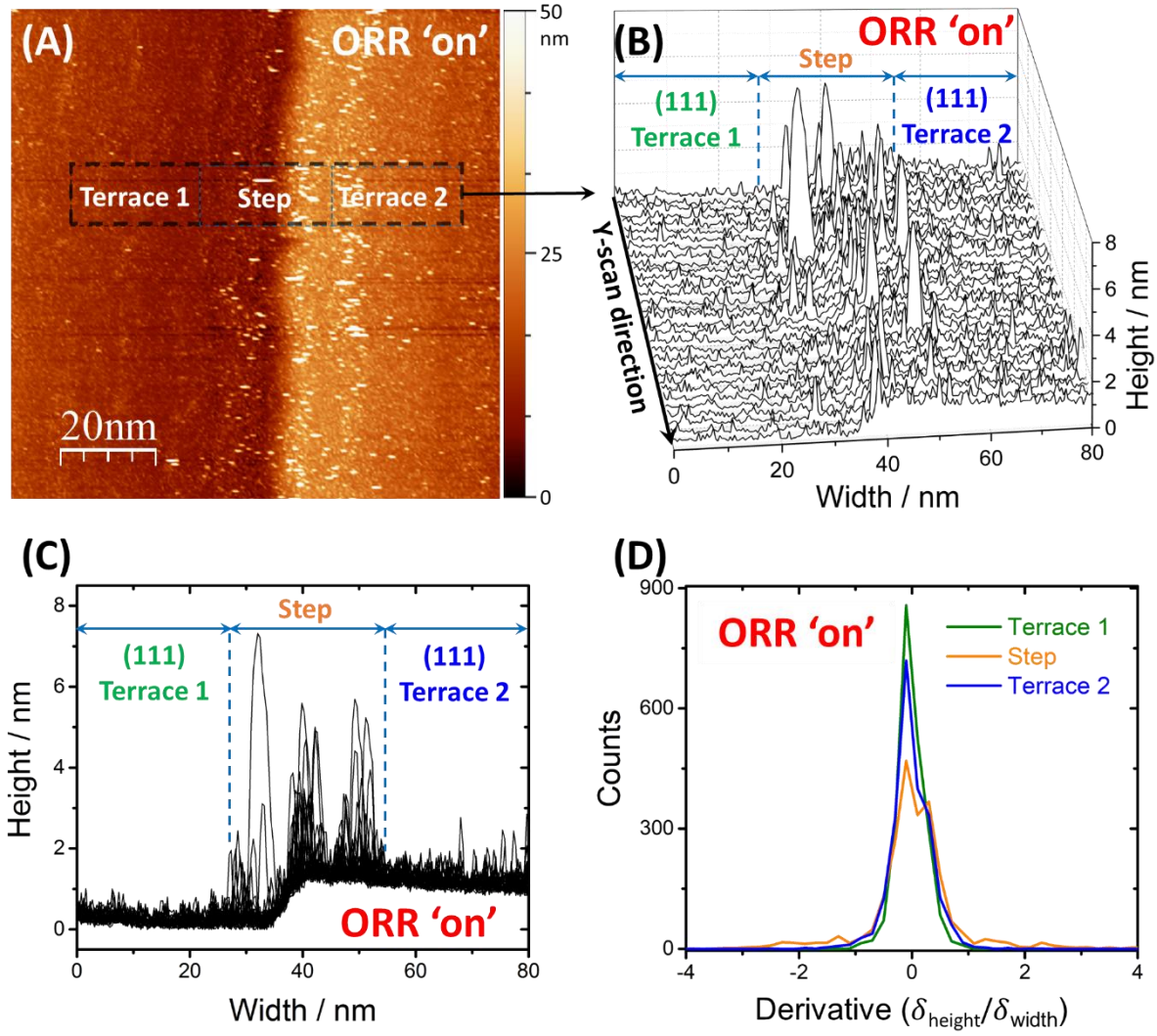


*Figure 62.* ***Constant current mode EC-STM measurement on Pt(111) under ORR 'on' condition in air-saturated 0.1 M $HClO_4$.*** *Sample potential: 200 mV vs SSC, tip potential: 500 mV vs SSC, current setpoint: 1.5 nA, scan rate: 0.5 Hz. (A) recorded image. (B) and (C) The line scans in the black dashed box in (A). The line scans are divided into three parts, namely terrace 1, step, and terrace 2. (D) Derivative analysis of the defined three parts.*

### 4.1.6 Verification of the Proposed Concept – Summary

The n-EC-STM was tested with aqueous catalytic systems including the HER and the ORR on nanostructured samples. It has been proven that the n-EC-STM is capable of identifying catalytically active centers under reaction conditions. For certain systems, for instance, the HER on Pt(111) in 0.1 M $HClO_4$, the location of the active centers (for example, the concavities of step-like defects) can be directly revealed. Moreover, a proper analysis of the noise features can show the dissimilarity of different active sites, for instance, the different activity of the

edge atoms and center surface atoms of Pd monoatomic islands on Au(111) in 0.1 M $H_2SO_4$ towards the HER. All these results confirmed knowledge and expectations from the literature.

During all the EC-STM measurements, the experimental parameters were carefully controlled. The lateral width (particularly in the x-direction) of most of the noise features in the captured HER 'on' images are less than the length of 15 atoms (just a few nanometers) which is much less than the critical size (45–1000 nm) of the electrochemically generated hydrogen nanobubbles at the electrode surface[185]. Therefore, the possibility of hydrogen gas bubble formation under reaction conditions causing the noise has been excluded. The resolution of the n-EC-STM is dependent on the investigated catalytic systems, *e.g.*, the surface morphology, the diffusion of the species that participate in the studied reactions, experimental parameters (*e.g.*, current setpoint, applied potential), and the quality of the tip. Both catalytic reactions producing electroactive species (for instance, $H_2$ of the HER) and others that have relatively inert products (for instance, $H_2O$ of the ORR) can be studied. All the reactions that can affect the effective tunneling barrier will lead noise features to the resulting images or line scans. In the case of ORR, the adsorption of oxygen followed by the different reaction intermediates and their disappearance as well as the diffusion of species in the gap between tip and sample might be decisive. Comparing the n-EC-STM analysis of the HER and ORR, the faster reaction, *i.e.*, HER, resulted in larger (in height or tip current) noise features, especially in the presence of the additional Faradaic contribution (the HOR at the tip). This methodology can be easily utilized in different laboratories for the studies of other catalytic systems, particularly the systems where the nature of the active sites is still under debate or remains unknown.

## 4.2 N-EC-STM – Other Applications

The verification of the n-EC-STM methodology was conducted with well-studied catalytic systems. Subsequently, other systems where the nature of the electrocatalytically active centers still is unclear were studied using the verified n-EC-STM methodology. The studied systems are the ORR and HER on Pt(111) in alkaline media, the HER on Pt sub-monolayer islands supported on a Au substrate and transition metal dichalcogenides (TMDs) in acidic media.

### 4.2.1 ORR on Pt(111) in Alkaline Media

This section shows the n-EC-STM results from the investigation of the ORR on a single crystalline Pt(111) surface in three aqueous alkaline media, 0.1 M KOH, LiOH, and CsOH. The results reveal the ORR activity of different active centers at Pt(111) surface in alkaline media. Each sub-chapter contains the results obtained in one alkaline medium, including the CV of the Pt(111), the EC-STM images under reaction conditions, and the derivative analysis of the recorded noise features.

#### 4.2.1.1 ORR on Pt(111) in Potassium Hydroxide Electrolyte (KOH)

Figure 63 shows a typical CV of Pt(111) in 0.1 M KOH, and the potential region where the ORR is enabled (ORR 'on') can be seen. Similar to the experiments conducted in acidic media (Chapter 4.1.5), the applied potential in the case of ORR 'off' was chosen to be around 0 V with respect to the quasi Pt reference electrode. The two current peaks around -0.1 V *vs* Pt indicate the adsorption and desorption of the O-species. The HER 'on' potential range is also present in the CV and was used in the HER studies (Chapter 4.2.2).

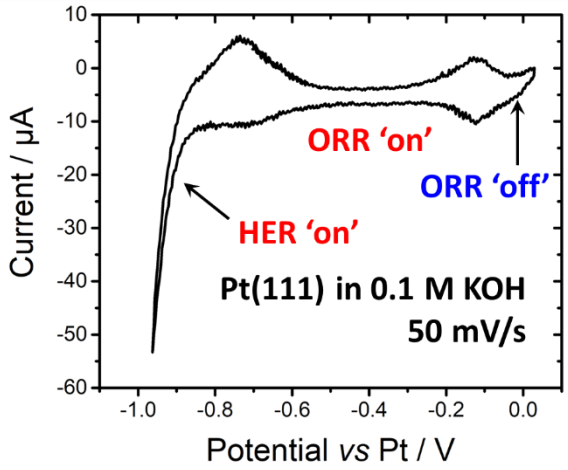


*Figure 63.* ***Typical CV of Pt(111) in 0.1 M KOH at a scan rate of 50 mV/s measured in the EC-STM cell.***

Successively recorded EC-STM images for approximately the same surface area (minor drift) on the Pt(111) are shown in Figure 64. The sample potential was switched between ORR 'on' and 'off' halfway through each image. During the EC-STM measurement, the noise features immediately covered the surface when the ORR was turned on and disappeared when ORR

was eliminated. Interestingly, in each image, there are no obvious dissimilarities in the level of the noise at the step-like defects and on the (111) terraces. It seems that no particular surface sites are more active than other sites at the surface. This finding stands in contrast to the results in 0.1 M $HClO_4$ where the step-concavities of Pt(111) have clearly a higher activity towards the ORR than the (111) terraces.

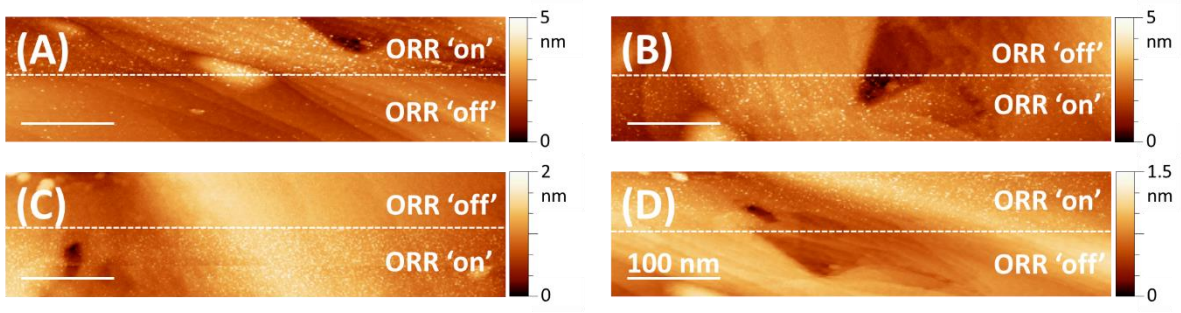


*Figure 64.* ***Constant current mode EC-STM images of Pt(111) in 0.1 M KOH under ORR 'on' and ORR 'off' conditions.*** *Scan rate: 0.5 Hz, current setpoint: 1.5 nA. The sample potential was -50 mV vs Pt for the case of ORR 'off' and the ORR 'on' potential was varied in different images. The ORR 'on' potentials were (A) -250 mV vs Pt, (B) -200 mV vs Pt, (C) -100 mV vs Pt, and (D) -150 mV vs Pt, respectively. The tip potential was the halfway potential between the sample potentials of ORR 'on' and 'off'. The white dashed lines indicate the position where the potential was changed.*

To have a closer look at the noise level on the step-like defects with higher lateral resolution, the EC-STM images over one monoatomic step at the Pt(111) surface were taken and are shown in Figure 65.A and B. The image in Figure 65.A was obtained while oxygen reduction was taking place. The noise level throughout the whole image was roughly the same. Most importantly, the step was again not more active than the (111) terraces. As shown in Figure 65.B, when switching the sample potential repeatedly, the noise stayed on the same level at the potential of ORR 'on' and disappeared when ORR was turned 'off', regardless of the surface structure.

The height profiles (2D projection in Figure 65.C and 3D plot in Figure 65.D) of equidistant line scans taken from the EC-STM image in Figure 65.B show that almost no noise features appeared when ORR was eliminated. Therefore, the noise features at sufficient potentials (ORR 'on') are directly correlated with the ORR. Moreover, in the line scans of ORR 'on' (in both Figure 65.C and D), these noise features have approximately the same height, indicating that the ORR activity at the step-like defect sites is not higher than the (111) terrace sites at the Pt(111) surface in 0.1 M KOH.

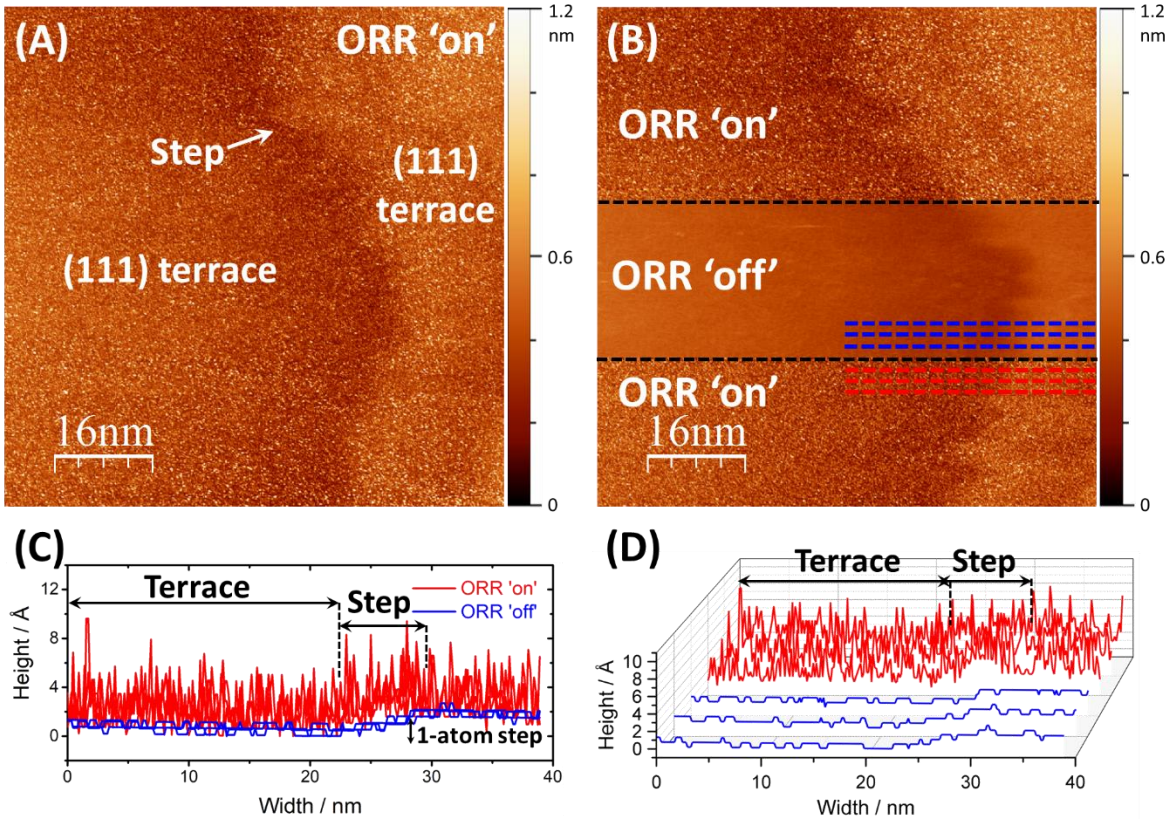


*Figure 65.* ***Constant current mode EC-STM images of a Pt(111) surface in 0.1 M KOH.*** *(A) Image (90 nm x 90 nm) of a monoatomic step and neighboring terraces under ORR 'on' condition (-250 mV vs Pt). (B) Image (80 nm x 80 nm) over approximately the same area under the conditions of ORR 'on' (-250 mV vs Pt) and 'off' (-50 mV vs Pt). Dashed black lines show the position where the sample potential was changed. Tip potential: -150 mV vs Pt, current setpoint: 0.8 nA, scan rate: 1 Hz. Equidistant line scans (blue dashed lines in ORR 'off' region and red dashed lines in 'on' region, respectively) are taken for further analysis. (C) and (D) The 2D and the 3D view of the chosen line scans in (B).*

Another EC-STM image, obtained under the ORR 'on' condition, further compares the ORR activity of the step-like defects and the (111) terraces at the Pt(111) surface in 0.1 M KOH, as shown in Figure 66.A. Flat (111) terraces and two monoatomic steps can be seen in the EC-STM image. It seems that these two steps did not contribute higher noise signals compared to the (111) terraces. Three line scans across both steps are shown in Figure 66.B with different colors.

It is well-known that differently-coordinated surface sites at a Pt surface can have different electrocatalytic activities. For instance, on Pt(111), the step-concavities are much more active than the (111) terraces towards the ORR in acidic solutions[29]. However, the results obtained with Pt(111) in 0.1 M KOH demonstrate that these step-concavities are not more (or even less)

active than the (111) terraces, and the reason should be the presence of the alkali metal cations ($K^+$).

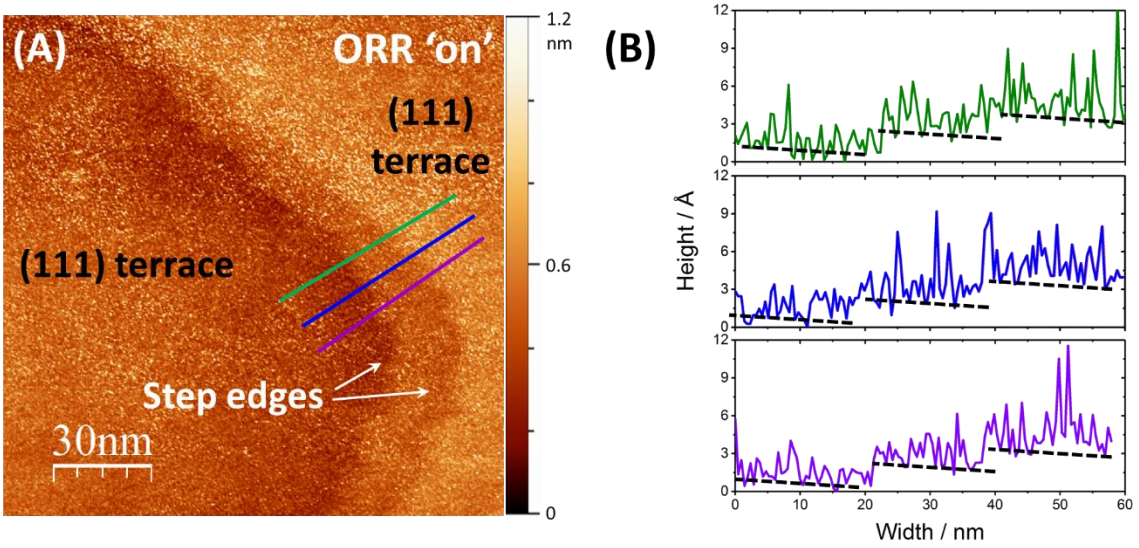


*Figure 66.* ***Constant current mode EC-STM images of Pt(111) in 0.1 M KOH under ORR 'on' condition.*** *(A) EC-STM image of Pt(111) at -250 mV vs Pt (ORR 'on'). Current setpoint: 0.8 nA, tip potential: -150 mV vs Pt, scan rate: 1 Hz. (B) Height profile of line scans taken from (A) with different colors. Dashed black lines are drawn to guide the eyes to the position of the (111) terraces.*

To confirm the reproducibility of the n-EC-STM results, a series of EC-STM images (Figure 67), over approximately the same area with three step-like defects, was successively recorded. The potential of the sample was switched to enable the ORR ('on') and stop the ORR ('off') in each image. Again, the noise features covered the whole surface when the ORR was enabled, regardless of the surface structure.

Each three equidistant and parallel line scans along the x-direction (considering the drift) are chosen from both the ORR 'off' and 'on' regions in Figure 67.D and are plotted together in Figure 67.E. The level of the noise on the upper terrace is approximately the same compared to that on the lower terrace. However, the step-like defect, particularly the part where the height changes roughly from ~7 Å to ~0 Å (a 2-atom step), is less ''noisy''.

Derivative frequency analysis was performed on the scan lines belonging to the defined step and terrace 2 with an identical number of data points, as shown in Figure 67.F. The comparison of the noise levels reveals that this 2-atom step-like defect was less active compared to the (111) terrace towards the ORR, in 0.1 M KOH.

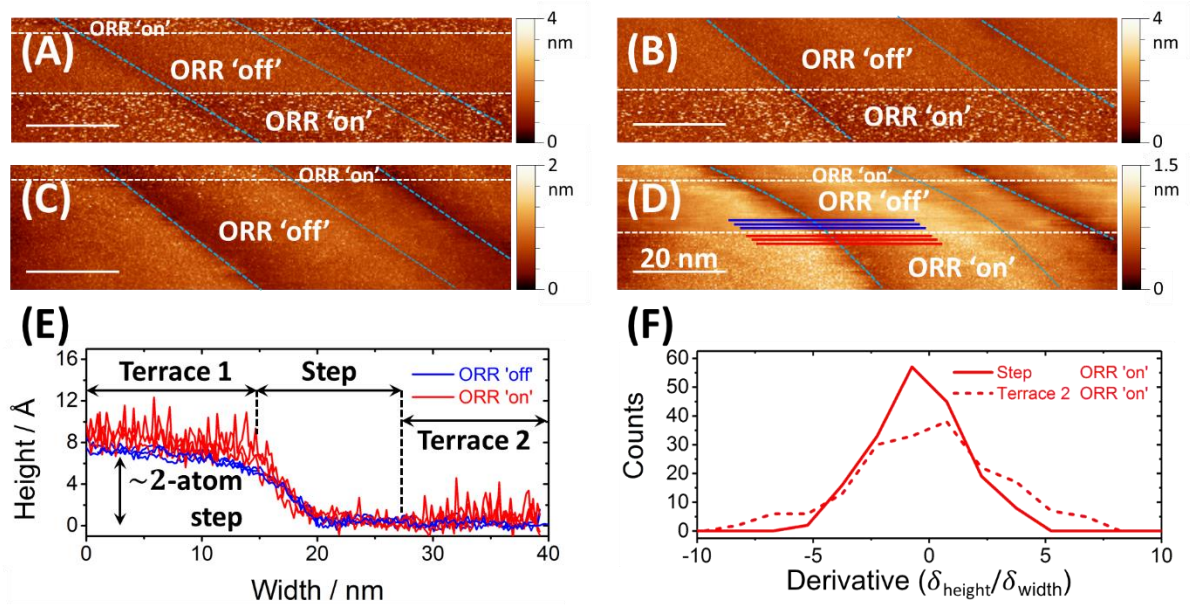


*Figure 67.* ***Successive constant current mode EC-STM images of Pt(111) in 0.1 M KOH and the derivative frequency analysis of selected line scans.*** *(A-D) A series of EC-STM images over approximately the same area (minor drift) when sample potential was switched between -250 mV (ORR 'on') and -50 mV (ORR 'off') vs Pt. Dashed light blue lines indicate the position of the step-like defects. White dashed lines mark the location where the potential was changed. Tip potential: -150 mV vs Pt, current setpoint: 1.5 nA, scan rate: 0.5 Hz for all images. (E) Height profile of lines scans selected from (D), labeled in blue (ORR 'off') and red (ORR 'on'). The profile is divided into three parts: terrace 1, step, and terrace 2. (F) Derivative frequency analysis for tunneling current on the step and on terrace 2 at the potential of ORR 'on'.*

#### 4.2.1.2 ORR on Pt(111) in Lithium Hydroxide Electrolyte (LiOH)

The experiments conducted in 0.1 M LiOH electrolyte were similar to those in KOH. The ORR 'on' and 'off' potentials applied to the Pt(111) electrode were selected according to the CV of the Pt(111) in 0.1 M LiOH obtained in the EC-STM cell, as shown in Figure 68.

Figure 69.A-D show a series of EC-STM images obtained while the sample potential was switched between that of the ORR 'on' and ORR 'off'. Analogous to the results in 0.1 M KOH, no inhomogeneity in the noise level is visible in the EC-STM images over relatively large surface areas. It should be noted that each image contains several step-like defects. However, none of these defects contributed larger noise features when the ORR was taking place, as compared to the (111) terraces.

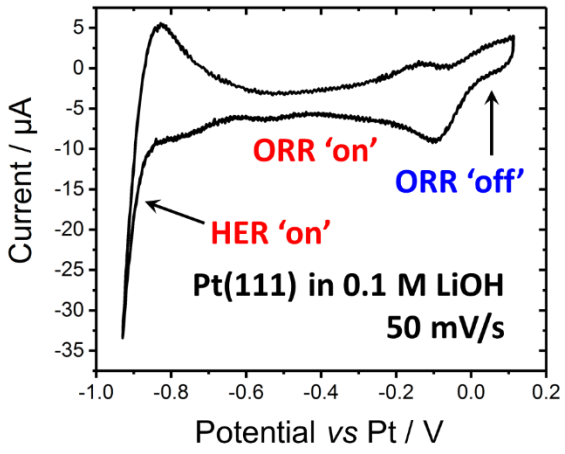


*Figure 68.* ***Typical CV of Pt(111) in 0.1 M LiOH at a scan rate of 50 mV/s obtain in the EC-STM cell.***

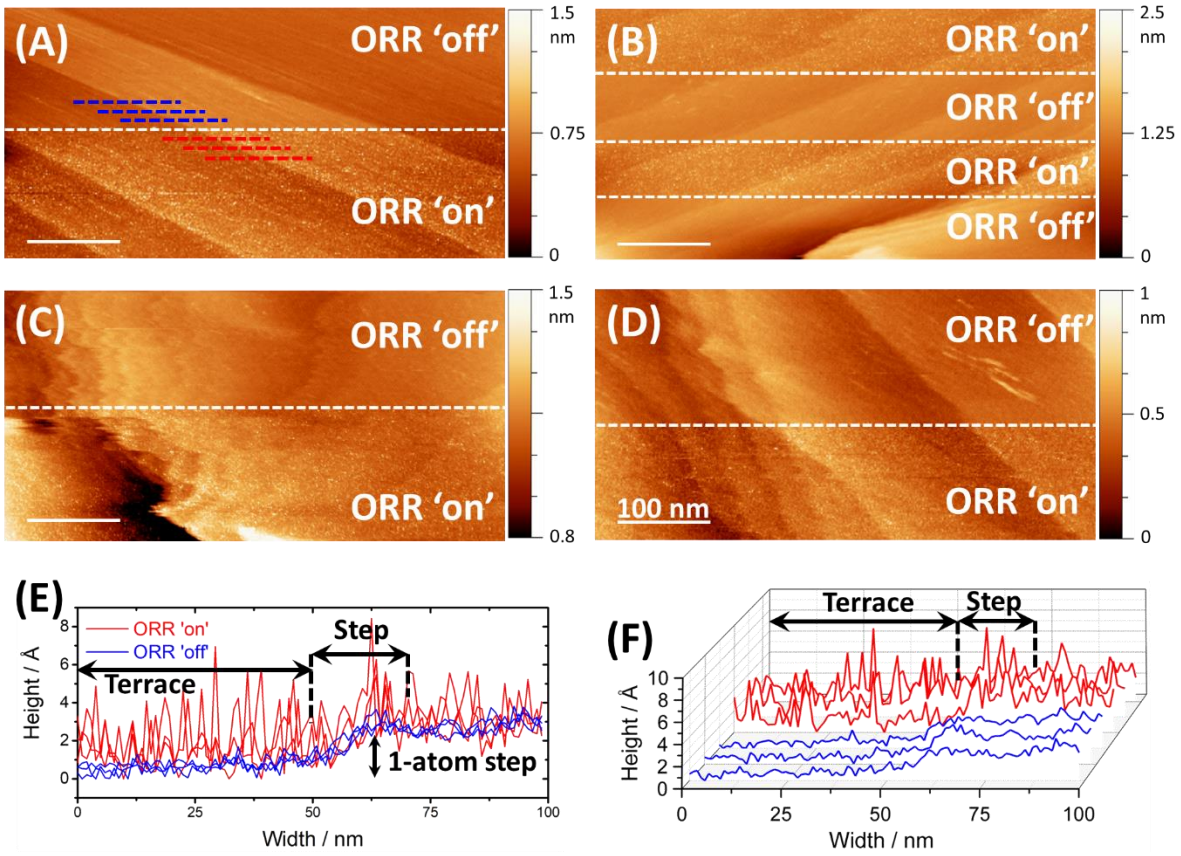


*Figure 69.* ***Constant current mode EC-STM images of a Pt(111) surface in 0.1 M LiOH.*** *(A-D) EC-STM images captured when sample potential was switched between -225 mV (ORR 'on') and -25 mV (ORR 'off') vs Pt. White dashed lines mark the location where the potential was switched. Tip potential: -125 mV vs Pt, scan rate: 0.5 Hz for all images. Current setpoint: (A) 1 nA, (B and C) 1.2 nA, and (D) 1.4 nA. (E) and (F) Lines scans over a monoatomic step selected from (A).*

Figure 69.A and B are represented as 3D images in Figure 70.A and B. The blue and red arrows point out the scanned areas when the ORR was 'off' and 'on', respectively. The boundaries between the areas captured at different overpotentials are clear, as the noise features are dense spikes only covering the ORR 'on' regions. Again, no protruding noise features can be seen on the step-like defects under the ORR 'on' condition.

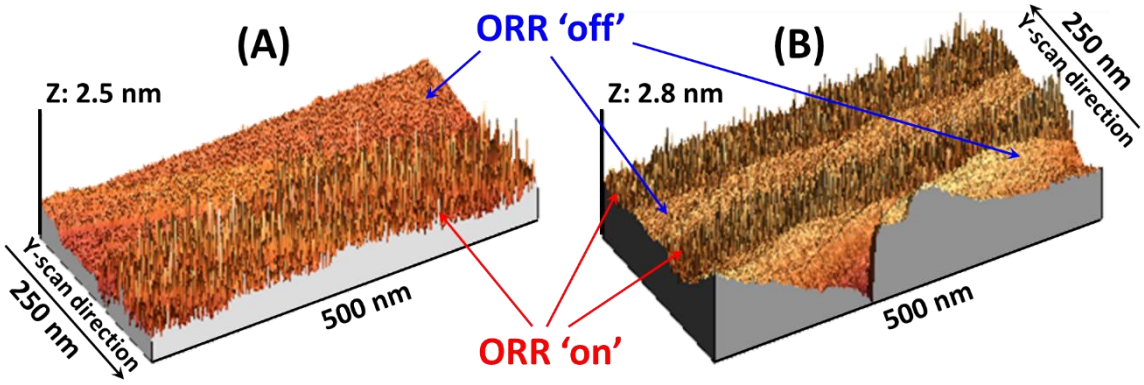


*Figure 70.* ***3D representations of the constant current mode EC-STM images of a Pt(111) surface in 0.1 M LiOH.*** *(A) and (B) 3D representations of the EC-STM images shown in Figure 69.A and B, respectively. The ORR 'off' (-25 mV vs Pt) and 'on' (-225 mV vs Pt) regions are indicated by the blue and red arrows, respectively. The black arrows show the y-scan directions for each image.*

So far, the n-EC-STM study has been focused on the comparison of the ORR activity of sub-nanometer step-like defects and (111) terraces on Pt(111) in alkaline media. However, due to the broadening effect of the EC-STM measurement, the noise features generated on the sub-nanometer-size defects were potentially submerged in the noise from the terraces. Therefore, large-size defects, where the density of step-concavities and step-convexities are much larger compared to that of single sub-nanometer steps and (111) terraces, were also investigated by the n-EC-STM.

Figure 71.A and B show two EC-STM images over a large defect (~4 nm in height) at the Pt(111) surface in 0.1 M LiOH. When comparing the level of the noise observed on this large defect and on the (111) terraces at the potential of ORR 'on', no obvious difference can be seen. The line scans taken from the image in Figure 71.A, as shown in Figure 71.C and D, confirm the fact that even such a relatively large defect cannot contribute major noise features under ORR 'on' condition. This suggests that, on Pt(111), large defects containing numerous step-concavities

and step-convexities are not more active than the (111) terrace sites towards the ORR in 0.1 M LiOH.

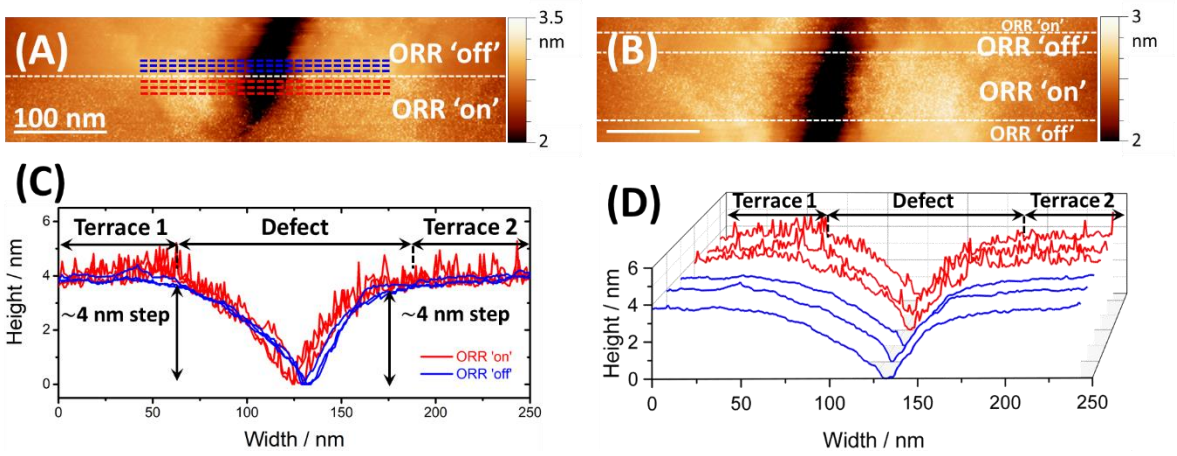


*Figure 71.* ***Successive constant current mode EC-STM images of a Pt(111) surface area containing a large defect in 0.1 M LiOH.*** *(A) and (B) EC-STM images over approximately the same area (minor drift) when the sample potential was switched between -275 mV (ORR 'on') and -25 mV (ORR 'off') vs Pt. White dashed lines mark the location where the sample potential was changed. Current setpoint: 0.5 nA, tip potential: -150 mV vs Pt, scan rate: 0.5 Hz. It should be noted that the height scale starts from 2 nm to compensate the loss of the color-contrast caused by the deep defect in the middle of the images. (C), (D) 2D and 3D height profiles of line scans over the defect, taken from the image in (A).*

### 4.2.1.3 ORR on Pt(111) in Cesium Hydroxide Electrolyte (CsOH)

Figure 72 shows a typical CV of the Pt(111) electrode in 0.1 M CsOH at a scan rate of 50 mV/s obtained in the EC-STM cell. The potential parameters required for the n-EC-STM measurements were selected accordingly.

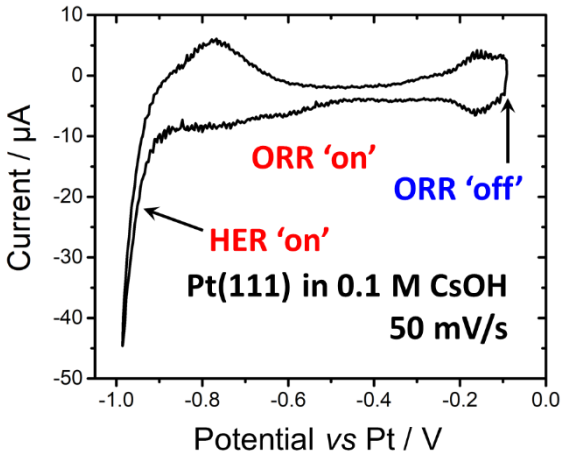


*Figure 72.* ***Typical CV of Pt(111) in 0.1 M CsOH measured in the EC-STM cell at a scan rate of 50 mV/s.***

A series of EC-STM images, as shown in Figure 73, were captured while the sample potential was switched between that of the ORR 'on' and the ORR 'off' conditions in each image. A similar phenomenon can be seen, compared with the EC-STM images (with large image sizes) captured in the KOH and the LiOH electrolytes, that the noise features covered the whole surface without noticeable dissimilarities, regardless of the surface structure, while the ORR was taking place at the Pt(111) surface.

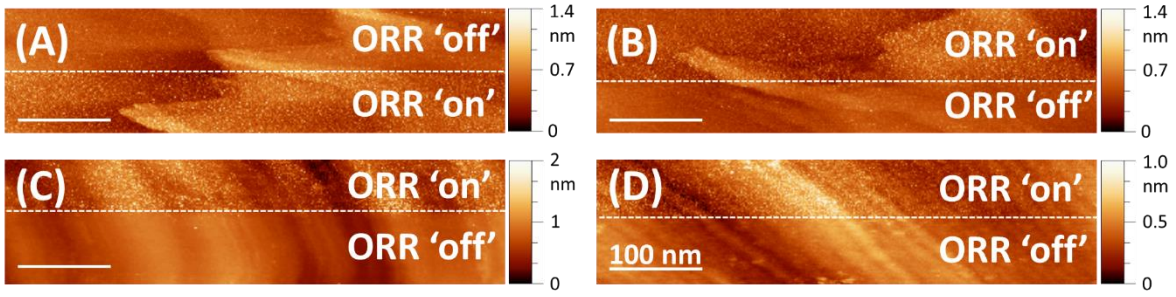


*Figure 73.* ***Constant current mode EC-STM images of a Pt(111) surface in 0.1 M CsOH.*** *The sample potential was switched between -250 mV (ORR 'on') and -50 mV (ORR 'off') vs Pt halfway through each image. White dashed lines mark the location where the potential was switched. Current setpoint: 0.8 nA, tip potential: -150 mV vs Pt, scan rate: 0.5 Hz.*

Figure 74.A depicts an EC-STM image measured under the same conditions as for the images in Figure 73. The resolution of Figure 74.A is higher, so that one can have a closer look at the noise features on the step-like defects. The equidistant line scans taken from Figure 74.A reveal a monoatomic step and two (111) terrace regions, as shown in Figure 74.B. It appears that noise features around the step edge are not higher than those on the (111) terraces.

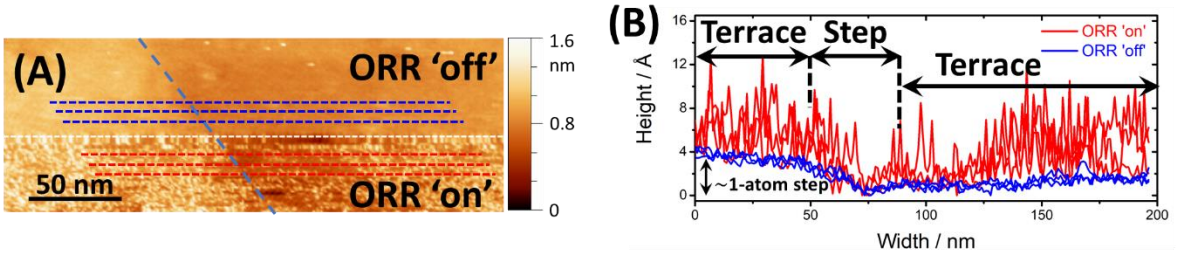


*Figure 74.* ***Constant current mode EC-STM image of Pt(111) surface in 0.1 M CsOH and line scans.*** *The sample potential was switched between -250 mV (ORR 'on') and -50 mV (ORR 'off') vs Pt halfway through the image. White dashed lines mark the location where the potential was switched. Current setpoint: 0.8 nA, tip potential: -150 mV vs Pt and scan rate: 0.5 Hz.*

#### 4.2.1.4 ORR on Pt(111) in Alkaline Media – Summary

The n-EC-STM has been employed to find the active centers for the ORR at single crystalline Pt(111) surface in alkaline electrolytes, including 0.1 M KOH, 0.1 M LiOH and 0.1 M CsOH electrolytes. Interestingly, there are no extraordinarily ‘‘noisy’’ spots at the Pt(111) surface under the ORR ‘on’ conditions in alkaline media. This means that the step-like defects (or step-concavities) do not act as enhanced active centers as compared to the (111) terrace sites for the ORR in alkaline electrolytes used in the measurements. In the case of KOH and CsOH (*e.g.*, Figure 67 and Figure 74), the step-like defects are seemingly even less active than the (111) terraces.

Considering the inevitable broadening effect in (EC-) STM measurements, the n-EC-STM cannot sufficiently distinguish the noise contribution from the sub-nanometer step-like defects if the (111) terraces surround the step-like defects are more active. The noise features on the step-like structures, if they are less active towards the ORR, can be submerged by the broadened higher noise features generated from more active terraces in the vicinity of the defects.

The macroscopic data already reported that the ORR activity of stepped Pt single crystal electrodes in alkaline media decreases with increasing density of step-like defects[53]. Additionally, a recent study showed that the ORR activity of single crystalline Pt(111) at 0.9 V *vs* RHE in KOH and CsOH electrolytes is at least two times higher than that in $HClO_4$[111]. The n-EC-STM results indicate that the activity of the (111) terrace sites certainly governs the overall ORR activity of the single crystalline Pt(111) surface in alkaline media. This finding is in contrast to the well-known fact that the active centers in acidic media are the step-concavities at the Pt(111) surface. To find the reason why the defect sites, *e.g.*, step concavities, are not the active centers for the ORR on Pt(111) in alkaline media, further investigations and other research methods are required. However, the influence of the electrolyte spectator ions should be taken into account, and the presence of the alkali metal cations in the alkaline media can be a promising answer.

The recently mentioned non-covalent or quasi-covalent interaction between the alkali metal cations and the adsorbed reaction intermediates[51, 188] are likely to be the reason. The alkali metal cations can affect the ORR activity of the Pt electrode by changing the binding energy of the reaction intermediates. The n-EC-STM analysis results indicate that the alkali metal

cations excessively weaken the binding energy of the Pt(111) surface sites to the adsorbed O-species. Therefore, the concavity site, which is located close to the top of the ‘‘volcano’’ without considering the effect from the electrolyte or the spectator ions, moves over the optimal point and ends up on the weak side of the ‘‘volcano’’ in alkaline media, as shown in Figure 75. However, the (111) terrace site, which is less active towards the ORR than the concavity site in acidic media (Figure 16), becomes more active (Figure 75). Consequently, the geometrically optimized step-concavities in the case of acidic media become less active towards the ORR due to the effect of the alkali metal cations, and the (111) terrace site dominates the overall ORR activity of the Pt(111) electrode in alkaline media.

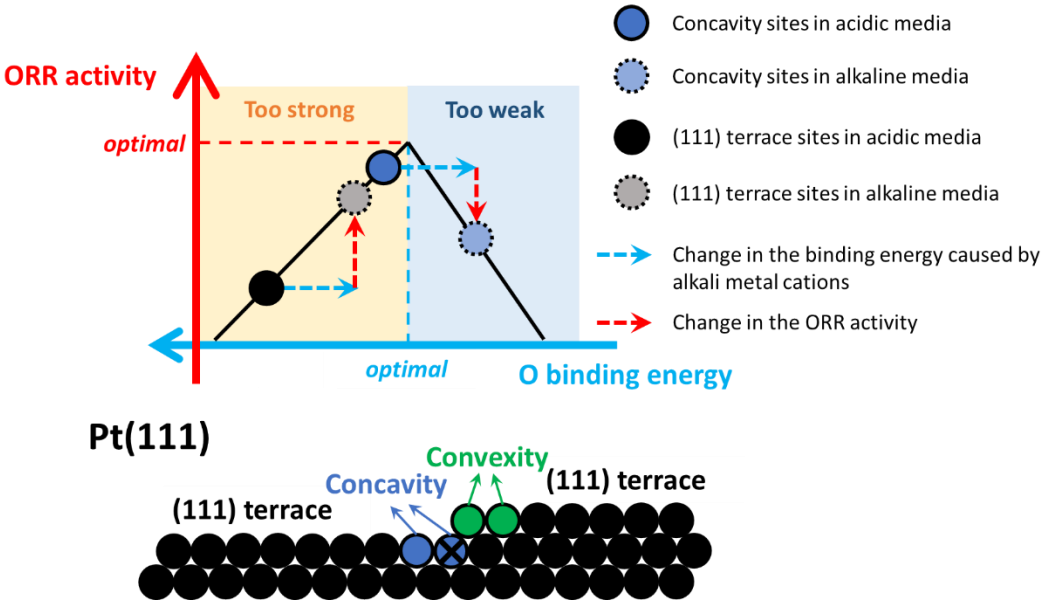


*Figure 75.* ***An illustration of the effect of the alkali metal cations on the O binding energy on the Pt(111) concavity and (111) terrace sites in alkaline media.*** *The ball model shows the typical structures of a Pt(111) surface, e.g., the (111) terrace, the step-concavity (blue) and the step-convexity (green).*

However, the n-EC-STM does not quantitatively compare the effect of different alkali metal cations (changing the electrolyte from one alkaline medium to another one was not possible during EC-STM measurements) or differentiate how much the alkali metal cations affect the O-species binding energy on the step-concavities and on the (111) terrace sites. The obtained results have already indicated a general effect of the alkali metal cations on the ORR catalytic activity of the Pt electrode surface. This conclusion can be tested with other catalyst materials using various investigation methods, and it is expected to impact the rational design of catalytic systems involving alkali metal cations.

### 4.2.2 HER on Pt(111) in Potassium Hydroxide Electrolyte (KOH)

The applied potentials in the case of HER 'off', which were not negative enough to enable the HER, can still start the reduction of oxygen at the Pt surface. Therefore, the n-EC-STM investigation for the HER on Pt(111) in the 0.1 M KOH electrolyte was not as straightforward as that for the ORR. Except for that, all HER measurements followed the same strategy that was used for the ORR studies in alkaline media. The HER 'on' and 'off' potential parameters were selected according to the CV shown in Figure 63. The HOR taking place at the tip increased the tip current offset. Consequently, the measurements in the case of the HER normally required a larger current setpoint than in the case of the ORR.

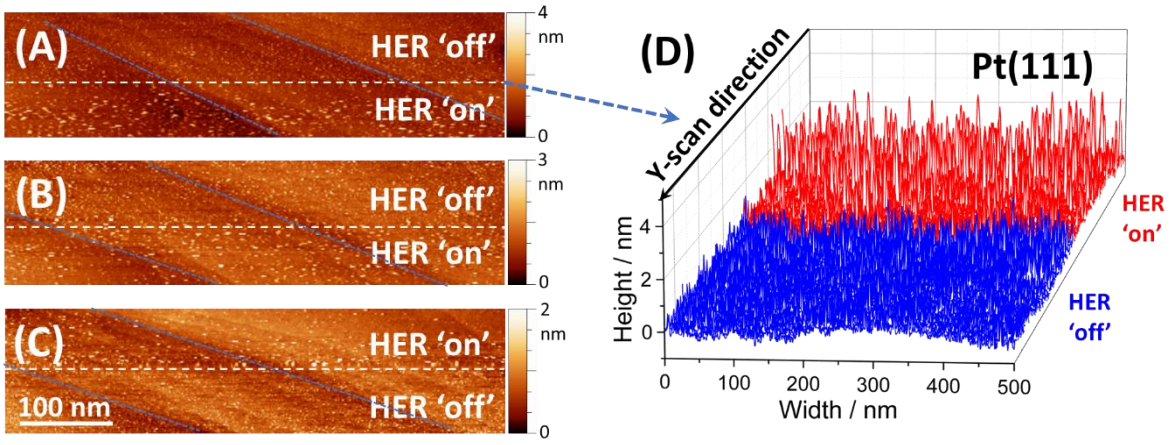


*Figure 76.* ***Successive constant current mode EC-STM images of the Pt(111) surface in 0.1 M KOH.*** *(A-C) EC-STM images over approximately the same surface area (with a minor drift) when the sample potential was switched between -890 mV (HER 'on') and -700 mV (HER 'off') vs Pt halfway through each image. Dashed white lines indicate where the potential was changed. Dashed blue lines mark roughly the locations of the step-like defects. Current setpoint: 0.8 nA, tip potential: -740 mV (HER 'on') and -550 mV (HER 'off') vs Pt (constant potential bias), scan rate: 0.5 Hz. (D) Line scans taken from (A), blue (HER 'off') and red (HER 'on').*

In 0.1 M KOH, as shown in Figure 76.A-C, no matter whether there was hydrogen evolving or not, noise features covered the whole electrode surface. However, the noise level in the case of HER 'on' was much higher than in the case of HER 'off', as shown in Figure 76.D (line scans taken from Figure 76.A). This is likely due to the fact that catalytic reactions (ORR or HER) were taking place during the whole imaging time, but the current density at the potential of the HER 'on' was higher than that in the case of HER 'off' (as can be seen in Figure 63). Additionally, the oxidation of the evolved hydrogen at the tip also contributed extra noise signal.

Taking a closer look at the HER ‘on’ regions in Figure 76.A-C, there is no noticeable dissimilarity between the level of the noise obtained on the (111) terraces and on the step-like defects. This is analogous to the n-EC-STM results of the ORR on Pt(111) in alkaline media (Chapter 4.2.1). This leads to the assumption that the alkali metal cations affect the HER activity of the Pt(111) surface in the same way they influence the ORR activity of the Pt(111) surface in alkaline media.

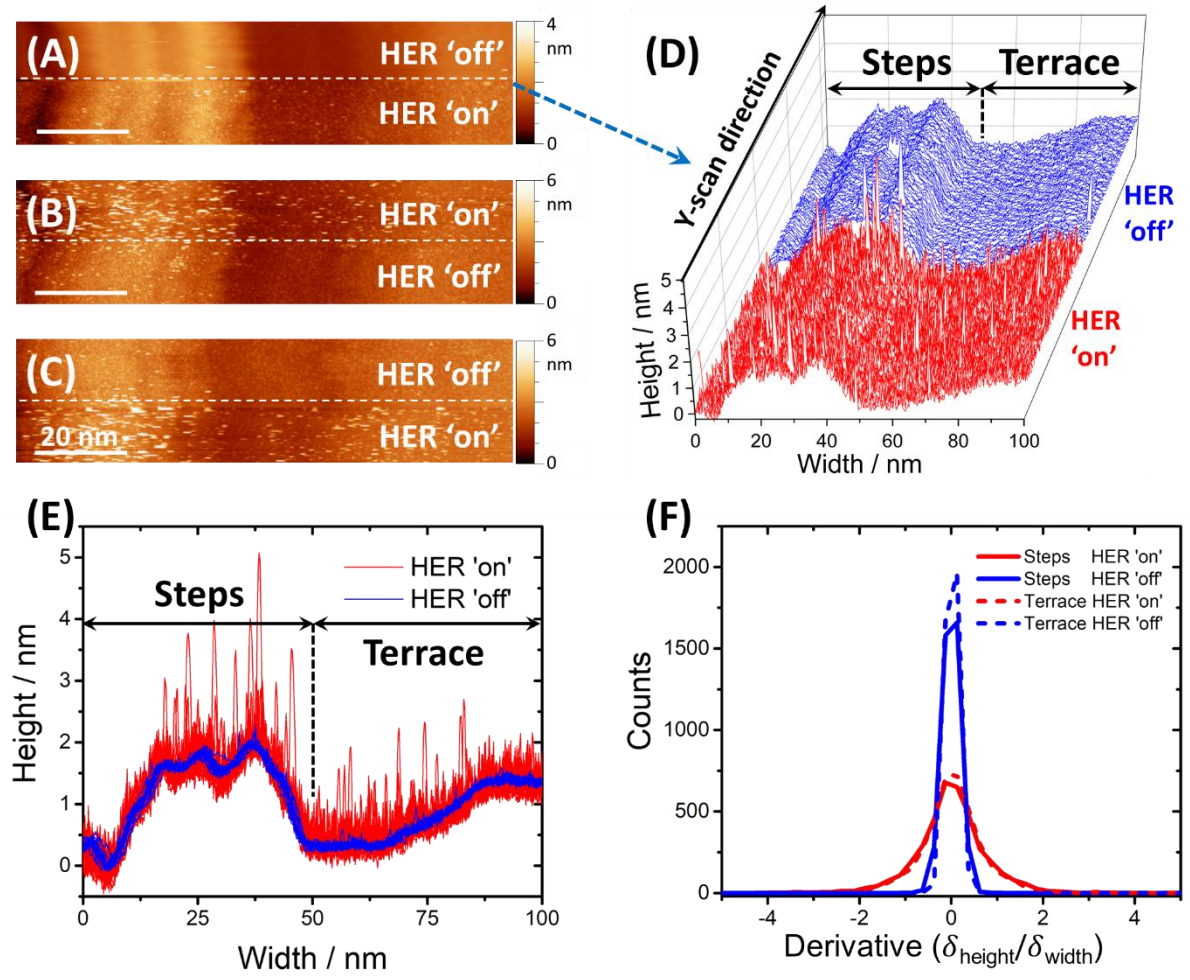


*Figure 77.* ***Constant current mode EC-STM images of a Pt(111) surface in 0.1 M KOH.*** *(A-C) EC-STM images obtained over approximately the same surface area when the sample potential was switched between -910 mV (HER ‘on’) and -800 mV (HER ‘off’) vs Pt in (A, C) and between -890 mV (HER ‘on’) and -790 mV (HER ‘off’) vs Pt in (B), respectively. Current setpoint: 2 nA in (A) and 2.2 nA in (B-C), constant potential bias (tip potential - sample potential): 100 mV, scan rate: 1 Hz. (D) and (E) 3D and 2D line scans taken from (A). The ‘‘steps’’ region (0-50 nm) contained several step-like defects, and the ‘‘terrace’’ region (50-100 nm) had a (111) terrace with minor defects. (F) Derivative frequency analysis for the defined ‘‘steps’’ and ‘‘terrace’’ sides (data point of every 4$^{th}$ line scan) in the case of HER ‘on’ and ‘off’.*

To further compare the HER activity of the defects and the (111) terraces, EC-STM images were captured over an area on Pt(111) with several step-like defects (left side) and a (111) terrace (right side, with minor defects), as shown in Figure 77.A-C. The same phenomenon that large noise features immediately covered the defects and terraces whenever and wherever the HER was enabled, regardless of the structure of the Pt(111) surface, can be observed in all images (Figure 77.A-C).

Figure 77.D and E exhibit the height profile of the line scans taken from Figure 77.A. The scanned surface can be divided into two regions with the same width in the x-direction, the ‘‘step’’ region and the ‘‘terrace’’ region, respectively. The same level of noise can be seen on both the ‘‘step’’ and the ‘‘terrace’’ regions under the HER ‘on’ condition. Additionally, the derivative frequency analysis (Figure 77.F) reinforces the even noise level from both sides. Therefore, this defective (‘‘step’’) region of the Pt(111) surface did not contain such active sites which contributed noticeably higher HER activities compared to the (111) terrace sites.

In summary, on Pt(111), the step-like defects are at least not more active than the (111) terrace sites towards the HER in 0.1 M KOH, in contrast to the finding obtained in acidic media (Chapter 4.1.1). It seems that the alkali metal cations affect the ORR activity and the HER activity of the active sites of the Pt(111) surface similarly. Consequently, the (111) terrace sites dominate the overall HER activity of the Pt(111) in 0.1 M KOH. The surface sites around the step-like defects, *e.g.*, step concavities, play minor roles in the activity. The reason could be that the non-covalent or quasi-covalent interactions between the alkali metal cations and the adsorbed H-species, weaken the H-binding energy on the Pt electrode, as it was suggested elsewhere[114]. The mechanism is similar to the one mentioned in the ORR studies, as shown in Figure 75.

### 4.2.3 HER on Pt Islands/Au(111) in Perchloric Acid ($HClO_4$)

As shown in Chapter 4.1.3, the geometrical factors and the foreign (Au) substrate can significantly influence the HER activity of the active sites of monoatomic Pd islands. However, nanostructured Pt-based materials are still among the best candidates for HER catalysts. The nanostructured Pt on an inert Au substrate, as a comparison to the Pd islands on Au, should be of interest to investigate. Therefore, the n-EC-STM was employed to study the HER activity

of Pt sub-monolayer islands on single crystalline Au(111) in 0.1 M $HClO_4$, and particularly compare the activity of the Pt/Au boundary and the Pt island surface.

Fully-packed monoatomic thick Pt islands on the Au(111) substrate can be seen using STM in air, as shown in Figure 78.A. The inserted height profile of the line scans over the selected islands show that the average height of the islands is about 0.25 nm, which is approximately the typical height of a Pt monoatomic layer. However, the captured shape of the Pt islands was influenced by the drift and the STM broadening effect. Figure 78.B exhibits a typical CV of the sample in 0.1 M $HClO_4$ measured in the EC-STM cell. The potential region in which the HER is enabled can be seen in the CV.

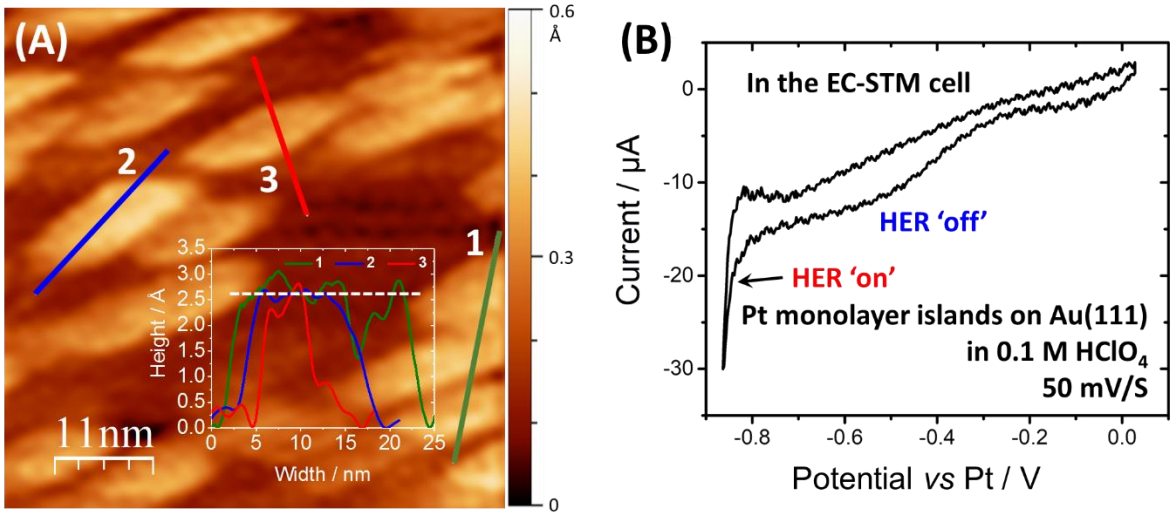


*Figure 78.* ***Constant current mode STM and typical CV of the deposited Pt sub-monolayer islands on Au(111) in the EC-STM cell.*** *(A) An STM image of the sample surface after Pt sub-monolayer island deposition and inserted height profile of the selected line scans. Current setpoint: 0.4 nA, scan rate: 0.5 Hz. (B) Typical CV of the sample in air-saturated 0.1 M $HClO_4$ obtained in the EC-STM cell at a scan rate of 50 mV/s. The HER 'on' potential range can be seen in the CV.*

EC-STM images were taken over one of the deposited Pt islands with different sample potentials. The sample potential was first set to a value at which no HER can take place (HER 'off') and then switched to a more negative potential to enable the HER on Pt (HER 'on'), but not negative enough to start the HER on the Au substrate. Figure 79.A and B show two EC-STM images captured before and after switching the sample potential, respectively. The shape of the Pt island changed slightly between the images because of the drift. The HER 'on' image

exhibits strong noise features only on the Pt island, and the level of noise is approximately the same all over the whole Pt island.

Figure 79.C compares the lines scans across approximately the same position in Figure 79.A and B. In the case of the HER 'on', the noise features are much larger and appear to be homogeneously distributed on the island. This indicates that the HER activity of all surface sites on the Pt islands supported by Au(111) was roughly the same. The Pt atoms located at the Pt/Au boundary were not more active than those in the middle of the Pt island.

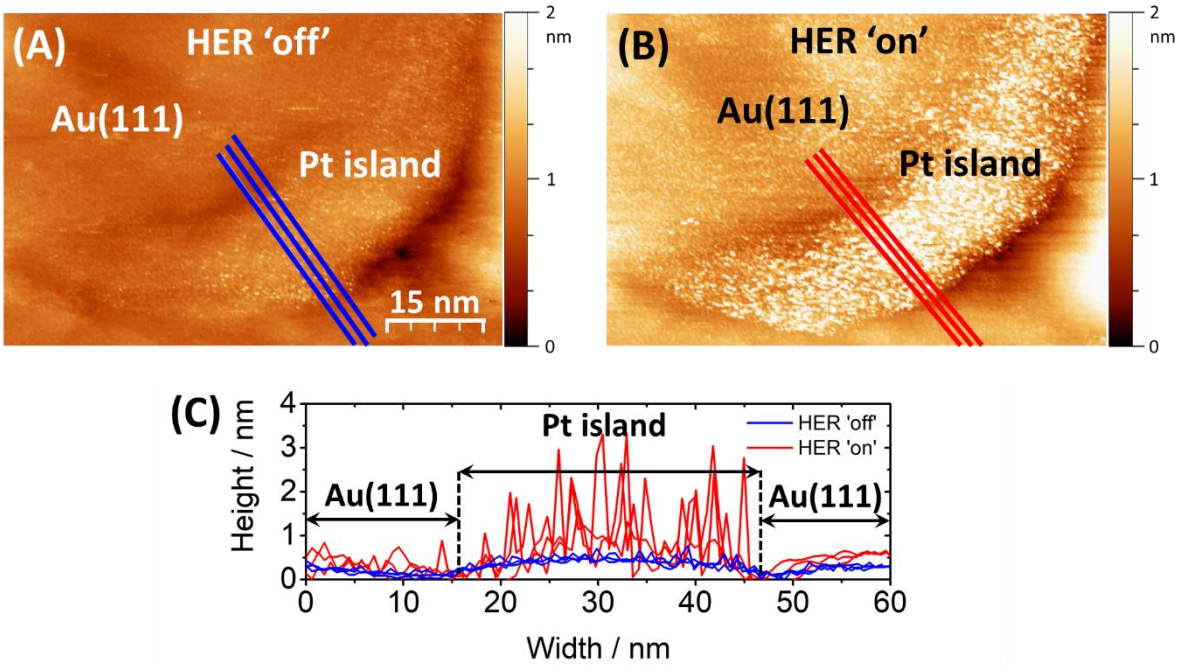


*Figure 79.* ***Constant current mode EC-STM images in 0.1 M $HClO_4$ over a Pt island on Au(111) with different sample potentials.*** *Sample potential: (A) -250 mV (HER 'off'), (B) -790 mV (HER 'on') vs Pt, constant potential bias: 190 mV, current setpoint: 0.8 nA, scan rate: 0.5 Hz. (C) Comparison of the selected line scans from (A) blue and (B) red.*

To precisely compare the HER activity of the edge and the surface of the Pt islands, EC-STM images focused on the Pt/Au boundary were measured. Figure 80.A and B show two EC-STM images of the Pt island captured at the potential of the HER 'off' and the HER 'on', respectively. Substantially, the noise features on a Pt island became stronger when the sample potential was switched from -250 mV (HER 'off') to -790 mV (HER 'on') *vs* Pt. Figure 80.C compares three equidistant line scans taken in approximately the same region from Figure 80.A and B, respectively, and Figure 80.D exhibits all the line scans extracted from the region marked by a

white rectangle (6 nm × 90 nm) in Figure 80.B. The Pt/Au boundary seems to be as ‘‘noisy’’ as the Pt island surface, in the case of the HER ‘on’.

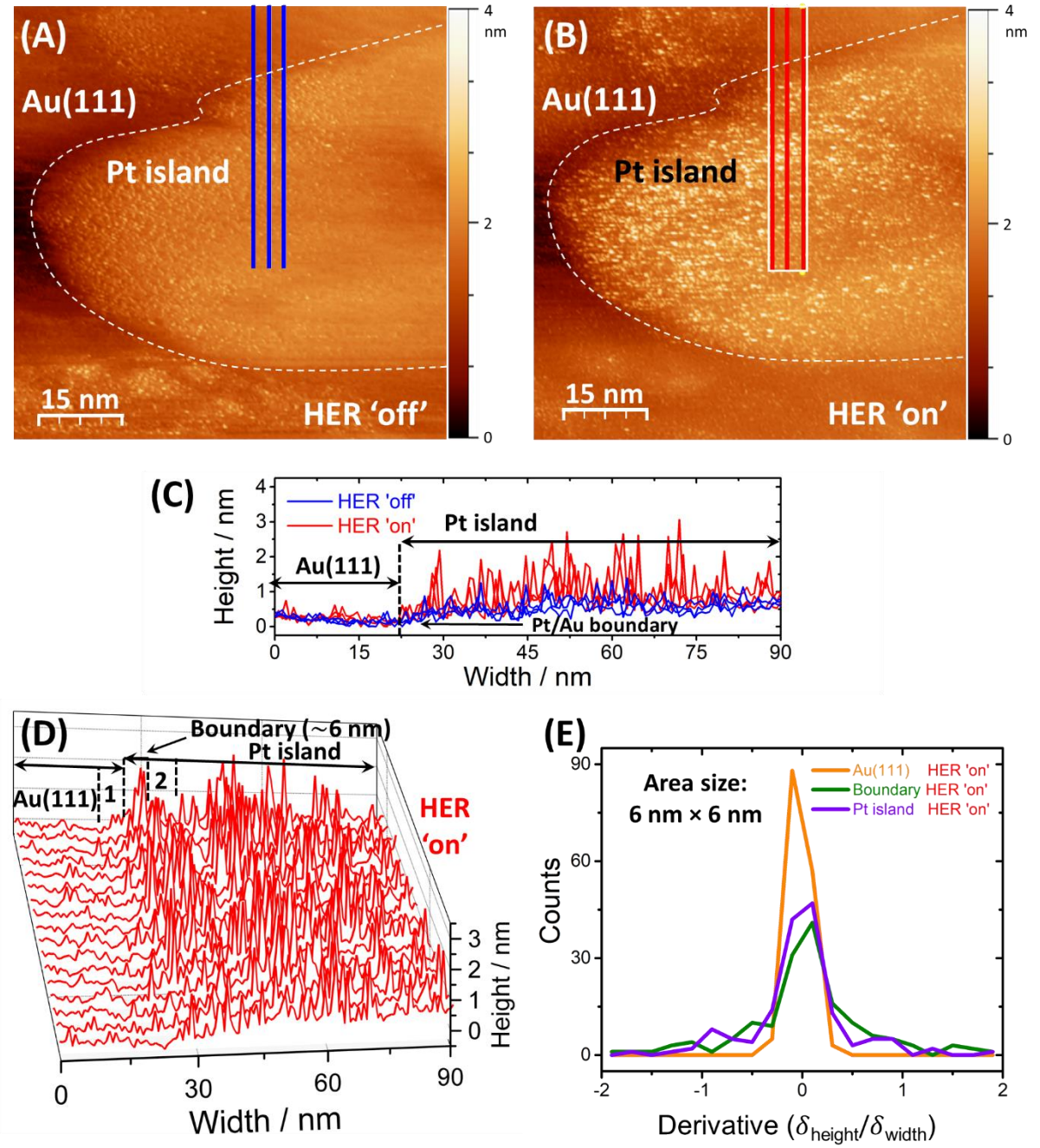


*Figure 80.* ***Constant current mode EC-STM images of Pt islands on Au(111) in 0.1 M $HClO_4$ and the derivative frequency analysis.*** *(A) and (B) EC-STM images over approximately the same surface area when the sample potential was switched between (A) -250 mV (HER ‘off’) and (B) -790 mV (HER ‘on’) vs Pt. Current setpoint: 1 nA, constant potential bias: 190 mV, scan rate: 2 Hz. (C) Comparison of the selected line scans marked in different colors in (A) and (B). (D) All line scans in the white rectangle in (B). (E) Derivative frequency analysis of the noise features from the defined boundary and the neighboring regions (each 6 nm × 6 nm) in (D).*

The study of the HER activity of Pd islands on Au(111) in 0.1 M $H_2SO_4$ had proven that the most active sites are located on the Pd/Au boundary. However, the width of such active centers is not larger than ~1 nm. Therefore, in order to determine the level of noise at the Pt/Au boundary, the width of the boundary should also be of the order of nanometers. As shown in Figure 80.D, the width of the boundary is chosen to be 6 nm, and the derivative frequency analysis was performed for noise features in the defined boundary region, and in the neighboring regions, namely the Au(111) surface (region 1) and the Pt island surface (region 2), with the same width, as shown in Figure 80.E. Except for Au(111), which is much less active towards HER, the noise levels on the Pt island surface and at the Pt/Au boundary are approximately the same.

Unlike the case of the Pd sub-monolayer islands on Au(111) in 0.1 M $H_2SO_4$, the n-EC-STM study of the HER on Pt sub-monolayer islands supported on Au(111) in 0.1 M $HClO_4$ indicates homogeneously distributed HER activity all over the Pt islands. The activity of the Pt atoms at the Pt/Au boundary is at least not higher than that of the Pt atoms located in the center of the Pt islands. This result suggests that the total HER activity of this catalytic system simply depends on the Pt coverage or mass loading on the Au substrate. However, the effect of anions in the electrolytes, *e.g.*, the $SO_4^{2-}$ in the case of Pd islands and the $ClO_4^-$ in the case of Pt islands, had been neglected during the investigations. Indeed, the $SO_4^{2-}$ adsorption on Au and Pt electrode surfaces have a considerable impact on the electrochemical or electrocatalytic properties of the electrodes[189, 190]. Therefore, the anion effect should be considered in further investigations.

Besides the effect of the anions (*e.g.*, the $SO_4^{2-}$ and $ClO_4^-$), the electronic structure of the catalyst should be considered. In the case of Pd islands on Au, the Au substrate influences the electronic properties of the Pd atoms differently and the most active centers towards the HER are located at the island edge. However, in the case of Pt islands on Au, such phenomena were not observed. It seems that the electronic properties of the Pt atoms at the island edge and at the island surface supported on Au are very similar that no difference in the HER activity was pronounced. This interpretation is in line with the hypothesis in literature[40, 191, 192], that most likely the strain effect (lattice difference between the Pt adlayers and the Au substrate leads to the change of the Pt interatomic distance) plays a major role in the case of Pt islands, however, both strain and ligand effects are important in the case of Pd islands.

### 4.2.4 HER on Transition Metal Dichalcogenides (TMDs) in Perchloric Acid ($HClO_4$)

The TMDs are semiconducting electro(photo)catalysts and can be oxidized irreversibly at sufficiently anodic potentials in aqueous electrolytes[193, 194]. In order to enable the (EC-) STM measurements on the semiconducting TMDs, a relatively high potential bias was used to generate the tunneling current[195, 196]. Additionally, to prevent the oxidation of the TMDs, the applied potential to the TMD samples was kept in the region where no anodic current can be seen, according to the CV recorded prior to each EC-STM measurement. The HER activity of the $MoS_2$ and the $MoSe_2$ flakes supported on less active (*e.g.*, Au) substrates were investigated. Moreover, point-like defects were generated by the helium ion beam using a HIM instrument in order to activate the inert basal plane of the $MoS_2$ flakes towards the HER.

#### 4.2.4.1 HER on Molybdenum Disulfide ($MoS_2$) Flakes in Perchloric Acid ($HClO_4$)

Figure 81.A shows an STM image of the boundary of a $MoS_2$ flake and the GC substrate. The $MoS_2$ flake had a layered structure with a total thickness of ~15 nm. The high-resolution image in Figure 81.B provides the atomic structure (considering drift) of the $MoS_2$ top surface. Interestingly, the captured patterns at the $MoS_2$ surface seem to be the combinations of several Mo and S atoms (see the inserted atomic configuration in Figure 81.B) instead of single S or Mo atoms. Using this ‘‘atomically-resolved’’ image as a reference, performing similar (EC-) STM measurements can distinguish the TMD flakes from the flat substrates, *e.g.*, Au(111), of which the atomically-resolved STM image was already accomplished.

The rough surface of the GC substrate is not ideal for recognizing noise features caused by the HER. Therefore, single crystalline Au(111) was chosen to be the substrate for the following n-EC-STM investigations. First of all, it is necessary to locate the $MoS_2$ flakes on the Au substrate by taking high-resolution STM images. The imaged structures on the $MoS_2$ flake should be in a good agreement with the image shown in Figure 81.B.

In 0.1 M $HClO_4$, the CV of a sample of $MoS_2$ flakes supported on Au(111) was performed in the EC-STM cell as shown in Figure 82. The potential region where the HER can take place can be seen in the CV. To minimize the HER and avoid the oxidation of the $MoS_2$ for the case of HER ‘off’ in the EC-STM measurements, the sample potentials were chosen to be around (but not significantly more positive than) the actual zero-current point in the CV. Because the EC-STM

cell is exposed to air, there was $O_2$ dissolved in the electrolyte, and the ORR at $MoS_2$ should not be totally ignored. However, for the EC-STM measurements in this thesis, the concentration of dissolved $O_2$ from the air was much lower compared to the one of protons in acidic media, and the ORR is more ''sluggish'' at $MoS_2$. Moreover, the active centers of $MoS_2$ towards both the HER and the ORR are the Mo-edge sites[197]. Therefore, the contribution from the ORR should be considered as a minor factor in the identification of the HER active centers.

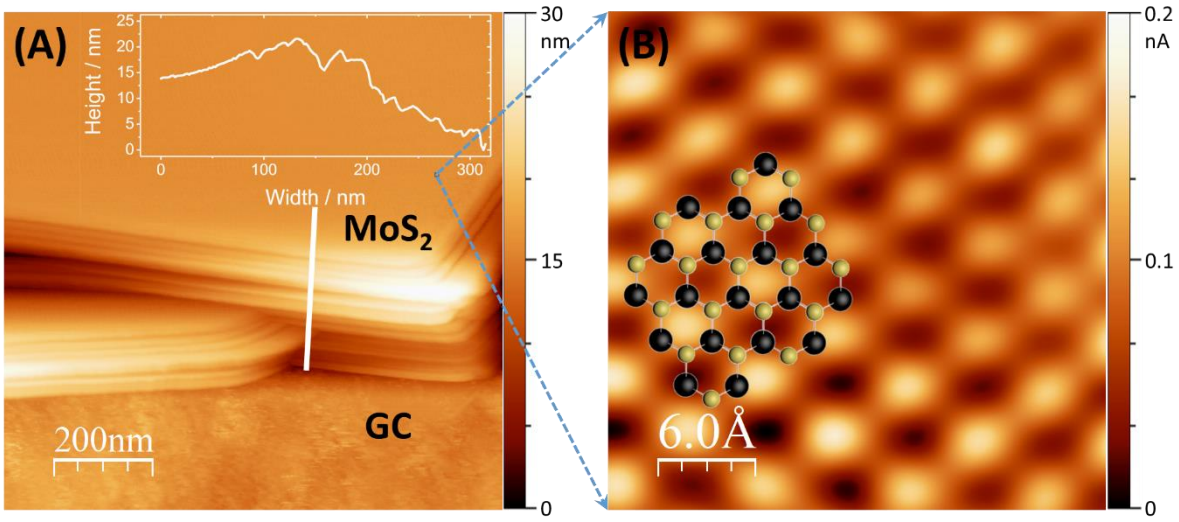


*Figure 81.* ***STM images of a $MoS_2$ flake supported on glassy carbon (GC).*** *(A) Constant current mode STM image with an inserted height profile of the white line scan. Current setpoint: 0.5 nA, potential bias: 1 V, scan rate: 0.5 Hz. (B) Constant height mode STM image on the $MoS_2$ basal plane with an atomic configuration (yellow/black balls represent S/Mo atoms). Current setpoint: 1 nA, potential bias: 1 V, scan rate: 60 Hz.*

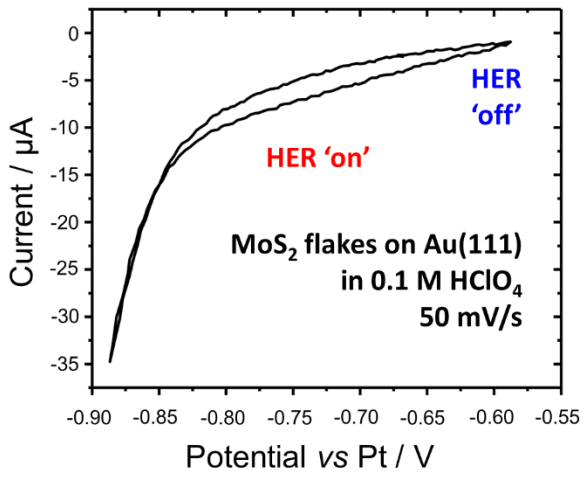


*Figure 82.* ***Typical CV of a sample of $MoS_2$ flakes supported on Au(111) in 0.1 M $HClO_4$ measured in the EC-STM cell at a scan rate: 50 mV/s.***

Once the 0.1 M $HClO_4$ electrolyte was introduced into the EC-STM cell and the potential of the HER 'on', *e.g.*, -900 mV *vs* Pt which is not sufficient to enable the HER on Au, was applied to the sample, the tunneling current noise features appeared on the $MoS_2$ flakes in the captured EC-STM images. These noise features are likely to be correlated with the HER on the $MoS_2$ flakes, and this is also a strategy to locate the $MoS_2$ flakes in the presence of the electrolyte. After ensuring that the observed objects were the $MoS_2$ flakes, the EC-STM measurements were focused on differentiating the activity of various surface structures of the flakes, namely the $MoS_2$/Au boundary, the step-like defects in the $MoS_2$ basal plane and the $MoS_2$ basal plane without defects. While performing EC-STM imaging, the sample potential was gradually changed from -600 mV *vs* Pt, where the HER was minimized (HER 'off'), to -900 mV *vs* Pt (HER 'on'). Two typical results over a $MoS_2$/Au boundary and a step-like defect in the $MoS_2$ basal plane are shown in Figure 83.A and B (3D representations in Figure 84 and Figure 85), respectively.

Figure 83.A exhibits a series of EC-STM images recorded at the boundary of the Au substrate and an ~8 nm thick $MoS_2$ flake with a minor drift. At -600 mV *vs* Pt, no noticeable noise features were observed, and the edge of the flake can be seen clearly. When the HER overpotential was increased stepwise, the noise features started appearing at the Au/ $MoS_2$ boundary (starting with the potential from -650 mV *vs* Pt). Comparing all the EC-STM images in Figure 83.A, the noise level increased and the noise features extended towards the Au side when the HER overpotential was increased. The comparison of the line scans (approximately at the same position for all potentials) represents the growth of the noise features with the increasing of the HER overpotential, as shown in Figure 83.C. The growth of the noise features seems to be correlated with the increase in the HER reaction rate. This result indicates that the active centers for the HER were located on the edge of the $MoS_2$ flakes in 0.1 M $HClO_4$. Figure 84 shows the 3D representations of EC-STM images in Figure 83.A. It can be seen that the noise features covered the edge of the flake completely when sufficient HER overpotentials were applied.

The same trend was observed on a step-like defect in the basal plane of the $MoS_2$, as shown in Figure 83.B. The noise features were generated from the edge of the step and grew with the increase of the HER overpotential. Figure 83.D compares the lines scans taken from all EC-STM images and indicates the same conclusion that the level of noise increased when higher

HER overpotential was applied. However, the noise features only appeared around the edge of the defect. Therefore, the step-like defect seems to be another type of active centers of the $MoS_2$ flake towards the HER in 0.1 M $HClO_4$, confirming the observation in the images. Figure 85 presents the 3D versions of the EC-STM images in Figure 83.B, where the approximate positions of the edge of the defect are marked with blue arrows.

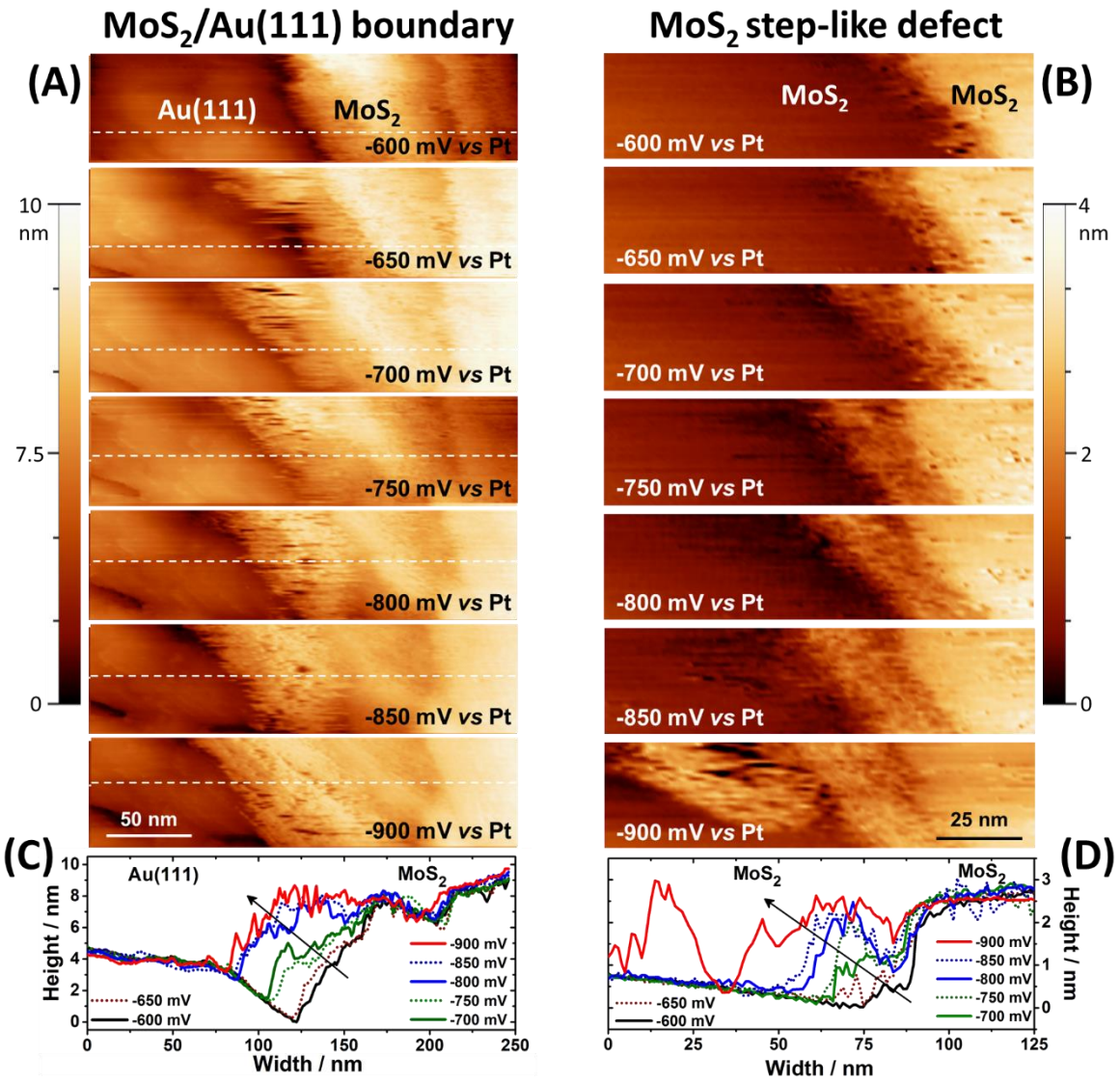


*Figure 83.* ***Two series of constant current mode EC-STM images of a $MoS_2$/Au(111) boundary and a step-like defect in the $MoS_2$ basal plane in 0.1 M $HClO_4$ and selected line scans.*** *(A) EC-STM images of a $MoS_2$/Au(111) boundary when the sample potential was switched from -600 mV (HER 'off') to -900 mV vs Pt stepwise. Current setpoint: 3 nA, tip potential: -200 mV vs Pt, scan rate: 0.5 Hz. (B) EC-STM images of a step-like defect in the basal plane when the sample potential was switched from -600 mV (HER 'off') to -900 mV vs Pt stepwise. Current setpoint: 3 nA, tip potential: -200 mV vs Pt, scan rate: 0.5 Hz. (C) Selected line scans across approximately the same area (white dashed line in every image, drift-effect corrected in y-direction) in (A). (D) Line scans of the top line of each image in (B).*

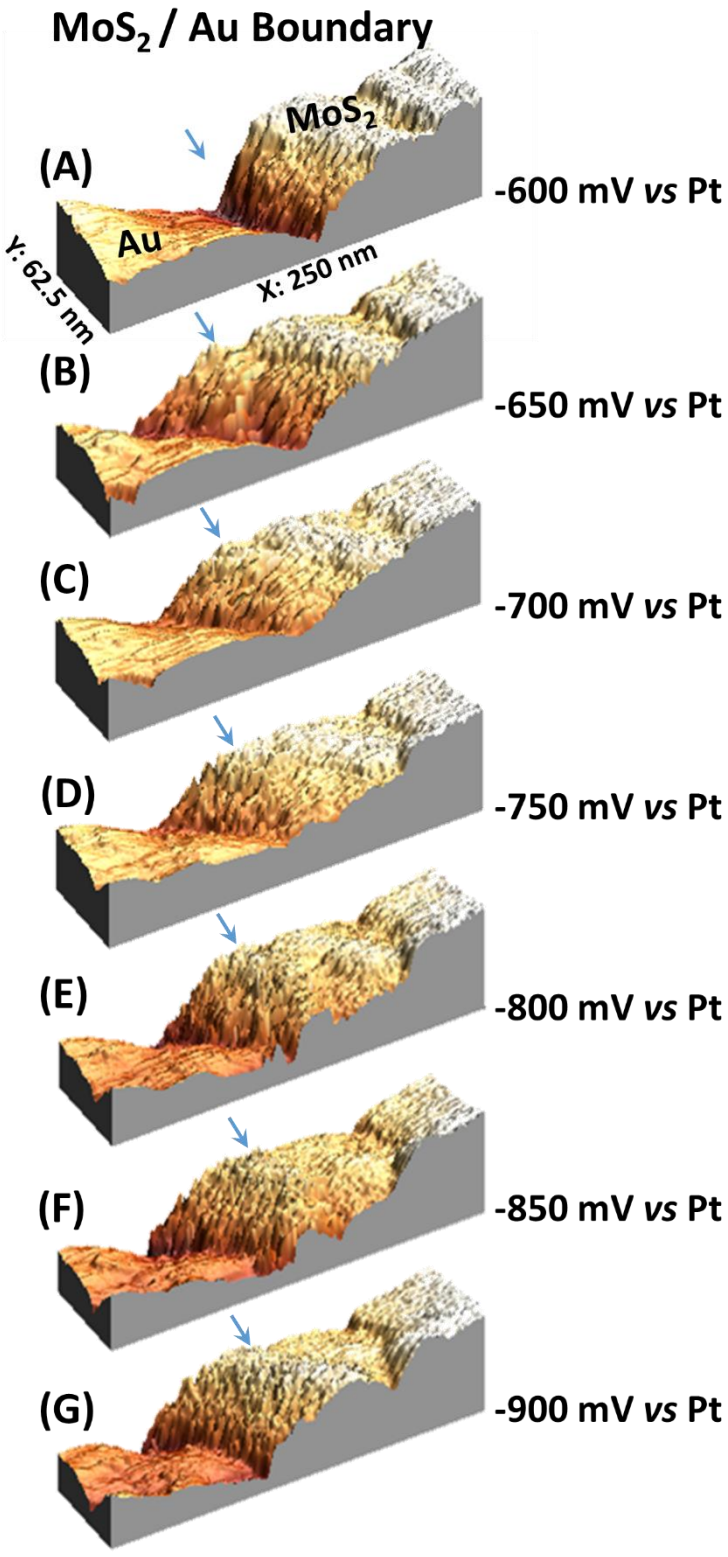


*Figure 84.* ***3D representations of images in Figure 83.A.*** *Blue arrow points out approximately the location of the edge of the $MoS_2$ flake.*

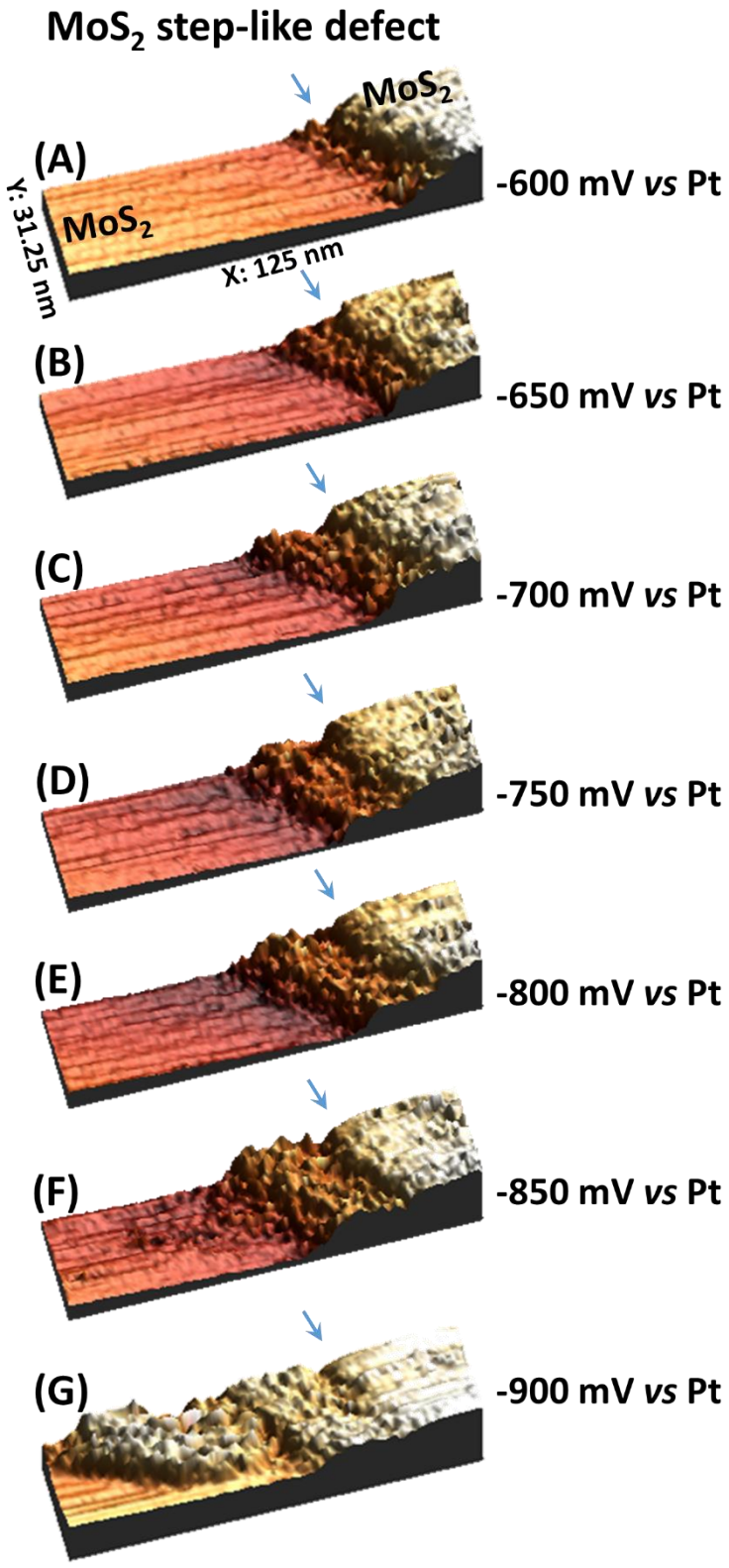


*Figure 85.* ***3D representations of images in Figure 83.B.*** *Blue arrow points out the location of the step edge.*

Another analysis was carried out in order to evaluate the level of noise at different potentials without the influence of the surface topography, as shown in Figure 86. For the line scans in Figure 83.C and D, Figure 86.A and B present the topographic change by subtracting the line scan at -600 mV *vs* Pt (surface topography) from each line scan under HER 'on' conditions, respectively. The resulting height profiles directly reveal the increased reaction rate of the hydrogen evolution on the flake edge and on the step-like defect in the basal plane, with the increasing of the HER overpotential. Particularly, the oxidation of the evolved $H_2$ at the tip (additional Faradaic contribution) should be taken into account.

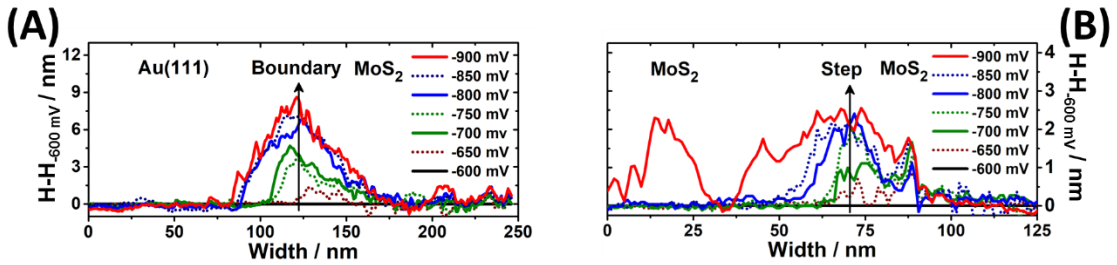


*Figure 86.* ***Height profile of the line scans in Figure 83.C and D with the line scan taken at -600 mV vs Pt subtracted.*** *(A) and (B) Resulting height profiles from Figure 83.C and D after subtracting, respectively. Black arrows indicate the extension direction of noise features.*

It should be noted that there were no noticeable noise features generated on the basal plane of the $MoS_2$ flake at any potential in Figure 83. It seems that the basal plane was not active towards the HER under the measurement conditions. Therefore, the obtained result is one of the first direct evidence of the active centers of the $MoS_2$ flakes supported on Au(111) for the HER in 0.1 M $HClO_4$ being located on the flake edges and the step-like defects in the basal plane. Interestingly, the noise features were mostly generated on the ''edge-plane'' instead of the top sites of the flake edge and the step-like defect, regardless of the sample potential. It has been suggested that the as-prepared basal plane of TMD 2D materials has a lack of sulfur- (S-) vacancies due to the diffusion of S atoms that heals the S-vacancies[198, 199]. Additionally, the H binding energy of the basal plane sites is further away from the optimal value compared to that of the Mo atoms of the flake edge[57]. Considering all the facts mentioned above, the active centers of the $MoS_2$ flakes towards the HER in acidic media are likely the sites where the Mo atoms are coordinatively unsaturated, for instance, the flake edge and the S-vacancies.

### 4.2.4.2 HER on Molybdenum Diselenide ($MoSe_2$) Flakes in Perchloric Acid ($HClO_4$)

The $MoSe_2$ was reported to have higher activity towards the HER compared to the $MoS_2$[200, 201]. However, like in the case of $MoS_2$, there is a lack of direct evidence of the nature (*e.g.*, location, structure) of the active sites on $MoSe_2$ towards the HER. The active centers of the $MoSe_2$ flakes were also studied using the n-EC-STM in 0.1 M $HClO_4$. Prior to each EC-STM measurement, CVs of the $MoSe_2$ flakes on GC and on Au(111) were measured in the electrochemical ($H_2$-saturated) and the EC-STM cells (air-saturated), respectively. As shown in Figure 87.A and B, the CVs confirmed that the $MoSe_2$ flakes have a similar HER activity compared to the $MoS_2$ flakes and the oxidation of the $MoSe_2$ flakes can take place at the potential of ~0.45 V *vs* Pt in the EC-STM cell (in the presence of $O_2$).

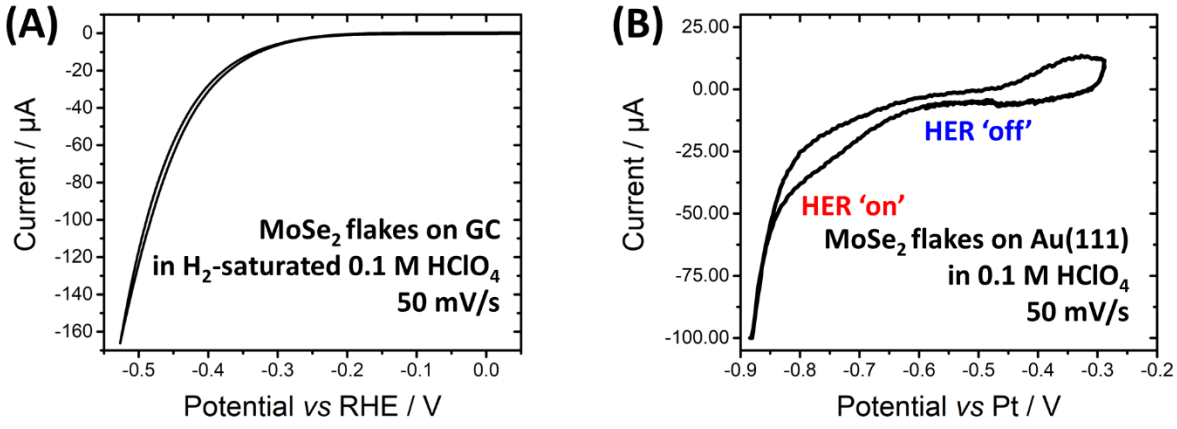


*Figure 87.* ***Typical CVs of the $MoSe_2$ flakes coated GC and Au(111) substrates.*** *(A) CV in $H_2$-saturated 0.1 M $HClO_4$ recorded in an electrochemical cell. (B) CV in air-saturated 0.1 M $HClO_4$ measured in the EC-STM cell. Scan rate: 50 mV/s.*

The STM was employed to measure the morphology of the $MoSe_2$ flakes on GC. Figure 88.A shows an STM image of the boundary of a ~7 nm thick $MoSe_2$ flake and the GC substrate. The basal plane of the flake was flat and had no noticeable defects. A high-resolution image on the basal plane was captured, as shown in Figure 88.B, revealing the ''atomic-structure'' of the basal plane. However, similar to the case of $MoS_2$, each bright spot in Figure 88.B is more correlated with a ''circle'' consisting of three S atoms and three Mo atoms. This was crucial to afterwards locating the $MoSe_2$ flakes on the single crystalline Au(111) surface, which was also atomically flat.

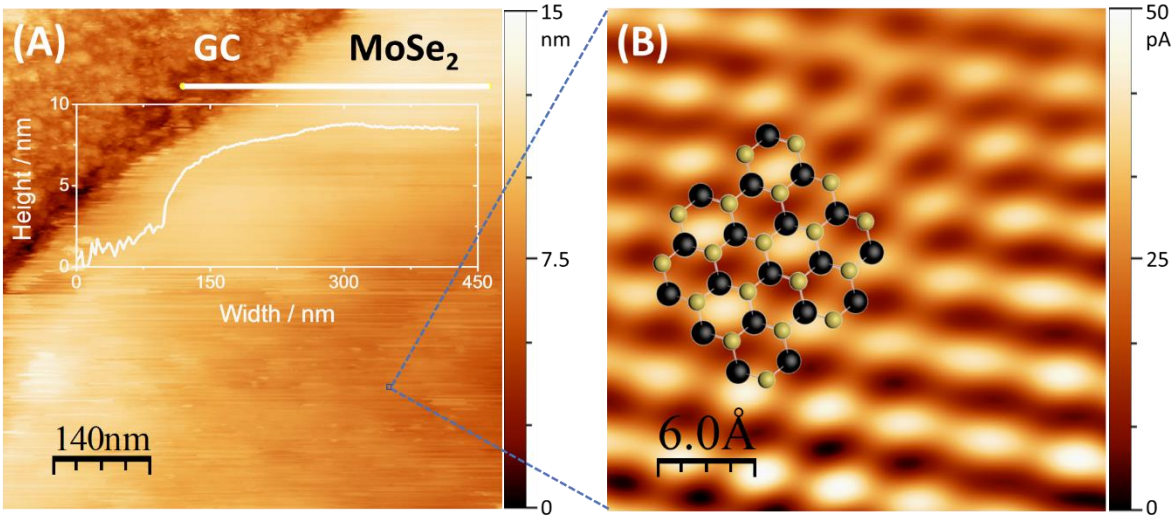


*Figure 88.* ***STM images of a $MoSe_2$ flake on GC.*** *(A) Constant current mode STM image of the boundary of a $MoSe_2$ flake and GC substrate and height profile of the white line across the $MoSe_2$/GC boundary. (B) High-resolution constant height mode STM image captured on the basal plane. The ball model (yellow/black balls represent Se/Mo atoms) is guide to the eyes visualizing the atomic structure.*

The goal of the n-EC-STM was to compare the HER activity of the step-like defects and the basal plane on the $MoSe_2$ in 0.1 M $HClO_4$. Figure 89.A shows a series of EC-STM images across approximately the same position (y-axis scan was disabled), where a larger step-like defect (indicated by black arrow) with three smaller step-like defects (indicated by blue arrows) on the $MoSe_2$ flake can be seen. During the EC-STM measurements, a potential of -500 mV *vs* Pt was first applied to the sample, and the resulting image shows no noticeable noise features on the $MoSe_2$. Afterwards, when the sample potential was changed stepwise to more negative values, noise features started to appear around all the defects. At the same time, the size and the number of those noise features were growing with increasing HER overpotential. The surface of the basal plane, where no defects can be seen, contributed no noise features at any applied potential. Finally, the noise features covered the surface around the defects at a potential of -800 mV *vs* Pt, and the tip retracted completely at a potential of ~-850 mV *vs* Pt.

Figure 89.B compares the height profile of the line scans taken from each image. It can be seen that the level of noise increased with increasing HER overpotential. At higher overpotentials, the noise features are of the order of nanometers, which is probably due to the additional Faradaic contribution (HOR at the tip). According to the n-EC-STM results, the step-like defects of the as-prepared $MoSe_2$ seemed to be more active towards the HER than those of $MoS_2$,

since the noise features appeared at more positive potentials in the case of $MoSe_2$. However, this conclusion requires further investigations, because the n-EC-STM cannot provide a precise quantitative comparison of the noise features obtained from different measurements.

Figure 90 exhibits the 3D representation of the EC-STM images in Figure 89.A with additional labels. The topography of the noise features is better recognizable in the 3D images. When increasing the HER overpotential, more noise ‘‘spikes’’ with larger sizes appeared around the defects. The surface far away from those defects remained flat regardless of the applied potential. As the noise features can be both on the larger and smaller step-like defects, it is likely that all step-like structures (defects or over/under-coordinated sites) are the active centers for the HER on $MoSe_2$.

Comparing the noise features that appeared on the $MoS_2$ and those on the $MoSe_2$ samples at sufficient potentials, there are several differences that should be noted. The bubble-like noise features in the case of $MoS_2$ were generated on the ‘‘edge-plane’’ of the flake edge and the defects, however in the case of $MoSe_2$, the spike-like noise features were found on the top of the step-like defects. The reason for such a difference in the noise features on different TMD catalysts is still unknown. Probably, this is due to the difference in the HER mechanisms on the $MoS_2$ and $MoSe_2$, or difference in the H binding energy of the active sites on the $MoS_2$ and the $MoSe_2$. Additionally, the H binding energy of the S, Se and Mo atoms likely influence the shape and the distribution of the noise features, for instance, the bubble-like noise in the case of $MoS_2$ was possibly due to the so-called hydrogen spill-over effect[202, 203], which was not observed on the $MoSe_2$.

The results demonstrate that the active centers of the TMD 2D flakes towards the HER are only the flake edges and the step-like defects in the aqueous electrolyte of 0.1 M $HClO_4$. This conclusion is expected to positively influence the development, the rational design and particularly the commercialization of the TMD-based catalysts.

So far, the n-EC-STM have for the first time revealed the active centers towards the HER on $MoS_2$ and $MoSe_2$ 2D flakes. The n-EC-STM is able to identify the active centers of metallic catalysts but also non-metallic (semi-) conducting materials, for instance, the TMDs. It can distinguish the activity difference of nanometer-scale structures and provide a reliable assessment of newly-developed catalyst materials.

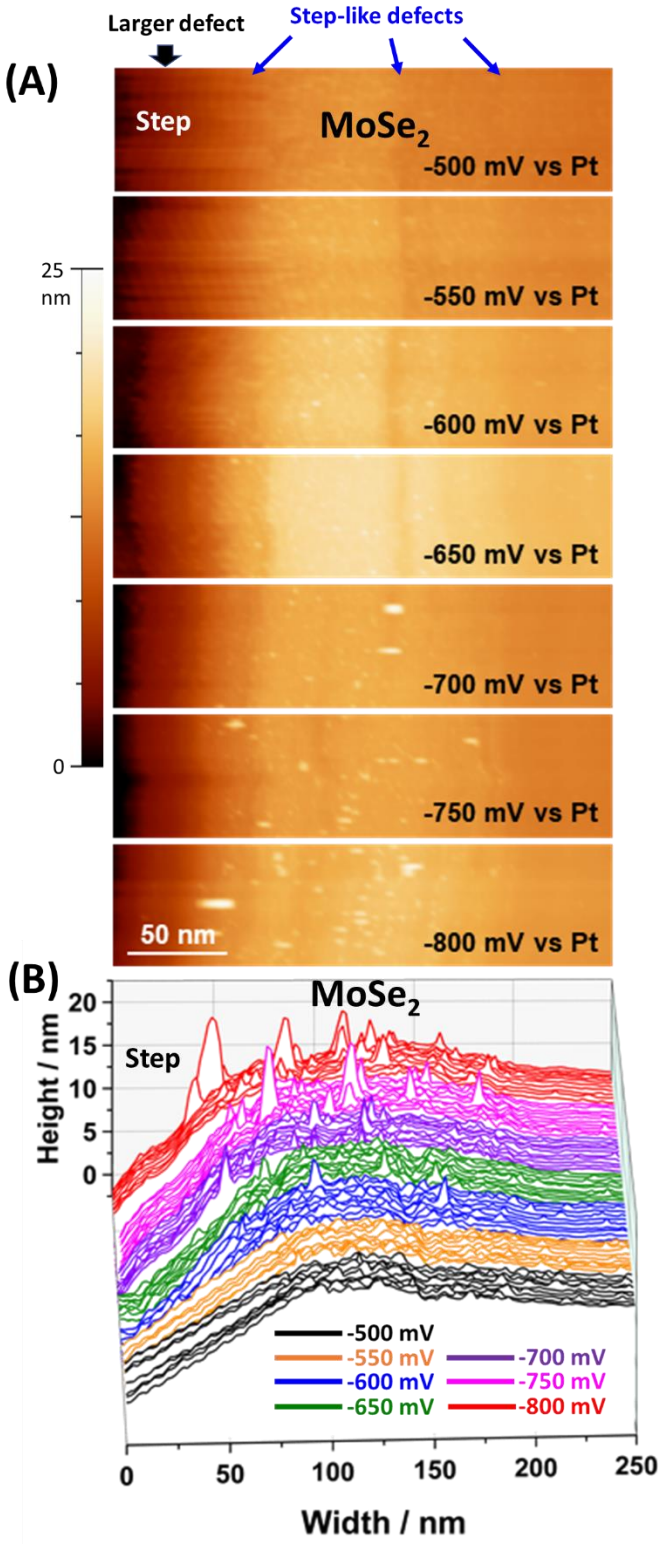


*Figure 89. (A) Successively recorded constant current mode EC-STM images in 0.1 M $HClO_4$ from the potential of -500 mV (HER 'off') to -800 mV vs Pt. Y-axis scan was disabled (minor drift). Approximately, the tip was scanning across the same line across a large step-like defect in the $MoSe_2$ basal plane. The black arrow shows the edge of the large defect. The blue arrows indicate the location of smaller step-like defects. Current setpoint: 2.0 nA, tip potential: -50 mV vs Pt, scan rate: 0.5 Hz. (B) Comparison of the line scans taken from each image.*

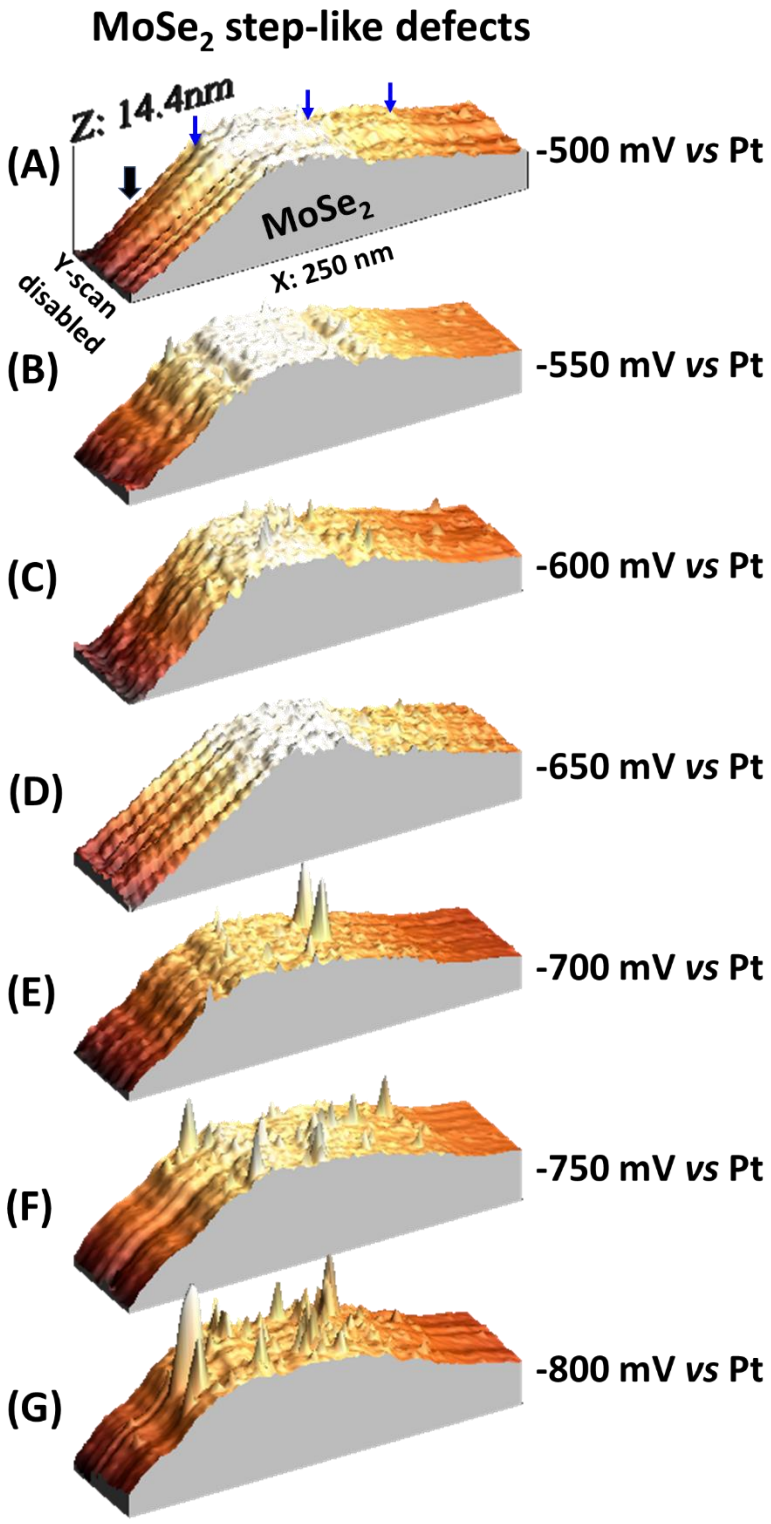


*Figure 90.* ***3D representation of the EC-STM images in Figure 89.A.*** *The black arrow shows the location of a larger step-like defect and the blue arrows indicate the location of three smaller step-like defects.*

### 4.2.4.3 Activating the Basal Plane of the $MoS_2$ Flakes Using Helium Beam

The results shown in Chapter 4.2.4.1 and Chapter 4.2.4.2 suggest that the defective sites of the $MoS_2$ and $MoSe_2$ are likely the active sites towards the HER in 0.1 M $HClO_4$. It is already reported that, in the case of $MoS_2$, the H binding energy of the basal plane sites is far from the optimum compared to that of the Mo atoms located on the flake edge[57]. One strategy to promote the electrocatalytic activity of the $MoSe_2$ and $MoS_2$ flakes is to create more defects in the inert basal plane. As reported, creating S-vacancies in the basal plane can be a successful strategy of activating the basal plane of the $MoS_2$ flakes towards the HER[57]. However, this has not been proved by means of direct instrumental investigations.

Fortunately, helium ion microscopy (HIM) provides a way of introducing evenly distributed point-like defects into the $MoS_2$ surfaces. Two types of samples, namely $MoS_2$ flakes on GC and on Au(111), were prepared to evaluate the influence of the HIM treatment on the HER activity of the $MoS_2$ flakes. Figure 91.A and B compare the HER activity of the $MoS_2$ flakes before and after the HIM treatment. All activity measurements were performed in $H_2$-saturated 0.1 M $HClO_4$, and the RDE was employed in the case of Au(111) substrate.

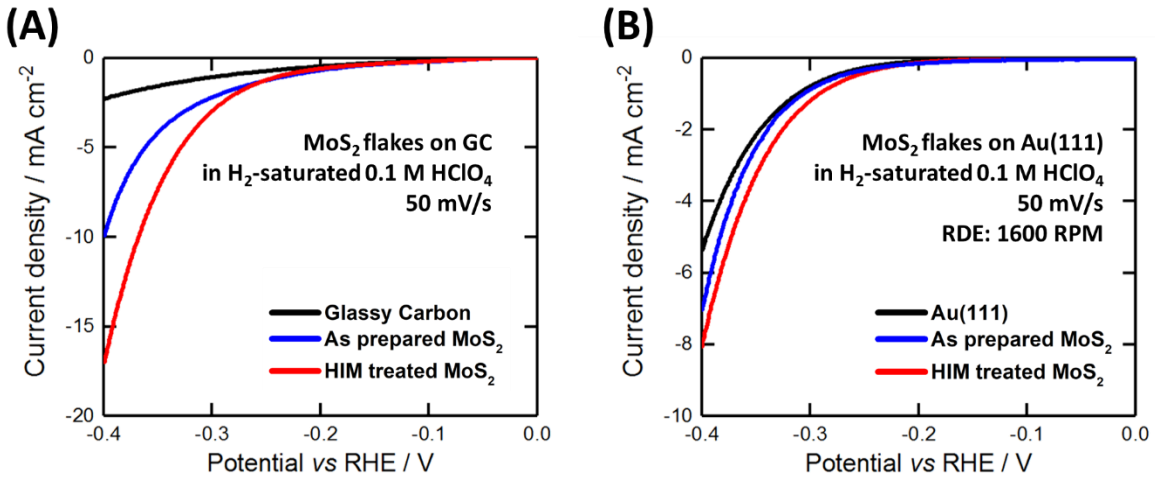


*Figure 91.* ***HER activity measurements for the $MoS_2$ flakes deposited on GC and Au(111) substrates in $H_2$-saturated 0.1 M $HClO_4$ in the electrochemistry cell before and after the helium ion beam treatment.*** *(A) The HER polarization curves (cathodic scans) of bare GC substrate, with $MoS_2$ flakes and after helium ion beam treatment. (B) The RDE HER polarization curves (cathodic scans) of a bare Au(111) substrate, with $MoS_2$ flakes and after helium ion beam treatment at 1600 revolutions per minute (RPM). All curves were measured at a scan rate of 50 mV/s. All current densities were normalized to the whole electrode surface area.*

As can be seen in Figure 91, the HIM treatment successfully improved the HER activity of the $MoS_2$ flakes, regardless of the substrate. It should be noted that, for each GC and Au substrate, the influence of the HIM treatment on the HIM activity of the bare substrate was calibrated, by performing HER activity measurement before and after HIM treatment. As expected, the HIM treatment was not able to activate the HER activity of the bare substrates. As reported, the HER activity of Au electrodes is significantly influenced by the surface structure[41] and a tiny amount of active contamination, *e.g.*, Pt, from the CE. However, the point-like defects created on the bare Au(111) sample by the HIM did not appear to increase the overall activity.

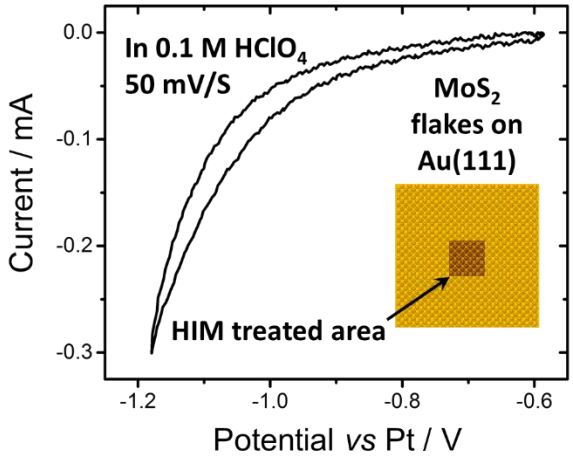


*Figure 92.* ***CV of the $MoS_2$ on Au(111) sample after HIM treatment in air-saturated 0.1 M $HClO_4$ obtained in the EC-STM cell.*** *Scan rate: 50 mV/s. Inserted graph illustrates the HIM treated area compared to the whole sample surface.*

As reported[57], the point-like defects (S-vacancies) generate active sites towards the HER on the basal plane. Therefore, the n-EC-STM was used to identify the HER active centers of HIM treated samples, and Au(111) was selected to be the substrate for EC-STM measurements.

Due to technical difficulties (*e.g.*, setup limitation and complicated software control) and the time-consuming characteristic of the HIM treatment, only a ~4 $mm^2$ surface in the center of each $MoS_2$ on Au(111) sample was treated by the helium ion beam, as shown in Figure 92. Prior to each set of EC-STM measurements, a CV of the sample was measured in the EC-STM cell. Figure 92 shows a CV obtained at a scan rate of 50 mV/s, and the HER can be minimized at around -0.6 V *vs* Pt.

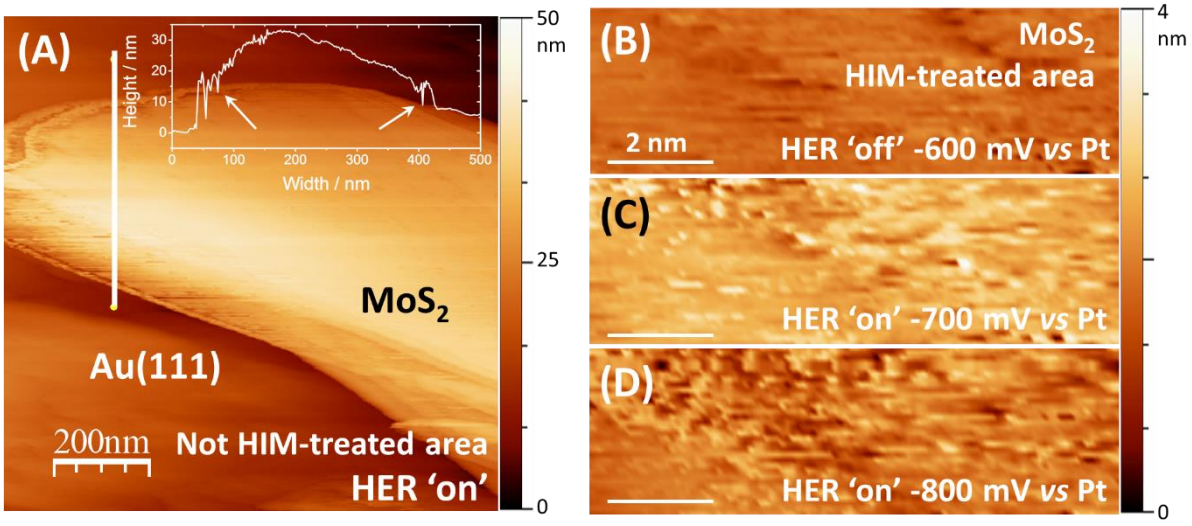


*Figure 93.* ***Comparison of the HER activity of HIM treated and not HIM treated $MoS_2$ flakes.*** *(A) Constant current mode EC-STM image of a not HIM-treated $MoS_2$ flake. Height profile of the position marked by the white line is inserted. White arrows indicate the location of the flake edges in the height profile. (B-D) Successive images of approximately the same area in the basal plane of one HIM-treated $MoS_2$ flake at different HER overpotentials, (B) -600 mV vs Pt (HER 'off'), (C) -700 mV vs Pt (HER 'on') and (D) -800 mV vs Pt (HER 'on'), respectively.*

To assess the activity improvement in the basal plane caused by the helium ion beam, EC-STM measurements were conducted for both the treated and untreated flakes in 0.1 M $HClO_4$. Figure 93.A shows an EC-STM image over a non-HIM-treated $MoS_2$ flake under the HER 'on' condition. The noise features can be seen only on the edge of the flake and on some defects in the basal plane, which is in agreement with the findings in Chapter 4.2.4.1.

On the surface of a HIM-treated $MoS_2$ flake, three EC-STM images were measured over approximately the same location at different sample potentials. As a comparison to the HER 'on' images, an EC-STM image (Figure 93.B) was captured under the condition of HER 'off', in which no noise features are visible. As shown in Figure 93.C and D, when the HER was enabled (HER 'on'), the noise features covered the whole scanned area. In each individual image, the level of noise is almost the same all over the image. Moreover, the difference of the noise level in different images can be seen in the derivative frequency analysis shown in Figure 94, in which the image recorded at -800 mV *vs* Pt shows the highest noise level. It seems that the evenly distributed point-like defects activated the basal plane of the $MoS_2$ flake towards the HER, and the activity of the HIM treated basal plane increased with the increasing of the HER overpotential.

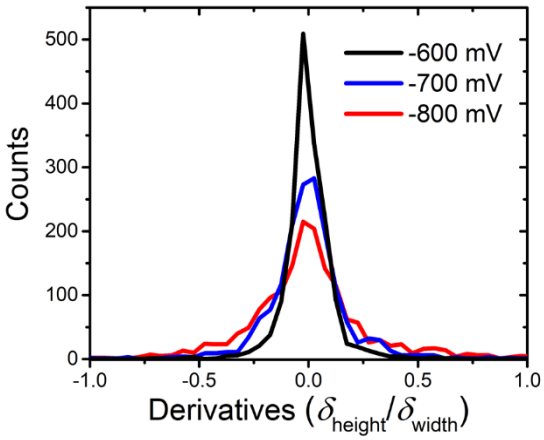


*Figure 94.* ***Derivative frequency analysis of the noise level for the EC-STM images in Figure 93.B (HER 'off', -600 mV vs Pt), C (HER 'on', -700 mV vs Pt) and D (HER 'on', -800 mV vs Pt).***

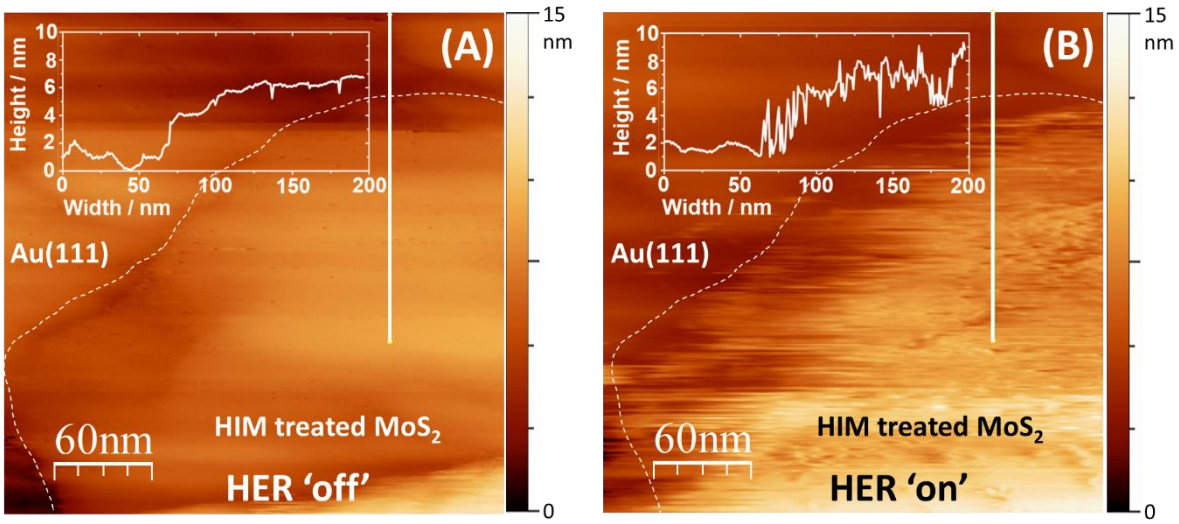


*Figure 95.* ***Constant current mode EC-STM measurements of a boundary of a HIM treated $MoS_2$ flake and the Au(111) substrate in 0.1 M $HClO_4$.*** *(A) EC-STM image of a $MoS_2$/Au(111) boundary at a potential of -600 mV vs Pt (HER 'off'). (B) EC-STM image of approximately the same area at a potential of -800 mV vs Pt (HER 'on'). Height profile of the line scan (white line) across roughly the same position is inserted in each image. Current setpoint: 1 nA, tip potential: -100 mV vs Pt, scan rate: 1 Hz.*

To compare the activity of the edge and the activated basal plane of the $MoS_2$ flake, EC-STM images over a HIM-treated-$MoS_2$/Au(111) boundary were taken at the potential of the HER 'off' and 'on', as shown in Figure 95.A and B, respectively. When there was no hydrogen evolving, the morphology of a ~6 nm thick $MoS_2$ flake without noticeable noise features can be seen in the image shown in Figure 95.A. Figure 95.B shows an EC-STM image of the same

area obtained while the HER was enabled. Interestingly, the level of noise is roughly the same all over the $MoS_2$ flake including the $MoS_2$/Au boundary under the HER 'on' condition (-800 mV *vs* Pt). The noise level in the basal plane is lower compared to that on the edge of the flake. However, considering the fact that, in the flake edge plane, the exposed Mo-edges of all $MoS_2$ single layers contain coordinatively unsaturated Mo sites, the density of active sites at the edge of the flakes are likely higher than that (*i.e.*, point-like defects) in the basal plane. Additionally, each noise feature was responsible for all active sites of a certain surface area not a single active site due to the resolution of the image in this particular case. Therefore, in this case, the difference in noise level between the edge and the basal plane is not directly related to the activity difference of single active sites, *i.e.*, the Mo-edge atom *vs* the S-vacancy. This result does not contradict the findings in literature[57].

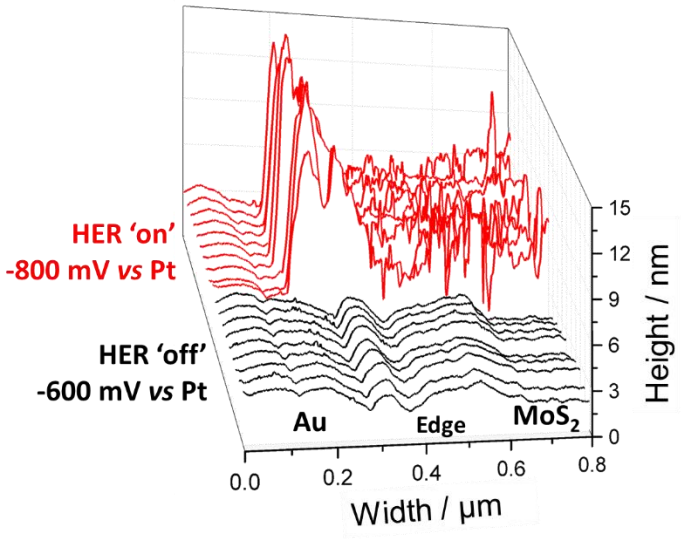


*Figure 96.* ***Line scans taken from a series of constant current mode EC-STM images of a boundary of a HIM treated $MoS_2$ flake and the Au(111) substrate in 0.1 M $HClO_4$.*** *The EC-STM images were captured over approximately the same area at the $MoS_2$/Au(111) boundary at -600 mV vs Pt (HER 'off'), -700 mV vs Pt (HER 'on') and -800 mV vs Pt (HER 'on'), respectively. Current setpoint: 0.5 nA, tip potential: -100 mV vs Pt, scan rate: 0.5 Hz. The red arrow indicates the location of the $MoS_2$/Au boundary.*

More EC-STM measurements were performed in order to further evaluate the influence of the HIM treatment on the HER activity of the basal plane. A series of EC-STM images were recorded at the boundary of a HIM treated $MoS_2$ flake and the Au(111) substrate at different potentials. Figure 96 shows the line scans taken from the images captured at -600 mV *vs* Pt (HER 'off') and -800 mV *vs* Pt (HER 'on'), respectively. When no hydrogen evolution was taking

place at the sample surface, no obvious noise features can be observed on both the Au and $MoS_2$. When applying higher HER overpotentials to the sample, the features appeared exclusively on the $MoS_2$, as shown in Figure 96.

At first glance, the $MoS_2$ flake is more active than the Au substrate towards the HER. At -800 mV *vs* Pt, the $MoS_2$ side was totally covered by the noise features. Additionally, large bubble-like noise features appeared on the edge of the $MoS_2$ flake and extended towards the Au side, which is similar to the findings on non-HIM-treated $MoS_2$ flakes under the HER 'on' condition.

The result indicates that, at sufficiently negative potentials, for instance, -800 mV *vs* Pt, more hydrogen can be generated from the edge of the flake, likely due to the higher density of active sites on the ''edge-plane'' (considering the layered structure of multilayer $MoS_2$ flakes and the relatively lower density of the point-like defects on the basal plane).

In summary, the point-like defects introduced using the helium ion beam of the HIM instrument can activate the inert basal planes of the $MoS_2$ flakes towards the HER in 0.1 M $HClO_4$. This attempt gives rise to a rational approach of tailoring the electrocatalytic activity of TMD-based catalysts by introducing well-controlled defects at the surface of the catalysts.

### 4.2.5 HER on Pt Nanoparticles/Au(111) in Perchloric Acid ($HClO_4$) – Chemical Sensitivity

In the previous studies, the deposited sub-monolayer Pd or Pt islands can be distinguished from the Au substrate by performing STM measurement with relative ease, for instance, the STM image shown in Figure 58. However, in many other cases this is not straightforward. For example, mapping metal nanoparticles deposited on a flat substrate is relatively challenging for (EC-) STM, because the tip can easily push away or pick up the particles, especially in the case of only van der Waals forces existing between the nanoparticles and the substrate. Moreover, if the deposited material and the substrate exhibit roughly the same surface structures (or surface roughness), it will be difficult to locate the deposited material in the resulting (EC-) STM images.

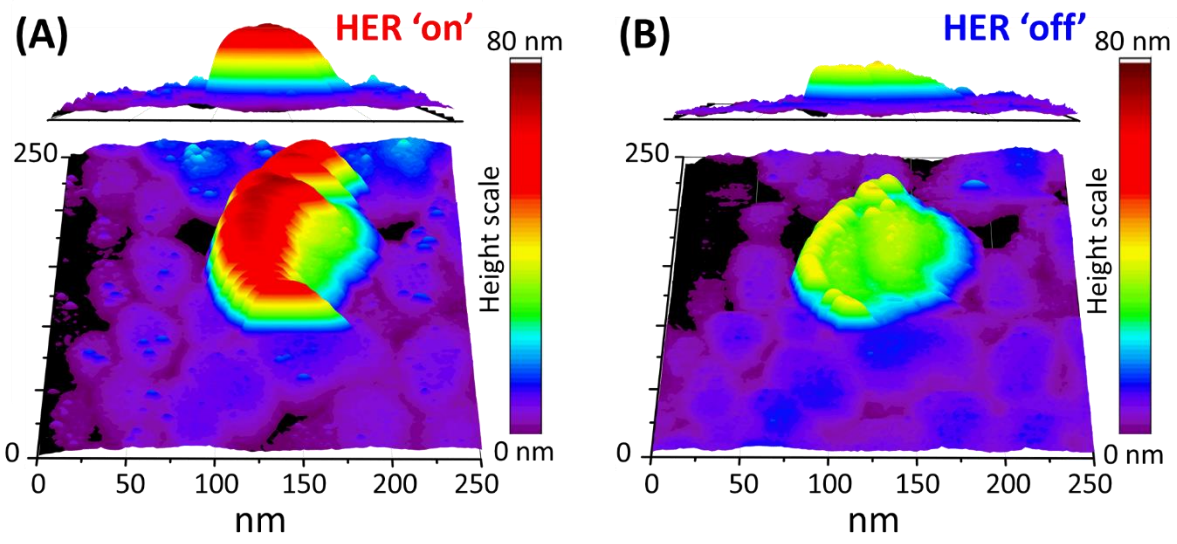


*Figure 97.* ***Continuously recorded constant current mode EC-STM images of a Pt nanoparticle-cluster on top of a protruding structure of the Au substrate in 0.1 M $HClO_4$.*** *(A) WE: −250 mV vs quasi-SSC (HER 'on'); tip potential: −150 mV vs quasi-SSC. (B) The potentials were shifted to 400 mV (tip) and 300 mV (WE) vs quasi-SSC (HER 'off'). The current setpoint was 1 nA for both images.*

The n-EC-STM has been used to investigate a catalytic system involving metal nanoparticles, namely the HER at Pt nanoparticles deposited on a Au substrate in 0.1 M $HClO_4$. The EC-STM image shown in Figure 97.A was taken over a protruding part on the sample when the applied potential was negative enough to enable the HER on Pt (not on Au). Figure 97.B shows another EC-STM image obtained over approximately the same area when the HER did not occur. Before comparing these two images, it was not clear whether the protruding part in the middle of each image consisted of a deposited Pt nanoparticle or just a large structure of the Au substrate. However, comparing the two EC-STM images, the apparent height of the protruding part dropped from the case of the HER 'on' to the case of the HER 'off', while no noticeable change can be seen elsewhere. This indicates that the protruding part was more active than the area around it. Under the HER 'on' condition, the HER was only taking place on the Pt nanoparticles and resulted in noise in the tunneling current. Additionally, the $H_2$ can be oxidized at the Pt/Ir tip, and consequently the resulting HOR contributed extra tip current which forced the tip to retract from the sample surface. Therefore, the protruding part was probably a Pt nanoparticle, or a cluster of nanoparticles. Interestingly, the tip did not push the nanoparticle(s) away during the EC-STM measurement, likely due to the tip retraction over the nanoparticle(s). The result shows that the n-EC-STM can be used to identify the active

metal nanoparticles located on an inert substrate under reaction conditions. Using Faradaic current (HOR at the tip) in the activity measurement of a nanoparticle is similar to the approach using EC-STM introduced by Meier *et al.*[37] where the tip is positioned around 10 nm away from the active nanoparticle.

The experimental procedure and the result also yield a method of direct instrumental identification of local surface chemical compositions (chemical sensitivity) with different activities or reactivity, particularly when the involved species can react at the tip evidently. This idea is not totally novel as it is long-established in the research field of scanning electrochemical microscopy (SECM). The sample-generation/tip-consumption (SG/TC) mode of SECM utilizes the same configuration[180]. However, compared to normal SECM setups, EC-STM can obtain a much higher resolution into the sub-nanometer scale. Compared to the above-mentioned EC-STM approach where the EC-STM tip was positioned over the interesting object (by about 10 nm)[37, 38], in this work, the topographic mapping and activity (reactivity) detection are performed simultaneously as the tip scans the sample surface laterally in normal constant current mode EC-STM.

# 5 Summary and Outlook

## 5.1 Summary

In this thesis, a novel instrumental method of *in-situ* identification of active sites in heterogeneous catalytic system is introduced and examined. The method has been proved here to be capable of distinguishing catalytically active centers with a nanometer-scale resolution for energy provision related catalytic systems, *e.g.*, hydrogen evolution and oxygen reduction reactions on metallic and non-metallic catalysts. The concept of the proposed method, the n-EC-STM, is that the intermediate steps of heterogeneous catalysis processes, *e.g.*, mass transfer processes, charge transfer processes, intermediates adsorption/desorption and disturbance in the double layer, vary the effective tunneling barrier and introduce fluctuations in the recorded tunneling current at the EC-STM tip under reaction conditions. The resulting fluctuations depend on the reaction conditions, the local activity and experimental parameters. A Faradaic contribution is inevitable in several cases but rather helpful for the identification of active sites.

In detail, catalytic systems, for which the location of active sites is commonly known, were used to prove the proposed concept. Afterwards, the method has been applied to several systems, where the active sites were unknown or not directly observed.

To assess the proposed n-EC-STM methodology, metallic catalysts including single crystalline Pt(111), Au(111) and Pt/Pd deposits were utilized. The n-EC-STM provided results that confirm knowledge from the available literature. In acidic media, the active sites of single crystalline Pt(111) are the step-concavities (Pt atoms at the bottom of step edges) for both HER and ORR. In sulfuric acid solution, Pd atoms located on the boundary between Pd islands and the substrate Au(111) are the most active for HER. The noise features are directly caused by local disturbance of the tunneling barrier introduced by catalytic reactions and can be eliminated by turning off the reactions. The “atomic-resolution” is necessary to have a clear view of the surface structure but not highly essential to locate the active sites at sub-nanometer scales.

For ORR and HER on Pt(111) in alkaline media, the step-like defects are not active compared to the (111) terraces. The findings suggest an influence of alkaline media on the activity of the Pt surface atoms. One hypothesis is that the presence of alkali metal cations excessively

weakens the binding energy of oxygen and hydrogen species on Pt at the concavity sites. Therefore, the concavity sites that are geometrically optimal in acidic media become less active.

In aqueous solution of perchloric acid, surface sites on Pt islands with an Au(111) substrate have similar activity towards the HER, *i.e.*, the Pt atoms at the boundary to the Au substrate are not more active. The actual mechanism and explanation in detail require further investigations.

Non-metallic transition metal dichalcogenides (TMDs), namely molybdenum disulfide and molybdenum diselenide were studied in acidic media for their applications as hydrogen evolution electrocatalysts. Edges of the TMD flakes and step-like defects are more active than the flat basal planes. Point-like defects generated by HIM treatment can activate the basal planes. To sum up, coordinatively unsaturated Mo surface sites are expected to be the active sites towards the HER.

Taken together, n-EC-STM measurements have succeeded in providing some of the first evidence about the location and different activity levels of active centers of heterogeneous electro-catalytic systems, with nanometer or even sub-nanometer resolution. The actual resolution depends on the studied systems. The results can confirm hypotheses based on reported theoretical and macroscopic observations. Moreover, n-EC-STM measurements can readily obtain the activity distribution on newly-developed catalysis systems and point out the direction of further investigations.

The capability of the n-EC-STM is limited by instrumental factors and the preparation of model samples. For instance, the tip material is a Pt/Ir alloy which is acceptable for conventional (EC-) STM measurements. However, reactive substances, *e.g.*, $H_2$ and $O_2$, can react at the tip and contribute a Faradaic current to the overall tip current. This Faradaic contribution at the tip enhances the noise level over active centers but probably decreases the resolution the n-EC-STM measurement due to the diffusion of these reactive substances. Inert materials and better insulation methods should be considered during the tip fabrication. At the same time, the sharpness of the prepared tip needs to be maintained.

Ideally, the n-EC-STM method can be used for all electronically conducting surfaces used in heterogeneous catalytic systems. However, only carefully designed model samples provide

the response which can be interpreted with relative ease. Only geometrically flat surfaces with nanometer-scale changes can be scanned by normal STM without crashing the tip. Surfaces with visible geometric or chemical composition differences are suitable for n-EC-STM analysis. Additionally, the resulting noise features contain less quantitative information compared to macroscopic electrochemical observations, for instance, activity measurements resulting from different studies can be roughly compared if the experimental environments were comparable.

With all the mentioned limitations, the proposed n-EC-STM method is still able to bring a considerable impact for the fundamental understanding and the rational design of heterogeneous catalytic systems. It requires normal EC-STM devices and acceptable amount of effort on the strategy of experimental procedures. The method, being combined with other research techniques, can provide reliable information of active centers and properly answer related questions.

## 5.2 Outlook

There are several open questions in this thesis including activity behaviors of Pd/Pt islands coated Au(111) in different acidic media, possible differences in the effect of different alkali metal cations, activity distribution on Pt(111) for HER in other alkaline media, and the actual geometry of the HIM introduced point-like defects. In general, the electrolyte components, which are normally ignored in heterogeneous catalysis studies, should be considered carefully. These questions should be addressed in the further investigations.

The n-EC-STM methodology is expected to inspire some attempts using other scanning microscopy instruments. Fluctuations caused by reactions in the recorded tunneling current can bring useful information. Similar strategies can be developed in other techniques, for instance, SECM, (EC-) AFM and SECPM, by which non-conductive objects can be studied. The interactions used in these techniques are Faradaic reactions, mechanical forces, van der Waals forces, potential differences in the overlapped double layers and so on. Connections between these interactions and the investigated objects will be the key to developing new identification methods. One example is a recently reported potential-sensing EC-AFM analysis for water-splitting reactions[204].

# Appendix

## Appendix A: Symbols and Abbreviations

| | |
|---|---|
| $\phi_{eff}$ | Effective Tunneling Barrier |
| $a$ | Chemical Activity |
| $A$ | Electrode Surface Area |
| **Å** | Angstrom |
| **Ag** | Silver |
| **Ar** | Argon |
| **Au** | Gold |
| $C$ | Concentration |
| **CE** | Counter Electrode |
| **Cl** | Chlorine |
| **Cs** | Cesium |
| **CsOH** | Cesium Hydroxide |
| **Cu** | Copper |
| **CV** | Cyclic Voltammetry or Cyclic Voltammogram |
| **DFT** | Density Functional Theory |
| **E** | Potential |
| $e$ | Electron |
| $E^0$ | Standard Electrode Potential |
| **EC** | Electrochemical |
| **EC-STM** | Electrochemical Scanning Tunneling Microscopy |
| **EDL** | Electrical (or Electric) Double Layer |
| $E_{eq}$ | Equilibrium Potential |
| **EQCM** | Electrochemical Quartz Crystal Microbalance |
| **FePc** | Iron-phthalocyanine |
| $G$ | Gibbs Free Energy |
| **GC** | Glassy Carbon |
| **GrC** | Graphic Carbon |
| $h$ | Planck's Constant |
| $H_2SO_4$ | Sulfuric Acid |
| $HClO_4$ | Perchloric Acid |
| **HER** | Hydrogen Evolution Reaction |
| **Hg** | Mercury |
| **HIM** | Helium Ion Microscopy |
| **HOPG** | Highly Oriented Pyrolytic Graphite |
| **HOR** | Hydrogen Oxidation Reaction |
| $I$ | Current |
| **Ir** | Iridium |
| $K$ | Reaction Rate |
| **K** | Potassium |
| $k^0$ | Standard Rate Constant |
| $k_b$ | Boltzmann Constant |

| | |
|---|---|
| **KOH** | Potassium Hydroxide |
| **Li** | Lithium |
| **LiOH** | Lithium Hydroxide |
| **MMS** | $Hg/HgSO_4$ Electrode in $K_2SO_4$ Saturated Aqueous Solution |
| **Mo** | Molybdenum |
| **MVM** | Metal-Vacuum-Metal |
| **N** | Nitrogen |
| $\eta$ | Overpotential |
| **OER** | Oxygen Evolution Reaction |
| **OH** | Hydroxide |
| **ORR** | Oxygen Reduction Reaction |
| ***Ox*** | Oxidized Species |
| **Pd** | Palladium |
| **Pt** | Platinum |
| ***R*** | Gas Constant |
| **RDE** | Rotating Disc Electrode |
| **RE** | Reference Electrode |
| ***Red*** | Reduced Species |
| **Rh** | Rhodium |
| **RHE** | Reversible Hydrogen Electrode |
| **S** | Sulfur |
| **Se** | Selenium |
| **SECM** | Scanning Electrochemical Microscopy |
| **SECPM** | Scanning Electrochemical Potential Microscopy |
| **SEM** | Scanning Electron Microscopy |
| **SG/TC** | Sample-Generation/Tip-Consumption |
| **SHE** | Standard Hydrogen Electrode |
| **SPM** | Scanning Probe Microscopy |
| **SSC** | Ag/AgCl Electrode in KCl Saturated Aqueous Solution (SSC) |
| **STM** | Scanning Tunneling Microscopy |
| ***T*** | Temperature |
| **t** | Time |
| **TMD** | Transition Metal Dichalcogenide |
| **UPD** | Underpotential Deposition |
| **V** | Vanadium |
| **WE** | Working Electrode |
| **XPS** | X-Ray Photoelectron Spectroscopy |
| $\varepsilon$ | Variable of Energy |
| $m$ | Mass |
| $\phi$ | Work Function |
| $\rho$ | Density of States |

# Appendix B: Publications, Conference Contributions and Stipend

**Publications:**

1. Garlyyev, B., Liang, Y., Butt, F. K., & Bandarenka, A. S. (2017). Engineering of highly active silver nanoparticles for oxygen electroreduction via simultaneous control over their shape and size. *Advanced Sustainable Systems*, 1(12) 1700117.
2. Pfisterer, J. H. K.,(1) Liang, Y.,(1) Schneider, O., & Bandarenka, A. S. (2017). Direct instrumental identification of catalytically active surface sites. *Nature*, *549* (7670), 74-77.
3. Yun, J., Schiegg, F., Liang, Y., Scieszka, D., Garlyyev, B., Kwiatkowski, A., Wagner, T. & Bandarenka, A. S. (2018). Electrochemically formed $Na_xMn[Mn(CN)_6]$ thin film anodes demonstrate sodium intercalation and de-intercalation at extremely negative electrode potentials in aqueous media. *ACS Applied Energy Materials*, 1, 123–128
4. Pfisterer, J. H K., Liang, Y., Schneider, O., & Bandarenka, A. S. (2018). Katalytisch Aktive Zentren Direkt Abgebildet. *Physik in unserer Zeit*, 49(1), 6-7.
5. Garlyyev, B., Pohl, M. D., Čolić, V., Liang, Y., Butt, F. K., Holleitner, A., & Bandarenka, A. S. (2018). High oxygen reduction reaction activity of $Pt_5Pr$ electrodes in acidic media. *Electrochemistry Communications*, 88, 10-14.
6. Dinkelacker, F., Marzak, P., Yun, J., Liang, Y., & Bandarenka, A. S. (2018). A multistage mechanism of lithium intercalation into graphite anodes in presence of the solid electrolyte interface. *ACS Applied Materials & Interfaces*, 10, 14063–14069.
7. Xue, S., Garlyyev, B., Watzele, S., Liang, Y., Fichtner, J., Pohl, M. D., & Bandarenka, A. S. (2018). Influence of alkali metal cations on the hydrogen evolution reaction activity of Pt, Ir, Au and Ag electrodes in alkaline electrolytes. *ChemElectroChem*, 5 (17), 2326-2329.
8. Scieszka, D., Sohr, C., Scheibenbogen, P., Marzak, P., Yun, J., Liang, Y., Fichtner, J. & Bandarenka, A. S. (2018). Multiple potentials of maximum entropy of a $Na_2Co[Fe(CN)_6]$ battery electrode material: does the electrolyte composition control the interface? *ACS Applied Materials & Interfaces*, 10 (25), 21688-21695.
9. Garlyyev, B., Liang, Y., Xue, S., Watzele, S., Fichtner, J., Li, W. J., Xing, D. & Bandarenka, A. S. (2018). Theoretical and experimental identification of active electrocatalytic surface sites. *Current Opinion in Electrochemistry*, *accepted*.

10. Liang, Y., Pfisterer, J. H. K., McLaughlin, D., Csoklich, C., Seidl, L., Bandarenka, A. S. & Schneider, O. (2018). Electrochemical scanning probe microscopies in electrocatalysis. *Small Methods*, *accepted*.
11. Liang, Y.,[(1)] McLaughlin, D.,[(1)] Csoklich, C., Schneider, O. & Bandarenka, A. S. (2019). The Nature of Active Centers Catalyzing Oxygen Electro-Reduction at Platinum Surfaces in Alkaline Media. *Energy & Environmental Science, accepted*.
12. Liang, Y.,[(1)], Csoklich, C.,[(1)] McLaughlin, D., Schneider, O. & Bandarenka, A. S. Hydrogen evolution reaction at Pt and Pd atomic layers on au surfaces investigated by noise ECSTM. *In preparation*.
13. Mitterreiter, E.,[(1)] Liang. Y.,[(1)] Golibrzuch, M., McLaughlin, D., Csoklich, C., Holleitner, A., Wurstbauer, U. & Bandarenka, A. S. Engineering and Visualization of Catalytic Hydrogen Evolution Sites under Reaction Conditions at the Surface of Two-dimensional Molybdenum Chalcogenides. *In preparation*.
14. Li, W., Watzele, S., El-Sayed, H. A., Kieslich, G., Liang, Y., Bandarenka, A. S., Rodewald, K., Rieger, B. & Fischer, R. A. Unprecedented high oxygen evolution activity of electrocatalysts derived from oriented metal-organic framework thin films. *In preparation*.

**Conference Contributions:**

Oral presentations:

1. The 9th Workshop on SECM and Related Techniques, August 2017, Warsaw, ‘‘What can electrochemical scanning tunneling microscopy reveal for heterogeneous catalysis?’’.

2. The 17th European Conference on Applications of Surface and Interface Analysis, September 2017, Montpellier, ‘‘What Can Electrochemical Scanning Tunneling Microscopy (ECSTM) Reveal for Heterogeneous Catalysis?’’.

3. 69th Annual Meeting of the International Society of Electrochemistry, September 2018, Bologna, ‘‘What Can Electrochemical Scanning Tunneling Microscopy Reveal for Heterogeneous Catalysis’’.

4. Electrochemistry 2018, Electrochemical Surface Science: From Fundamentals to Applications, September 2018, Ulm, ‘‘Direct Instrumental Identification of Catalytically Active Site Using Electrochemical Scanning Tunneling Microscopy’’.

5. Invited talk at the Institute of Electrochemistry, Ulm University, November 2018, Ulm, ‘‘Direct Instrumental Identification of Catalytically Active Site Using Electrochemical Scanning Tunneling Microscopy’’.

6. Invited talk at the Max-Planck-EPFL Nanolab, EPFL, November 2018, Lausanne, ‘‘Direct Instrumental Identification of Catalytically Active Site Using Electrochemical Scanning Tunneling Microscopy’’.

**Research Funding:**

Dr.-Ing. Leonhard-Lorenz-Stiftung, Technische Universität München, 2018

# Appendix C: Key Publication

The verification of the proposed concept has been published as:

LETTER

doi:10.1038/nature23661

# Direct instrumental identification of catalytically active surface sites

Jonas H. K. Pfisterer[1]*, Yunchang Liang[1,2,3]*, Oliver Schneider[2] & Aliaksandr S. Bandarenka[1,3,4]

**The activity of heterogeneous catalysts—which are involved in some 80 per cent of processes in the chemical and energy industries—is determined by the electronic structure of specific surface sites that offer optimal binding of reaction intermediates. Directly identifying and monitoring these sites during a reaction should therefore provide insight that might aid the targeted development of heterogeneous catalysts and electrocatalysts (those that participate in electrochemical reactions) for practical applications. The invention of the scanning tunnelling microscope (STM)[1,2] and the electrochemical STM[3,4] promised to deliver such imaging capabilities, and both have indeed contributed greatly to our atomistic understanding of heterogeneous catalysis[5–8]. But although the STM has been used to probe and initiate surface reactions[9,10], and has even enabled local measurements of reactivity in some systems[11–13], it is not generally thought to be suited to the direct identification of catalytically active surface sites under reaction conditions. Here we demonstrate, however, that common STMs can readily map the catalytic activity of surfaces with high spatial resolution: we show that by monitoring relative changes in the tunnelling current noise, active sites can be distinguished in an almost quantitative fashion according to their ability to catalyse the hydrogen-evolution reaction or the oxygen-reduction reaction. These data allow us to evaluate directly the importance and relative contribution to overall catalyst activity of different defects and sites at the boundaries between two materials. With its ability to deliver such information and its ready applicability to different systems, we anticipate that our method will aid the rational design of heterogeneous catalysts.**

The idea of using STMs for more than just imaging is almost as old as the STM itself. So too is so-called scanning noise microscopy, which exploits the noise of the STM within the vacuum gap between the STM tip and the surface being probed to allow imaging at zero potential bias[14].

Our concept of STM-based identification of catalytically active surface sites is based on the idea that, under reaction conditions, the parameters that define the quantum-mechanical tunnelling barriers for electrons over active sites will be different, and will vary with time, compared with those over non-active sites. If one considers for example the interface between an electron conductor (electrode) and a liquid ion conductor (electrolyte), then local catalytic processes might be expected to continuously alter the quantum-tunnelling barriers by, for instance, changing the electrolyte composition or inducing adsorption and desorption within the narrow gap between the STM tip and the sample surface (it is known that even water molecules change the properties of these barriers[15]). Therefore, the tunnelling current measured between the tip and the sample under a constant bias should also change, in a way that reflects these local processes. Figure 1a, b sketches this basic concept, and shows how a comparison of the tunnelling current as a function of time and at different potentials over different surface sites makes it then possible to map the location of the active catalytic centres. The mapping can also be carried out using other electrochemical (EC)-STM modes, such as the so-called constant-current mode, where variations in the vertical position of the tip rather than variations in current are recorded. The noise analysis can be done in both cases with relative ease, illustrated by the histograms in Fig. 1a, b.

The EC-STM data in Fig. 1c, d—obtained for a platinum(111) (Pt(111)) electrode with flat terraces and step-like surface defects, and in contact with an aqueous 0.1 M perchloric acid ($HClO_4$) electrolyte—illustrate that one can indeed detect different 'noise levels' over different surface sites that are active for the hydrogen-evolution reaction (HER). Terrace sites and step sites generally exhibit different catalytic activities for the HER[16,17] and are thus expected to contribute differently to the temporal changes in the tunnelling barriers. Indeed, if the electrode potential is negative enough to initiate the HER (but not sufficient to produce gas bubbles; see Methods), then the STM signal reveals noticeable differences (Fig. 1c): under reaction conditions, the detected noise level is systematically higher at step-like defects than at terraces (for experimental conditions see Methods and Extended Data Figs 1, 2).

As the STM tip is scanned across the surface, the temporal tunnelling-barrier fluctuations result in a 'spatial noise'. When the electrode potential is shifted towards values where no HER is possible, the noise level at the step and at the terrace is approximately the same. Figure 1d further demonstrates that the specific noise features appear systematically at platinum steps under reaction conditions. Therefore, we hypothesize that the increased noise level results from the reactants and products changing the tunnelling barrier locally with time, and that the catalytically active surface sites in this system are situated at steps. Although the Faradaic current due to hydrogen oxidation at the STM tip will contribute to the response shown in Fig. 1c, d, this contribution should be minor (see Methods for further discussion). We also note that even without reaching sub-nanometre resolution, the data in Fig. 1c, d are in good agreement with recent theoretical calculations showing that the active HER sites are likely to be located at the step concavities of platinum electrodes[17], and with the fact that polycrystalline platinum is more active than Pt(111), probably because defects play a major role[17].

Measurements obtained using specially constructed polycrystalline platinum and gold samples (see Methods and Extended Data Figs 3, 4) further establish the correlation between the STM noise level and reactivity. In comparison with platinum, gold is a much less active catalyst of the HER[18], and this difference is clearly seen in the STM noise measurements (Extended Data Figs 5–7).

Although general confirmation of theoretical predictions is frequently possible without sub-nanometre resolution (see Fig. 1), detailed and spatially highly resolved information on the catalytically active surface sites is often desired. This can in principle be provided using our approach, but resolution will be limited by STM showing 'conductivity

[1]Physics of Energy Conversion and Storage, Physik-Department, Technische Universität München, James-Franck-Straße 1, 85748 Garching, Germany. [2]Institut für Informatik VI, Technische Universität München, Schleißheimerstraße 90a, 85748 Garching, Germany. [3]Nanosystems Initiative Munich (NIM), Schellingstraße 4, 80799 Munich, Germany. [4]Catalysis Research Center TUM, Ernst-Otto-Fischer-Straße 1, 85748 Garching, Germany.
*These authors contributed equally to this work.

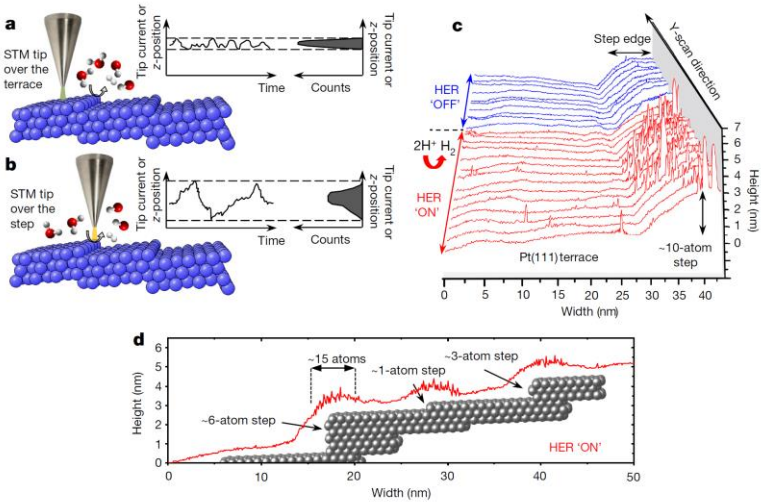


**Figure 1 | Revealing catalytic sites under reaction conditions.** **a**, **b**, A scheme explaining the concept. When the local environment between the STM tip and the sample changes (in this case, when the tip is over a terrace, **a**, versus a step, **b**, in the sample), the tunnelling barrier also changes over time, in a way that is driven by the changes in approaching and departing reactants and products. In this scenario, increased tunnelling-current noise is likely to appear when the tip is over a step edge, which is more active than the terrace sites. If the STM is operated in constant-current mode, then the noise is revealed in the measured *z*-position (the height of the STM tip over the sample). **c**, STM line scans (constant-current mode) obtained over a Pt(111) surface in 0.1 M $HClO_4$, when the potential of the sample is either sufficiently negative or too positive to initiate the HER (which is therefore either 'ON' or 'OFF'). **d**, A typical STM line scan over the Pt(111) surface in 0.1 M $HClO_4$ under HER conditions.

maps' that can only in some cases be easily correlated with the atomic or molecular geometry of the surface.

To explore the spatial resolution of our approach further, we studied an example involving islands of an active HER catalyst, palladium, on a less-active gold support, Au(111). Figure 2a shows an STM image of the sample in air, revealing monoatomically high islands of palladium on the gold surface. The electronic properties of active palladium atoms in the centres of the islands and at their boundaries are altered dissimilarly by the non-active gold substrate, causing differences in HER activities that are revealed directly by the STM noise measurements in electrolyte (Fig. 2b–d). Figure 2b shows STM data that characterize the gold/palladium boundary under HER conditions in 0.1 M sulfuric acid, collected with an applied electrode potential that is negative enough to initiate hydrogen evolution on palladium, but not sufficient to do so on the less-active gold. By comparing Fig. 2a with Fig. 2b, one can see that the STM signals are highly non-uniform over the surface of the palladium under reaction conditions.

A closer look at the gold/palladium boundary (Fig. 2c) shows that the noise level of the tunnelling current is relatively small over the surface of gold, noticeably higher over the surface of palladium, and systematically largest over only a few atoms of palladium that are close to the boundary. These observed differences, quantified in the histograms in Fig. 2d, suggest that in this system only one to three palladium atoms along the island boundary give the greatest contribution to the observed HER activity. This finding suggests directly that, in order to increase the activity of this catalytic system, it is necessary to maximize the surface abundance of palladium atoms located at gold/palladium boundaries. Covering the entire gold surface with palladium would, according to Fig. 2c, be far less effective—in good agreement with indirect experimental evidence[19–21] and theoretical calculations[22] for this particular system.

HER is one of the fastest electrocatalytic reactions, producing large amounts of hydrogen localized at the catalyst surface. However, many catalytic processes are much slower and involve low concentrations of reactants and/or products. One example is the oxygen-reduction reaction (ORR)[23], where the concentration of the dissolved oxygen in aqueous electrolytes at room temperature is normally as low as about 5 mM (ref. 24). To probe the performance of our STM noise measurement approach in mapping local catalytic activity in such systems, we

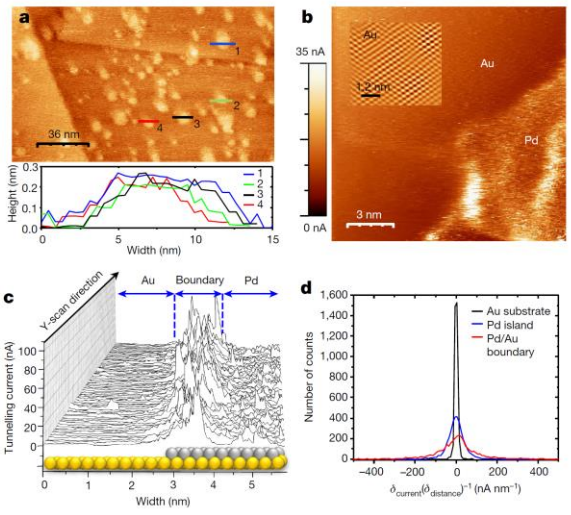


**Figure 2 | STM characterization of nanostructured surfaces under HER conditions.** **a**, Monoatomically high islands of Pd on an Au(111) surface (no electrolyte, constant-current mode). Top, an STM image of the sample in air. Bottom, line scans of selected Pd islands. **b**, An STM image of the boundary between a Pd island and the Au(111) substrate under HER conditions in 0.1 M sulfuric acid (constant-height mode). The inset shows an atomically resolved image of the Au(111) substrate. **c**, Detailed STM line scans for the case shown in **b** (the atomic-ball model is a guide to the eyes). **d**, Statistical analysis of the STM line scans shown in **c**, over Au, Pd and the Au/Pd boundary (current derivatives are used to construct the histograms; see Methods).

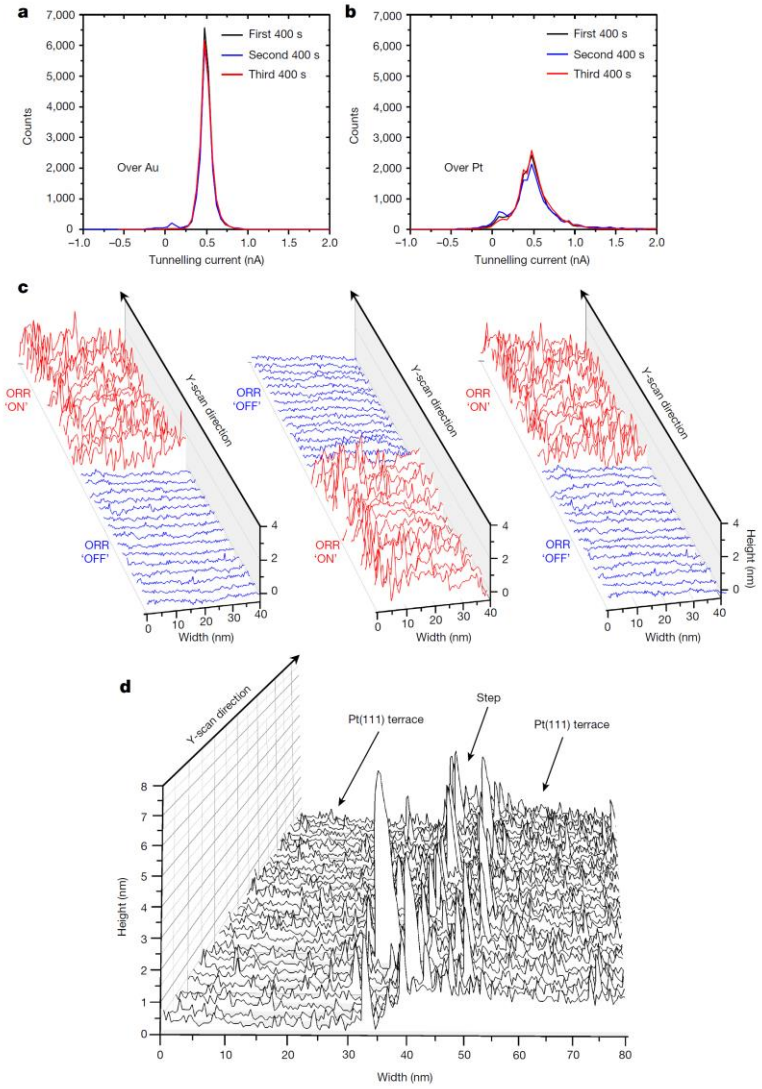


**Figure 3 | STM characterization of polycrystalline Au, Pt and Pt(111) samples under ORR conditions in 0.1 M $HClO_4$. a**, Histograms characterizing the tunnelling-current noise over the surface of polycrystalline Au. **b**, Corresponding histograms obtained over the surface of polycrystalline Pt. **c**, Results of repetitive ORR 'ON' and 'OFF' STM noise experiments at the same terrace of a Pt(111) sample. **d**, STM line scans at the surface of a Pt(111) electrode under ORR conditions, where both terraces and steps can be visualized.

first used less-active polycrystalline gold and catalytically active (for the ORR) platinum placed in 0.1 M $HClO_4$ (Fig. 3a, b). Figure 3a, b show current histograms (similar to those illustrated in Fig. 1a, b) that were obtained under ORR conditions by recording the tunnelling current over roughly the same site at the surface of either gold or platinum in contact with air-saturated aqueous electrolyte (conditions that are close to those found in some fuel cells and metal–air batteries). The histograms in each set are very reproducible, with the sharper peaks in Fig. 3a revealing a relatively low noise level on gold, and the wider peaks in Fig. 3b signalling the higher activity of platinum towards the ORR.

Figure 3c illustrates the results of 'ON–OFF' ORR experiments using a Pt(111) terrace in contact with 0.1 M $HClO_4$ solution saturated with air. When the potential of the sample is set such that no ORR can take place (see Methods and Extended Data Fig. 8), the EC-STM line profiles demonstrate a moderate noise level. In contrast, when the electrode potential is lowered by several hundred millivolts so that oxygen can be easily reduced, the level of noise increases drastically, as was seen in the HER experiments (compare Fig. 3c with Fig. 1c and Fig. 2).

A more complex sample for imaging is a Pt(111) surface with step-like defects; here, both the terraces and the steps are active towards the ORR (Fig. 3d). However, the latter seem to contribute more to the overall activity, as the noise level is systematically greater at the steps. This observation agrees with numerous reports on the ORR activity of electrodes with step-like defects, with the most active ORR sites on platinum surfaces (as in the HER) expected to be located at Pt(111) terraces close to the step concavities[25–30].

Taken together, these observations establish that STM noise analysis can locate active catalytic sites that exhibit different activity levels even

under the demanding conditions associated with an electrochemical interface. The best resolution achievable will depend on the surface under study, the diffusion of reactants and products, and the features of the imaging system (such as microscope properties, the tip material, and other purely experimental factors and parameters). But, as our observations regarding the distribution of active sites for the ORR and HER on platinum and gold/palladium surfaces have shown, STM noise analysis will frequently be sufficient to distinguish between the relative contributions of different sites to the overall activity, in order to make decisions about how to optimize the construction of real-world catalysts in terms of the abundance and placement of defects and material boundaries. We expect that this information can be readily obtained using model systems and simple STM experiments, which should be accessible to many laboratories worldwide. When used in conjunction with a recent theoretical method[30] for identifying active sites using generalized coordination numbers, the impact on our ability to rationally design heterogeneous catalysts could be substantial. In closing, we note that the noise measurements also endow the EC-STM investigations with a certain level of chemical selectivity, in that atoms such as palladium and gold can be readily distinguished according to noise level, even though this is not straightforward to do when using images recorded in absence of a reaction (see Fig. 2a; for more examples relating to platinum/gold nanoclusters, see Methods and Extended Data Fig. 9).

**Online Content** Methods, along with any additional Extended Data display items and Source Data, are available in the online version of the paper; references unique to these sections appear only in the online paper.

**Received 20 September 2016; accepted 11 July 2017.**


1. Binnig, G., Rohrer, H., Gerber, C. & Weibel, E. Surface studies by scanning tunneling microscopy. *Phys. Rev. Lett.* **49,** 57–61 (1982).
2. Binnig, G., Rohrer, H., Gerber, Ch. & Weibel, E. Tunneling through a controllable vacuum gap. *Appl. Phys. Lett.* **40,** 178–180 (1982).
3. Liu, H.-Y., Fan, F.-R. F., Lin, C. W. & Bard, A. J. Scanning electrochemical and tunneling ultramicroelectrode microscope for high-resolution examination of electrode surfaces in solution. *J. Am. Chem. Soc.* **108,** 3838–3839 (1986).
4. Itaya, K. & Tomita, E. Scanning tunneling microscope for electrochemistry—a new concept for the in situ scanning tunneling microscope in electrolyte solutions. *Surf. Sci.* **201,** L507–L512 (1988).
5. Thomas, J. M. & Thomas, W. J. *Principles and Practice of Heterogeneous Catalysis* 2nd edn (John Wiley, 2014).
6. Chorkendorff, I. & Niemantsverdriet, J. W. *Concepts of Modern Catalysis and Kinetics* (John Wiley, 2006).
7. Bell, T. A. The impact of nanoscience on heterogeneous catalysis. *Science* **299,** 1688–1691 (2003).
8. Jaramillo, T. F. *et al.* Identification of active edge sites for electrochemical $H_2$ evolution from $MoS_2$ nanocatalysts. *Science* **317,** 100–102 (2007).
9. Nørskov, J. K. Surface chemistry: catalysis frozen in time. *Nature* **414,** 405–406 (2001).
10. Hahn, J. & Ho, W. Oxidation of a single carbon monoxide molecule manipulated and induced with a scanning tunneling microscope. *Phys. Rev. Lett.* **87,** 166102 (2001).
11. Zambelli, T., Wintterlin, J., Trost, J. & Ertl, G. Identification of the "active sites" of a surface-catalyzed reaction. *Science* **273,** 1688–1690 (1996).
12. Meier, J., Friedrich, K. A. & Stiming, U. Novel method for the investigation of single nanoparticle reactivity. *Faraday Discuss.* **121,** 365–372 (2002).
13. Wolfschmidt, H., Weingarth, D. & Stimming, U. Enhanced reactivity for hydrogen reactions at Pt nanoislands on Au(111). *ChemPhysChem* **11,** 1533–1541 (2010).
14. Möller, R., Esslinger, A. & Koslowski, B. Noise in vacuum tunneling: application for a novel scanning microscope. *Appl. Phys. Lett.* **55,** 2360–2362 (1989).
15. Hugelmann, M. & Schindler, W. Tunnel barrier height oscillations at the solid/liquid interface. *Surf. Sci.* **541,** L643–L648 (2003).
16. Koper, M. T. M. Structure sensitivity and nanoscale effects in electrocatalysis. *Nanoscale* **3,** 2054–2073 (2011).
17. Tymoczko, J., Calle-Vallejo, F., Schuhmann, W. & Bandarenka, A. S. Making the hydrogen evolution reaction in PEM electrolyzers even faster. *Nat. Commun.* **7,** 10990 (2016).
18. Perez, J., Gonzalez, E. R. & Villullas, H. M. Hydrogen evolution reaction on gold single-crystal electrodes in acid solutions. *J. Phys. Chem. B* **102,** 10931–10935 (1998).
19. Pandelov, S. & Stimming, U. Reactivity of monolayers and nano-islands of palladium on Au(111) with respect to proton reduction. *Electrochim. Acta* **52,** 5548–5555 (2007).
20. Kibler, L. A. Hydrogen electrocatalysis. *ChemPhysChem* **7,** 985–991 (2006).
21. Hernandez, F. & Baltruschat, H. Hydrogen evolution and Cu UPD at stepped gold single crystals modified with Pd. *J. Solid State Electrochem.* **11,** 877–885 (2007).
22. Björketun, M. E. *et al.* Hydrogen evolution on Au(111) covered with submonolayers of Pd. *Phys. Rev. B* **84,** 045407 (2011).
23. Stephens, I. E. L., Bondarenko, A. S., Grønbjerg, U., Rossmeisl, J. & Chorkendorff, I. Understanding the electrocatalysis of oxygen reduction on platinum and its alloys. *Energy Environ. Sci.* **5,** 6744–6762 (2012).
24. Battino, R. (ed.) *Oxygen and Ozone: Solubility Data Series* Vol. 7 (Pergamon, 1981).
25. Takesue, Y., Nakamura, M. & Hoshi, N. Structural effects on the oxygen reduction reaction on the high index planes of $Pt_3Co$. *Phys. Chem. Chem. Phys.* **16,** 13774–13779 (2014).
26. Rurigaki, T., Hitotsuyanagi, A., Nakamura, M., Sakai, N. & Hoshi, N. Structural effects on the oxygen reduction reaction on the high index planes of $Pt_3Ni$: n(111)–(111) and n(111)–(100) surfaces. *J. Electroanal. Chem.* **716,** 58–62 (2014).
27. Kuzume, A., Herrero, E. & Feliu, J. M. Oxygen reduction on stepped platinum surfaces in acidic media. *J. Electroanal. Chem.* **599,** 333–343 (2007).
28. Hitotsuyanagi, A., Nakamura, M. & Hoshi, N. Structural effects on the activity for the oxygen reduction reaction on n(111)–(100) series of Pt: correlation with the oxide film formation. *Electrochim. Acta* **82,** 512–516 (2012).
29. Bandarenka, A. S., Hansen, H. A., Rossmeisl, J. & Stephens, I. E. L. Elucidating the activity of stepped Pt single crystals for oxygen reduction. *Phys. Chem. Chem. Phys.* **16,** 13625–13629 (2014).
30. Calle-Vallejo, F. *et al.* Finding optimal surface sites on heterogeneous catalysts by counting nearest neighbors. *Science* **350,** 185–189 (2015).


**Acknowledgements** We thank the Deutsche Forschungsgemeinschaft (DFG; project BA 5795/3-1) and the cluster of excellence Nanosystems Initiative Munich (NIM) for financial support. O.S. acknowledges funding from Toyota Motor Europe.

**Author Contributions** J.H.K.P. and Y.L. conducted the experiments, performed the data analysis and contributed to manuscript preparation. A.S.B. developed the basic idea, wrote large parts of the manuscript and supervised J.H.K.P. and Y.L. in their experimental work. O.S. suggested the use of the palladium/gold system, contributed background knowledge, advised Y.L. in his experimental work and contributed to the manuscript-drafting process. All the authors participated in discussing the results and writing the manuscript.

**Author Information** Reprints and permissions information is available at www.nature.com/reprints. The authors declare no competing financial interests. Readers are welcome to comment on the online version of the paper. Publisher's note: Springer Nature remains neutral with regard to jurisdictional claims in published maps and institutional affiliations. Correspondence and requests for materials should be addressed to A.S.B. (bandarenka@ph.tum.de).

**Reviewer Information** *Nature* thanks S. Boettcher, P. Davies and J. Kunze-Liebhäuser for their contribution to the peer review of this work.

# References


[1] Petit, J. R., Jouzel, J., Raynaud, D., Barkov, N. I., Barnola, J. M., Basile, I., Bender, M., Chappellaz, J., Davis, M., Delaygue, G., Delmotte, M., Kotlyakov, V. M., Legrand, M., Lipenkov, V. Y., Lorius, C., Ritz, P. C., Saltzman, E. & Delmotte, M. (1999). Climate and atmospheric history of the past 420,000 years from the Vostok ice core, Antarctica. *Nature*, 399(6735), 429.

[2] Cox, P. M., Betts, R. A., Jones, C. D., Spall, S. A. & Totterdell, I. J. (2000). Acceleration of global warming due to carbon-cycle feedbacks in a coupled climate model. *Nature*, 408(6809), 184.

[3] Solomon, S., Plattner, G. K., Knutti, R. & Friedlingstein, P. (2009). Irreversible climate change due to carbon dioxide emissions. *Proceedings of the National Academy of Sciences*, 106(6), 1704-1709.

[4] Panwar, N. L., Kaushik, S. C. & Kothari, S. (2011). Role of renewable energy sources in environmental protection: a review. *Renewable and Sustainable Energy Reviews*, 15(3), 1513-1524.

[5] Rebut, P. H. (1995). ITER: the first experimental fusion reactor. *In Fusion Technology 1994* (pp. 85-118).

[6] Larminie, J. & Lowry, J. (2012). Electric vehicle technology explained. John Wiley & Sons.

[7] Seinfeld, J. H. & Pandis, S. N. (2016). Atmospheric chemistry and physics: from air pollution to climate change. John Wiley & Sons.

[8] Crabtree, G. W., Dresselhaus, M. S. & Buchanan, M. V. (2004). The hydrogen economy. *Physics Today*, 57(12), 39-44.

[9] Barreto, L., Makihira, A. & Riahi, K. (2003). The hydrogen economy in the 21st century: a sustainable development scenario. *International Journal of Hydrogen Energy*, 28(3), 267-284.

[10] Nørskov, J. K., Studt, F., Abild-Pedersen, F. & Bligaard, T. (2014). *Fundamental concepts in heterogeneous catalysis.* John Wiley & Sons Inc., Hoboken, New Jersey.

[11] Ross, J. R. (2011). Heterogeneous catalysis: fundamentals and applications. Elsevier.

[12] Döbereiner, J. W. (1823). Neu entdeckte merkwürdige Eigenschaften des Platinsuboxyds, des oxydirten Schwefel-Platins und des metallischen Platinstaubes. *J. Chem. (Schweigger)*, 38, 321

[13] Berzelius, J. J. (1835). *Jahresbericht*, 15, 23, 243. *Annual report submitted to the Swedish Academy on March 31 by Berzelius*.

[14] Ostwald, W. (1902). *Physikalische Zeitschrift*, 3, 313.

[15] Ostwald, W. (1909). On Catalysis, Nobel Lecture. *The Nobel Prize in Chemistry 1909*.

[16] Haber, F. (2002). The synthesis of ammonia from its elements. *Nobel Lecture, June 2, 1920. Resonance*, 7(9), 86-94.

[17] Bosch, C. (1932). The development of the chemical high pressure method during the establishment of the new ammonia industry. *Nobel Lectures: Chemistry*, 1941, 197-235.

[18] Smil, V. (1999). Detonator of the population explosion. *Nature*, 400(6743), 415.

[19] Bozso, F., Ertl, G., Grunze, M. & Weiss, M. (1977). Interaction of nitrogen with iron surfaces: I. Fe (100) and Fe (111). *Journal of Catalysis*, 49(1), 18-41.

[20] Imbihl, R., Behm, R. J., Ertl, G. & Moritz, W. (1982). The structure of atomic nitrogen adsorbed on Fe (100). *Surface Science*, 123(1), 129-140.

[21] Ertl, G., Lee, S. B. & Weiss, M. (1982). Kinetics of nitrogen adsorption on Fe (111). *Surface Science*, 114(2-3), 515-526.

[22] Ertl, G. (1983). Primary steps in catalytic synthesis of ammonia. *Journal of Vacuum Science & Technology A: Vacuum, Surfaces, and Films*, 1(2), 1247-1253.
[23] Ertl, G. (2008). Reactions at surfaces: from atoms to complexity (Nobel Lecture). *Angewandte Chemie International Edition*, 47(19), 3524-3535.
[24] Taylor, H. S. (1925). A theory of the catalytic surface. *Proceedings of the Royal Society of London. Series A, Containing Papers of a Mathematical and Physical Character*, 108(745), 105-111.
[25] Zambelli, T., Wintterlin, J., Trost, J. & Ertl, G. (1996). Identification of the ''active site'' of a surface-catalyzed reaction. *Science*, 273(5282), 1688-1690.
[26] Somorjai, G. A. & Li, Y. (2010). *Introduction to surface chemistry and catalysis*. John Wiley & Sons.
[27] Liu, H. Y., Fan, F. R. F., Lin, C. W. & Bard, A. J. (1986). Scanning electrochemical and tunneling ultramicroelectrode microscope for high-resolution examination of electrode surfaces in solution. *Journal of the American Chemical Society*, 108(13), 3838-3839.
[28] Itaya, K. & Tomita, E. (1988). Scanning tunneling microscope for electrochemistry - a new concept for the in situ scanning tunneling microscope in electrolyte solutions. *Surface Science*, 201(3), L507-L512.
[29] Calle-Vallejo, F., Tymoczko, J., Colic, V., Vu, Q. H., Pohl, M. D., Morgenstern, K., Loffreda, D., Sautet, P., Schuhmann, W. & Bandarenka, A. S. (2015). Finding optimal surface sites on heterogeneous catalysts by counting nearest neighbors. *Science*, 350(6257), 185-189.
[30] Jaramillo, T. F., Jørgensen, K. P., Bonde, J., Nielsen, J. H., Horch, S. & Chorkendorff, I. (2007). Identification of active edge sites for electrochemical $H_2$ evolution from $MoS_2$ nanocatalysts. *Science*, 317(5834), 100-102.
[31] Binnig, G. & Rohrer, H. (1983). Scanning tunneling microscopy. *Surface Science*, 126(1-3), 236-244.
[32] Thomas, J. M. & Thomas, W. J. (2014). *Principles and practice of heterogeneous catalysis.* John Wiley & Sons.
[33] Chorkendorff, I. & Niemantsverdriet, J. W. (2017). *Concepts of modern catalysis and kinetics.* John Wiley & Sons.
[34] Bell, A. T. (2003). The impact of nanoscience on heterogeneous catalysis. *Science*, 299(5613), 1688-1691.
[35] Hahn, J. R. & Ho, W. (2001). Oxidation of a single carbon monoxide molecule manipulated and induced with a scanning tunneling microscope. *Physical Review Letters*, 87(16), 166102.
[36] Nørskov, J. K. (2001). Surface chemistry: Catalysis frozen in time. *Nature*, 414(6862), 405.
[37] Meier, J., Friedrich, K. A. & Stimming, U. (2002). Novel method for the investigation of single nanoparticle reactivity. *Faraday Discussions*, 121, 365-372.
[38] Wolfschmidt, H., Weingarth, D. & Stimming, U. (2010). Enhanced reactivity for hydrogen reactions at Pt nanoislands on Au(111). *ChemPhysChem*, 11(7), 1533-1541.
[39] Tymoczko, J., Calle-Vallejo, F., Schuhmann, W. & Bandarenka, A. S. (2016). Making the hydrogen evolution reaction in polymer electrolyte membrane electrolysers even faster. *Nature communications*, 7, 10990.
[40] Pandelov, S. & Stimming, U. (2007). Reactivity of monolayers and nano-islands of palladium on Au(111) with respect to proton reduction. *Electrochimica Acta*, 52(18), 5548-5555.
[41] Kibler, L. A. (2006). Hydrogen electrocatalysis. *ChemPhysChem*, 7(5), 985-991.
[42] Hernandez, F. & Baltruschat, H. (2007). Hydrogen evolution and Cu UPD at stepped gold single crystals modified with Pd. *Journal of Solid State Electrochemistry*, 11(7), 877-885.

[43] Björketun, M. E., Karlberg, G. S., Rossmeisl, J., Chorkendorff, I., Wolfschmidt, H., Stimming, U. & Nørskov, J. K. (2011). Hydrogen evolution on Au(111) covered with submonolayers of Pd. *Physical Review B*, 84(4), 045407.

[44] Katsounaros, I., Cherevko, S., Zeradjanin, A. R., & Mayrhofer, K. J. (2014). Oxygen electrochemistry as a cornerstone for sustainable energy conversion. *Angewandte Chemie International Edition*, 53(1), 102-121.

[45] Cheng, F. & Chen, J. (2012). Metal-air batteries: from oxygen reduction electrochemistry to cathode catalysts. *Chemical Society Reviews*, 41(6), 2172-2192.

[46] Takesue, Y., Nakamura, M. & Hoshi, N. (2014). Structural effects on the oxygen reduction reaction on the high index planes of $Pt_3Co$. *Physical Chemistry Chemical Physics*, 16(27), 13774-13779.

[47] Rurigaki, T., Hitotsuyanagi, A., Nakamura, M., Sakai, N. & Hoshi, N. (2014). Structural effects on the oxygen reduction reaction on the high index planes of $Pt_3Ni$: n(111)-(111) and n(111)-(100) surfaces. *Journal of Electroanalytical Chemistry*, 716, 58-62.

[48] Kuzume, A., Herrero, E. & Feliu, J. M. (2007). Oxygen reduction on stepped platinum surfaces in acidic media. *Journal of electroanalytical chemistry*, 599(2), 333-343.

[49] Hitotsuyanagi, A., Nakamura, M. & Hoshi, N. (2012). Structural effects on the activity for the oxygen reduction reaction on n(111)-(100) series of Pt: correlation with the oxide film formation. *Electrochimica Acta*, 82, 512-516.

[50] Bandarenka, A. S., Hansen, H. A., Rossmeisl, J. & Stephens, I. E. (2014). Elucidating the activity of stepped Pt single crystals for oxygen reduction. *Physical Chemistry Chemical Physics*, 16(27), 13625-13629.

[51] Strmcnik, D., Kodama, K., Van der Vliet, D., Greeley, J., Stamenkovic, V. R. & Marković, N. M. (2009). The role of non-covalent interactions in electrocatalytic fuel-cell reactions on platinum. *Nature chemistry*, 1(6), 466-472.

[52] Jensen, K. D., Tymoczko, J., Rossmeisl, J., Bandarenka, A. S., Chorkendorff, I., Escudero-Escribano, M. & Stephens, I. E. (2018). Elucidation of the Oxygen Reduction Volcano in Alkaline Media using a Copper-Platinum (111) Alloy. *Angewandte Chemie International Edition*, 57(11), 2800-2805.

[53] Rizo, R., Herrero, E. & Feliu, J. M. (2013). Oxygen reduction reaction on stepped platinum surfaces in alkaline media. *Physical Chemistry Chemical Physics*, 15(37), 15416-15425.

[54] Dešić, M. N., Popović, M. M., Obradović, M. D., Vračar, L. M. & Grgur, B. N. (2005). Study of gold-platinum and platinum-gold surface modification and its influence on hydrogen evolution and oxygen reduction. *Journal of the Serbian Chemical Society*, 70(2), 231-242.

[55] Wang, Q. H., Kalantar-Zadeh, K., Kis, A., Coleman, J. N. & Strano, M. S. (2012). Electronics and optoelectronics of two-dimensional transition metal dichalcogenides. *Nature nanotechnology*, 7(11), 699-712.

[56] Chia, X., Eng, A. Y. S., Ambrosi, A., Tan, S. M. & Pumera, M. (2015). Electrochemistry of nanostructured layered transition-metal dichalcogenides. *Chemical reviews*, 115(21), 11941-11966.

[57] Li, H., Tsai, C., Koh, A. L., Cai, L., Contryman, A. W., Fragapane, A. H., Zhao, J., Han, H. S., Manoharan, H. C., Abild-Pedersen, F. & Nørskov, J. K. (2016). Activating and optimizing $MoS_2$ basal planes for hydrogen evolution through the formation of strained sulphur vacancies. *Nature materials*, 15(1), 48.

[58] Trasatti, S. (2010). Electrode potential and double layer. *Handbook of Fuel Cells* (eds W. Vielstich, A. Lamm, H. A. Gasteiger and H. Yokokawa). John Wiley & Sons.

[59] Schmickler, W. & Santos, E. (2010). *Interfacial electrochemistry*. Springer Science & Business Media.

[60] Helmholtz, H. V. (1853). Ueber einige Gesetze der Vertheilung elektrischer Ströme in körperlichen Leitern mit Anwendung auf die thierisch-elektrischen Versuche. *Annalen der Physik*, 165(6), 211-233.
[61] Grahame, D. C. (1947). The electrical double layer and the theory of electrocapillarity. *Chemical Reviews*, 41(3), 441-501.
[62] Bockris, J. M., Devanathan, M. A. V. & Muller, K. (1963). On the structure of charged interfaces. *Proceedings of the Royal Society of London A: Mathematical, Physical and Engineering Sciences*, 274(1356), 55-79.
[63] Bard, A. J. & Faulkner, L. R. (2001). *Electrochemical methods: fundamentals and applications*, 2nd. John Wiley & Sons Inc., New York.
[64] Tanimoto, S. & Ichimura, A. (2013). Discrimination of inner-and outer-sphere electrode reactions by cyclic voltammetry experiments. *Journal of Chemical Education*, 90(6), 778-781.
[65] Demortier, A. & Bard, A. J. (1973). Electrochemical reactions of organic compounds in liquid ammonia. I. Reduction of benzophenone. *Journal of the American Chemical Society*, 95(11), 3495-3500.
[66] Arrhenius, S. (1889). Über die Dissociationswärme und den Einfluss der Temperatur auf den Dissociationsgrad der Elektrolyte. *Zeitschrift für physikalische Chemie*, 4(1), 96-116.
[67] Arrhenius, S. (1889). Über die Reaktionsgeschwindigkeit bei der Inversion von Rohrzucker durch Säuren. *Zeitschrift für physikalische Chemie*, 4(1), 226-248.
[68] Evans, M. G. & Polanyi, M. (1935). Some applications of the transition state method to the calculation of reaction velocities, especially in solution. *Transactions of the Faraday Society*, 31, 875-894.
[69] Eyring, H. (1935). The activated complex in chemical reactions. *The Journal of Chemical Physics*, 3(2), 107-115.
[70] Bockris, J. O. M. & Reddy, A. K. (2000). *Modern electrochemistry 2B: electrodics in chemistry, engineering, biology and environmental science (Vol. 2)*. Springer Science & Business Media.
[71] Vojvodic, A. & Nørskov, J. K. (2015). New design paradigm for heterogeneous catalysts. *National Science Review*, 2(2), 140-143.
[72] Sabatier, P. (1920). La catalyse en chimie organique. *Librairie Polytechnique*, Paris et Liège.
[73] Trasatti, S. (1972). Work function, electronegativity, and electrochemical behaviour of metals: III. Electrolytic hydrogen evolution in acid solutions. *Journal of Electroanalytical Chemistry and Interfacial Electrochemistry*, 39(1), 163-184.
[74] Nørskov, J. K. (1990). Chemisorption on metal surfaces. *Reports on Progress in Physics*, 53(10), 1253.
[75] Nørskov, J. K. (1991). Electronic factors in catalysis. *Progress in surface science*, 38(2), 103-144.
[76] Hammer, B. & Nørskov, J. K. (1995). Why gold is the noblest of all the metals. *Nature*, 376(6537), 238-240.
[77] Hammer, B. & Nørskov, J. K. (1995). Electronic factors determining the reactivity of metal surfaces. *Surface Science*, 343(3), 211-220.
[78] Hammer, B. & Nørskov, J. K. (2000). Theoretical surface science and catalysis—calculations and concepts. *Advances in Catalysis*, 45, 71-129.
[79] Nørskov, J. K., Abild-Pedersen, F., Studt, F. & Bligaard, T. (2011). Density functional theory in surface chemistry and catalysis. *Proceedings of the National Academy of Sciences*, 108(3), 937-943.
[80] Calle-Vallejo, F., Koper, M. T. & Bandarenka, A. S. (2013). Tailoring the catalytic activity of electrodes with monolayer amounts of foreign metals. *Chemical Society Reviews*, 42(12), 5210-5230.

[81] Greeley, J., Jaramillo, T. F., Bonde, J., Chorkendorff, I. & Nørskov, J. K. (2006). Computational high-throughput screening of electrocatalytic materials for hydrogen evolution. *Nature* Materials, 5(11), 909-913.
[82] Abild-Pedersen, F., Greeley, J., Studt, F., Rossmeisl, J., Munter, T. R., Moses, P. G., Skúlason, E., Bligaard, T. & Nørskov, J. K. (2007). Scaling properties of adsorption energies for hydrogen-containing molecules on transition-metal surfaces. *Physical Review Letters*, 99(1), 016105.
[83] Nørskov, J. K., Bligaard, T., Rossmeisl, J. & Christensen, C. H. (2009). Towards the computational design of solid catalysts. *Nature Chemistry*, 1(1), 37-46.
[84] Greeley, J. (2016). Theoretical heterogeneous catalysis: scaling relationships and computational catalyst design. *Annual Review of Chemical and Biomolecular Engineering*, 7, 605-635.
[85] Stephens, I. E.L., Bondarenko, A. S., Grønbjerg, U., Rossmeisl, J. & Chorkendorff, I. (2012). Understanding the electrocatalysis of oxygen reduction on platinum and its alloys. *Energy & Environmental Science*, 5(5), 6744-6762.
[86] Blum, L. (1977). Theory of electrified interfaces. *The Journal of Physical Chemistry*, 81(2), 136-147.
[87] Kolb, D. M. (2001). Electrochemical surface science. *Angewandte Chemie International Edition*, 40(7), 1162-1181.
[88] Kundu, D., Black, R., Berg, E. J. & Nazar, L. F. (2015). A highly active nanostructured metallic oxide cathode for aprotic Li-$O_2$ batteries. *Energy & Environmental Science*, 8(4), 1292-1298.
[89] Colic, V., Pohl, M. D., Scieszka, D. & Bandarenka, A. S. (2016). Influence of the electrolyte composition on the activity and selectivity of electrocatalytic centers. *Catalysis Today*, 262, 24-35.
[90] Bandarenka, A. S. & Koper, M. T. (2013). Structural and electronic effects in heterogeneous electrocatalysis: Toward a rational design of electrocatalysts. *Journal of Catalysis*, 308, 11-24.
[91] Grammatikopoulos, P., Cassidy, C., Singh, V. & Sowwan, M. (2014). Coalescence-induced crystallisation wave in Pd nanoparticles. *Scientific Reports*, 4, 5779.
[92] Turner, J. A. (1999). A realizable renewable energy future. *Science*, 285(5428), 687-689.
[93] (2004). Special Report: Toward a Hydrogen Economy. *Science*, 305(5686), 957-976.
[94] Wroblowa, H. S. & Razumney, G. (1976). Electroreduction of oxygen: A new mechanistic criterion. *Journal of Electroanalytical Chemistry and Interfacial Electrochemistry*, 69(2), 195-201.
[95] Moussallem, I., Jörissen, J., Kunz, U., Pinnow, S. & Turek, T. (2008). Chlor-alkali electrolysis with oxygen depolarized cathodes: history, present status and future prospects. *Journal of Applied Electrochemistry*, 38(9), 1177-1194.
[96] Ramaswamy, N., Hakim, N. & Mukerjee, S. (2008). Degradation mechanism study of perfluorinated proton exchange membrane under fuel cell operating conditions. *Electrochimica Acta*, 53(8), 3279-3295.
[97] Shao, M., Chang, Q., Dodelet, J. P. & Chenitz, R. (2016). Recent advances in electrocatalysts for oxygen reduction reaction. *Chemical Reviews*, 116(6), 3594-3657.
[98] Katsounaros, I., Schneider, W. B., Meier, J. C., Benedikt, U., Biedermann, P. U., Cuesta, A., Auer, A. A. & Mayrhofer, K. J. (2013). The impact of spectator species on the interaction of $H_2O_2$ with platinum-implications for the oxygen reduction reaction pathways. *Physical Chemistry Chemical Physics*, 15(21), 8058-8068.
[99] Morales-Guio, C. G., Stern, L. A. & Hu, X. (2014). Nanostructured hydrotreating catalysts for electrochemical hydrogen evolution. *Chemical Society Reviews*, 43(18), 6555-6569.

[100] Gasteiger, H. A., Kocha, S. S., Sompalli, B. & Wagner, F. T. (2005). Activity benchmarks and requirements for Pt, Pt-alloy, and non-Pt oxygen reduction catalysts for PEMFCs. *Applied Catalysis B: Environmental*, 56(1), 9-35.

[101] Wagner, F. T., Lakshmanan, B. & Mathias, M. F. (2010). Electrochemistry and the future of the automobile. *The Journal of Physical Chemistry Letters*, 1(14), 2204-2219.

[102] Wang, Y., Chen, K. S., Mishler, J., Cho, S. C. & Adroher, X. C. (2011). A review of polymer electrolyte membrane fuel cells: technology, applications, and needs on fundamental research. *Applied energy*, 88(4), 981-1007.

[103] Sharaf, O. Z. & Orhan, M. F. (2014). An overview of fuel cell technology: Fundamentals and applications. *Renewable and Sustainable Energy Reviews*, 32, 810-853.

[104] Hinnemann, B., Moses, P. G., Bonde, J., Jørgensen, K. P., Nielsen, J. H., Horch, S., Chorkendorff, I. & Nørskov, J. K. (2005). Biomimetic hydrogen evolution: $MoS_2$ nanoparticles as catalyst for hydrogen evolution. *Journal of the American Chemical Society*, 127(15), 5308-5309.

[105] Kong, D., Cha, J. J., Wang, H., Lee, H. R. & Cui, Y. (2013). First-row transition metal dichalcogenide catalysts for hydrogen evolution reaction. *Energy & Environmental Science*, 6(12), 3553-3558.

[106] Chhowalla, M., Shin, H. S., Eda, G., Li, L. J., Loh, K. P. & Zhang, H. (2013). The chemistry of two-dimensional layered transition metal dichalcogenide nanosheets. *Nature chemistry*, 5(4), 263-275.

[107] Kibler, L. A. (2003). Preparation and characterization of noble metal single crystal electrode surfaces. *International Society of Electrochemistry*.

[108] Krupski, K., Moors, M., Jóźwik, P., Kobiela, T. & Krupski, A. (2015). Structure determination of Au on Pt (111) surface: LEED, STM and DFT study. *Materials*, 8(6), 2935-2952.

[109] Calle-Vallejo, F., Pohl, M. D., Reinisch, D., Loffreda, D., Sautet, P., & Bandarenka, A. S. (2017). Why conclusions from platinum model surfaces do not necessarily lead to enhanced nanoparticle catalysts for the oxygen reduction reaction. *Chemical science*, 8(3), 2283-2289.

[110] Greeley, J., Stephens, I. E. L., Bondarenko, A. S., Johansson, T. P., Hansen, H. A., Jaramillo, T. F., Rossmeisl, J., Chorkendorff, I. & Nørskov, J. K. (2009). Alloys of platinum and early transition metals as oxygen reduction electrocatalysts. *Nature chemistry*, 1(7), 552-556.

[111] Batyr, G., Xue, S., Pohl, M. D., Reinisch, D. & Bandarenka, A. S. (2018). Oxygen electroreduction at high-index Pt electrodes in alkaline electrolytes: a decisive role of the alkali metal cations. *ACS Omega,* 3(11), 15325-15331.

[112] Koper, M. T. (2011). Structure sensitivity and nanoscale effects in electrocatalysis. *Nanoscale*, 3(5), 2054-2073.

[113] Subbaraman, R., Tripkovic, D., Strmcnik, D., Chang, K. C., Uchimura, M., Paulikas, A. P., Stamenkovic, V. & Markovic, N. M. (2011). Enhancing hydrogen evolution activity in water splitting by tailoring $Li^+$-$Ni(OH)_2$-Pt interfaces. *Science*, 334(6060), 1256-1260.

[114] Xue, S., Garlyyev, B., Watzele, S., Liang, Y., Fichtner, J., Pohl, M. D. & Bandarenka, A. S. (2008). Influence of alkali metal cations on the hydrogen evolution reaction activity of Pt, Au and Ag electrodes in alkaline electrolytes. *ChemElectroChem*, *accepted.*

[115] Baldauf, M. & Kolb, D. M. (1996). Formic acid oxidation on ultrathin Pd films on Au (hkl) and Pt (hkl) electrodes. *The Journal of Physical Chemistry*, 100(27), 11375-11381.

[116] Hara, M., Linke, U. & Wandlowski, T. (2007). Preparation and electrochemical characterization of palladium single crystal electrodes in 0.1 M $H_2SO_4$ and $HClO_4$: Part I. Low-index phases. *Electrochimica Acta*, 52(18), 5733-5748.

[117] Yoshimoto, S., Kim, Y. G., Sato, K., Inukai, J. & Itaya, K. (2012). Potential-induced phase transition of low-index Au single crystal surfaces in propylene carbonate solution. *Physical Chemistry Chemical Physics*, 14(7), 2286-2291.

[118] Zhang, J., Vukmirovic, M. B., Xu, Y., Mavrikakis, M. & Adzic, R. R. (2005). Controlling the Catalytic Activity of Platinum-Monolayer Electrocatalysts for Oxygen Reduction with Different Substrates. *Angewandte Chemie International Edition*, 44(14), 2132-2135.

[119] Chen, J., Lim, B., Lee, E. P. & Xia, Y. (2009). Shape-controlled synthesis of platinum nanocrystals for catalytic and electrocatalytic applications. *Nano Today*, 4(1), 81-95.

[120] Chen, A. & Holt-Hindle, P. (2010). Platinum-based nanostructured materials: synthesis, properties, and applications. *Chemical Reviews*, 110(6), 3767-3804.

[121] Zhou, X., Jiang, J., Ding, T., Zhang, J., Pan, B., Zuo, J. & Yang, Q. (2014). Fast colloidal synthesis of scalable Mo-rich hierarchical ultrathin $MoSe_{2-x}$ nanosheets for high-performance hydrogen evolution. *Nanoscale*, 6(19), 11046-11051.

[122] Ding, Y., Wang, Y., Ni, J., Shi, L., Shi, S. & Tang, W. (2011). First principles study of structural, vibrational and electronic properties of graphene-like $MX_2$ (M= Mo, Nb, W, Ta; X= S, Se, Te) monolayers. *Physica B: Condensed Matter*, 406(11), 2254-2260.

[123] Huang, Y. L., Chen, Y., Zhang, W., Quek, S. Y., Chen, C. H., Li, L. J., Hsu, W. T., Change, W. H., Zheng, Y. J., Chen, W. & Wee, A. T. (2015). Bandgap tunability at single-layer molybdenum disulphide grain boundaries. *Nature communications*, 6, 6298.

[124] Parzinger, E., Mitterreiter, E., Stelzer, M., Kreupl, F., Ager, J. W., Holleitner, A. W. & Wurstbauer, U. (2017). Hydrogen evolution activity of individual mono-, bi-, and few-layer $MoS_2$ towards photocatalysis. *Applied Materials Today*, 8, 132-140.

[125] Voiry, D., Salehi, M., Silva, R., Fujita, T., Chen, M., Asefa, T., Shenoy, V. B., Eda, G. & Chhowalla, M. (2013). Conducting $MoS_2$ nanosheets as catalysts for hydrogen evolution reaction. *Nano Letters*, 13(12), 6222-6227.

[126] Kibsgaard, J., Chen, Z., Reinecke, B. N. & Jaramillo, T. F. (2012). Engineering the surface structure of $MoS_2$ to preferentially expose active edge sites for electrocatalysis. *Nature materials*, 11(11), 963-969.

[127] Cuesta, A., Kibler, L. A. & Kolb, D. M. (1999). A method to prepare single crystal electrodes of reactive metals: application to Pd (hkl). *Journal of Electroanalytical Chemistry*, 466(2), 165-168.

[128] Paunovic, M. & Schlesinger, M. (2006). *Fundamentals of electrochemical deposition (Vol. 45)*. John Wiley & Sons Inc.

[129] Brülle, T. & Stimming, U. (2009). Platinum nanostructured HOPG - Preparation, characterization and reactivity. *Journal of Electroanalytical Chemistry*, 636(1), 10-17.

[130] Brülle, T., Denisenko, A., Sternschulte, H. & Stimming, U. (2011). Catalytic activity of platinum nanoparticles on highly boron-doped and 100-oriented epitaxial diamond towards HER and HOR. *Physical Chemistry Chemical Physics*, 13(28), 12883-12891.

[131] Hachiya, T., Honbo, H. & Itaya, K. (1991). Detailed underpotential deposition of copper on gold(III) in aqueous solutions. *Journal of Electroanalytical Chemistry and Interfacial Electrochemistry*, 315(1-2), 275-291.

[132] Herrero, E., Buller, L. J. & Abruña, H. D. (2001). Underpotential deposition at single crystal surfaces of Au, Pt, Ag and other materials. *Chemical Reviews*, 101(7), 1897-1930.

[133] Liu, Y., Gokcen, D., Bertocci, U. & Moffat, T. P. (2012). Self-terminating growth of platinum films by electrochemical deposition. *Science*, 338(6112), 1327-1330.

[134] Binnig, G., Rohrer, H., Gerber, C. & Weibel, E. (1982). Tunneling through a controllable vacuum gap. *Applied Physics Letters*, 40(2), 178-180.

[135] Binnig, G., Rohrer, H., Gerber, C. & Weibel, E. (1982). Surface studies by scanning tunneling microscopy. *Physical Review Letters*, 49(1), 57.
[136] Paschen, F. (1889). Ueber die zum Funkenübergang in Luft, Wasserstoff und Kohlensäure bei verschiedenen Drucken erforderliche Potentialdifferenz. *Annalen der Physik*, 273(5), 69-96.
[137] Meek, J. M. (1940). A theory of spark discharge. *Physical Review*, 57(8), 722.
[138] Earhart, R. F. (1901). XI. The sparking distances between plates for small distances. *The London, Edinburgh, and Dublin Philosophical Magazine and Journal of Science*, 1(1), 147-159.
[139] Whittaker, E. (1951). *A History of the Theories of Aether and Electricity: Vol. I: The Classical Theories; Vol. II: The Modern Theories, 1900-1926 (Vol. 1).* Courier Dover Publications.
[140] Fowler, R. H. & Nordheim, L. (1928). Electron emission in intense electric fields. *Proceedings of the Royal Society of London. Series A, Containing Papers of a Mathematical and Physical Character*, 119(781), 173-181.
[141] Carter, E. (1914). Discharge potentials across very short distances. *Physical Review*, 3(6), 453.
[142] Rother, F. (1914). Der Elektrizitätsübergang bei sehr kleinen Kontaktabständen und die Elektronenatmosphären der Metalle. *Annalen der Physik*, 349(16), 1238-1272.
[143] Razavy, M. (2003). *Quantum theory of tunneling.* World Scientific.
[144] Wolfram, T. (1978). Inelastic Electron Tunneling Spectroscopy: *Proceedings of the International Conference, and Symposium on Electron Tunneling*, Springer-Verlag, New York.
[145] Young, R., Ward, J. & Scire, F. (1972). The topografiner: an instrument for measuring surface microtopography. *Review of Scientific Instruments*, 43(7), 999-1011.
[146] Meyer, E., Hug, H. J. & Bennewitz, R. (2004). *Scanning probe microscopy: the lab on a tip.* Springer Science & Business Media.
[147] Tersoff, J. & Hamann, D. R. (1983). Theory and application for the scanning tunneling microscope. *Physical Review Letters*, 50(25), 1998.
[148] Tersoff, J. & Hamann, D. R. (1985). Theory of the scanning tunneling microscope. *Physical Review B*, 31(2), 805.
[149] Bardeen, J. (1961). Tunnelling from a many-particle point of view. *Physical Review Letters*, 6(2), 57.
[150] Bai, C. (2000). *Scanning tunneling microscopy and its application (Vol. 32).* Springer Science & Business Media.
[151] Gewirth, A. A. & Niece, B. K. (1997). Electrochemical applications of in situ scanning probe microscopy. *Chemical Reviews*, 97(4), 1129-1162.
[152] Halbritter, J., Repphun, G., Vinzelberg, S., Staikov, G. & Lorenz, W. J. (1995). Tunneling mechanisms in electrochemical STM - distance and voltage tunneling spectroscopy. *Electrochimica Acta*, 40(10), 1385-1394.
[153] Hugelmann, M. & Schindler, W. (2003). Tunnel barrier height oscillations at the solid/liquid interface. *Surface Science*, 541(1), L643-L648.
[154] Hugelmann, M. & Schindler, W. (2004). In Situ Distance Tunneling Spectroscopy at Au (111)/0.02 M HClO4 From Faradaic Regime to Quantized Conductance Channels. *Journal of the Electrochemical Society*, 151(3), E97-E101.
[155] Schindler, W., Hugelmann, M. & Hugelmann, P. (2005). In situ scanning probe spectroscopy at nanoscale solid/liquid interfaces. *Electrochimica Acta*, 50(15), 3077-3083.
[156] Simeone, F. C., Kolb, D. M., Venkatachalam, S. & Jacob, T. (2007). The Au(111)/electrolyte interface: a tunnel-spectroscopic and DFT investigation. *Angewandte Chemie International Edition*, 46(46), 8903-8906.

[157] Tymoczko, J., Schuhmann, W. & Bandarenka, A. S. (2013). A versatile electrochemical cell for the preparation and characterisation of model electrocatalytic systems. *Physical Chemistry Chemical Physics*, 15(31), 12998-13004.
[158] Wieckowski, A. (1999). *Interfacial electrochemistry: theory, experiment, and applications.* CRC Press.
[159] Gómez-Marín, A. M., Rizo, R. & Feliu, J. M. (2013). Some reflections on the understanding of the oxygen reduction reaction at Pt (111). *Beilstein Journal of Nanotechnology*, 4, 956.
[160] Gómez, R., Orts, J. M., Álvarez-Ruiz, B. & Feliu, J. M. (2004). Effect of temperature on hydrogen adsorption on Pt(111), Pt(110), and Pt(100) electrodes in 0.1 M $HClO_4$. *The Journal of Physical Chemistry B*, 108(1), 228-238.
[161] Biegler, T., Rand, D. A. J. & Woods, R. (1971). Limiting oxygen coverage on platinized platinum; relevance to determination of real platinum area by hydrogen adsorption. *Journal of Electroanalytical Chemistry and Interfacial Electrochemistry*, 29(2), 269-277.
[162] Daubinger, P., Kieninger, J., Unmüssig, T. & Urban, G. A. (2014). Electrochemical characteristics of nanostructured platinum electrodes–a cyclic voltammetry study. *Physical Chemistry Chemical Physics*, 16(18), 8392-8399.
[163] Lasia, A. (2006). On the mechanism of the hydrogen absorption reaction. *Journal of Electroanalytical Chemistry*, 593(1), 159-166.
[164] Vielstich, W., Yokokawa, H. & Gasteiger, H. A. (2009). *Handbook of fuel cells: fundamentals technology and applications.* John Wiley & Sons Inc.
[165] Jaffe, B., Cook, W. R. & Jaffe, H. (1971). *Piezoelectric Ceramics.* Academic Press Inc. New York.
[166] Curie, J. (1880). Développement par compression de l'électricité polaire dans les cristaux hémièdres à faces inclinées. *Bulletin de la Société française de minéralogie*, 3, 90.
[167] Curie, J. & Curie, P. (1880). Sur l'électricité polaire dans les cristaux hémièdre à faces inclinées. présentée par m. desains. *Comptes rendus de l'Académie des sciences*, 91, 383-6.
[168] Curie, J. & Curie, P. (1881). Contractions et dilatations produites par des tensions électriques dans les cristaux hémièdres à faces inclinées. *Compt. Rend*, 93, 1137-1140.
[169] Bentley, C. L., Perry, D., & Unwin, P. R. (2018). Stability and placement of Ag/AgCl quasi-reference counter electrodes in confined electrochemical cells. *Analytical chemistry*, 90(12), 7700-7707.
[170] Dean, J. A. (1999). *Lange's chemistry handbook*. McGrawHill, Inc.
[171] Horcas, I., Fernández, R., Gomez-Rodriguez, J. M., Colchero, J., Gómez-Herrero, J. W. S. X. M. & Baro, A. M. (2007). WSXM: a software for scanning probe microscopy and a tool for nanotechnology. *Review of scientific instruments*, 78(1), 013705.
[172] Battino, R. (Ed.). (2015). *Oxygen and Ozone: Solubility Data Series (Vol. 7).* Elsevier.
[173] Trasatti, S. & Petrii, O. A. (1991). Real surface area measurements in electrochemistry. *Pure and Applied Chemistry*, 63(5), 711-734.
[174] Kunze, J., Maurice, V., Klein, L. H., Strehblow, H. H. & Marcus, P. (2004). In situ STM study of the duplex passive films formed on Cu(111) and Cu(001) in 0.1 M NaOH. *Corrosion Science*, 46(1), 245-264.
[175] Gu, J. Y., Cai, Z. F., Wang, D. & Wan, L. J. (2016). Single-Molecule Imaging of Iron-Phthalocyanine-Catalyzed Oxygen Reduction Reaction by in Situ Scanning Tunneling Microscopy. *ACS Nano*, 10(9), 8746-8750.
[176] Tao, F., Tang, D., Salmeron, M. & Somorjai, G. A. (2008). A new scanning tunneling microscope reactor used for high-pressure and high-temperature catalysis studies. *Review of Scientific Instruments*, 79(8), 084101.

[177] Möller, R., Esslinger, A. & Koslowski, B. (1989). Noise in vacuum tunneling: application for a novel scanning microscope. *Applied Physics Letters*, 55(22), 2360-2362.
[178] Rasmussen, P. B., Hendriksen, B. L. M., Zeijlemaker, H., Ficke, H. G. & Frenken, J. W. M. (1998). The "reactor STM": A scanning tunneling microscope for investigation of catalytic surfaces at semi-industrial reaction conditions. *Review of Scientific Instruments*, 69(11), 3879-3884.
[179] Schoiswohl, J., Surnev, S. & Netzer, F. P. (2005). Reactions on inverse model catalyst surfaces: atomic views by STM. *Topics in Catalysis*, 36(1-4), 91-105.
[180] Bard, A. J., Fan, F. R. F., Kwak, J. & Lev, O. (1989). Scanning electrochemical microscopy. Introduction and principles. *Analytical Chemistry*, 61(2), 132-138.
[181] Pfisterer, J. H., Liang, Y., Schneider, O. & Bandarenka, A. S. (2017). Direct instrumental identification of catalytically active surface sites. *Nature*, 549(7670), 74.
[182] Lyding, J. W., Skala, S., Hubacek, J. S., Brockenbrough, R. & Gammie, G. (1988). Variable-temperature scanning tunneling microscope. *Review of scientific instruments*, 59(9), 1897-1902.
[183] Renner, C., Niedermann, P., Kent, A. D. & Fischer, O. (1990). A versatile low-temperature scanning tunneling microscope. *Journal of Vacuum Science & Technology A: Vacuum, Surfaces, and Films*, 8(1), 330-332.
[184] Borisenko, N., Zein El Abedin, S. & Endres, F. (2006). In situ STM investigation of gold reconstruction and of silicon electrodeposition on Au (111) in the room temperature ionic liquid 1-butyl-1-methylpyrrolidinium bis (trifluoromethylsulfonyl) imide. *The Journal of Physical Chemistry B*, 110(12), 6250-6256.
[185] Zhang, L., Zhang, Y., Zhang, X., Li, Z., Shen, G., Ye, M., Fan, C., Fang, H. & Hu, J. (2006). Electrochemically controlled formation and growth of hydrogen nanobubbles. *Langmuir*, *22*(19), 8109-8113.
[186] Wolfschmidt, H., Baier, C., Gsell, S., Fischer, M., Schreck, M. & Stimming, U. (2010). STM, SECPM, AFM and electrochemistry on single crystalline surfaces. *Materials*, 3(8), 4196-4213.
[187] Novoselov, K. S., Jiang, D., Schedin, F., Booth, T. J., Khotkevich, V. V., Morozov, S. V. & Geim, A. K. (2005). Two-dimensional atomic crystals. *Proceedings of the National Academy of Sciences of the United States of America*, 102(30), 10451-10453.
[188] Katsounaros, I. & Mayrhofer, K. J. (2012). The influence of non-covalent interactions on the hydrogen peroxide electrochemistry on platinum in alkaline electrolytes. *Chemical Communications*, 48(53), 6660-6662.
[189] Ataka, K. I. & Osawa, M. (1998). In situ infrared study of water−sulfate coadsorption on gold(111) in sulfuric acid solutions. *Langmuir*, 14(4), 951-959.
[190] Kolics, A. & Wieckowski, A. (2001). Adsorption of bisulfate and sulfate anions on a Pt(111) electrode. *The Journal of Physical Chemistry B*, 105(13), 2588-2595.
[191] Wang, D., Xin, H. L., Hovden, R., Wang, H., Yu, Y., Muller, D. A., DiSalvo, F. J., & Abruña, H. D. (2013). Structurally ordered intermetallic platinum–cobalt core–shell nanoparticles with enhanced activity and stability as oxygen reduction electrocatalysts. *Nature materials*, 12(1), 81.
[192] Zhang, J., Lima, F. H. B., Shao, M. H., Sasaki, K., Wang, J. X., Hanson, J., & Adzic, R. R. (2005). Platinum monolayer on nonnoble metal−noble metal core−shell nanoparticle electrocatalysts for $O_2$ reduction. *The Journal of physical chemistry B*, 109(48), 22701-22704.
[193] Bonde, J., Moses, P. G., Jaramillo, T. F., Nørskov, J. K. & Chorkendorff, I. (2009). Hydrogen evolution on nano-particulate transition metal sulfides. *Faraday discussions*, 140, 219-231.
[194] KC, S., Longo, R. C., Wallace, R. M. & Cho, K. (2015). Surface oxidation energetics and kinetics on $MoS_2$ monolayer. *Journal of Applied Physics*, 117(13), 135301.

[195] Neddermeyer, H. (1996). Scanning tunnelling microscopy of semiconductor surfaces. *Reports on Progress in Physics*, 59(6), 701.

[196] Kubby, J. A. & Boland, J. J. (1996). Scanning tunneling microscopy of semiconductor surfaces. *Surface Science Reports*, 26(3-6), 61-204.

[197] Jayabal, S., Saranya, G., Wu, J., Liu, Y., Geng, D., & Meng, X. (2017). Understanding the high-electrocatalytic performance of two-dimensional $MoS_2$ nanosheets and their composite materials. *Journal of Materials Chemistry A*, 5(47), 24540-24563.

[198] Le, D., Rawal, T. B. & Rahman, T. S. (2014). Single-layer $MoS_2$ with sulfur vacancies: structure and catalytic application. *The Journal of Physical Chemistry C*, 118(10), 5346-5351.

[199] Surrente, A., Dumcenco, D., Yang, Z., Kuc, A., Jing, Y., Heine, T., Kung, Y., Maude, D. K., Kis, A. & Plochocka, P. (2017). Defect Healing and Charge Transfer-Mediated Valley Polarization in $MoS_2$/$MoSe_2$/$MoS_2$ Trilayer van der Waals Heterostructures. *Nano letters*, 17(7), 4130-4136.

[200] Xu, S., Lei, Z. & Wu, P. (2015). Facile preparation of 3D $MoS_2$/$MoSe_2$ nanosheet-graphene networks as efficient electrocatalysts for the hydrogen evolution reaction. *Journal of Materials Chemistry A*, 3(31), 16337-16347.

[201] Ambrosi, A., Sofer, Z. & Pumera, M. (2015). 2H → 1T phase transition and hydrogen evolution activity of $MoS_2$, $MoSe_2$, $WS_2$ and $WSe_2$ strongly depends on the $MX_2$ composition. *Chemical Communications*, 51(40), 8450-8453.

[202] Tseung, A. C. C. & Chen K. Y. (1997). Hydrogen spill-over effect on Pt/$WO_3$ anode catalysts. *Catalysis Today*, 38(4), 439-443.

[203] Tsiouvaras, N., Martínez-Huerta, M. V., Paschos, O., Stimming, U., Fierro, J. L. G. & Peña, M. A. (2010). PtRuMo/C catalysts for direct methanol fuel cells: Effect of the pretreatment on the structural characteristics and methanol electrooxidation. *International Journal of Hydrogen Energy*, 35(20), 11478-11488.

[204] Nellist, M. R., Laskowski, F. A., Qiu, J., Hajibabaei, H., Sivula, K., Hamann, T. W. & Boettcher, S. W. (2018). Potential-sensing electrochemical atomic force microscopy for in operando analysis of water-splitting catalysts and interfaces. *Nature Energy*, 3(1), 46.